DEVELOPING HIGH-PERFORMANCE TITANIUM ALLOYS THROUGH ADDITIVE MANUFACTURING

DAN XINGDONG

PhD

The Hong Kong Polytechnic University

2026

The Hong Kong Polytechnic University

Department of Industrial and Systems Engineering

Developing High-Performance Titanium Alloys through Additive Manufacturing

DAN Xingdong

A thesis submitted in partial fulfillment of the requirements for the degree of Doctor of Philosophy

August 2025

CERTIFICATE OF ORIGINALITY

I hereby declare that this thesis is my own work and that, to the best of my knowledge and belief, it reproduces no material previously published or written, nor material that has been accepted for the award of any other degree or diploma, except where due acknowledgement has been made in the text.

_________________________(Signed)

Dan Xingdong (Name of student)

Abstract

Titanium and its alloys have long been valued for their high strength-to-weight ratio, corrosion resistance, and biocompatibility, making them crucial in aerospace, biomedical, and energy applications. Despite these advantages, a long-standing challenge persists in achieving an optimal balance between strength and ductility. Conventional alloying and thermomechanical processing strategies often enhance one property at the expense of the other. Recently, heterostructured materials have emerged as a promising design concept to overcome this trade-off by combining soft and hard phases to promote hetero-deformation-induced (HDI) strengthening. Simultaneously, additive manufacturing (AM), particularly laser-directed energy deposition (L-DED), enables spatial control of alloy composition and microstructure in a layer-by-layer manner, providing a new platform for the fabrication of titanium alloys with in-situ alloying and engineered heterostructures. This thesis explores AM-enabled strategies to enhance the mechanical performance of titanium alloys (especially α-titanium alloys) via two synergistic approaches: (i) in-situ aluminum alloying to optimize solid-solution strengthening and microstructural refinement, and (ii) spatially controlled compositional and structural heterogeneity to harness interface-mediated strengthening mechanisms.

Chapter 1 introduces the background of titanium and its alloys, including phase stability (α/α+β/β systems), recognized microstructures (equiaxed, lamellar, bimodal), and the strength–ductility dilemma; it also outlines the promise of AM for titanium alloys and key concepts in heterostructured materials (definitions, typical architectures—bimodal, gradient, lamellar—and their strengthening effects in overcoming the trade-off).

Chapter 2 describes the experimental methodology, including L-DED (LENS™) processing under controlled atmosphere, parameter selection and scan strategy, and fabrication of both homogeneous and heterogeneous Ti–Al builds alongside as-cast comparators; the comprehensive characterization methods (X-ray diffraction, optical microscopy, scanning electron microscopy with energy-dispersive spectroscopy, electron probe microanalysis, electron backscatter diffraction, transmission/scanning transmission electron microscopy), the mechanical property evaluation testing (vickers microhardness, uniaxial tension with digital image correlation), and thermal property measurements.

In Chapter 3, a series of Ti-Al alloys with Al concentrations ranging from 0 to 6 at% were fabricated via LENS™. Compared to conventional as-cast counterparts, the AM-fabricated Ti-6Al samples exhibited ~90% improvement in yield strength and ~100% enhancement in ductility. These superior properties are attributed to the formation of refined basketweave α grains and high dislocation density induced by the rapid solidification conditions of AM.

Chapter 4 builds upon this alloying strategy by designing a heterogeneous multi-gradient Ti/Ti-10Al architecture, achieved through dynamic modulation of powder feedstock during printing. The resulting structure consisted of alternating soft and hard regions with gradient composition and microstructure. This heterostructure achieved an impressive combination of ~760 MPa yield strength and ~33% fracture strain — outperforming both homogeneous Ti and Ti-10Al samples. The enhanced mechanical synergy is governed by the gradient stress partitioning, strain delocalization, and ductility compensation across chemically graded interfaces.

In Chapter 5, a lamellar Ti-3.5Al/Ti-6Al-4V heterostructure was developed to investigate the role of interfacial stresses in AM. The significant mismatch in thermal expansion coefficients (CTE) between the layers generated residual stress fields and geometrically necessary dislocations (GNDs), leading to strong back-stress hardening. This engineered structure exhibited a yield strength of ~1090 MPa and an elongation of ~10%, simultaneously exceeding the strength and ductility of homogeneous Ti-6Al-4V. Microstructural analyses confirmed that hetero-deformation-induced (HDI) hardening and crack deflection at interfaces played key roles in the observed mechanical enhancements.

Chapter 6 consolidates the major findings of this thesis into a unified framework, demonstrating how in-situ alloying, spatially engineered heterostructure, and interface design can be effectively integrated through AM to overcome the conventional strength-ductility trade-off in titanium alloys. Chapter 7 outlines future research directions, including: (i) the application of post-processing treatments such as cold rolling, annealing, and heat treatments to assess their impact on microstructural stability and mechanical synergy in AM-fabricated heterostructures; (ii) the integration of real-time monitoring during L-DED to enable microstructure-by-design strategies; and (iii) systematic comparisons between AM-induced and conventionally fabricated heterostructures to evaluate interfacial characteristics, dislocation-based strengthening mechanisms, and strain hardening behavior.

List of Publications

* Corresponding author.

1. **X. Dan**, C. Ren, Z. Song, S. Waqar, D. Zhang, M. Wang, Q. Liu, Y. Sun, X. Chen, W. Jiang, S. Ni, J. Lu, K.C. Chan, L. Liu, J. Pan, Y. Zhu, Z. Chen*. Exceptional strength and ductility in heterogeneous multi-gradient TiAl alloys through additive manufacturing, **Acta Materialia**, 2024, 281, 120395.
2. **X. Dan**, C. Ren, D. Zhang, X. Chen, Q. Liu, H. Shi, K.C. Chan, S. Ni, D. Xiang, H. Sun, Z. Liu, Z. Chen*. Enhanced strength and ductility in α-titanium alloys through in-situ alloying via additive manufacturing, **Journal of Alloys and Compounds** 2025, 180598.
3. **X. Dan**, C. Ren, H. Wen, X. Chen, H. Shi, Q. Liu, D. Zhang, K.C. Chan, Z. Chen*. Transcending the Rule-of-Mixtures via Coefficient of Thermal Expansion Mismatch-Driven Interfacial Strengthening in Additively Manufactured Ti Alloy Heterostructures. **Submitted**.
4. C. Ren, T. Liang, S. Jin, Z. Song, **X. Dan**, Q. Liu, Y. Sun, M. Wang, Y. Du, C. Wang, H. Pan*, Z. Chen*. Exceptional strength and antibacterial durability in hierarchically structured Cu-bearing 316L stainless steel through additive manufacturing. **Journal of Materials Research and Technology**, 2025, 36 5273-5285.
5. Q. Liu, C. Ren, Z. Song, **X. Dan**, J. Ju, T. Yang, S. Ni, J. Lu, L. Liu, J. Pan, Z. Chen*. High-strength and high-conductivity additively manufactured Cu-O alloy enabled by cellular microstructure. **Additive Manufacturing**, 2024, 88, 104244.
6. S. Waqar, S. Hussain, C. Ren, M. Wang, A. Nazir, **X. Dan**, C. Wang, Z. Chen*. Superior strength and energy absorption capability of LPBF metallic functionally graded lattice structures. **Thin-Walled Structures**, 2024, 205, 112471.
7. Q. Liu, S. Jin, C. Ren, D. Zhang, Z. Pu, H. Wen, Y. Ran, **X. Dan**, X. Chen, S. Ni, J. Lu, Chen, Z. Reducing solidification cracks and enhancing mechanical

performance in additively manufactured Cu-Ti alloys via chemical fluctuation manipulation. **Virtual and Physical Prototyping**, 20(1), e2522274.

8. X. Chen, C. Ren, H. Shi, Liu, Q., **X. Dan**, Y. Sun, ... & Z. Chen* . In-Situ Alloying of Titanium Nitride Nanoparticles via Laser Powder Bed Fusion for Fabricating High-Strength, Ductile Titanium Alloys. **Materials Science and Engineering: A**, 148921.

Conference

1. **X. Dan**, Y. Zhu, Z. Chen*. Exceptional strength and ductility in heterogeneous multi-gradient TiAl alloys through additive manufacturing, The 2nd International Conference on Heterostructured Materials, Chongqing, China, Dec 2024, **Poster (Best poster award)**.

2. **X. Dan**, Z. Chen*. Interfacial strain localization and dislocation-mediated strengthening in additive manufacturing heterostructures, The 1st International Conference on Future of AM, Singapore, Aug 2025, **Oral presentation**.

Acknowledgements

Firstly, I would like to extend my deepest gratitude to my chief supervisor, Prof. Zibin Chen, for his invaluable guidance and unwavering support throughout my entire Ph.D. research journey. Our weekly discussions have not only facilitated steady progress but also significantly deepened my critical thinking and my understanding of the scientific challenges encountered during my research. Prof. Chen's insightful questions and novel inspirations have been pivotal in encouraging my divergent thinking and enhancing the quality of my research. His assistance in experiment design and meticulous attention to my manuscript preparation, including rigorous questioning and constructive suggestions, have been instrumental in refining my work. Prof. Chen's profound expertise in material science and his dedication to student development truly embody the qualities of an exceptional supervisor.

I would also like to extend my heartfelt appreciation to my co-supervisor, Prof. K.C. Chan, whose valuable support, and insightful recommendations greatly enriched my manuscripts and broadened my scientific perspectives.

My sincere thanks go to all my colleagues at The Hong Kong Polytechnic University — Dr. Chuanxi Ren, Dr. Saad Waqar, Dr. Ze Pu, Dr. Dongdong Zhang, Dr. Hongning Wen, Mr. Qi Liu, Mr. Zizheng Song, Mr. Xuanlai Chen, Mr. Hengchao Shi, Mr. Shengxi Jin, Mr. Yifan Chen, Ms. Yating Ran, and Ms. Yixuan Sun, among many others — for their companionship, and fruitful discussions. Their constant friendship and collaborative spirit provided an engaging and supportive environment throughout my Ph.D. journey. Special acknowledgment to Dr. Ruien Hu and Mr. Kenneth, whose extensive training and dedicated assistance with the experimental facilities were indispensable to the successful execution of my experiments.

Additionally, I am deeply grateful to my cherished friends — Dr. Yihao Xu, Mr. Yicheng Chen, and many others scattered across different cities and countries — whose unwavering support, continuous encouragement, and heartfelt inspiration have greatly sustained my motivation and determination during both the rewarding moments and challenging times of this academic journey.

My profound gratitude extends to my family, whose unconditional love, understanding, and constant encouragement have provided a steadfast foundation for my studies and life in Hong Kong. Their unwavering belief in me has been an enduring source of strength, comfort, and inspiration.

Lastly, I would like to sincerely acknowledge myself — for the perseverance, resilience, courage, and unwavering dedication necessary to navigate and ultimately complete this extensive and challenging Ph.D. endeavor.

Table of Contents

List of Figures

List of Tables

NOMENCLATURE

AM	additive manufacturing	**OM**	optical microscopy
DED	directed energy deposition	**SEM**	scanning electron microscopy
SLM	selective laser melting	**EDS**	energy-dispersive X-ray spectroscopy
HCP	hexagonal close-packed	**BCC**	body-centered cubic
GND	geometrically necessary dislocation	**XRD**	X-ray diffraction analysis
Ti	titanium	**EBSD**	electron backscatter diffraction
Al	aluminium	**EMPA**	electron probe microanalysis
LENS	laser engineered net shaping	**WEDM**	wire-cut electrical discharge machining
YS	yield strength	**TEM**	transmission electron microscopy
UTS	ultimate tensile strength	**STEM**	scanning transmission electron microscopy
IPF	inverse pole figure	**SRO**	short-range ordering
KAM	kernel average misorientation	**DIC**	digital image correlation
HDI	hetero-deformation-induced	**CTE**	coefficient of thermal expansion

Chapter 1 Introduction

1.1 Introduction to titanium and its alloys

1.1.1 Classification and characteristics of titanium alloys

Titanium and its alloys have attracted significant interest across industries due to their exceptional combination of properties, including high specific strength, excellent fracture toughness, good high-temperature performance, and outstanding corrosion resistance. These distinctive attributes position titanium alloys as indispensable materials for demanding structural applications, notably within the aerospace, biomedical, automotive, military, marine, and architectural engineering sectors, as well as power generation industries [1-3]. The unique capability of titanium alloys to retain mechanical integrity under extreme environmental conditions, coupled with favorable weight-to-performance ratios, has driven continuous innovations and sustained research efforts aimed at improving and optimizing their performance.

Titanium is intrinsically an allotropic element, which contains two primary crystallographic phases: an α-phase with a hexagonal close-packed (hcp) structure at temperature below 882°C, and a β-phase with a body-centered cubic (bcc) structure stable above this critical temperature [4], as depicted in Fig. 1.1. This intrinsic allotropic transformation strongly influences the microstructure formation, mechanical properties, and ultimately, the applicability of titanium alloys in various engineering fields. Accordingly, titanium alloys are categorized based on their microstructures and constituent phases, mainly α, α+β, and β alloys, each possessing distinct properties optimized through alloying and thermomechanical treatments [5].

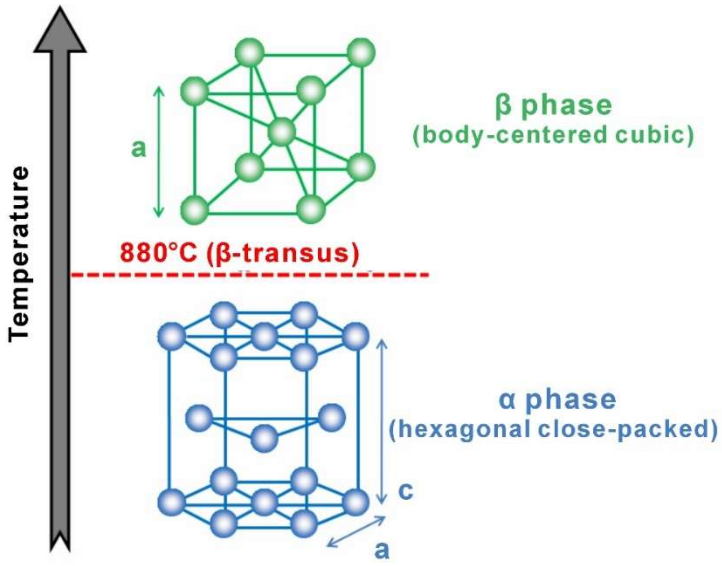

Fig. 1.1 Schematic drawing of the allotropic transformation in commercially pure titanium [6].

The introduction of alloying elements substantially modifies titanium's α/β-phase equilibria. Depending on their impact on the phase transformation temperature (β-transus) and relative stability of α or β phases, alloying elements are classified broadly into three categories [4, 6, 7]: (1) α-stabilizers: Elements such as aluminum (Al), gallium (Ga), tin (Sn), germanium (Ge), oxygen (O), and zirconium (Zr) raise the β-transus temperature, thus stabilizing the α-phase at higher temperatures. Al, notably, is widely used due to its effectiveness in enhancing strength and reducing alloy density. (2) β-stabilizers: Elements including vanadium (V), molybdenum (Mo), chromium (Cr), iron (Fe), nickel (Ni), manganese (Mn), cobalt (Co), and copper (Cu) lower the β-transus temperature, allowing the β-phase to remain stable at room temperature. V and Mo are particularly significant, commonly used to create alloys with improved strength and formability. (3) Neutral elements: Elements such as Sn and Zr exert minimal influence on the β-transus temperature, primarily affecting alloy strength and corrosion resistance without dramatically altering phase equilibria. The quantitative effect of typical alloying elements on β-transus temperatures and phase stability is illustrated schematically in Fig. 1.2.

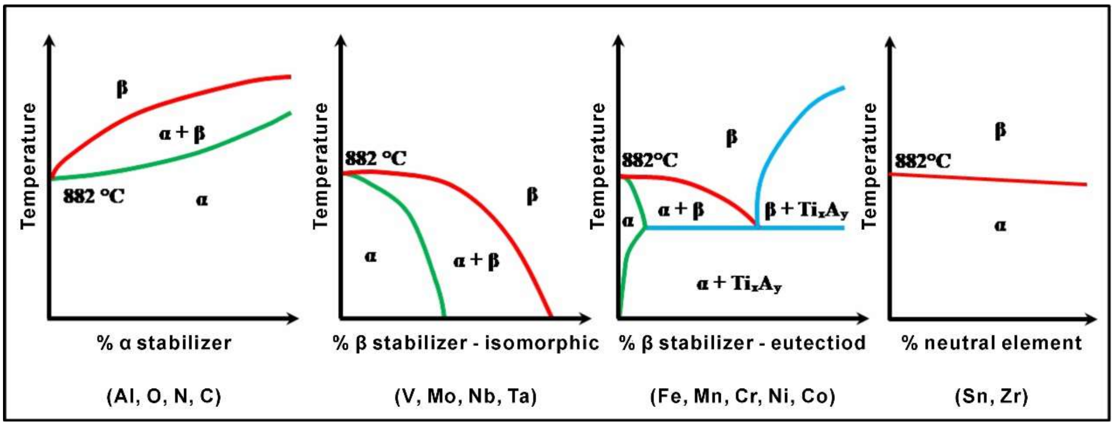

Fig. 1.2 Main alloy elements on the β-transus temperature and on the stability of phase α and β in titanium alloys [4].

Based on the predominant phases and their stability ranges, titanium alloys are classified into three fundamental categories: α-titanium alloys, α+β titanium alloys, and β titanium alloys (including metastable β alloys) [8, 9]: (1) α and near-α titanium alloys: These alloys consist primarily of α-phase with small amounts of β-stabilizers or neutral elements. They demonstrate excellent corrosion resistance, weldability, and creep resistance, making them ideal for high-temperature aerospace applications. However, they typically offer lower strength and limited formability at room temperature compared to β-containing alloys [6]. (2) α+β titanium alloys: These dual-phase alloys provide a balance between the properties of α and β phases. The α-phase imparts good strength and thermal stability, while the β-phase improves ductility and hardenability. This class includes the most widely used alloy in the world — Ti-6Al-4V, accounting for over 50% of global titanium alloy usage. The α+β alloys can be heat-treated and forged for enhanced mechanical properties and exhibit good corrosion and fatigue resistance [7, 10]. (3) β and metastable β titanium alloys: These alloys are stabilized to retain the β-phase at room temperature, either completely or partially, and can be categorized into metastable and stable β groups. Metastable β alloys offer high strength after solution treatment and aging, excellent formability, and lower elastic modulus, making them attractive for aerospace and biomedical load-bearing implants. However, they often exhibit poor creep resistance [11, 12]. A summary of representative commercial titanium alloys and their composition classifications is presented in Table 1.1.

Table 1.1 Classification and representative compositions of commercial titanium alloys [13].

Alloys	**Examples (wt%)**	**Typical applications**
α alloys	CP-Ti, Ti-5Al-2.5Sn	Heat exchangers, airframes
Near-α alloys	Ti-2.5%Cu Ti-8%Al-1%Mo-1%V Ti-6%Al-5%Zr-0.5%Mo-0.2%Si Ti-6%Al-4%Zr-2%Sn-2%Mo-0.08%Si Ti-5.5%Al-3%Zr-3.5%Sn-0.33%Mo-1%Nb-0.3%Si Ti-5.8%Al-3.5%Zr-4%Sn-0.5%Mo-0.7%Nb-0.3%Si	Jet engines, compressor disks
α+β alloys	Ti-6%Al-4%V Ti-4%Al-4%Mo-2%Sn-0.5%Si Ti-4%Al-4%Mo-4%Sn-0.5%Si Ti-6%Al-6%V-2%Sn Ti-6%Al-4%Zr-2%Sn-1%Mo	Implants, airframes, turbine blades

Β and Metastable β alloys	Ti-3%Al-8%V-6%Cr-4%Mo-4%Zr Ti-15%V-3%Cr-3%Sn-3%Al Ti-6%V-6%Mo-5.7%Fe-2.7%Al	Biomedical implants, springs

In summary, the classification of titanium alloys is fundamentally governed by the allotropic transformation behavior of titanium and the stabilizing effect of alloying elements. Through rational alloy design and control of α and β phase stability, titanium alloys offer a wide range of performance characteristics suitable for various structural, biomedical, and high-temperature applications. However, each class of alloy exhibits intrinsic trade-offs — particularly in balancing strength, ductility, and thermal stability — which motivates the need for advanced processing routes and microstructure design strategies discussed in the subsequent sections.

1.1.2 Typical microstructures and mechanical properties

The above section 1.1.1 indicates that the microstructure and mechanical properties of titanium alloys are intrinsically governed by their underlying phase constituents, which are determined by alloy composition, phase stability, thermal history, and fabrication processes. The morphology, size, volume fraction, and spatial distribution of α and β phases critically influence tensile strength, ductility, fatigue resistance, creep behavior, and fracture toughness. As a result, tailoring microstructure via processing and heat treatment is central to the development of titanium alloys for high-performance applications [1, 14-16]. Typical microstructures and their related mechanical properties in titanium alloys are introduced below:

1.1.2.1 Lamellar microstructures

Lamellar (or colony) microstructures are commonly formed by slow cooling from the β-phase field, particularly in α+β and near-β alloys. Upon cooling through the β-transus, nucleation of the α-phase occurs preferentially along specific crystallographic orientations within prior β grains, forming colonies of parallel α lamellae. These lamellae are typically embedded within retained β-phase at inter-lamellar boundaries, producing a hierarchical α+β structure [17, 18], as shown in Fig. 1.3.

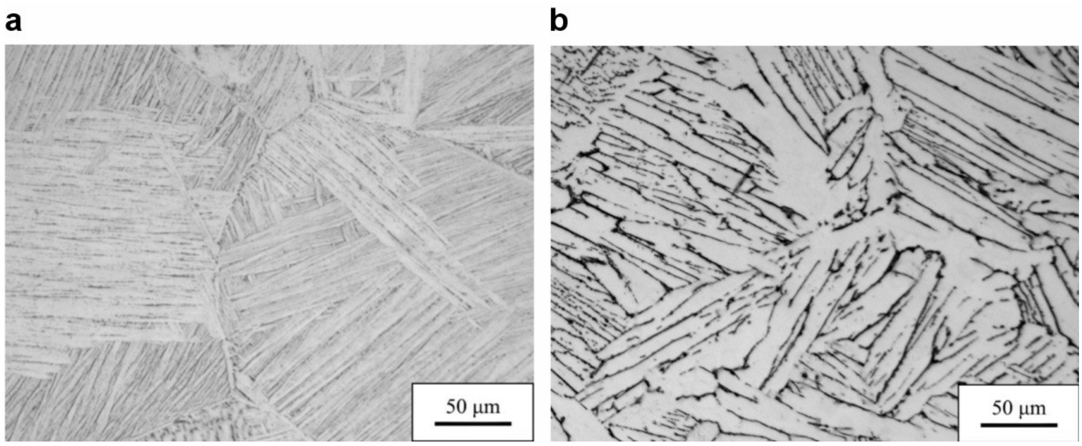

Fig. 1.3 Optical microscope images showing microstructure of Ti-5.4Al-3.7Sn-3.3Zr-0.5Mo-0.4Si alloy with typical lamellar microstructure [17].

The lamellar thickness and spacing are highly sensitive to the cooling rate: slower cooling generates coarse lamellae, enhancing creep resistance and fracture toughness, while faster cooling leads to finer α platelets, increasing strength but compromising ductility, as depicted in Fig. 1.4 [19, 20]. Furthermore, lamellar microstructures also exhibit a “Basketweave” and Widmanstätten morphology when α lamellae nucleate on multiple planes, forming interpenetrating colonies with different orientations. Basketweave structures result from random orientation of fine α plates, offering improved isotropy in mechanical properties. Widmanstätten structures, on the other hand, form through epitaxial growth of α on specific crystallographic planes in β, producing ordered lamellae with sharp interfacial angles [21]. Widmanstätten structures exhibit good fracture toughness and crack-arresting capabilities, commonly found in large-scale castings and forgings for aerospace engine disks. However, their anisotropic properties can lead to location-specific failure under complex loading, motivating continued microstructural refinement research.

In general, despite their relatively poor formability, lamellar structures offer superior resistance to crack propagation, high-temperature creep, and dwell fatigue — properties that are especially valuable for turbine components and aerospace engine parts [22, 23].

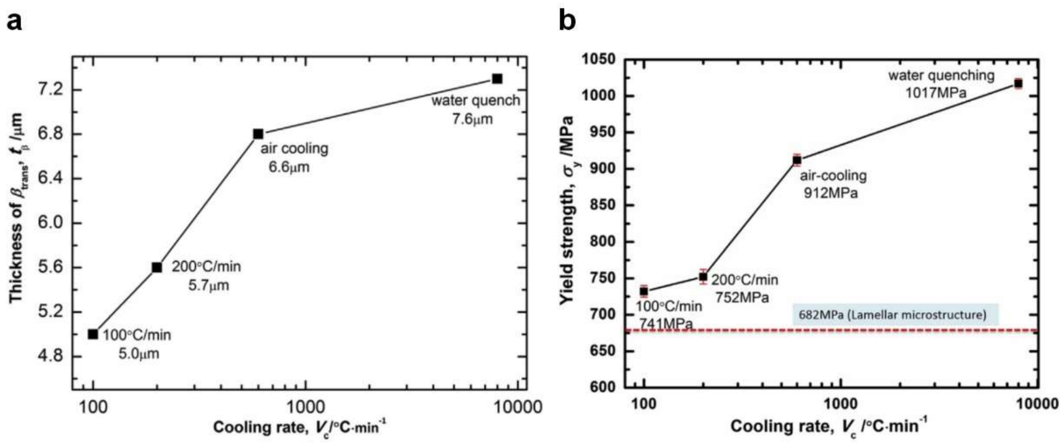

Fig. 1.4 The relationships between the cooling rate and resultant lamellar thickness and related mechanical properties. (a) Average thickness of transformed β regions in the bi-lamellar microstructures obtained through different cooling rates. (b) Yield strength of the bi-lamellar microstructures in the specimens at different cooling rates [20].

1.1.2.2 Equiaxed microstructures

Equiaxed microstructures consist of roughly spherical or globular α grains dispersed within a β or α+β matrix, typically formed through thermomechanical processing followed by recrystallization and sub-transus annealing (Fig. 1.5). Equiaxed α grains are often introduced through deformation below the β-transus and subsequent heat treatment that promotes grain growth and phase redistribution [24, 25]. Equiaxed structures are characterized by excellent ductility, fatigue resistance, and good formability, making them suitable for components subjected to complex forming operations or requiring high fracture toughness. Their isotropic mechanical properties also provide design advantages in components with non-directional loading. The size, volume fraction, and distribution of equiaxed α grains critically affect yield strength and elongation, often requiring careful optimization [26].

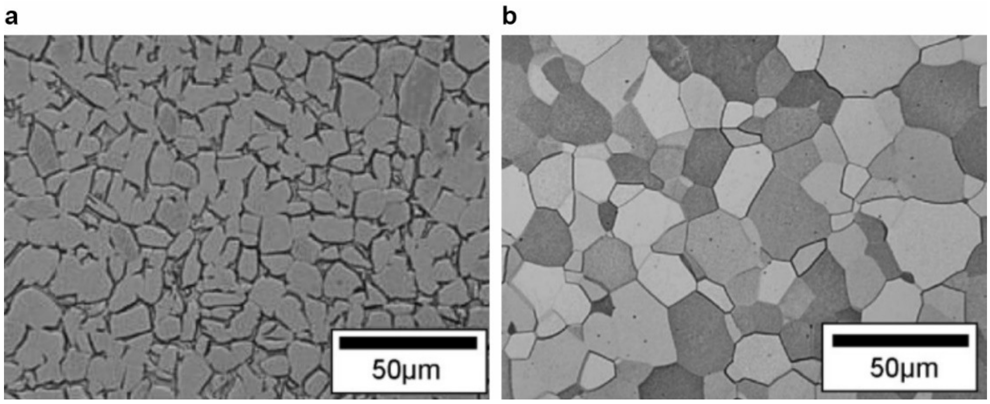

Fig. 1.5 Optical micrographs of typical equiaxed grains in titanium alloys at high working temperature [27, 28]. (a) Ti-6Al-4V. (b) Ti-6.85Al-1.6V.

1.1.2.3 Bimodal microstructures

Bimodal (or duplex) microstructures are composed of a combination of equiaxed primary α (α_P) grains and lamellar α+β regions. This structure is typically obtained by heat treating in the α+β region, allowing retention of equiaxed α grains while transforming β into lamellar α+β upon cooling [29], with the typical morphologies shown in Fig.1.6. The volume fraction of α_p and interlamellar spacing in the transformed β matrix significantly influences mechanical performance. This bimodal microstructure usually offers a favourable balance between strength and ductility: equiaxed α grains contribute to plasticity and fatigue resistance, while lamellar regions provide strength and crack deflection pathways. Bimodal structures are prevalent in high-performance α+β alloys like Ti-6Al-4V, where simultaneous optimization of tensile strength (~900–1100 MPa) and elongation (~10–15%) is often required [30].

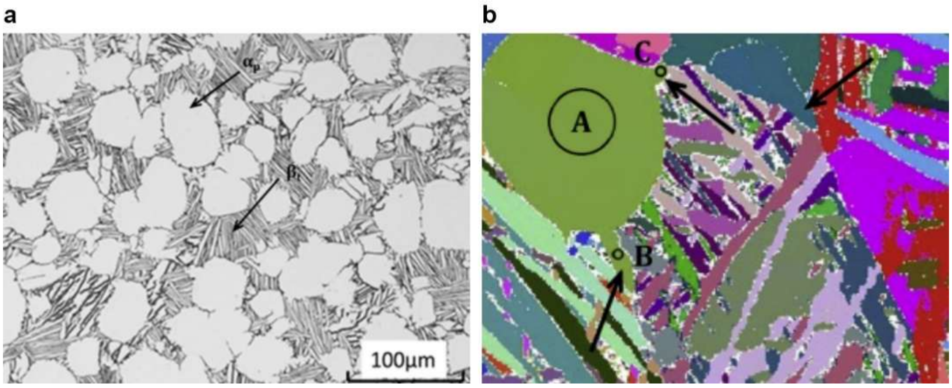

Fig. 1.6 Typical grain morphologies of bimodal microstructure in titanium alloys [29]. (a) OM image reveals the microstructure of Ti60 billet. (b) Corresponding EBSD image.

1.1.2.4 Martensitic microstructures

When titanium alloys, particularly metastable β or near-β alloys, are subjected to rapid cooling (e.g., water quenching from the β region), diffusionless transformation of β-phase results in the formation of martensitic α' (hcp) or α" (orthorhombic) phases [31, 32]. These acicular, needle-like structures exhibit ultrafine morphology and high dislocation densities (Fig. 1.7), imparting significant hardness and strength.

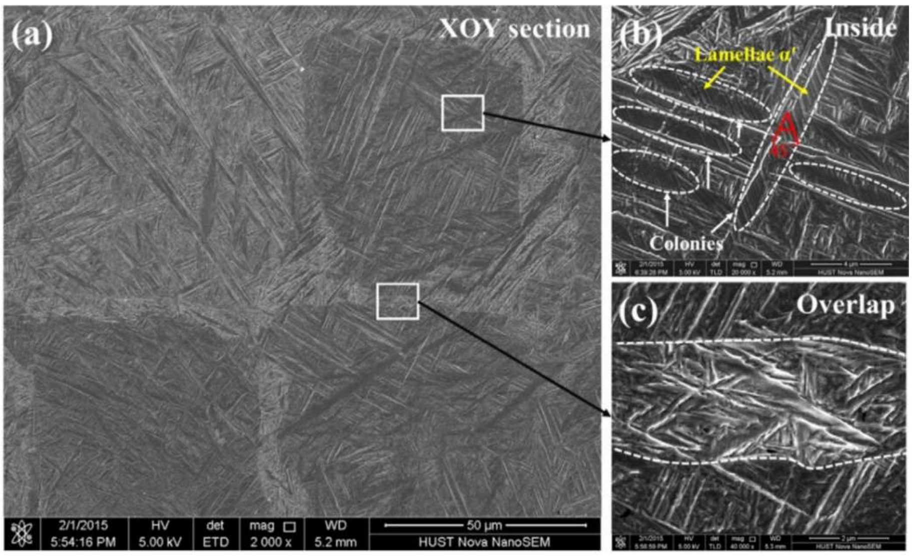

Fig. 1.7 SEM images of Ti-6Al-4V showing the typical martensitic structure induced by rapid solidification [33].

Martensitic microstructures are often metastable and can decompose into more thermodynamically stable α+β structures during aging or post-treatment, a process exploited in precipitation-hardening β-Ti alloys. However, as-quenched martensitic structures typically suffer from reduced ductility and toughness [34].

Typically, Ti-6Al-4V processed via selective laser melting (SLM) commonly exhibits fine α' martensite due to extremely high cooling rates (>10^6 K/s), resulting in elevated tensile strength (>1100 MPa) but limited elongation (<8%) [33]. Therefore, thermal post-treatments such as annealing or hot isostatic pressing (HIP) are often employed to restore ductility and tailor properties.

1.1.2.5 Grain boundary α and microtextured

In some processing conditions, especially in forged or additively manufactured parts, grain boundary α precipitates can form along prior β grain boundaries. These α layers act as barriers to dislocation motion and crack propagation but may also serve as sites for fatigue crack initiation, particularly under cyclic loading [16]. The crystallographic texture developed during deformation and phase transformation also plays a vital role. Strong basal textures in α-phase can cause anisotropic yield behaviour and mechanical response [35, 36]. Controlling the texture via thermomechanical processing or AM printing strategies is therefore critical in titanium component design.

1.1.2.6 Microstructure and mechanical properties relationships

The above sections introduced typical microstructures in titanium alloys, and their resultant mechanical properties. In summary, the interplay between microstructure and mechanical behaviour in titanium alloys can be broadly understood through the following relationships in Table 1.2:

Table 1.2 Typical microstructure and resultant mechanical performance in titanium alloys [7, 8, 14].

Microstructure	**Strength**	**Ductility**	**Fatigue resistance**	**Fracture toughness**
Coarse lamellar	Low-Medium	Medium	High	High
Fine lamellar	Medium-High	Medium-Low	Medium	Medium
Equiaxed	Medium	High	High	Medium-High
Bimodal	High	Medium-High	High	High
Martensitic	Very High	Low	Low	Low
Widmanstätten	Medium	Medium	High	High

These structure–property relationships reveal a central theme in titanium alloy design: the strength–ductility trade-off. Finer structures (e.g., martensite) improve strength but often sacrifice ductility, whereas coarse-grained or equiaxed structures enhance toughness and elongation but with lower strength. Bimodal and engineered heterogeneous structures are often employed to optimize the balance.

In summary, the microstructural landscape of titanium alloys is diverse and highly tunable through processing and composition. From lamellar to martensitic and bimodal to Widmanstätten architectures, each microstructure provides a distinct suite of mechanical properties. However, the intrinsic trade-offs — particularly between strength and ductility — pose persistent challenges in alloy design. These limitations motivate the exploration of new microstructural engineering strategies, such as additive manufacturing or heterostructure design, to dissociate the strength-ductility trade-off deformation behaviours and unlock next-generation titanium alloy performance.

1.2 Basics of AM for titanium alloys

1.2.1 Introduction to AM

Additive manufacturing (AM) has emerged as a disruptive and transformative technology in the field of advanced materials processing. Unlike conventional fabrication methods such as casting, forging, and machining, AM builds three-dimensional (3D) components in a layer-by-layer fashion directly from digital models [37, 38]. This near-net-shape capability not only minimizes material waste but also allows for the fabrication of components with complex geometries and internal features that would be difficult or impossible to produce using traditional approaches [39]. Due to its ability to combine design freedom, rapid prototyping, and material efficiency, AM has been increasingly adopted in high-performance applications across aerospace, biomedical, energy, and automotive industries [40, 41]. In aerospace, AM enables the production of lightweight yet structurally efficient parts, such as topology-optimized brackets and fuel injector nozzles that would otherwise require assembly of multiple subcomponents [42]. In the biomedical field, AM supports patient-specific implant design based on medical imaging, allowing for customized geometries that promote better biocompatibility and osseointegration [43]. In the energy and automotive industries, AM accelerates product development by facilitating the rapid fabrication and repair of hardware components, such as heat exchangers, tooling fixtures, and pressure vessels [44, 45].

From a technological standpoint, AM encompasses a broad family of processing techniques, each offering unique capabilities tailored to specific material systems and design requirements. Among the most prominent methods used for metallic materials are selective laser melting (SLM) [46], electron beam melting (EBM) [47, 48], direct energy deposition (DED) [49, 50], and wire arc additive manufacturing (WAAM) [51], as illustrated in Fig. 1.8.

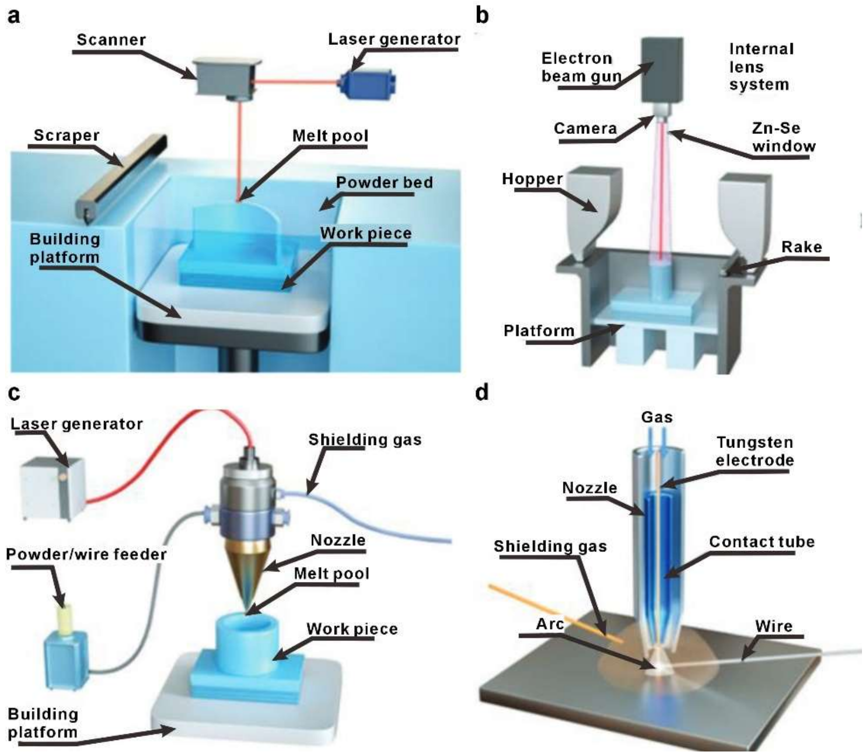

Fig. 1.8 The schematic drawing of some commonly used metal AM technologies. (a) Selective laser melting (SLM). (b) Electron beam melting (EBM). (c) Laser-directed energy deposition (DED). (d) Wire-arc additive manufacturing (WAAM) [52].

The different procedures of these AM technologies provide them with distinct characteristics. Normally, SLM and EBM are more suitable for small-scale fabrication since they guarantee the accuracy of parts and surface quality. In comparison, DED and WAAM can manufacture large-sized components with high printing rates and can provide more flexibility in compositional and microstructural design. The characteristic features of these commonly used AM technologies were summarized in Table 1.3. Despite the differences, these methods are classified as fusion-based AM processes, where a high-energy heat source — typically a laser or an electron beam — is used to locally melt metallic wires or powders, forming a transient melt pool that rapidly solidifies to create each layer [53, 54]. In fusion-based AM, the melt pool formation and its subsequent solidification are central to defining the final microstructure. When the powder bed is irradiated by the heat source, the local temperature can rise sharply above the melting point of the metal, leading to the rapid creation of microscale melt pools. These melt pools then solidify under steep thermal gradients (~10^7 K/m) and high cooling rates (~10^6 K/s), conditions that promote nonequilibrium solidification phenomena, such as grain refinement, cellular or dendritic morphologies, and even martensitic transformations in specific alloy systems [55-57].

Table 1.3 Characteristic features of various fusion-based AM techniques [56, 58-60].

	Powder bed fusion		Directed energy deposition	
Techniques	Selective laser melting	Electron beam melting	Laser engineered net shaping	Wire arc additive manufacturing
Parameters	Laser power; Scan speed; Hatch spacing; Layer thickness	Beam power; Scan speed; Hatch spacing; Layer thickness; Pre-heat temperature	Laser power; Powder feedrate; Scan speed; Hatch spacing; Layer thickness	Arc power; Wire diameter; Wire feedrate; Travel speed
Typical output power (W)	100 – 600	500 – 3000	1000 – 3000	1000 – 5000
Beam spot size (mm)	0.04 – 0.5	0.4 – 1	1 – 3	1 – 10

Characteristic size of melt pool (mm)	~ 0.1	~ 0.1	~ 0.1	~ 1
Temperature gradient (K/mm)	$10^3 - 10^4$	$10^2 - 10^3$	$10^2 - 10^4$	10 – 200
Cooling rate (K/s)	$10^5 - 10^7$	$10^3 - 10^5$	$10^3 - 10^4$	$10^2 - 10^3$
Main features	High precision	Vacuum chamber; Low residual stress	Multi-material printing; Large component fabrication ability	High deposition rates; Large component fabrication ability

The thermal environment during AM is further complicated by repeated thermal cycling — as each layer is deposited, it reheats and partially remelts the layers beneath, resulting in complex thermal histories [61]. This cumulative heating and cooling effect can lead to intrinsic heat treatment phenomena, where solid-state transformations (e.g., precipitation, recovery, recrystallization) occur within the already deposited layers [62, 63]. Moreover, the process parameters — including laser/electron beam power, scan speed, hatch spacing, and layer thickness — have profound effects on melt pool dynamics and final material quality. These are often combined into a single figure of merit known as volumetric energy density (VED), defined as $VED = \frac{P}{vht}$, where P is laser beam power, v is scan speed, h is hatch distance, and t is layer thickness [64]. While VED has proven useful for basic process control. At low VED, insufficient melting causes lack-of-fusion defects with irregular pores. At excessively high VED, overheating can lead to keyholing, vaporization, and the formation of spherical gas porosity. Therefore, achieving full density and optimal mechanical properties requires operating within a narrow and well-controlled processing window [65, 66].

Despite these advances, microstructural control in AM remains a central challenge. The highly localized and transient thermal gradients lead to strong epitaxial growth of grains, especially along the build direction, often resulting in anisotropic properties. For cubic metals such as titanium and nickel-based alloys, epitaxial growth tends to align with the <100> direction, driven by the thermal gradient and solidification front velocity [67]. Residual stresses generated during thermal contraction further contribute to high dislocation densities and can lead to warping or cracking if not properly mitigated [68]. In addition, unlike the traditional fabrication strategies, in which adding alloy elements can effectively control the overall microstructure, these alloying strategies in AM affect microstructural evolution through the phenomenon of constitutional supercooling, which determines the morphology of the solidification front (planar → cellular → dendritic → equiaxed, as schematically shown in Fig. 1.9), is governed by the equation:

$$Q = m_l c_O (k - 1)$$

where m_l is the slope of the liquidus, c_0 is the solute concentration in a binary alloy in wt% and k is the partition coefficient [69]. Such compositional modifications induce supercooling, altering grain morphology from columnar to equiaxed and refining grain sizes, significantly influencing mechanical properties. A systematic analysis of these compositional effects on supercooling behavior is summarized comprehensively in Table 1.4, highlighting critical insights into alloying strategies within AM contexts.

Table 1.4 Calculated $m_l(k-1)$ values for elements in titanium [69-71].

Element	$\boldsymbol{m_l}$	$\boldsymbol{k}$	$\boldsymbol{m_l(k-1)}$

Hf	-0.7	→1	→0
Al	-2.1	→1	→0
V	-4.7	→1	→0
Sn	-0.8	→1	→0
Zr	-2.4	0.86	0.3
Pb	-6.6	0.84	1.1
Cr	-8.1	0.81	1.5
Pd	-10.5	0.77	2.4
Pt	-8.4	0.70	2.5
Bi	-5.5	0.54	2.5
Fe	-18	0.79	3.8
Cu	-10.6	0.39	6.5
Mn	-13.1	0.55	5.9
Y	-8.8	0.09	7.93
O	27.6	1.37	10.8
Ni	-23.8	0.4	14.3
Si	-32.5	0.35	21.7

In summary, additive manufacturing offers a unique platform to design not only the geometry but also the microstructure of metallic components. By controlling solidification dynamics and thermal cycles at the microscale, AM enables the formation of fine, hierarchical, and spatially varied microstructures that can be engineered to achieve tailored mechanical performance, as depicted in Fig.1.9 below. However, the complexity of the process also introduces challenges in defect control, reproducibility, and predictability. A deeper understanding of microstructure evolution and its relationship with process parameters remains crucial for fully unlocking the potential of AM in the design of next-generation high-performance materials.

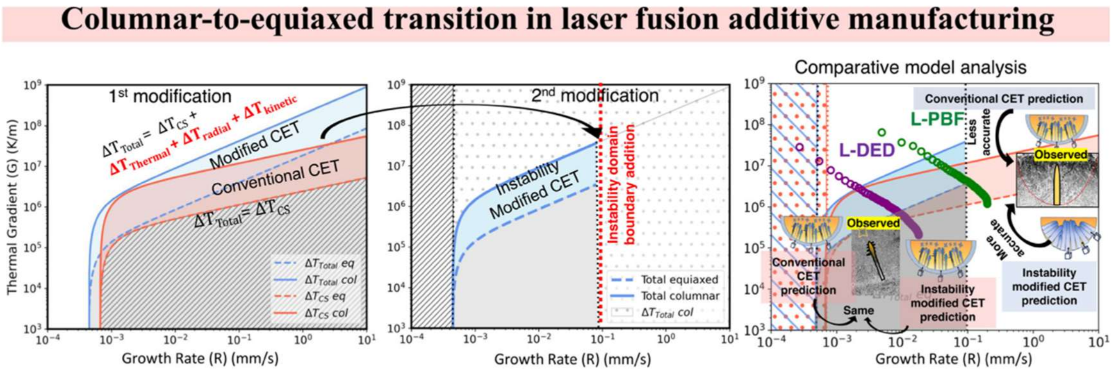

Fig. 1.9 The columnar-to-equiaxed transition in laser fusion AM [72].

1.2.2 Recent advances in AM titanium alloys

Titanium alloys are especially well-suited for AM due to their high affinity for oxygen and nitrogen, low thermal conductivity, and relatively high melting point, which pose challenges for traditional processing [73, 74]. Fusion-based AM processes such as SLM, EBM, and DED are capable of fabricating both fully dense and architected titanium components with minimal post-processing. These methods allow for intricate part geometries with site-specific properties and hierarchical microstructures. The vacuum or inert gas environments used in AM processes are particularly advantageous for minimizing contamination during the melting and solidification of titanium alloys [75-77].

The primary benefit of AM for titanium alloys lies in its ability to tailor complex microstructures, thereby achieving properties unattainable through traditional fabrication methods. The thermal history during AM — including rapid melting and solidification followed by repetitive thermal cycling — critically influences microstructural formation and evolution. This has been extensively detailed in the review by DebRoy et al. [38], where it was shown that local melt pool conditions directly impact microstructure morphology, texture development, grain refinement, and defect formation. For instance, EBM-produced titanium alloys, notably Ti-6Al-4V, typically exhibit lamellar α+β microstructures within columnar prior-β grains, as reported by Mohsen [78]. These structures result from relatively moderate cooling rates facilitated by higher preheat temperatures (600 – 700°C). Lamellar structures provide beneficial combinations of strength, ductility, and fracture toughness, particularly important for aerospace applications requiring high fatigue resistance and damage tolerance. On the other hand, the faster cooling rates of SLM predominantly yield martensitic α' phases that significantly enhance tensile strength but decrease ductility [79, 80]. Thus, post-processing heat treatments are often essential for achieving optimal mechanical properties in SLM-produced titanium alloys.

Mechanical properties of AM titanium alloys often surpass their traditionally manufactured counterparts, particularly in strength and fatigue resistance. Tshephe et al. [81] reviewed various AM-produced Ti alloys, noting that optimized SLM-produced Ti–6Al–4V achieved tensile strengths of approximately 1200 MPa, significantly exceeding traditionally cast or forged Ti–6Al–4V. Similarly, Xu et al. [82] fabricated commercial pure Ti by SLM, achieving a good combination of strength and ductility, which usually cannot be attained by conventional manufactured counterparts.

In addition, the rapid evolution of AM technologies has not only advanced conventional pure titanium and α+β titanium alloys but has also invigorated interest in novel alloy compositions better suited for AM-specific conditions. For example, metastable β-titanium alloys, such as Ti–24Nb–4Zr–8Sn (Ti2448), are receiving increasing attention due to their low elastic modulus, superior biocompatibility, and excellent mechanical properties ideal for biomedical implants. EBM and SLM processing of these metastable β-alloys offer refined grain structures and improved fatigue resistance, presenting notable advantages over traditional alloys for biomedical applications, including orthopedic implants and bone substitutes [11, 83]. Moreover, titanium aluminide (TiAl) alloys, with their exceptional high-temperature strength and oxidation resistance, are gaining traction in aerospace and automotive industries as lightweight structural materials [84]. However, producing crack-free TiAl components using AM techniques such as EBM remains challenging due to their inherent brittleness. Huang et al. [85] described successful strategies to fabricate nearly full-density TiAl components with minimal internal defects by utilizing SLM, highlighting ongoing advances and challenges in AM fabrication of TiAl alloys.

Despite the clear advantages, significant challenges remain for widespread industrial adoption of AM titanium alloys. Cost-effectiveness, reproducibility, and scalability of AM processes and materials are ongoing concerns. Furthermore, high material and operational costs, especially for powder-based processes like SLM and EBM, limit broader adoption in cost-sensitive industries. Continuous improvements in powder metallurgy, recycling strategies, and processing efficiencies are thus critical. Moreover, comprehensive understanding and control over microstructure evolution during complex thermal cycles remain incomplete. Future research must address these gaps, integrating high-fidelity simulation models, real-time monitoring technologies, and advanced material characterization tools to establish robust process–structure–property relationships. Most importantly, titanium and its alloys have been widely used as structural materials, the inherent strength–ductility trade-off in titanium alloys, however, remains a significant challenge even in AM contexts. To address this, besides traditional alloying additions which have been discussed above, recent research efforts have proposed and focused on heterostructure engineering — deliberate creation of spatially heterogeneous microstructures to synergistically enhance both strength and ductility, which will be discussed in the following sections.

1.3 Basics of heterostructure engineering

1.3.1 Fundamentals of heterostructured materials

The long-standing strength–ductility trade-off has constrained the development of structural metallic materials for decades. Traditionally, high strength is achieved through grain refinement or solid solution strengthening at the expense of plasticity, whereas high ductility is often associated with coarse-grained microstructures that lack sufficient barriers to dislocation motion. To transcend this limitation, a new class of materials — heterostructured (HS) materials — has emerged. These materials are designed with spatially distinct microstructural zones that vary significantly in strength, grain size, phase composition, or physical properties [86-88]. Unlike conventional homogeneous microstructures, HS materials leverage mechanical incompatibility between constituent domains to induce back-stress and forward-stress fields during plastic deformation. This interaction gives rise to hetero-deformation-induced (HDI) strengthening and HDI strain hardening, the primary mechanisms underlying their superior mechanical performance [89, 90]. As shown schematically in Fig. 1.10, the deformation of soft domains is constrained by adjacent hard regions, leading to the accumulation of geometrically necessary dislocations (GNDs) at interfaces. These dislocations generate long-range internal stress fields — back-stresses in soft zones and forward-stresses in hard zones — that elevate flow stress and enhance strain hardening, thereby delaying necking and improving uniform elongation [90, 91].

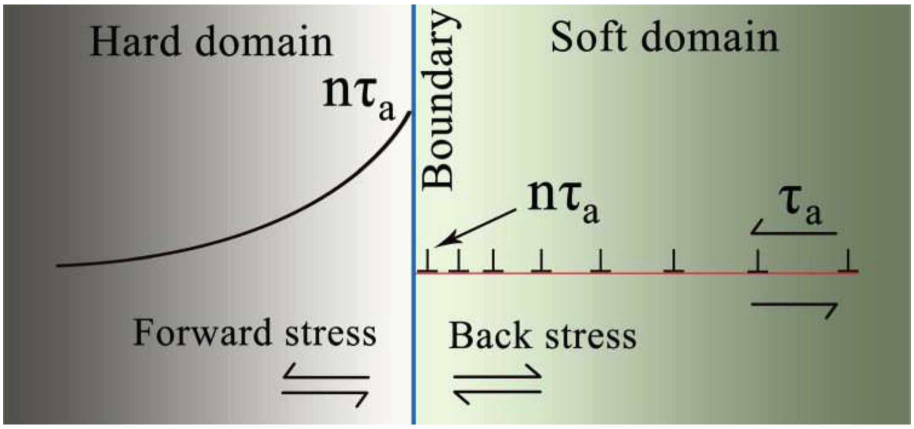

Fig. 1.10 Schematics of a GND pile-up, inducing back stress in the soft domain, which in turn induces forward stress in the hard domain [89].

Historically, the concept of heterostructured materials has deep roots in natural biological systems, such as the nacre and bamboo structure, which exhibit exceptional mechanical resilience and toughness due to their inherently heterogeneous microstructures. Inspired by these biological examples, recent materials science research has extensively explored bio-inspired structural designs, leading to a burgeoning interest in synthetic heterostructured metallic materials. The increasing availability of advanced manufacturing techniques, for example, rolling followed by annealing (thermos-mechanical processing), accumulative roll bonding, severe plastic deformation (SPD), powder metallurgy, surface mechanical attrition treatment (SMAT), and AM, has significantly facilitated the intentional design and fabrication of complex heterostructures in metallic systems, driving rapid advancements in this field [92-94].

In recent decades, various types of heterostructured materials have been developed to achieve targeted combinations of mechanical properties. Key examples include gradient structures, lamellar and bimodal structures, harmonic core-shell structures, and layered composites, each distinguished by the specific arrangement and distribution of microstructural features:

(a) Gradient Structures (GS): These structures exhibit spatial gradients in grain size, phase composition, or mechanical properties, typically transitioning smoothly from hard, fine-grained surfaces to softer, coarse-grained interiors. Gradient structures are particularly effective in delaying localized deformation and improving damage tolerance. For example, Lu et al. designed a pure copper sample with controllable patterning of gradient nanotwinned components, exhibiting extraordinary combination of strength and ductility, which cannot be attained by homogeneous counterparts [95, 96].

(b) Heterogeneous Lamella Structures (HLS): Characterized by alternating layers of fine-grained hard zones and coarse-grained soft zones, these materials exhibit strong interface strengthening and superior strain-hardening capabilities. Lamellar structures have been extensively investigated in metals such as copper, steel, and titanium, consistently demonstrating exceptional combinations of strength and ductility [97, 98].

(c) Bimodal and Harmonic Structures: Bimodal structures integrate a mixture of coarse and ultrafine grains uniformly distributed throughout the material, promoting strain compatibility and efficient dislocation storage. Harmonic structures adopt a core-shell arrangement, with hard cores embedded within softer shells, optimizing mechanical stability under complex loading conditions [99-101].

(d) Layered and Multilayered Structures: Layered composites consist of alternating thin layers of different metallic or composite materials, offering high strength and toughness through interfacial mechanisms such as dislocation pile-ups, interfacial sliding, and stress transfer between layers [102, 103].

The abovementioned advanced manufacturing techniques and typical resultant heterogeneous microstructure are depicted in Fig. 1.11. The distinct microstructural configurations induced tailored stress distributions and deformation mechanisms, enabling a flexible, application-driven approach to material design.

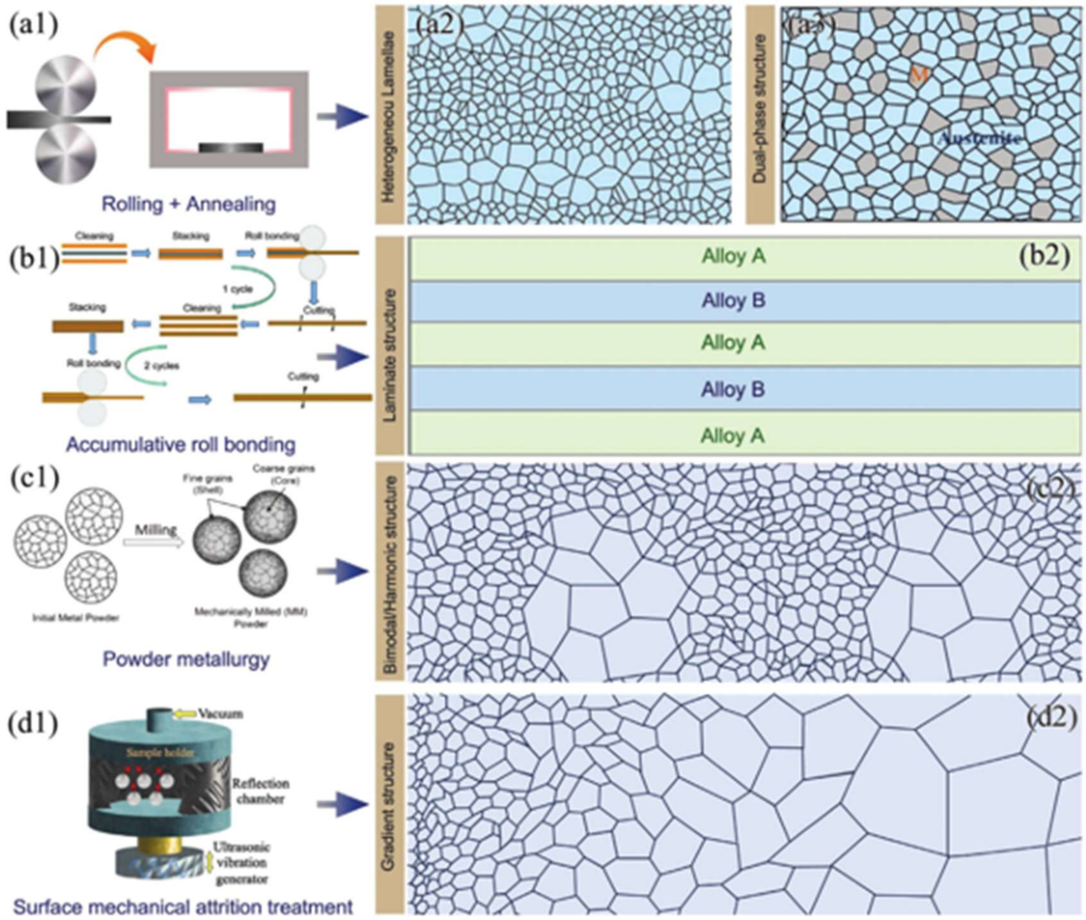

Fig. 1.11 Schematic illustration of the typical manufacturing and processing methods and resultant heterogeneous microstructures [87]. (a1-a3) The method of rolling and annealing used to produce heterogeneous lamellae structure and dual/multi-phase structure [104]. (b1, b2) ARB method employed to fabricate the laminate structure [105]. (c1, c2) Mechanical milling process used to prepare bimodal/harmonic structure [106]. (d1, d2) SMAT processing route and the produced gradient structure [107].

1.3.2 Recent advances and applications in metallic heterostructure

The above section thoroughly reviewed the fundamental conception and typical manufacturing techniques of HS materials. Recent research has substantially expanded the understanding and application of heterostructured metallic materials in various alloy systems, including copper, aluminum, steel, magnesium, titanium, and medium/high entropy alloys. Significant progress has been achieved through experimental investigations, advanced characterization techniques, and multiscale modeling, which together have elucidated fundamental deformation mechanisms and guided innovative structural designs. This section delivers systematic reviews of metallic heterostructure materials.

(a) Copper Alloys: Copper and its alloys were among the first systems explored for heterostructure design. K. Lu et al. [108] pioneered HS copper with a gradient nanograined surface produced by surface mechanical attrition treatment (SMAT), achieving superior tensile strength and ductility combination compared to uniform nanograined Cu. Subsequent developments introduced lamellar, bimodal, and core-shell HS Cu structures, where dislocation accumulation at boundaries, twin formation, and grain rotation play central roles in strain accommodation [109, 110].

(b) Aluminum Alloys: In aluminum systems, bimodal and harmonic structures have demonstrated notable performance. Gradient nanostructures created by friction stir processing (FSP) enable progressive yielding and uniform stress distribution. Studies also highlight that dislocation pile-ups at hard/soft interfaces enhance back stress hardening [111]. The adoption of SPD and controlled recrystallization has further expanded the design space of HS Al alloys.

(c) Steel Systems: Heterostructure engineering has shown great promise in both carbon and stainless steels. Dual-phase (ferrite–martensite) [112] and TRIP-assisted (transformation-induced plasticity) steels [113] inherently possess heterogeneity. However, deliberate lamination, gradient, or bimodal designs enhance mechanical synergy. For example, layered bainitic-austenitic steels show ultra-high strength (~1.2 GPa) while maintaining elongation above 25%, owing to progressive strain-induced martensitic transformation and HDI stress stabilization [114].

(d) Magnesium Alloys: Given the limited slip systems in Mg due to its HCP structure, achieving ductility is a primary challenge. HS strategies, especially bimodal and dual-texture structures, have improved formability. Rolling-bonding (HPRB) processed AZ91 alloy with a fine-grained surface and coarse-grained interior achieved high strength (~400 MPa) and elongation (~15%) simultaneously. It has been reported that diversified strain accommodation mechanisms are stimulated by strain partitioning near hetero-interfaces in the multiscale hetero-structure. In particular, non-basal slips have been activated effectively relaxing local stress concentration and achieving stable plastic flow at a high-stress state, which is beneficial to improving strain-hardening ability and strength-ductility synergy [115].

(e) Medium and High Entropy Alloys: Unlike traditional alloys based on one or two dominant elements, MEAs and HEAs are characterized by severe lattice distortion, sluggish diffusion, and high configurational entropy, which suppresses long-range ordering and stabilizes disordered solid solution phases. However, compositional energy fluctuations intrinsic to their multicomponent nature also facilitate the emergence of chemical and structural heterogeneities at various scales. These heterogeneities, often deliberately introduced through thermomechanical or processing strategies, provide a productive platform for hetero-deformation-induced (HDI) strengthening, leading to superior strain hardening capability and mechanical synergy [116]. A notable example is the cold-rolled and partially recrystallized CoCrNi medium entropy alloy (MEA), which achieved a heterogeneous grain structure (HGS) comprising nano-grains (<250 nm), ultrafine grains (250 nm–1 μm), and micron-sized grains (~2.3 μm), with an overall average grain size of 330 nm. Tensile testing at 298 K yielded a remarkable tensile yield strength of 1150 MPa and uniform elongation exceeding 30%. Even more strikingly, the yield strength and ductility further increased at cryogenic temperatures (77 K), attributed to enhanced strain hardening and twin formation. In contrast, a uniform-grained CoCrNi MEA with a similar average grain size (~199 nm) exhibited comparable strength but only ~2% elongation, underscoring the critical role of grain size heterogeneity and HDI hardening in mechanical enhancement [117].

(f) Titanium Alloys: While the abovementioned alloy systems have demonstrated the transformative potential of hierarchical heterogeneities in achieving superior mechanical performance, among these, titanium and its alloys stand out due to their broad application, and their long-standing challenges in overcoming the strength–ductility trade-off. One of the earliest and clearest demonstrations of HDI strengthening in titanium was achieved in commercially pure Ti through the introduction of a lamellar heterostructure. Wu et al. [98] employed asymmetric rolling followed by partial recrystallization to generate alternating regions of coarse grains (CGs) and ultrafine grains (UFGs). This periodic microstructure activated back-stress hardening during tensile deformation, where GNDs accumulated at the CG/UFG interfaces. The resulting structure achieved a yield strength of 900 MPa — comparable to fully UFG Ti — while maintaining elongation close to that of CG Ti. The simultaneous improvement was attributed to effective strain partitioning and HDI stress contributions, which delayed necking and enabled more uniform plastic flow. Similar observations were made by Li et al. [118], who found that the alternating coarse and fine grain layers led to elevated <c+a> dislocations and densely populated pile-ups of <a> dislocations at the interface, contributing to superior mechanical performance.

Although the above strategies underscore the potential of heterostructures in conventionally processed titanium alloys, they are frequently limited by geometric inflexibility, processing complexity, and scalability constraints. In contrast**,** AM provides unparalleled spatial control of composition and microstructure, especially for layer-wise or functionally graded architectures. For instance, DED fabrication enables compositional grading within the build offering by its multiple powder feeds. Recent work has employed EDE to fabricate layered TC4/TC4-2.5 Ni structures, with sharp compositional changes across layers. These chemically heterogeneous structures promote dislocation pile-up at interfaces, similar to the HDI mechanism seen in lamellar UFG/CG structures, but now realized through in-situ alloying and solidification dynamics [119].

Together, these studies confirm that heterostructure engineering — whether through conventional processing or AM — offers a pathway to overcome the strength–ductility trade-off in alloys, as summarized in Fig. 1.12. AM, in particular, unlocks multi-scale control of these heterogeneities, offering a flexible platform for producing functionally graded, spatially tailored, and compositionally engineered titanium components. However, the inherent variability and sensitivity of AM processes complicate the reliable production of these targeted heterostructures. Issues such as undesired porosity, local variations in microstructure due to fluctuations in heat input, and anisotropic texture formation frequently arise, negatively impacting the consistency and repeatability of the improvement of mechanical performance of the heterostructure materials [45, 60]. Additionally, accurately predicting and controlling microstructural evolution under the complex thermal conditions of AM demands advanced characterization techniques, full understanding of deformation mechanisms, sophisticated computational modeling, and real-time process monitoring that remain undeveloped, limiting academic research development and widespread industrial adoption.

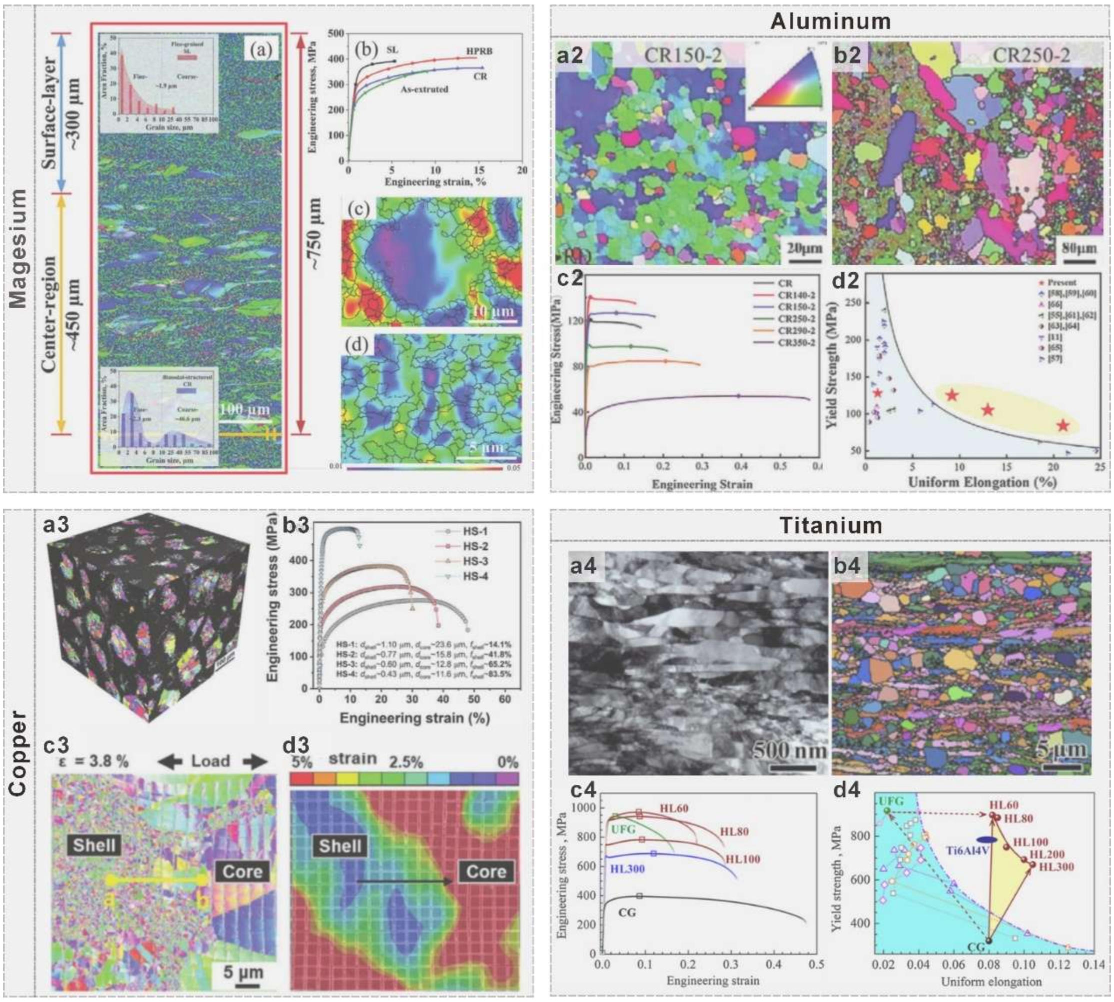

Fig. 1.12 Summarization of the heterostructured material in various alloy systems. (a1-d1) The AZ91 magnesium alloy with a multiscale heterostructure through the hard plate rolling bonding process [115]. (a2-d2) Microstructural characteristics, mechanical properties of layered pure titanium fabricated by cold rolling [111]. (a3-d3) The heterogeneous copper alloys with core-shell structure [109]. (a4-d4) The heterogeneous pure titanium with lamellae structure [118].

1.4 Remaining challenges and research objectives

1.4.1 Challenges in alloying titanium via AM

Despite significant advancements, AM of titanium alloys still faces several critical challenges. The inherent rapid solidification and complex thermal cycling characteristics of AM often induce pronounced residual stresses, anisotropic mechanical properties, and microstructural defects such as porosity, keyhole voids, and micro-cracks [120, 121]. These defects are detrimental to mechanical integrity, fatigue resistance, and reliability, posing significant barriers to widespread industrial adoption, particularly in critical structural applications such as aerospace, automotive, and biomedical components. Traditional methods typically rely on extended thermal exposure and controlled cooling rates, allowing stable and predictable transformations, uniform solute distribution, and manageable residual stress [122, 123] . In contrast, AM techniques like laser powder bed fusion (L-PBF), electron beam melting (EBM), and directed energy deposition (DED) involve extremely rapid solidification and complicated thermal history, significantly affecting solute distribution, microstructure homogeneity, and phase stability. In AM-fabricated titanium alloys with elements additions, these rapid thermal conditions frequently result in non-equilibrium microstructures, pronounced elemental segregation, and solute trapping phenomena [124]. The addition of elements (α-stabilizer and β-stabilizers) can exacerbate these issues, as it directly influences the solidification path, phase nucleation, and transformation kinetics of titanium alloys under AM conditions. Consequently, precise control of adding elements content distribution, and its influence on microstructural evolution during AM remains challenging and requires careful tuning of process parameters such as laser power, scanning speed, and hatch spacing.

In addition to process-related limitations, the alloy design space for titanium remains largely unexplored beyond traditional compositions such as Ti-6Al-4V. Recent interest has increasingly shifted toward lean alloying strategies and simpler, robust compositions such as α-titanium alloys enriched with controlled additions of aluminum. These alloys promise enhanced mechanical properties, including higher strength and ductility combinations, through tailored microstructural engineering [2, 125]. However, realizing these potentials via AM processes demands rigorous understanding of elemental effects on microstructural stability, solidification behavior, and property development during rapid cooling and thermal cycling conditions typical of AM processes.

Thus, compared to conventional methods, alloy design and optimization through AM require deeper fundamental insights and advanced control strategies to reliably produce titanium alloys with desired microstructural characteristics and mechanical properties.

1.4.2 Challenges in introducing heterostructures through AM

In addition to alloy design and optimization by AM, the intrinsic strength–ductility trade-off remains a major challenge in AM-fabricated titanium alloys. Conventionally processed titanium alloys generally exhibit limited capacity for simultaneous improvement in strength and ductility due to uniform microstructures and limited opportunities for tailored deformation mechanisms. Recent advances in heterostructure engineering, however, suggest potential pathways to circumvent this longstanding limitation by harnessing microstructural gradients, phase heterogeneity, and strategic elemental additions [89, 92]. However, precisely achieving the intended heterostructure configurations, such as gradient structures, lamellar composites, or bimodal grain distributions, remains highly challenging. The complexities inherent in AM processing — including non-uniform thermal cycles, dynamic melt pool behaviors, and rapid cooling rates — create substantial difficulties in maintaining controlled and stable heterostructures throughout component fabrication.

Effective heterostructure design requires precisely controlled spatial variation in microstructural features, such as grain size gradients, compositional differences, and distinct phase distribution. However, the inherent variability and sensitivity of AM processes complicate the reliable production of these targeted heterostructures. Issues such as undesired porosity, local variations in microstructure due to fluctuations in heat input, and anisotropic texture formation frequently arise, negatively impacting the consistency and repeatability of the improvement of mechanical performance of the heterostructure materials [45, 60]. Additionally, accurately predicting and controlling microstructural evolution under the complex thermal conditions of AM demands advanced characterization techniques, full understanding of deformation mechanisms, sophisticated computational modeling, and real-time process monitoring that remain undeveloped, limiting academic research development and widespread industrial adoption.

Furthermore, post-processing techniques such as heat treatments and surface modifications, often essential for stabilizing heterostructures and reducing residual stresses, introduce additional complexities, potentially altering or diminishing the carefully designed microstructural heterogeneities achieved during initial AM fabrication. Thus, a critical need exists to advance fundamental understanding and technological capabilities to reliably design, fabricate, and control heterostructures in AM-produced titanium alloys, effectively harnessing their full potential for enhanced mechanical performance.

In summary, critical research gaps persist in achieving defect-free AM parts with optimized mechanical properties, specifically in understanding the synergistic interactions of alloying elements, AM-induced thermal dynamics on its microstructure, and controlled heterostructure architectures.

1.4.3 Research objectives

Given the outlined challenges and the potential advantages offered by AM and heterostructure engineering, this thesis is dedicated to advancing fundamental understanding and developing practical methodologies for fabricating high-performance titanium alloys. Specifically, this research aims to achieve exceptional strength–ductility synergy through systematic alloy design, controlled microstructural engineering, and AM processing. The research objectives are clearly defined as follows:

1. Develop α-titanium alloys with tailored aluminum additions via additive manufacturing. Investigate systematically the influence of controlled Al addition on solidification behavior, elemental distribution, microstructural evolution, and phase stability of α-titanium alloys fabricated using DED.

2. Enhanced mechanical properties through heterostructure engineering via additive manufacturing. Explore and develop innovative AM processing strategies to reliably introduce heterogeneous microstructures, such as graded grain structures, bimodal microstructures, and lamellar heterostructures, into titanium alloys. Evaluate the effectiveness of these intentionally introduced heterostructures in simultaneously enhancing strength and ductility, examining detailed strength mechanisms.

3. Investigate interface engineering in AM-fabricated titanium heterostructures. Specifically, explore how interfacial strain localization and geometrically necessary dislocation (GND) accumulation contribute to dislocation-mediated strengthening. This objective aims to uncover the mechanistic role of heterointerfaces in tailoring mechanical responses and achieving enhanced strength–ductility synergy.

By fulfilling these research objectives, this thesis aims to deliver critical insights into alloy design and additive manufacturing processes, advancing the fundamental understanding of heterostructure engineering and establishing robust methodologies for the next-generation fabrication of high-performance titanium alloys.

1.5 Thesis outline

This thesis is structured as follows: In Chapter 2, we outline the research methodology, covering feedstock preparation, AM fabrication via the LENS™ system, conventional casting, post-processing, and the characterization techniques used. Then, Chapter 3 investigates aluminum addition in α-Ti alloys, revealing how rapid solidification refines grains and enhances dislocation activity to simultaneously improve strength and ductility. Building on this, Chapter 4 explores multi-gradient

Ti/Ti–Al heterostructures, where gradient stress partitioning and ductility compensation drive exceptional performance. Chapter 5 then focuses on interface engineering in layered Ti–3.5Al/Ti–6Al–4V structures, showing how thermomechanical mismatch and geometrically necessary dislocations boost strength while soft layers suppress crack propagation. Finally, Chapter 6 synthesizes these findings, emphasizing AM's capability to tailor microstructures and interfaces to overcome the strength–ductility trade-off, and Chapter 7 concludes with future research directions, from post-treatment effects to real-time microstructural control and comparisons with conventional processing.

Chapter 2 Methodology

2.1 Overview

This chapter outlines the detailed methodologies employed throughout this research project. Section 2.2 introduces the AM facilitates and clearly describes the laser directed energy deposition (OPTOMEC LENS^{TM} MR-7) system. The whole manufacturing process includes material preparation, optimizing AM-manufactured parameters, specific manufacturing strategies for homogeneous and heterogeneous titanium specimens, and post-heat treatment methods. For the purpose of comparison, the conventional Ti samples have also been fabricated by arc melting manufacturing process, which has also been detailed in this section. Section 2.3 extensively presents advanced microstructural characterization techniques, including optical microscopy (OM), scanning electron microscopy (SEM), X-ray diffraction analysis (XRD), electron backscatter diffraction (EBSD), electron probe microanalysis (EPMA), and transmission electron microscopy (TEM). Section 2.4 details the mechanical performance evaluation methods, specifically microhardness and tensile testing measurements, to thoroughly assess the mechanical performance. Finally, Section 2.5 provides procedures for thermal property measurements, such as thermal expansion and thermal conductivity assessments, critical for understanding microstructural stability and residual stress development during AM process.

2.2 Manufacturing of specimens

2.2.1 Feedstock materials and preparation

The feedstock powders utilized for AM fabrication include gas-atomized commercially pure titanium (CP-Ti) powder (ASTM Grade 1, 0.087 O, 0.01 C, 0.18 Fe, 0.004 N, balance Ti [wt%]; Avimetal Powder Metallurgy Technology Co., Ltd.), pre-alloyed atomized Ti-54Al powder (24.52 Al, 0.01 C, 0.01 N [wt%]; Beijing Xing Rong

Yuan Technology Co., Ltd.), and Ti-6Al-4V powder (6.39 Al, 4.05 V, balance Ti [wt%]; Avimetal Powder Metallurgy Technology Co., Ltd.). These powders, characterized by a particle size distribution ranging from 50 μm to 103 μm (with a median diameter (D50) of 81.2 μm), demonstrate a spherical morphology and smooth surfaces, which are instrumental in facilitating optimal flowability during the printing process, as depicted in Figs. 2.1a-b.

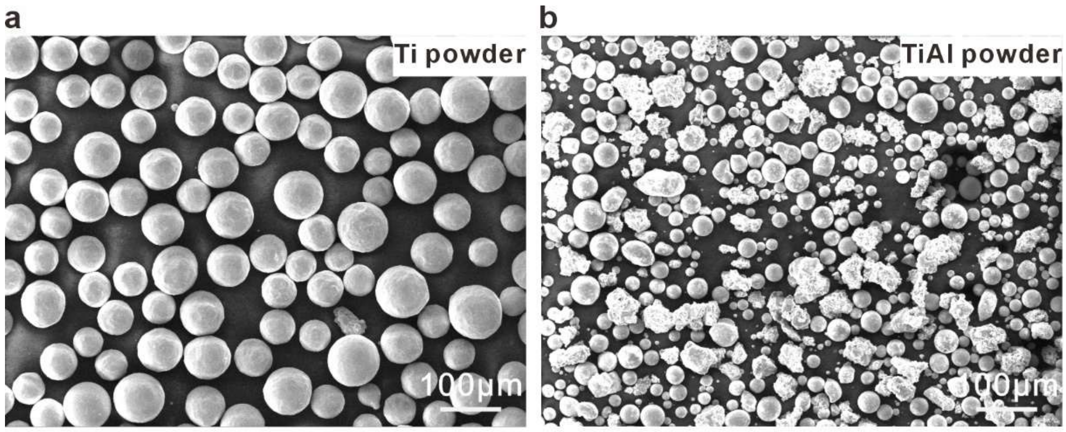

Fig. 2.1 The typical SEM images reveal surface morphologies of the powder particles. (a) Ti powder particles. (b) Pre-alloyed TiAl powder particles.

2.2.2 LENS fabrication process

2.2.2.1 Printing parameters

In this study, all specimens produced using AM technology were fabricated with the OPTOMEC LENS^{TM} MR-7 system, with the profile display shown in Fig. 2.2a. As previously mentioned, this system is a type of laser-directed energy deposition system and is primarily composed of a high-power laser source, a powder feeding system, and a substrate workbench. The schematic drawing depicted in Fig. 2.2b reveals that during the fabrication process, metallic powders are transported by a carrier gas through a powder delivery nozzle, forming a focused powder stream. When this stream intersects with the laser beam, the powders instantly melt, creating a molten pool on the surface of the fixed substrate. As the system follows a layer-by-layer deposition strategy based on a predesigned 3D model from CAD software, the final component is gradually built up. To prevent oxidation, which is a critical concern due to the high reactivity of titanium and its alloys to oxygen [126], and ensure operator safety, the build chamber was thoroughly purged with high-purity argon gas prior to fabrication. The oxygen concentration was reduced to below 100 parts per million (ppm) before initiating the manufacturing process.

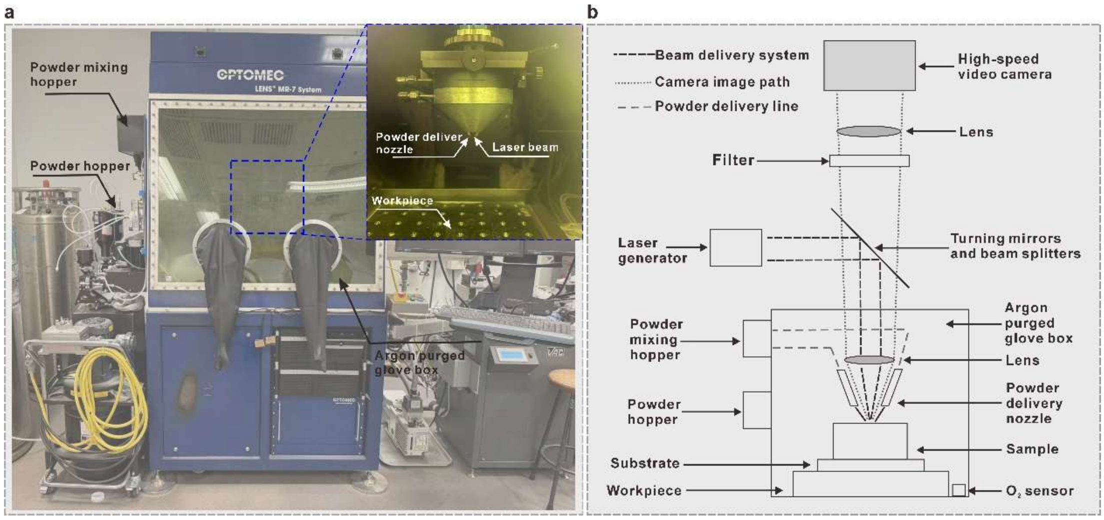

Fig. 2.2 Introduction to the OPTOMEC LENS^{TM} MR-7 system. (a) Image of the system illustrating the key components including the high-power laser source, powder feeding system, and substrate stage. (b) Schematical drawing illustrating the work principles of the LENS system [127].

Moreover, the fabrication quality of titanium alloys in AM processes is highly sensitive to processing conditions. A key parameter governing the energy input and thermal history during the build is the Volumetric Energy Density (VED), which can be expressed as:

$$VED = \frac{P}{vht}$$

where P is the laser power (W), v is the scanning speed (mm/s), h is the hatch distance (mm), and t is the layer thickness (mm). This expression quantifies the amount of laser energy delivered per unit volume of material and serves as an important predictor for microstructural evolution, melt pool dynamics, and defect formation, including porosity and lack-of-fusion zones.

In this study, special consideration was given to the hatch distance due to its direct relationship with the laser beam diameter. The OPTOMEC LENS™ MR-7 system used herein operates with a laser spot diameter of approximately 600 µm. Based on literature and empirical optimization, the hatch spacing was set to 300 µm, corresponding to 50% beam overlap. This selection has been widely reported to promote optimal lap joint efficiency and minimize unmelted regions between adjacent tracks [59, 97].

To systematically optimize the fabrication parameters and identify a suitable processing window for titanium alloys in this study, a series of parameter combinations was carefully designed and experimentally tested. These parameters include variations in laser power, scanning speed, and layer thickness. The influence of these variables on build quality — particularly in terms of surface morphology, internal porosity, and metallurgical bonding — was thoroughly assessed. All combinations were evaluated for their effects on part quality, including porosity, the existence of microcracks, and metallurgical bonding. The list of selected parameters used in this study is summarized in Table 2.1.

Table 2.1 The ideal process parameters of LENS^{TM} fabricated samples.

Parameters	*P (W)*	*t (µm)*	*h (µm)*	*v (mm/s)*
Samples	400	100	300	10

P, laser power; T, layer thickness; H, hatch distance; V, scanning speed.

2.2.2.2 Fabrication strategies for homogeneous samples

In this study, both homogeneous titanium alloys (Ti-Al systems and Ti-6Al-4V) and heterogeneous alloys (Ti/Ti-Al and Ti-3.5Al/Ti-6Al-4V systems) were fabricated using L-DED. For the fabrication of homogeneous samples, a bidirectional scanning strategy was employed, in which the laser scanned alternately along the X and Y axes with a 90° rotation between successive layers. This scanning pattern, illustrated in Fig. 2.3, was selected to promote uniform energy input, minimize thermal anisotropy, and enhance microstructural homogeneity throughout the build. The use of such a cross-hatched scanning strategy is well-established in directed energy deposition processes, as it helps mitigate directional thermal gradients that could otherwise result in residual stress accumulation and anisotropic mechanical behavior.

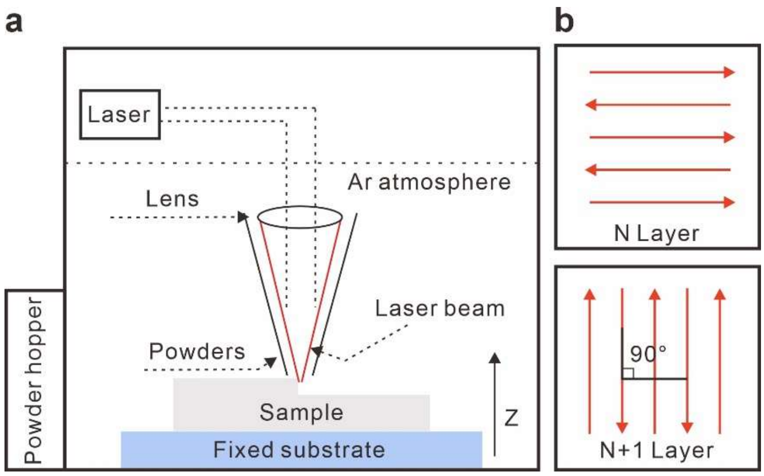

Fig. 2.3 Fabrication of titanium alloys in this study. (a) Schematic representation of the printing process employing the LENS^{TM} process. (b) Printing strategy for consecutive layers.

2.2.2.3 Fabrication strategies for hetegeneous samples

For the heterogeneous samples, spatial control over chemical composition was achieved by loading different titanium alloy powders into separate powder hoppers and dynamically adjusting the feed rates during the deposition process. Two types of heterostructured systems were fabricated in this study: the Ti/Ti-Al multi-gradient alloy and the Ti-3.5Al/Ti-6Al-4V lamellar heterostructure. An alternating deposition strategy was adopted for both, as shown in Fig. 2.4.

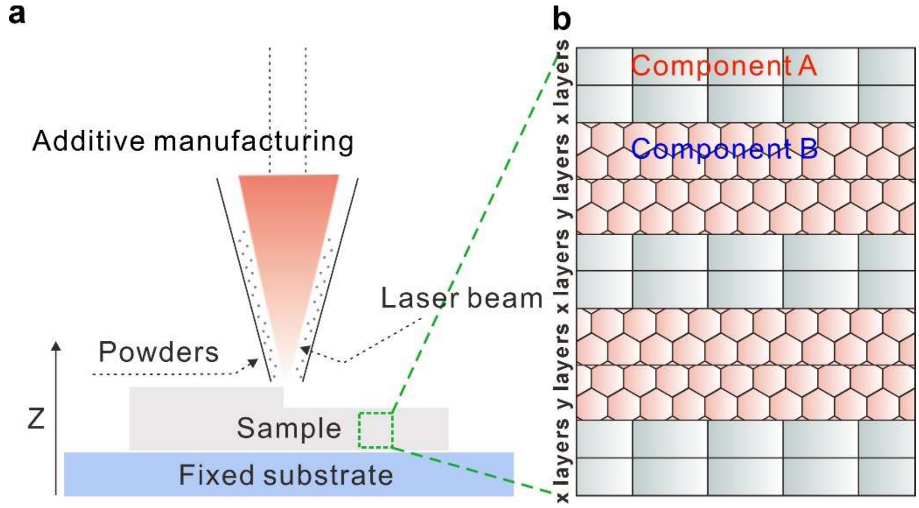

Fig. 2.4 Schematic illustration of the heterostructured sample fabrication process via additive manufacturing. (a) Schematic representation of the LENS™ deposition process. (b) Illustration of the heterogeneous layering strategy achieved through precise control of powder feed rates, enabling the introduction of microstructural and compositional heterogeneity. Here, *x* and *y* denote the number of deposited layers, while Components A and B represent different powder compositions used to construct the alternating heterogeneous architecture.

In the Ti/Ti-Al system, four layers of commercially pure titanium (CP-Ti) were first deposited using a feed rate of 0.15 g/s. This was followed by two layers of Ti-10Al, achieved through the co-feeding of CP-Ti (0.15 g/s) and Ti-54Al (0.03 g/s) powders to achieve the target composition. This layer sequence was repeated to construct the complete multi-gradient sample.

For the Ti-3.5Al/Ti-6Al-4V heterostructure, two layers of Ti-3.5Al were alternated with two layers of Ti-6Al-4V, using powder feed rates of 0.2 g/s and 0.3 g/s, respectively. This layering sequence was repeated until the final part reached the desired dimensions of 35 mm (length) × 16 mm (width) × 3 mm (height). The laser processing parameters used for the fabrication of both the heterogeneous Ti-Al system and the Ti-3.5Al/Ti-

6Al-4V heterostructure are summarized in Table 2.2.

Table 2.2 Parameters for LENS^{TM} fabricated heterogeneous multi-gradient Ti-Al and layered Ti-3.5Al/Ti-6Al-4V specimens.

Parameters	*P (W)*	*t (μm)*	*v (mm/s)*	FOP 1 (g/s)	FOP 2 (g/s)
Multi-gradient Ti-Al	400	50	10	0.15	0 and 0.03
Layered Ti-3.5Al/Ti-6Al-4V	400	50	10	0.2	0.3

P, laser power; T, layer thickness; H, hatch distance; V, scanning speed; FOP 1, feed rate of powder hopper 1; FOP 2, feed rate of powder hopper 2.

2.2.3 Conventional as-cast method

For comparative purposes, conventionally produced as-cast Ti–Al alloys were fabricated using an electric arc melting process, as illustrated in Fig. 2.5a. In this process, high-purity titanium (Ti) and aluminum (Al) ingots (each with a purity of 99.99%) were used as starting materials to ensure compositional accuracy and minimize the influence of impurities.

The schematic drawing depicted in Fig. 2.5b indicates that the arc melting process operates by generating a high-temperature electric arc between a tungsten electrode and a copper crucible under an inert gas atmosphere. The arc provides sufficient thermal energy to melt the metallic ingots rapidly. To suppress oxidation — an especially critical concern for titanium-based alloys due to their high reactivity with oxygen at elevated temperatures — the melting was carried out under a high-purity argon environment. Prior to the electric arc ignition, the vacuum chamber was evacuated to a pressure of approximately 5×10^{-3} Pa, and subsequently backfilled with argon until the pressure stabilized at 0.5 Pa. This two-step atmosphere control ensured an ultra-low oxygen environment during melting, thereby minimizing oxygen content and preventing the formation of oxygen-enriched embrittled zones, which are detrimental to the properties of Ti alloys.

To ensure chemical homogeneity, the Ti and Al ingots were remelted seven times under identical conditions. Between each melt, the ingots were manually flipped using a water-cooled copper tong to enhance mixing and eliminate compositional gradients or unmelted inclusions. Following the final melt, the homogenized alloy was cast into a water-cooled copper mold, facilitating rapid solidification and reducing the risk of elemental segregation. The mold cavity dimensions were tailored to match those of the additively manufactured specimens, ensuring consistency in sample geometry for subsequent mechanical and microstructural comparisons.

This process provided well-controlled, compositionally homogeneous reference samples to benchmark the mechanical and microstructural performance of Ti-Al alloys fabricated via additive manufacturing.

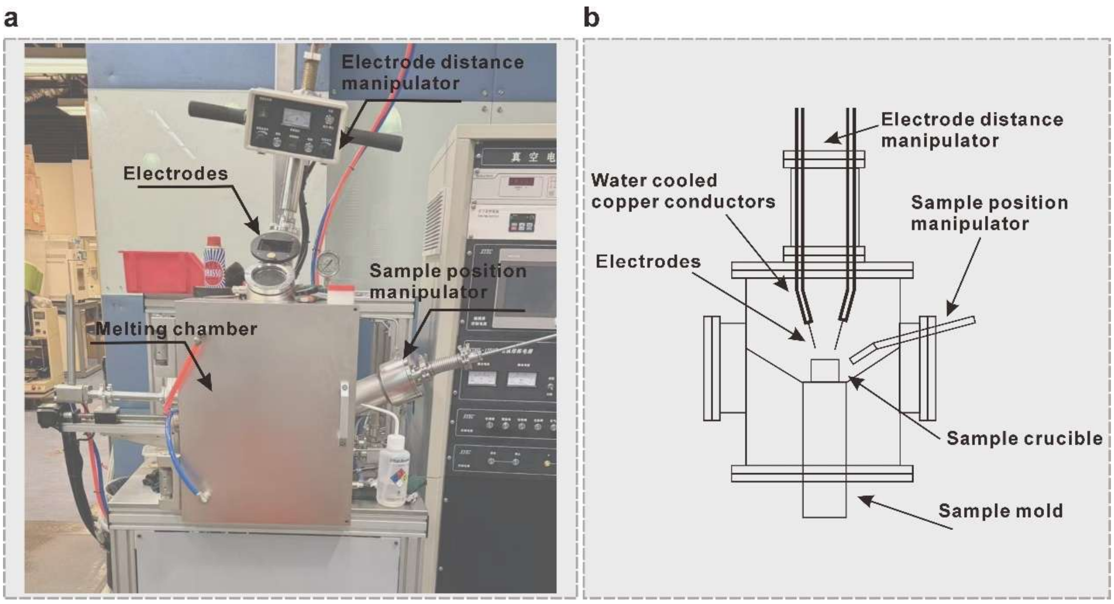

Fig. 2.5 Introduction to the arc melting system. (a) Image of the arc melting system illustrating the key components including the electrode melting system and working chamber. (b) Schematic drawing illustrating the work principles of the arc melting system.

2.2.4 Post-heat treatment process

All post-heat treatments in this study were conducted using a horizontal tube furnace on the fabricated samples. Prior to each treatment, the furnace was preheated to the target temperature to ensure a stable and uniform thermal environment during specimen insertion. To minimize oxidation during high-temperature exposure, high-purity argon gas was continuously purged through the tube to maintain an inert environment throughout the entire heat treatment process.

Specimens were placed in an alumina crucible and inserted into the central isothermal zone of the furnace once the desired temperature was reached. The heating temperature and holding time were carefully selected based on the experimental design. After the heat treatment, samples were either furnace-cooled or air-cooled, depending on the intended cooling rate required for microstructural tailoring.

2.3 Microstructural characterization techniques

2.3.1 Optical microscopy and scanning electron microscopy

Initial microstructural analysis of the as-fabricated and as-cast specimens was carried out using an Olympus B53X optical microscope (OM). This allowed for a preliminary assessment of surface quality, pore distribution, crack formation, and general microstructural uniformity. OM imaging provided an essential first insight into the build integrity and morphological characteristics across different fabrication routes. For example, the formability and quality of the fabricated samples were evaluated via OM, as depicted in Figs. 2.6a-c. Cross-sectional OM images revealed that all samples — both homogeneous and heterogeneous manufactured by AM—exhibited nearly pore-free morphologies, confirming the effectiveness of the optimized processing parameters, demonstrating consistent deposition, strong interlayer bonding, and minimal defect formation across all specimens by utilizing the AM printing parameters listed in above Table 2.2.

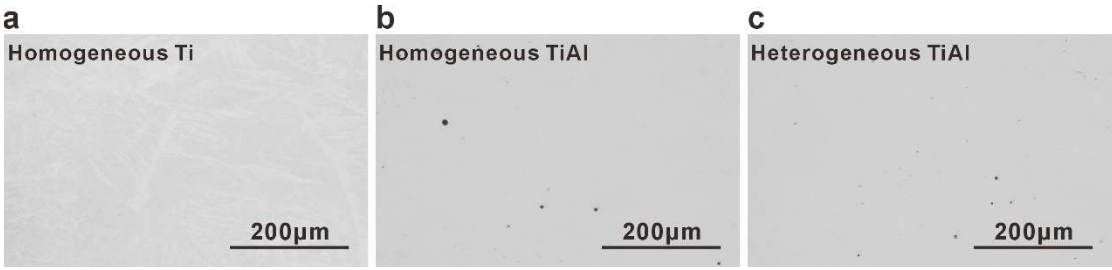

Fig. 2.6 Fabrication of the homogeneous/heterogeneous specimens. (a-c) The OM images obtained from cross-sectional surfaces of the as-built homogeneous Ti, homogeneous TiAl, and heterogeneous TiAl specimens reveal nearly pore-free morphologies within the sample interior.

For higher-resolution analysis, a Tescan Mira scanning electron microscope (SEM) was employed to investigate microstructural features such as grain morphology, phase boundaries, and solidification structures. The SEM was equipped with an energy-dispersive X-ray spectroscopy (EDS) system to enable compositional mapping and elemental analysis, particularly focusing on the distribution of aluminum within the Ti matrix in both homogeneous and heterogeneous regions.

The specimens for OM and SEM characterization were sectioned using wire-cut electrical discharge machining (WEDM) to preserve geometric fidelity and minimize surface damage. Standard metallographic preparation procedures were followed: samples were ground with SiC abrasive papers of progressively finer grit sizes (up to 4000 grit), polished using diamond suspensions and colloidal silica, and then etched with Kroll's reagent (3% hydrofluoric acid, 6% nitric acid, balance water) for approximately 10 seconds. This etching process effectively revealed phase boundaries and grain structures necessary for both qualitative and quantitative microstructural evaluation.

2.3.2 X-ray diffraction analysis

Phase identification of all the specimens was carried out using X-ray diffraction (XRD) on a Rigaku SmartLab 9 kW diffractometer equipped with a Cu $K\alpha_1$ radiation source (λ = 1.5406 Å). Scans were performed over a diffraction angle (2θ) range of 20° to 90°, with a step size of 0.02° and a scanning speed of 5°/min, providing sufficient resolution for accurate phase determination. The incident beam was operated under standard Bragg–Brentano geometry, and all measurements were conducted on polished cross-sectional surfaces of the specimens to ensure consistent and representative analysis. The acquired diffraction patterns were compared with standard reference databases to identify phase constituents and assess potential phase transformations induced by alloying, additive manufacturing, or subsequent heat treatments.

2.3.3 Electron backscatter diffraction and electron probe microanalysis

To obtain detailed crystallographic and grain orientation information, electron backscatter diffraction (EBSD) was conducted using a Thermo Fisher Apreo 2S SEM operating at an accelerating voltage of 20 kV. The system was equipped with Oxford Instruments' AztecCrystal software, enabling automated acquisition and analysis of orientation imaging microscopy (OIM) data. EBSD mapping was utilized to characterize grain size, grain boundary character (e.g., low-angle vs. high-angle boundaries), and texture evolution in both homogeneous and heterogeneous regions of the AM-fabricated and conventionally cast specimens.

Before EBSD analysis, specimens underwent meticulous surface preparation. After standard mechanical grinding and polishing, electropolishing was performed in an electrolyte composed of 6% perchloric acid, 34% butanol, and 60% methanol (by volume). The electropolishing was carried out at a temperature of –20 °C and a current of 0.4 A, ensuring smooth, damage-free surfaces suitable for high-quality diffraction pattern acquisition.

For compositional analysis, electron probe microanalysis (EPMA) was performed using a JEOL JXA-8230 microanalyzer. This technique provided high-resolution elemental maps and quantitative analysis of the spatial distribution of aluminum and titanium within the fabricated samples. EPMA was particularly important for evaluating elemental homogeneity and detecting segregation or diffusion zones at interfaces in the heterogeneous structures, especially those formed by alternating layers of CP-Ti and Ti-Al alloy.

Together, EBSD and EPMA analyses offered a comprehensive understanding of the microstructural and chemical architecture of the materials, revealing the correlations between processing strategy, crystallographic features, and elemental distribution in both the AM-fabricated and conventionally fabricated specimens.

2.3.4 Transmission electron microscopy

To probe the microstructural features at the nano- and atomic scales, transmission electron microscopy (TEM) analyses were performed using a JEOL JEM-2100F microscope operating at an accelerating voltage of 200 kV. Both conventional TEM and scanning transmission electron microscopy (STEM) modes were employed to investigate sub-grain features, dislocation structures, phase interfaces, and potential nanoscale precipitates that may contribute to strengthening or influence deformation behavior.

Sample preparation for TEM is critical due to the stringent requirements for electron transparency. Specimens were initially mechanically ground to a thickness of approximately 30 μm, followed by precision ion milling using a Gatan Precision Ion Polishing System II (PIPS II). The ion milling protocol involved three sequential stages: rough milling at 5 kV and ±7°, fine polishing at 3 kV and ±5°, and final cleaning at 1 kV and ±5° for 30 minutes. This multi-step thinning process was carefully optimized to minimize surface amorphization and ensure high-quality electron-transparent foils suitable for high-resolution imaging and diffraction analysis.

TEM provided critical insights into the nanoscale characteristics of grain boundaries, the distribution and morphology of α and β phases, and the presence of interface defects or solute clusters, especially in regions engineered with compositional heterogeneity. These observations were essential for understanding the underlying mechanisms governing strength and ductility in both homogeneous and heterogeneous samples fabricated by additive manufacturing.

2.4 Mechanical evaluation methods

2.4.1 Vickers microhardness testing

Vickers microhardness testing was conducted to evaluate local hardness variations and to assess the influence of microstructural heterogeneity along the build direction. Measurements were performed on mirror-polished cross-sections prepared parallel to the Z-axis (build direction) using a Struers Duramin-40 A3 microhardness tester.

A test load of 500 grams (4.9 N) was applied with a dwell time of 10 seconds for each indentation, in accordance with standard testing practices for metallic materials. To capture spatial variations in hardness, especially in heterogeneous samples, measurements were taken at 100 μm intervals along the build direction. A total of 12 indentations were made for each sample, and the resulting values were averaged to produce representative hardness profiles.

2.4.2 Tensile testing

Uniaxial tensile testing was performed to evaluate the macroscopic mechanical properties—specifically, yield strength, ultimate tensile strength, strain distribution and ductility—of both additively manufactured and conventionally produced titanium alloy samples. For the conventionally produced samples, tensile bars were extracted from ingots fabricated via arc melting. Multiple positions were selected within each ingot to ensure repeatability and account for possible local heterogeneity in microstructure or composition.

For the AM-fabricated samples, tensile bars tensile bars were prepared perpendicular to the build direction—that is, within the plane of each deposited layer—rather than along the layer-stacking direction. This sampling orientation was intentionally selected to avoid the anisotropic effects commonly associated with layer-wise additive manufacturing, such as interlayer defects and reduced bonding strength along the build direction. Furthermore, the final built thickness of the AM samples was approximately 2 mm, which is consistent with the gauge section thickness of the tensile bars. This design minimizes potential microstructural gradients across the sample thickness and ensures fair comparison with the as-cast counterparts.

All tensile tests were conducted at room temperature using a ZwickRoell Z020 universal testing machine under a constant strain rate of 1×10^{-3} s^{-1}. Dog-bone-shaped specimens were precisely machined by wire electrical discharge machining (WEDM) to minimize thermal or mechanical damage. The specimens had a gauge diameter of 2 mm, a gauge length of 10 mm, and an overall length of 25 mm—dimensions optimized for small-volume AM builds while ensuring reliable stress–strain measurement.

To achieve statistically reliable data, three tensile tests were performed for each specimen category (homogeneous, heterogeneous, and as-cast), and average values along with standard deviations were reported. Prior to testing, the specimen surfaces were mechanically ground to generate an optically rough surface suitable for speckle pattern generation, which is essential for digital image correlation (DIC) analysis.

The strain field during tensile deformation was analyzed in real-time using the laserXtens 2-120 HP/TZ system, integrated with the LaVision-DaVis data acquisition software. This high-resolution, non-contact extensometer system relies on DIC to track local displacements by monitoring the evolution of a laser-illuminated speckle pattern applied to the specimen surface, as illustrated in Fig. 2.7. A grid facet size of 20 pixels with a facet overlap of 80% was used, resulting in a grid spacing of 0.051×0.051 mm.

The setup enabled accurate capture of full-field strain distributions, facilitating detailed analysis of strain localization, necking behavior, and fracturing mechanisms.

This integrated approach to tensile testing and in situ strain mapping enabled a comprehensive evaluation of how processing route and compositional architecture influence mechanical performance, thereby supporting the broader research objectives of the study.

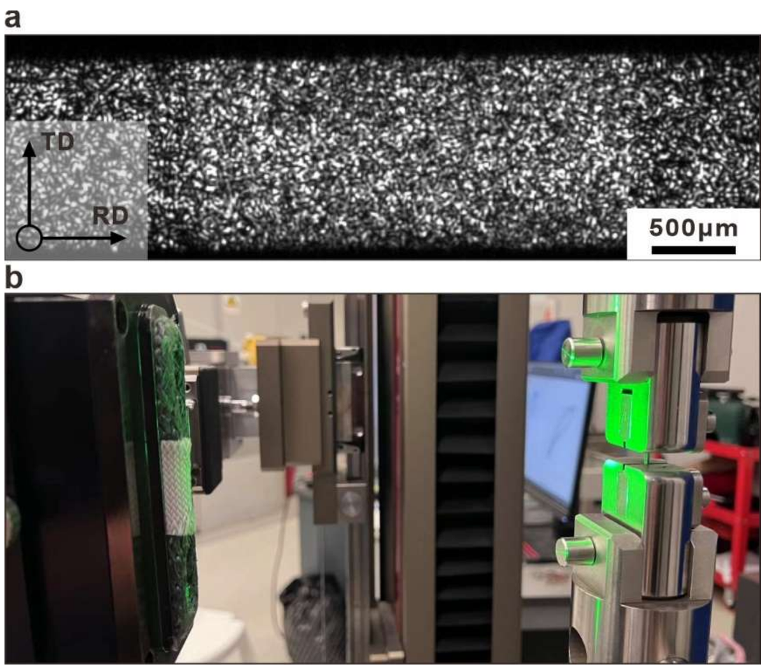

Fig. 2.7 Experimental setup for room temperature tensile test with a system for attendant DIC. (a) The random speckle pattern illustrated by laser light on the specimen. (b) Experimental setup including the laser and CCD camera for capturing speckle images during tensile testing. The spatial resolution in the DIC experiment is 50 μm, determined by the grid facet size and facet overlap.

2.5 Thermal property measurements

To better understand the thermophysical behavior of the fabricated alloys under AM conditions, thermal property characterization was performed. These measurements included the coefficient of thermal expansion (CTE) and thermal conductivity, which are critical for evaluating residual stress development, dimensional stability, and microstructural evolution during the rapid thermal cycles inherent to AM processes.

The CTE was measured using a NETZSCH DIL402 C dilatometer under a controlled heating rate of 5 K/min. This technique provided precise data on thermal expansion behavior as a function of temperature, which is particularly important for analyzing mismatch stresses in heterogeneous structures and for guiding thermomechanical simulations.

The thermal conductivity was assessed using a NETZSCH LFA 467 laser flash analyzer, in combination with a NETZSCH LF427 heat flow meter apparatus. This combined setup allowed for accurate, non-destructive evaluation of the alloys' ability to conduct heat property that strongly affects melt pool dynamics, cooling rate, and the resulting grain morphology during AM processing.

Together, these thermal property measurements provided critical input for interpreting the solidification behavior, residual stress development, and phase stability of the printed titanium alloys, particularly in systems where compositional heterogeneity or interface complexity plays a significant role. These insights also support the design of AM process parameters to optimize mechanical performance and minimize thermal distortion.

Chapter 3 Enhanced Strength and Ductility in α-Titanium Alloys through in-situ Alloying via Additive Manufacturing

3.1 Introduction

As introduced in Chapter 1, AM offers distinct advantages in terms of shaping capabilities and microstructural control when compared to conventional metallurgical processes. Beyond its application to established commercial alloys, AM has recently garnered attention for the fabrication of titanium alloys. However, significant knowledge gaps still exist as a result of the restricted concerns surrounding low-alloyed titanium manufactured by AM. This restricts the exploration of titanium alloys with low prices but extraordinary mechanical properties. This chapter systematically investigates the effects of AM and in-situ alloying on the microstructural evolution and mechanical performance of low-alloyed α-titanium alloys compared to their conventional manufactured counterparts.

Titanium and its alloys are extensively utilized in aerospace and biomedical applications due to their exceptional strength-to-weight ratio, corrosion resistance, and high-temperature performance [2, 128]. Among them, α-titanium (α-Ti) is particularly noteworthy, where the strengthening effects by α-stabilizers such as O, N, and Al are widely established [129-132]. However, while the addition of α-stabilizers enhances the strength of α-Ti, they often reduce ductility significantly, making these alloys less appealing for commercial applications [124]. This challenge is especially pronounced in conventional manufacturing processes such as casting, where intrinsic defects and coarse microstructures further degrade the mechanical tensile ductility, necessitating a series of post-heat treatment processes [133, 134].

AM has recently emerged as a transformative technology capable of overcoming those inherent limitations in conventional methods [135]. Techniques such as laser-by-layer metal deposition have demonstrated the ability to produce alloys with enhanced mechanical properties by leveraging rapid solidification and complex thermal histories [39, 136-139]. These features enable the formation of refined and often non-equilibrium microstructures that are unattainable via conventional processing routes, leading to improved combinations of strength and ductility [140-143]. For instance, Zhang et al. [144] revealed that high-strength low-alloy (HSLA) steels fabricated using wire arc additive manufacturing (WAAM) achieved a higher combination of ultimate tensile strength (σ_{UTS}) of 972.5 MPa and total elongation (ε_{total}) of 17.1%, surpassing their as-cast counterparts, which exhibited lower strength (σ_{UTS} ~ 778.6 MPa) and reduced ductility (ε_{total} ~ 10.9%). Similarly, Avateffazeli et al. [145] observed simultaneous improvements in both strength and ductility in an Al-Cu-Mg-Ag-TiB_2 (A205) alloy produced via laser powder bed fusion (LPBF) compared to its conventionally cast counterparts, attributing these enhancements to the fine equiaxed and supersaturated aluminum grain structures formed under the high cooling rates inherent in the LPBF process. Kang et al. [146] further highlighted the influence of AM techniques on FeMnAlNi alloys, showing that directed energy deposition (DED) yields enhanced ductility while maintaining strength, in contrast to conventional casting counterparts.

In the context of titanium alloys, particularly low-alloyed α-Ti systems, the potential benefits of AM remain underexplored. Traditional methods for introducing alloying elements into titanium typically involve the melting and casting of pre-mixed ingots. These processes often lead to issues such as ingot inhomogeneity, which can cause micro- or macro- segregation [147], as well as β-fleck defects commonly observed in titanium alloys containing Fe or Cr [148]. Furthermore, achieving a homogeneous alloy composition through conventional routes usually requires long-term thermal treatments. These treatments are costly and challenging to apply to titanium alloys due to their high affinity for oxygen and the high diffusion rate of oxygen in the β phase at elevated temperatures [10]. In contrast, in-situ alloying — where elemental powders are blended and alloyed directly during the AM process —

offers a more flexible, efficient, and cost-effective alternative for compositional control. This approach allows for real-time control of alloy composition and enables the fabrication of compositionally graded or novel alloy systems that are difficult to achieve through traditional processing [132, 149]. Moreover, the rapid solidification inherent to AM processes helps suppress segregation and promotes the formation of refined or metastable microstructures. Although the in-situ alloying approach has demonstrated considerable potential in other alloy systems [150, 151], its application to low-alloyed α-Ti alloys remains largely unexplored. Introducing Al via in-situ alloying during AM presents a promising strategy to strengthen α-Ti while retaining or even enhancing ductility, owing to the microstructural control afforded by the process.

This study aims to develop high-performance, low-alloyed α-Ti alloys (Ti-Al) through in-situ alloying using laser engineered net shaping (LENS), a type of DED technique. By systematically comparing the mechanical properties of AM-fabricated Ti-Al alloys with their as-cast counterparts, this work highlights the capability of AM to simultaneously improve both strength and ductility. Notably, the Ti-6 at% Al alloy produced via AM achieved a yield strength (YS) of 795.3 MPa, an ultimate tensile strength (UTS) of 876.1 MPa, and an elongation to failure of nearly 20%, representing approximately a 90% increase in YS, 80% increase in UTS, and nearly double the ductility compared to the as-cast counterparts. Detailed microstructural analyses reveal that the superior performance of the AM samples stems from their refined grain structures, elevated dislocation densities, and enhanced solid solubility, all of which result from the rapid solidification and thermal cycling inherent to the AM process. These findings underscore the potential of AM — in combination with in-situ alloying — as a powerful platform for designing next-generation α-Ti alloys with tailored microstructures and optimized mechanical properties, paving the way for their expanded use in high-performance structural applications.

3.2 Results

3.2.1 Mechanical performance

The mechanical properties of Ti alloys fabricated using conventional methods, such as casting or forging, with small additions of Al — typically less than 10 at%Al without the presence of the α_2 phase — have been thoroughly investigated and well-documented [133, 152, 153]. These studies consistently show that increases in Al content, ranging from 0 to 6 at%, result in strength enhancement but come at the cost of significant reductions in ductility. In comparison, the engineering tensile stress-strain behavior of the AM Ti-x at%Al alloys was evaluated, as presented in Fig. 3.1a. Notably, the AM commercially pure titanium (CP-Ti) demonstrated the highest uniform elongation but correspondingly exhibited the lowest strength. As the Al content increased, the strength of the alloys improved while the ductility decreased. Among the various Al concentrations, the AM Ti-6 at%Al (hereafter referred to as AM Ti-6Al) sample displayed the most favorable combination of strength and ductility, with a yield strength (YS) of 795.3 MPa and an ultimate tensile strength (UTS) of 876.1 MPa, accompanied by a remarkable elongation to failure (ε_f) of nearly 20%.

For comparative purposes, a Ti-6 at%Al sample fabricated via casting (hereafter referred to as as-cast Ti-6Al) was also produced and tested, showing a YS of 417.2 MPa, UTS of 492.7 MPa, and ε_f of only 10.8%, consistent with previously reported data [133, 154]. Analysis of the strain hardening rate–true strain curves (Fig. 3.1b) derived from the stress–strain curves further revealed a significantly higher strain-hardening rate and greater true strain values in the AM Ti-6Al sample compared to its as-cast counterpart. These findings underscore the superior mechanical performance achieved through AM for low-alloyed Ti-Al alloys.

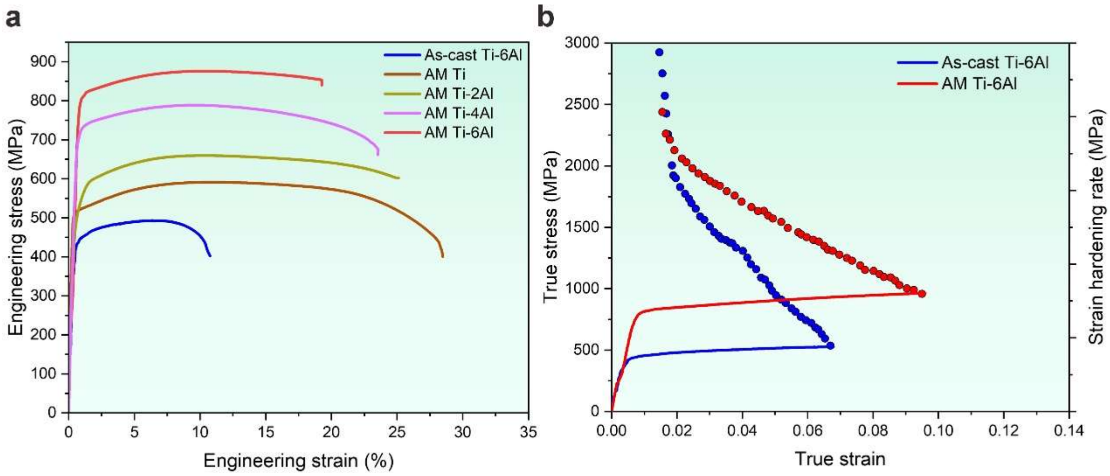

Fig. 3.1 Mechanical properties of as-cast Ti-6Al and AM Ti-x at%Al alloys. (a) Engineering stress–strain curves for as-cast Ti-6Al and AM Ti-x at% Al samples. (b) True stress–true strain curves and strain-hardening rate curves for as-cast and AM Ti-6Al alloys.

3.2.2 Microstructure analysis

While both the AM and casting processes introduce Al into Ti with identical compositions, the TiAl alloys produced by AM consistently demonstrate superior mechanical properties, including enhanced strength and ductility, compared to the as-cast counterpart. This discrepancy suggests that the distinct microstructural evolution resulting from the different fabrication techniques plays a critical role in determining the mechanical performance of the alloys. To further investigate the microstructural mechanisms responsible for this enhanced performance, a detailed analysis was conducted, focusing on the AM Ti-6Al sample with the optimal combination of strength and ductility, as well as its as-cast Ti-6Al counterpart. The following section presents an in-depth microstructural examination to elucidate how processing-induced features contribute to the observed differences in mechanical behavior.

Figure 3.2 presents the phase constituents of CP-Ti, pre-alloyed Ti-54 at%Al powders (hereafter referred to as Ti-54Al powder) used in the AM process, and both as-cast and AM Ti-6Al samples. Consistent with the Ti-Al phase diagram [155], the results show that CP-Ti powder contains only the α-Ti phase, while the Ti-54Al powder exhibits both the α_2-Ti_3Al and γ-TiAl phases. In examining the as-fabricated Ti-6Al samples from cross-sectional surfaces parallel to the build direction, it was found that both the as-cast and AM samples primarily consist of the α-Ti phase. Notably, neither the α_2-Ti_3Al and γ-TiAl phases were detected in the AM samples made from CP-Ti and Ti-54Al powders, indicating effective melting and homogeneous mixing during the AM process. Furthermore, a noticeable shift of XRD peaks towards higher angles in both as-cast and AM Ti-6Al samples, compared to the CP-Ti powder, indicates lattice distortion induced by the solid solution of Al in Ti, suggesting effective alloying in both manufacturing processes [156].

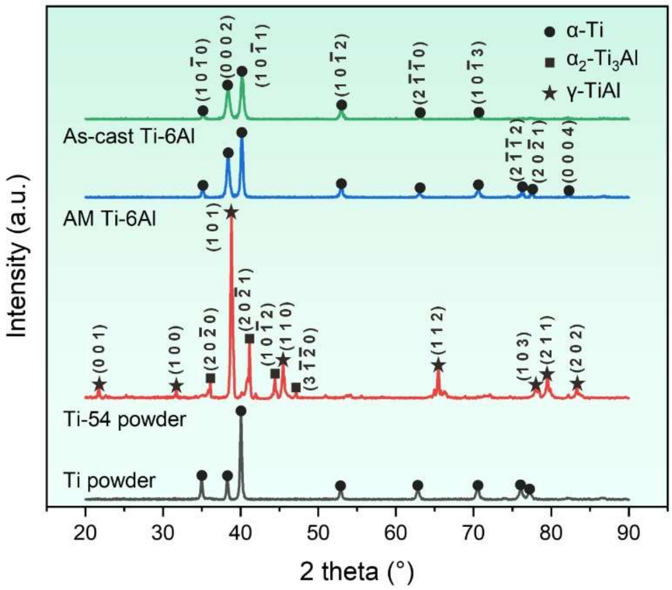

Fig. 3.2 Phase analysis of pure Ti and pre-alloyed Ti-54 at%Al powders, and Ti-6Al samples fabricated by casting and AM methods.

Figure 3.3 illustrates the microstructural characteristics of the as-cast and AM Ti-6Al samples as observed through OM and SEM. The OM images of the as-cast Ti-6Al samples (Figs. 3.3a1-a2) reveal a microstructure predominantly composed of uniformly distributed α-grains with large plate-like morphologies, interspersed with long, parallel α-columnar grains. This morphology is characteristic of the slow cooling rate associated with the β to α phase transformation in titanium alloys [157]. Higher magnification SEM images (Fig. 3.3a3) further confirm this microstructure, revealing prominently oriented α-columnar grains embedded within the larger plate-like grains. Complementary EDS mapping (Figs. 3.3a4-a5) indicates a relatively uniform distribution of Ti and Al elements, with Al concentrations consistently maintained at around 6 at%, demonstrating homogeneity throughout the sample.

In contrast, the microstructure of the AM Ti-6Al samples shows significant differences. The OM images (Figs. 3.3b1-b2) show a more refined grain structure, characterized by a predominantly uniform distribution of coarse α-grains with smaller plate-like morphologies. Additionally, these α-grains are adorned with smaller quantities of finer α-grains displaying basketweave morphologies, likely resulting from the rapid solidification rates inherent to the AM process. The corresponding SEM images and EDS mapping (Figs. 3.3b3-b5) provide further insights into the fine basketweave α-grains, which measure only a few micrometers in size, and confirm a uniform elemental distribution. The concentration of Al remains consistent at approximately 6 at%, similar to that of the as-cast samples. The absence of elemental segregation suggests that the observed microstructural differences are primarily attributable to the distinct thermal histories and solidification dynamics associated with the two fabrication methods, rather than compositional inconsistencies during processing.

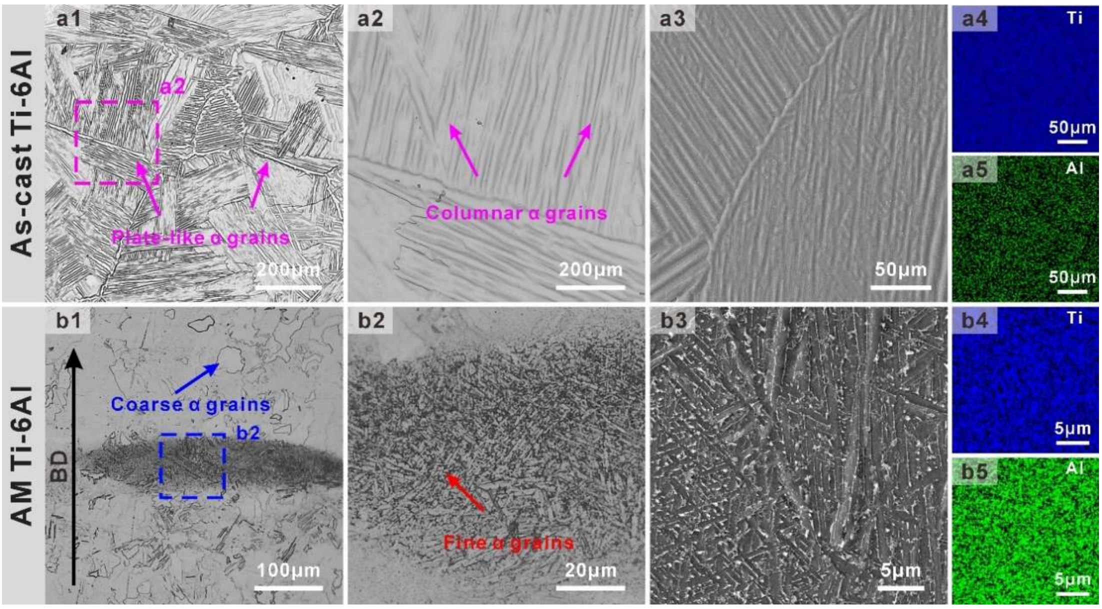

Fig. 3.3 Microstructural analysis of as-cast and AM Ti-6Al samples. (a1, a2) OM images of as-cast Ti-6Al samples show large, plate-like α-grains interspersed with parallel α-columnar grains. (a3) Higher magnification SEM image showing prominently oriented columnar grains embedded within the plate-like grains. (a4, a5) EDS mapping confirms uniform distribution of Al and Ti. (b1, b2) OM images of AM samples display coarse α-grains with finer plate-like and basketweave morphologies. (b3) Higher magnification SEM image reveals the appearance of finer basketweave grains measuring only a few micrometres. (b4, b5) EDS mapping shows uniform Al and Ti distribution.

To better investigate the microstructural differences in these samples, a comprehensive crystallographic analysis was performed using EBSD measurements, with the results presented in Fig. 3.4. In the as-cast Ti-6Al sample (Fig. 3.4a1), the inverse pole figure (IPF) map reveals large plate-like grains with no significant textural orientation. These grains are interspersed with columnar α-grains exhibiting low levels of intragranular misorientation, consistent with previous findings [158]. Quantitative grain size analysis (Fig. 3.4a2) reveals that the average grain size of the large plate-like α-grains is approximately 229.1 ± 59.9 μm, providing a clear statistical representation of the grain structure in the as-cast sample. The relatively large standard deviation observed is attributed primarily to variations in local nucleation density and inherent cooling-rate inhomogeneities associated with the casting process [159].

In contrast, the EBSD analysis of the AM Ti-6Al sample demonstrates a significantly refined microstructure, predominantly composed of coarse plate-like grains, which occupy approximately 75% of the observed area. These grains, marked by dark squares in Fig. 3.4b1 and further magnified in Fig. 3.4c1, have a considerably smaller average grain size of 25.3 ± 7.8 μm, as quantified in Fig. 3.4c2. Additionally, fine basketweave grains constituting approximately 25% of the observed microstructure (highlighted by blue squares in Fig. 3.4b1 and further detailed in Fig. 3.4d1) exhibit an even smaller average grain size of 5.7 ± 1.4 μm, as shown quantitatively in Fig. 3.4d2. Due to the rapid and uniform solidification rates characteristic of the AM process, the grain size distributions in the AM samples exhibit markedly lower standard deviations compared to their as-cast counterparts. In the meantime, similar to the as-cast sample, the AM Ti-6Al sample does not display any pronounced textural orientation, consistent with previously reported observations for AM titanium alloys [160].

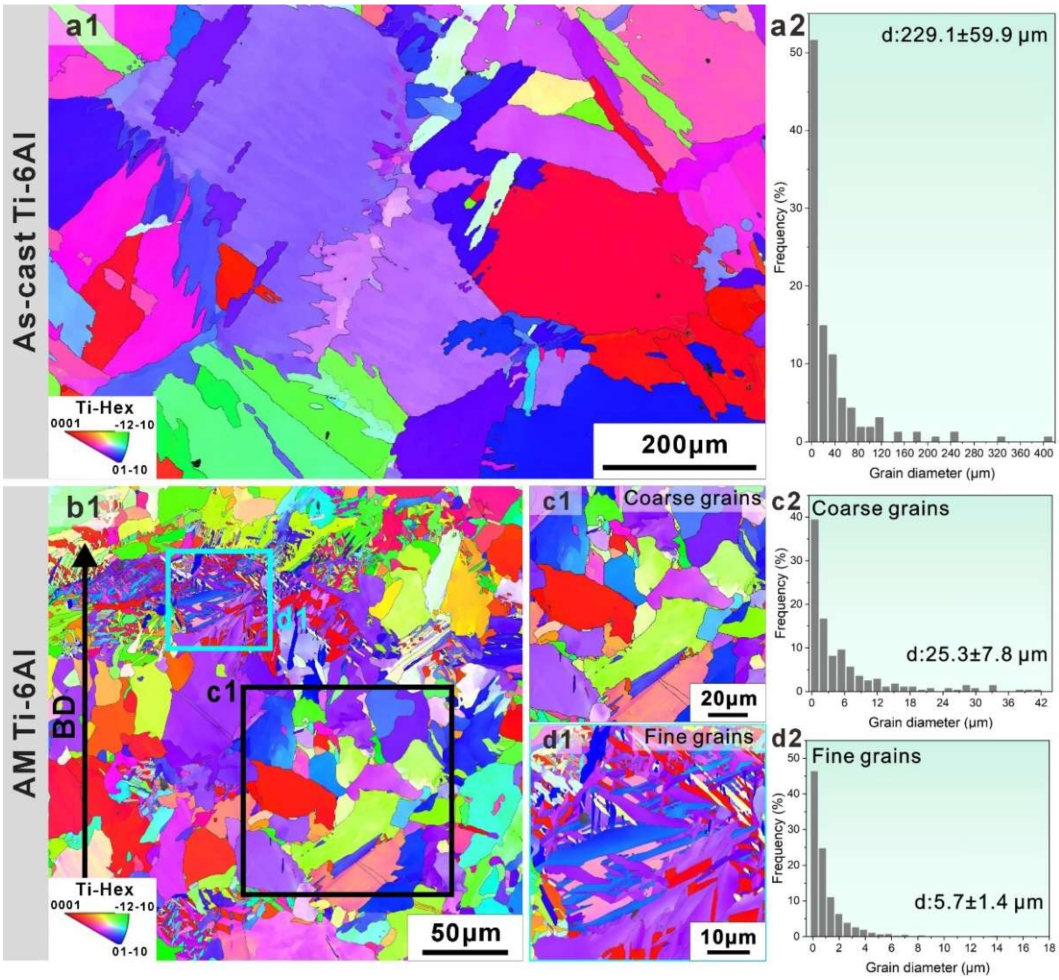

Fig. 3.4 EBSD analysis of the as-cast and AM Ti-6Al samples. (a1) IPF map of the as-cast sample, showing large plate-like grains with minimal textural orientation. (a2) Statistical analysis quantifying the average grain size of the large plate-like α-grains, measured at 229.1 ± 59.9 μm. (b1) IPF map of the AM sample, highlighting coarse plate-like grains (dark square) and finer basketweave grains (blue square). (c1, d1) Higher magnification views of the coarse and fine grains, respectively. (c2, d2) Grain size distribution of the coarse and fine grains, measured at 25.3 ± 7.8 μm and 5.7 ± 1.4 μm, respectively.

Considering the substantial impact of fabrication methods on grain size and morphology, as previously discussed, in-depth assessments of Kernel Average Misorientation (KAM) maps and GND densities were performed for both the as-cast and AM Ti-6Al samples, as depicted in Fig. 3.5. In the as-cast Ti-6Al alloys (Figs. 3.5a1-a2), the KAM map reveals pronounced local misorientations near sub-GBs and GBs. The corresponding GND density map indicates a relatively uniform distribution of dislocations within the large plate-like grains, with slightly elevated GND densities localized along GBs. Statistical analysis in Fig. 3.5a3 shows an average GND density of approximately (1.29 ± 0.06) $\times 10^{14}/m^2$, measured across multiple regions in the as-cast Ti-6Al sample.

In contrast, the AM Ti-6Al sample (Figs. 3.5b1-b2 and 3.5c1-c2) exhibits different characteristics. Although the KAM maps reveal a generally uniform distribution across the matrix, with higher misorientations near boundaries, the distribution of GND densities varies across different regions. In the coarse-grain regions, GND densities exhibit a relatively uniform distribution with an average value of approximately (4.45 ± 0.24) $\times 10^{14}/m^2$ (Fig. 3.5b3). However, in the finer basketweave grain regions, the GND densities increased significantly, reaching an average of approximately (17.88 ± 0.18) $\times 10^{14}/m^2$ (Fig. 3.5c3). This substantial increase is attributed primarily to the rapid solidification rates and unique thermal history inherent to the AM process, which not only refines the grain structure but also promotes the generation and accumulation of higher dislocation densities, particularly within finer-grained regions.

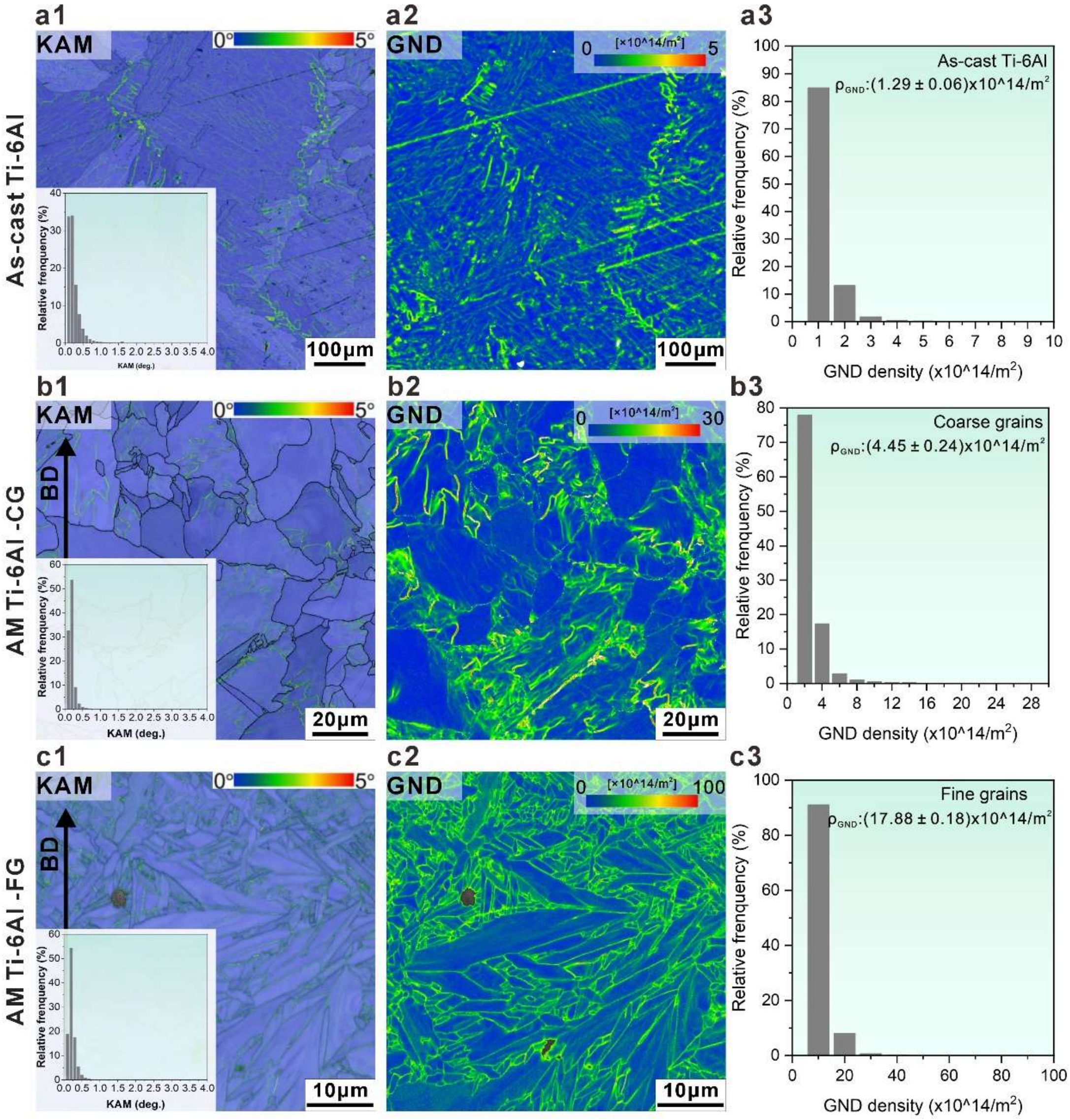

Fig. 3.5 In-depth analysis of KAM and GND densities in as-cast and AM Ti-6Al samples. (a1-c1) KAM maps illustrate local misorientations in the as-cast Ti-6Al sample, coarse grains, and fine grains in the AM Ti-6Al sample, respectively. Inset images show histograms of local misorientation distribution along with average KAM values. (a2-c2) Corresponding GND density maps highlighting the spatial distribution of dislocation densities across the regions. (a3-c3) Quantitative analyses of GND density, detailing the average dislocation densities for the as-cast Ti-6Al sample and for the coarse and fine grains in the AM Ti-6Al samples.

3.3 Discussions

3.3.1 Strengthening mechanisms

The tensile testing results (Fig. 3.1) indicate that the AM Ti-6Al sample demonstrates significantly enhanced mechanical properties, achieving an exceptional combination of ultrahigh strength and improved ductility compared to the as-cast counterpart. While the distinct microstructures resulting from the different manufacturing processes have been thoroughly characterized in the previous sections, it is essential to further elucidate the contributions of various strengthening mechanisms that arise from these microstructures and influence the yield strength (σ_y) of the AM Ti-6Al sample relative to the as-cast Ti-6Al alloy.

The yield strength of both the as-cast and AM Ti-6Al samples is expressed as the sum of contributions from individual strengthening mechanisms. These include the critical resolved shear stress of pure Ti (σ_{CRSS}) [161], solid solution strengthening due to Al addition (σ_{ss}), dislocation strengthening (σ_ρ), and grain boundary strengthening (σ_{GB}). Assuming that these mechanisms follow a linear mixture, the overall yield strength can be described by the following equation [162, 163]:

$$\sigma_y = \sigma_{CRSS} + \sigma_{ss} + \sigma_\rho + \sigma_{GB} \tag{3.1}$$

Given that the Al concentration remains consistent at 6 at% for both the as-cast and AM Ti-6Al samples, as evidenced in Fig. 3.3, it is reasonable to assume that the critical resolved shear stress of pure Ti (σ_{CRSS}) and the solid solution strengthening effect (σ_{ss}) are equivalent for both samples. Therefore, the observed increase in yield strength of the AM Ti-6Al sample compared to the as-cast Ti-6Al sample can be attributed primarily to other strengthening mechanisms. This increment in yield strength can be expressed as:

$$\sigma_{increment} = \Delta\sigma_{\rho} + \Delta\sigma_{GB} \tag{3.2}$$

Here, the $\Delta\sigma_{\rho}$ represents the dislocation strengthening due to increased dislocation density in the AM sample, and $\Delta\sigma_{GB}$ accounts for the extra grain boundary strengthening resulting from refined grain sizes in the AM sample.

Additionally, based on the EBSD analysis (Figs. 3.4 and 3.5), the microstructure of the AM Ti-6Al sample is composed of two distinct grain structures: predominantly coarse plate-like α grains and a smaller fraction of finer basketweave α grains, along with varying dislocation densities. Therefore, considering the rule of mixtures for composite materials comprising two components, the yield strength of the AM Ti-6Al sample can be determined as [102, 164]:

$$X = f_{fine}X_{fine} + f_{coarse}X_{coarse} \tag{3.3}$$

Where X is the composite yield strength, X_{fine} and X_{coarse} are the yield strengths of the individual components, and f_{fine} and f_{coarse} are their respective volume fractions. In the AM Ti-6Al sample, the volume fractions of the coarse and fine grains are 75% and 25%, respectively. Thus, the equation (3.2) can be further expanded as:

$$\sigma_{increment} = f_{fine}\,(\Delta\sigma_{\rho-fin} + \Delta\sigma_{GB-fine}) + f_{coars}\,(\Delta\sigma_{\rho-coarse} + \Delta\sigma_{GB-coarse})$$
(3.4)

Here, the individual parameter σ_{ρ} is attributed to dislocation hardening, described by the Taylor hardening model [165]:

$$\sigma_\rho = aM\mu b\sqrt{\rho} \tag{3.5}$$

Where a is the dislocation interaction constant (0.2 for α-Ti [166]), μ is the shear modulus (44 GPa for α-Ti [167]), M is the Taylor factor (1 for α-Ti [161]), b is the Burgers vector (0.290 nm [165, 168]), and ρ is the dislocation density that can be calculated by the following equation [169, 170]:

$$\rho = \frac{2\theta_{KAM}}{X_{step}b} \tag{3.6}$$

Here, X_{step} represents the EBSD scanning step size, which varies across the samples and regions, with values of 1μm for as-cast Ti-6Al, 0.15 μm for coarse-grain AM Ti-6Al, and 0.03 μm for fine-grain AM Ti-6Al sample. The parameter θ_{KAM} denotes the average local misorientation, obtained from EBSD statistics (Figs. 3.5a1-c1), and is calculated from the following expression:

$$\theta_{\mathrm{KAM}} = \exp\left[\frac{1}{N}\Sigma_1^i InKAM_{L,i}\right] \tag{3.7}$$

Where $KAM_{L,i}$ is the local KAM value at point t i, and N represents the total number of points within the test area [171].

Based on these parameters, the strength increments due to dislocation hardening in the AM sample are calculated as 103 ± 19 MPa for coarse grains ($\Delta\sigma_{\rho-coarse}$) and 391 ± 23 MPa for fine grains ($\Delta\sigma_{\rho-fine}$).

Similarly, grain boundary strengthening due to grain refinement can be calculated using the Hall-Petch relation [172]:

$$\sigma_{H-P} = k_{H-P} \cdot d^{-1/2} \tag{3.8}$$

Where d is the average grain size derived from SEM and EBSD statistics (Figs. 3.3 and 3.4), and k_{H-P} is the Hall-Petch coefficient for Ti alloys, ranging from 0.5 to 0.7 $\mathrm{MN} \cdot m^{-3/2}$ [173], with a value of 0.6 $\mathrm{MN} \cdot m^{-3/2}$ used for simplicity. Applying this equation, the grain boundary strengthening increments, relative to the as-cast sample, are calculated as 94 ± 22 MPa for coarse grains ($\Delta\sigma_{GB-coarse}$) and 240 ± 40 MPa for fine grains ($\Delta\sigma_{GB-fi}$).

Based on the equations and values provided, the strengthening increments from both dislocation and grain boundary mechanisms in the coarse and fine grains of the AM Ti-6Al sample, relative to the as-cast counterpart, have been thoroughly quantified and are presented in Fig. 3.6. The total strength increment for the AM Ti-6Al sample is calculated to be 329 ± 25 MPa. When combined with the yield strength of the as-cast sample, the theoretical yield strength of the AM sample is predicted to be 759 ± 30 MPa, which closely aligns with the experimentally measured value of 802 ± 10 MPa. This strong correlation between theoretical and experimental results highlights the significant strengthening effect achieved through additive manufacturing, primarily due to rapid solidification and microstructural refinement compared to the as-cast counterpart.

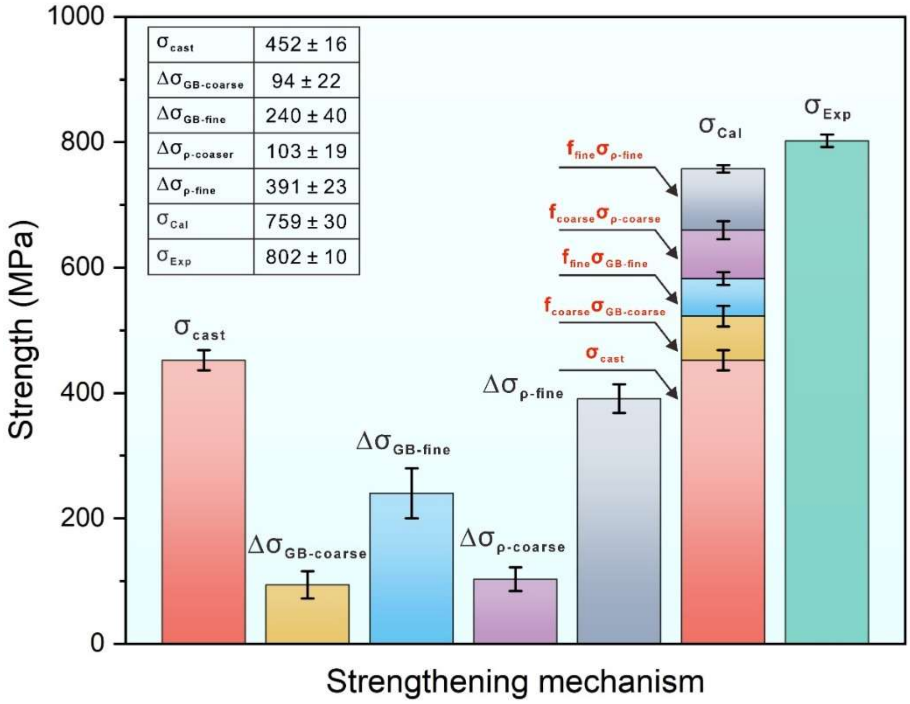

Fig. 3.6 Contributions of individual strengthening mechanism to the yield strength increment in the AM Ti-6Al sample compared to the as-cast Ti-6Al counterpart.

3.3.2 Origin of good ductility in the AM Ti-6Al sample

It is a long-standing principle in materials science that increasing strength almost inevitably comes at the expense of ductility—a trade-off so entrenched it is often regarded as unavoidable [174, 175]. In this study, however, we uncover a striking exception. The AM Ti-6Al sample not only exhibits increased strength, but also achieves markedly enhanced ductility, a rare and compelling combination. To unravel the mechanisms behind this unexpected synergy, we conducted an in-depth microstructural analysis prior and after deformation, presented in two sections.

3.3.2.1 Dislocation behaviors

An in-depth TEM analysis was performed on both the as-cast and AM Ti-6Al samples before deformation and after fracture, as shown in Fig. 3.7. In the as-cast sample (Figs. 3.7a-b), high-density dislocation arrays with a pronounced criss-cross morphology are observed throughout the matrix. These dislocations are predominantly long and straight, with limited dislocation activity observed beyond these pile-ups, indicative of restricted cross-slip and a tendency toward planar slip. Such planar slip behaviors, including dislocation pile-ups and localized deformation, are widely reported in α-titanium alloys containing aluminum additions and are typically associated with short-range ordering (SRO) [176, 177]. Previous studies have extensively documented that aluminum-induced SRO in as-cast Ti-Al alloys promotes a transition from wavy to planar slip, allowing dislocations to glide continuously along specific atomic planes and thus resulting in localized slip behaviors. This localization reduces the size of plastic deformation zones near fatigue crack tips, ultimately leading to a reduction in both ductility and fracture toughness [178-180]. Consequently, as macroscopic strain accumulates, planar slip can induce strain softening, influencing the overall mechanical response of the material [181, 182].

In contrast, the as-built AM Ti-6Al samples exhibit a high density of curved dislocations uniformly distributed within the grains, as shown in Fig. 3.7c. Unlike the casting process, which involves slow cooling, the rapid cooling rates in AM promote the formation of a supersaturated solid solution, as widely documented in the literature [183, 184]. This rapid solidification prevents Al segregation, thereby suppressing the formation of SRO. As a result, the absence of SRO enables dislocations to propagate more freely within the matrix, allowing for greater dislocation mobility and interaction, which accommodates plastic deformation more effectively [185].

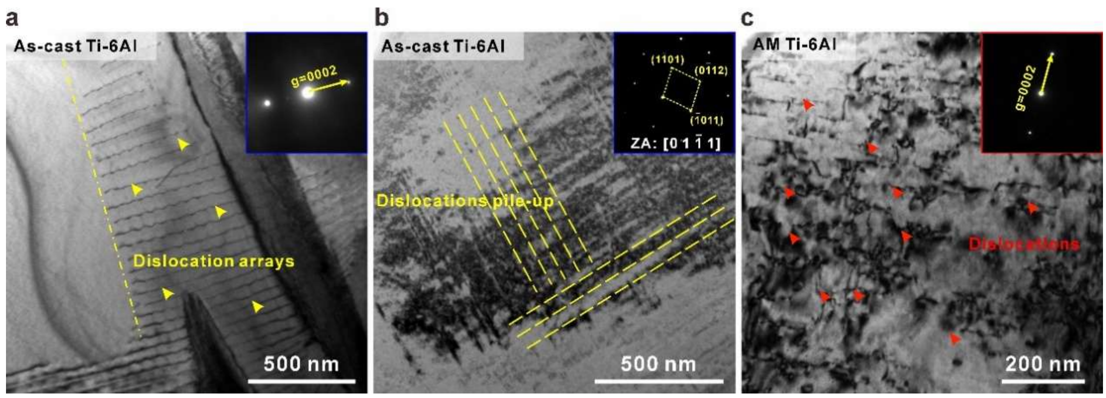

Fig. 3.7 Microstructural features of as-cast and AM Ti-6Al samples before deformation. (a, b) Bright-field TEM (BF-TEM) images of the as-cast Ti-6Al sample, showing dislocation pile-up configurations within the α-matrix. (c) BF-TEM image of the AM Ti-6Al sample, displaying predominantly curved dislocation configurations within the α-matrix.

The deformation behavior of both as-cast and AM Ti-6Al samples was further investigated through microstructural examination of the fractured samples, as shown in Fig. 3.8. In the as-cast Ti-6Al sample, deformation was dominated by planar slip, characterized by well-organized dislocation arrays that formed localized deformation zones (Figs. 3.8a and b). These planar slip bands restrict cross-slip and dislocation interactions, resulting in a rapid decline in strain-hardening capability and limited elongation prior to fracture. This behavior is typical of conventionally cast Ti alloys, where solute segregation and coarse microstructures promote embrittlement and impede dislocation mobility [148].

In contrast, the AM Ti-6Al sample reveals a high density of curved and entangled dislocation segments (Figs. 3.8c and d), reflecting significantly enhanced dislocation activity and strain-hardening capacity. This behavior arises primarily due to the absence of SRO, which facilitates dislocation mobility, encourages interactions among dislocations, and promotes activation of Frank-Read sources for dislocation multiplication and tangling [134]. The extensive formation of dislocation tangles (highlighted by red arrows in Fig. 3.8d) and frequent cross-slip contribute directly to sustained strain-hardening, even at high deformation stages, effectively delaying fracture initiation and enabling the concurrent achievement of high strength and ductility [186, 187]. These observations align closely with recent findings on AM-processed Ti alloys, where rapid solidification effectively suppresses micro-segregation, refines the microstructure, and promotes uniform deformation by enhancing dislocation interaction and multiplication [75, 188]. This distinctive dislocation behavior in the AM Ti-6Al sample underlies its ability to achieve superior combination of strength and ductility compared to conventional cast alloys.

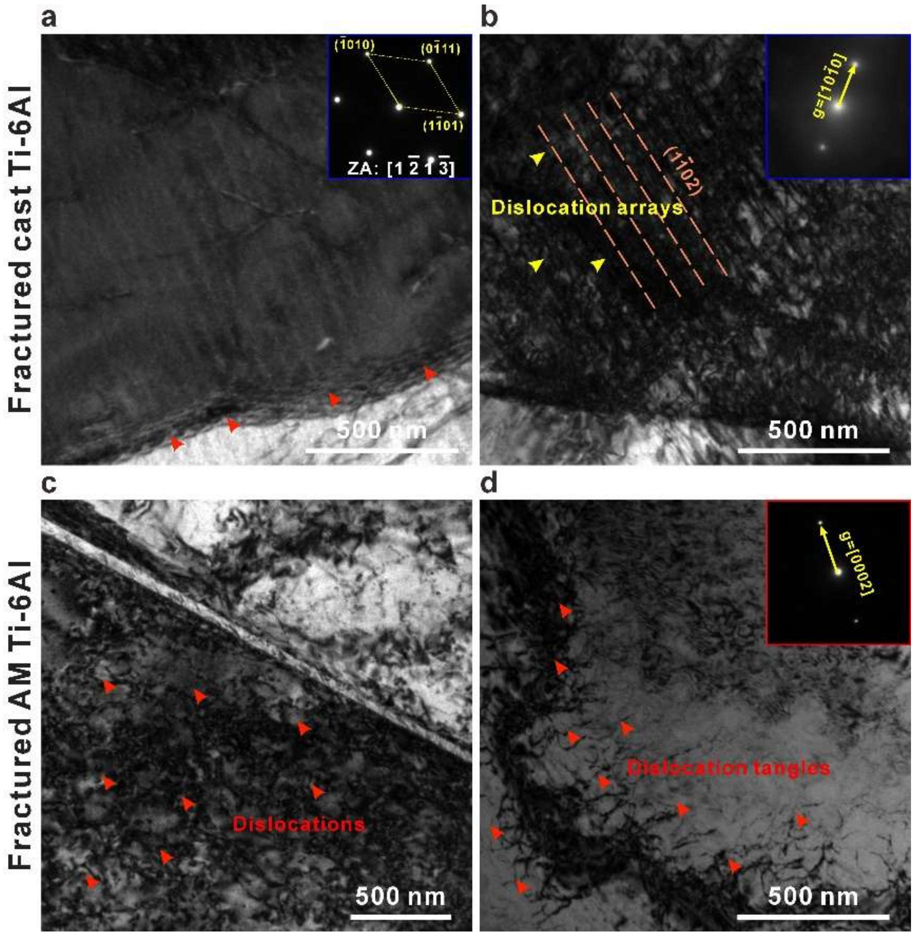

Fig. 3.8 Microstructural features of as-cast and AM Ti-6Al samples after fracture. (a, b) The BF-TEM images revealing dislocation configurations in the as-cast Ti-6Al sample after fracture. (c, d) The BF-TEM images showing dislocation configurations in the AM Ti-6Al sample post-fracture.

3.3.2.2 Crack propagation

Based on the observed dislocation behaviors, the as-cast Ti-6Al sample tends to localize strain more readily, thereby facilitating crack propagation along specific crystallographic directions. To gain further insight into the influence of dislocation behavior on mechanical properties, we investigated the crystallographic mechanisms of crack propagation in both as-cast and AM Ti-6Al samples.

EBSD analysis was performed on regions adjacent to the fracture surface of both samples (Figs. 3.9a1 and b1). In the as-cast Ti-6Al sample, interlamellar cracks are predominant, propagating primarily along the large plate-like grains. Within these grains, numerous microcracks are observed near the prominent interlamellar cracks, propagating along specific crystallographic orientations, as schematically delineated by red dotted lines and indicated by red arrows in the IPF and KAM maps (Figs. 3.9a2-a3). This behavior supports the hypothesis that planar dislocation activity, constrained to a single slip plane, leads to strain localization and preferential propagation of microcracks along specific planes, ultimately resulting in premature failure [189, 190].

In contrast, although interlamellar cracks are also present in the AM Ti-6Al sample (Fig. 3.9b2), the microcracks near the dominant large interlamellar cracks propagate in multiple directions, as evidenced by the elevated KAM values, schematically delineated by red dotted lines and marked by red arrows Fig. 3.9b3. This observation aligns with the dislocation behavior noted in the TEM images and suggests that the activation of multiple slip systems in the AM Ti-6Al sample not only facilitates dislocation entanglement during deformation but also impedes the propagation of microcracks along a single direction. This combined effect contributes to the simultaneous enhancement of both strength and ductility in the AM Ti-6Al sample [191, 192].

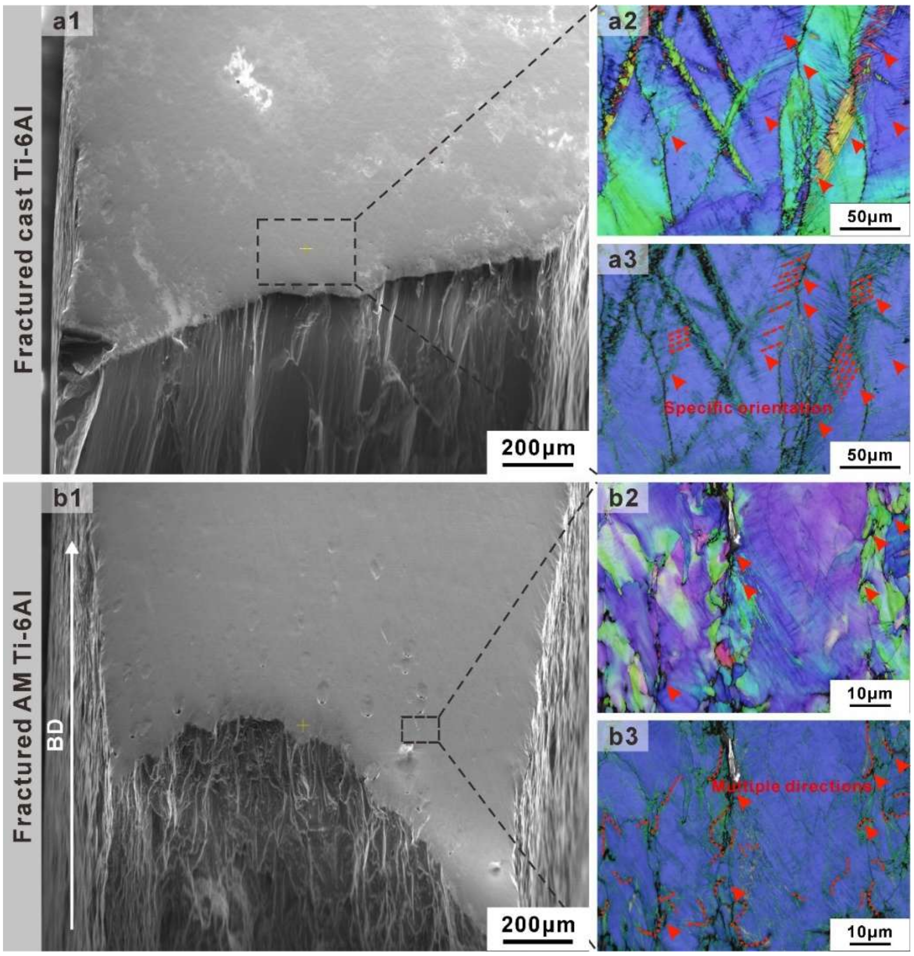

Fig. 3.9 EBSD analysis of crack propagation in the as-cast and AM Ti-6Al samples. (a1, b1) SEM images showing the examined areas of the as-cast and AM Ti-6Al samples. (a2, a3) IPF and KAM maps of the as-cast sample, highlighting dominant interlamellar cracks, with numerous microcracks propagating along specific crystallographic orientations within plate-like grains. (b2, b3) IPF and KAM maps of the AM sample illustrating dominant interlamellar cracks, with microcracks propagating in multiple directions.

The fractographic analyses of the as-cast and AM Ti-6Al samples reveal significant differences in fractured mechanisms, directly correlated with their respective microstructural evolutions (Fig. 3.10). The as-cast Ti-6Al sample exhibits predominantly brittle fracture features, evident by sharp, staircase-like cleavage facets with smooth contours (Figs. 3.10a1-a3). These columnar-shaped facets (highlighted by blue dotted lines in Fig. 3.10a3) align closely with the underlying α-columnar grain structures, signifying a predominantly trans-granular cleavage fracture. This brittle behavior is largely attributed to segregation-induced embrittlement resulting from solute partitioning inherent in conventional casting processes [147]. Specifically, micro-segregation leads localized, solute-enriched regions, significantly weakening grain boundaries and providing preferential pathways for rapid crack initiation and propagation [148]. The absence of dimples and the distinctly planar nature of these cleavage facets further confirms the limited plastic deformation preceding fracture, a characteristic feature of embrittlement arising from the inhomogeneities. Such segregation-induced defects act as intrinsic stress concentrators, diminishing fracture toughness and enhancing susceptibility to brittle failure.

In contrast, the AM Ti-6Al sample demonstrates a pronounced ductile fracture mode, characterized by a classic cup-and-cone fracture surface accompanied by significant necking (Fig. 3.10b1). Higher magnification observations (Figs. 3.10b2-b3) reveal densely distributed, deep and equiaxed dimples, indicative of substantial plastic deformation achieved through void nucleation, growth, and coalescence. This enhanced ductility is primarily attributed to the refined, segregation-free microstructure attained through rapid solidification conditions characteristic of additive manufacturing. The inherently high cooling rates during AM effectively suppress solute partitioning, thereby eliminating embrittling segregation and promoting chemical homogeneity. Such a homogenized microstructure facilitates more uniform strain distribution, while the refined grain morphology provides enhanced grain boundary strength, collectively hindering crack initiation and propagation [193, 194]. The clear transition from brittle cleavage in the as-cast sample to pronounced ductile dimpling in the AM-produced material highlights the critical role of AM in mitigating segregation embrittlement, ultimately enhancing mechanical performance and fracture resilience.

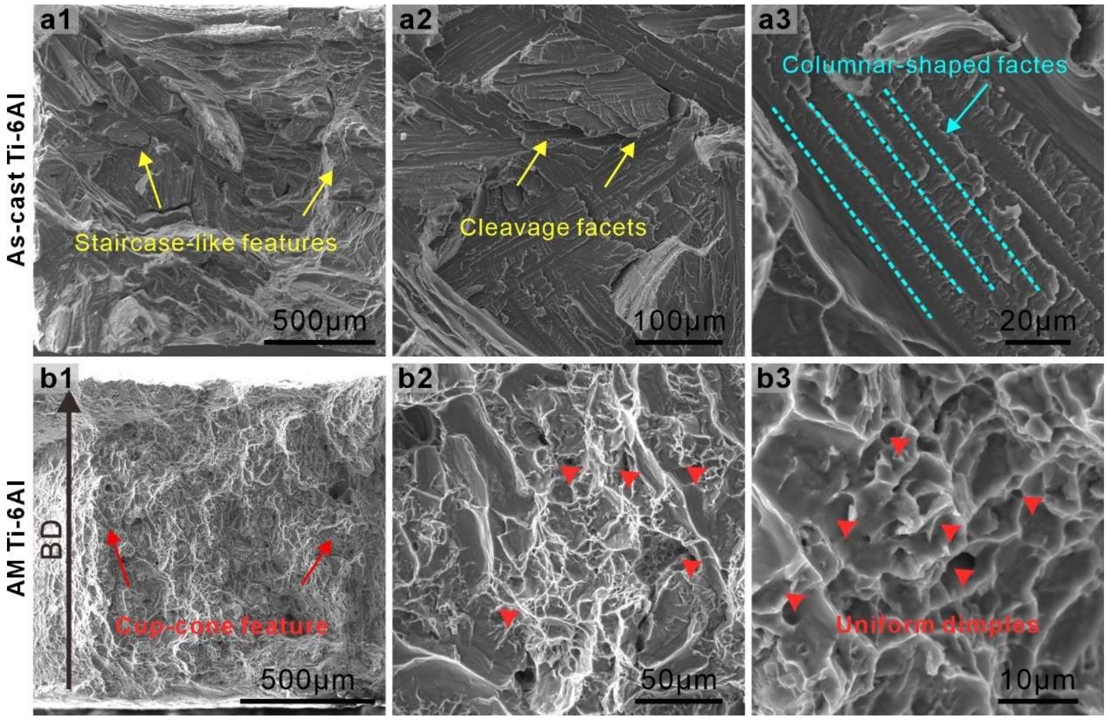

Fig. 3.10 Fracture morphologies of as-cast and AM Ti-6Al tensile samples. (a1) Overview of the fracture surface of the as-cast Ti-6Al tensile sample. (a2, a3) Higher-magnification images showing staircase-like cleavage facets indicative of brittle fracture. (b1) Overview of the fracture surface of the AM Ti-6Al tensile sample. (b2, b3) Enlarged views revealing a high density of deep, equiaxed dimples, characteristic of ductile fracture.

3.4 Conclusions

The comparison of the microstructural and mechanical properties of Ti-6Al alloys fabricated through both as-cast and AM processes has elucidated significant differences attributed to the distinct manufacturing techniques employed. The key findings are as follows:

(1) The AM Ti-6Al samples exhibited significantly improved tensile strength and ductility compared to their as-cast counterparts. Specifically, the AM Ti-6Al samples achieved a 90% improvement in YS, an 80% increase in UTS, and nearly a 100% enhancement in elongation to failure compared to the as-cast samples. These results strongly indicate that even low-alloy α-Ti alloys can achieve superior properties, making them a promising candidate for commercial applications utilizing AM methods.

(2) The enhancement in YS is directly associated with the microstructural advantages observed in the AM samples, including the presence of fine basketweave grains that effectively impede dislocation movement during deformation and enhance dislocation strengthening. Additionally, the increased dislocation densities within the fine basketweave grains also contribute to the YS, primarily as a result of the rapid cooling rates and complex thermal history characteristic of AM processes.

(3) The superior ductility observed in the AM Ti-6Al samples can be attributed to differences in dislocation behavior, with the as-cast samples predominantly exhibiting planar slip and the AM samples characterized by wavy slip. This variation in dislocation behavior is linked to differences in cooling rates: the low cooling rate of the as-cast samples promotes SRO, facilitating planar slip, while the high cooling rate associated with the additive manufacturing process allows for a supersaturated solid solution that encourages wavy slip. The intricate dislocation structure resulting from wavy slip enhances strain hardening and plastic deformation capacity. Furthermore, the dislocation tangles in the AM Ti-

6Al samples act as Frank-Read sources, promoting the formation of dislocation tangles and thereby enhancing the material's ability to undergo deformation without experiencing premature failure.

(4) The findings of this study underscore the potential of AM to produce low-alloy α-Ti with enhanced mechanical properties through the strategic manipulation of microstructure. The inherent advantages of AM, including rapid cooling rates and complex thermal histories, play a crucial role in improving ductility and strength. These enhancements offer promising avenues for the development of high-performance materials suitable for a wide range of applications.

Chapter 4 Exceptional Strength and Ductility in Heterogeneous Multi-gradient TiAl alloys through Additive Manufacturing

4.1 Introduction

In Chapter 3, we demonstrated that introducing Al into Ti via AM significantly enhances the alloy's strength without severely compromising its ductility, yielding superior mechanical properties compared to conventionally cast counterparts. Despite these promising improvements, the mechanical performance obtained still falls short of certain demanding structural applications, primarily due to the inherent strength-ductility trade-off when higher Al content is introduced. In this context, heterostructure materials could be a solution to mitigate this trade-off. As introduced in Chapter 1, recent advances in heterostructured materials suggest that the carefully designed hetero architectures could simultaneously enhance strength and ductility. Motivated by these insights, and recognizing the brittle but hard properties introduced by excessive Al additions, this chapter focuses on a novel heterogeneous multi-gradient TiAl alloy fabricated through AM. By strategically designing compositional and microstructural gradients, we aim to effectively mitigate embrittlement issues while exploiting the full potential of heterostructure-induced strengthening and toughening mechanisms.

α-Titanium (α-Ti) is predominantly associated with α-stabilizers such as O, N, and Al. It boasts a range of outstanding properties: outstanding weldability, pronounced notch toughness, superior specific strength, and good ductility (exceeding 20%), rendering it particularly suitable for demanding applications where ductility is paramount [195-197]. However, the attribute of good ductility exists primarily in non-alloyed α-Ti or low-alloyed α-Ti, wherein the strength of these alloys remains comparatively modest [198, 199]. In order to elevate its strength to meet the requirements of specific practical applications, the incorporation of α-stabilizing elements with suitable content becomes imperative. Nevertheless, this improvement in strength is frequently counterbalanced by a dramatic decline in ductility, exemplifying the infamous strength-ductility trade-off dilemma. Existing literature underscores that minor incorporations of either oxygen or aluminium result in compromises in ductility concurrent with strength augmentation – ductility plummeted by 200% upon introducing 0.3wt% oxygen or 4.0wt% Al [197]. Therefore, establishing an economical fabrication paradigm that bolsters strength without markedly compromising ductility remains crucial for advancing the structural applications of α-Ti.

Recently, significant advancements have brought heterostructure materials into the spotlight as highly promising candidates capable of achieving a superior combination of strength and ductility through the ingenious integration of appropriate microstructural designs. Consequently, these fosters improved strength and strain-hardening capabilities while minimizing reduction in ductility [91, 200-203]. In a previous study, Li et al. successfully fabricated a heterostructured pure Ti, characterized by alternating coarse and fine-grain layers, achieved through annealing and hot pressing techniques, demonstrated a noticeable enhancement in strength – rising from 292 MPa to 354 MPa – while maintaining appreciable ductility, with only a minor reduction from 54% to 53% when compared to its coarse-grain counterpart [102]. Similarly, Wu et al. highlighted a favourable synergy of strength and ductility in a heterogeneous lamella-structured Ti material, achieved by asymmetric rolling and partial recrystallization. It exhibited comparable ductility to coarse-grain Ti while showcasing strength similar to ultra-fine-grained Ti [202]. Nevertheless, conventional methods for crafting these heterostructures are burdened with intrinsic drawbacks, including prolonged processing time and substantial cost implications. These challenges become more pronounced when dealing with intricate geometries and precisely managing composition modulations during fabrication, rendering their realization inherently challenging.

To address these pressing challenges, AM has emerged as a promising solution, pioneering near-net-shaping production with heterogeneous configurations via compositional methods [204, 205]. Previous studies have demonstrated the capability of AM in introducing heterogeneous microstructures through in-situ compositional adjustments. Examples include the fabrication of a functionally graded material transitioning from Ti-6Al-4V to Al12Si via laser metal deposition (LMD) [206], and the microstructure transition gradients in dissimilar Ti alloys (Ti-5Al-5V-5Mo-3Cr/Ti-6Al-4V) via wire-arc AM [207], where noticeable changes in microstructure were observed across distinct components. Evidently, the advent of AM offers a distinct avenue for the exploration of innovative material design paradigms, shedding light on improving the overall performance of the near α-Ti alloys. Nevertheless, the research landscape still navigates substantial challenges, including limited enhancements in strength paired with noticeable sacrifices in ductility [208, 209], alongside concerns of embrittlement or cracking at the interfaces owing to differential thermal expansions, disparities in elastic moduli, and variations in yield strengths [210-213]. For instance, investigations on dual-phase Ti alloys, especially TA15 and Ti2AlNb, synthesized via laser AM, underscored strength augmentations from 1028 MPa to 1067 MPa, but at the evident expense of ductility, plunging from 13.2% to 8.0% [214]. Analogously, the incorporation of Invar 36 (64 wt% Fe, 36 wt% Ni) into Ti-6Al-4V alloys via AM has led to the emergence of intermetallic phases, e.g., FeTi (B2), Fe_2Ti (C14), Ni_3Ti (DO_{24}), $NiTi_2$. This has ultimately resulted in undesirable delamination, which renders them unsuitable for structural applications [212]. Therefore, there is a pressing requirement for a re-envision of design strategies capable of mitigating the concerns related to embrittlement at the interfaces.

Recent studies have proposed a strategy to address the issue of embrittlement at interfaces by incorporating elemental gradients to prevent premature fractures. For example, Wei et al. found that even when combining two seemingly unrelated materials, Ti6Al4V and Inconel 625, synergistic enhancements in both strength and ductility can still be achieved. This is attributed to the introduction of gradient materials transitioning between these two materials to avoid sudden transitions between layers [215]. In addition, Guan et al. discovered that the heterostructural alternating-layered CrMnFeCoNi/AlCoCrFeNiTi0.5 composite, which possesses two phases with distinctive hardness, can still achieve unparalleled strength and ductility due to the crack-restrained effect by the soft layer [216]. Inspired by these findings, this study explores an alternative lamellar structure for near α-Ti alloys. It incorporates graded materials for smooth transitions while avoiding brittle intermetallic compounds. In other words, the strategy involved the development of a lamellar structural Ti-Al/Ti heterostructure, which was rationalized by several compelling reasons: 1. The high solubility of Al in Ti at room temperature minimizes the likelihood of undesirable intermetallic compound formation; 2. The noticeable diffusion of Al in Ti might provide a smooth transition across layers, preventing large disparities in thermal expansion coefficients or variations in elastic moduli that could lead to undesirable delamination [217]; 3. The well-documented strengthening effect of Al in Ti may result in high strength in heterostructured alloys [22-25].

In this work, a multi-gradient α-Ti/Ti-10Al architecture was developed, which is characterized by an exceptional combination of strength – approaching that of the robust Ti-10Al alloy – and ductility, close to that of ductile pure Ti. Advanced characterization techniques have been employed to elucidate the comprehensive mechanisms that underlie these exceptional properties. Notably, critical diffusion behaviours of Al were observed during the additive manufacturing process, leading to the emergence of a novel heterogeneous multi-gradient structure characterized by distinctive compositional and structural gradients. The heterogeneous multi-gradient architecture imposes geometric constraints that demonstrate gradient strain partitioning during deformation, thereby enhancing work hardening and impeding crack initiation and propagation, ultimately achieving higher strength while preserving good ductility. This innovative structural design strategy presents a promising avenue for crafting superior Ti with a remarkable strength-ductility combination, with broader implications for other alloys where alloying may lead to undesirable reductions in ductility.

4.2 Results

4.2.1 Phase constitutions

Figure 4.1 displays the phase constituents of both powders and as-built specimens. The CP-Ti powder exhibited only α-Ti phase ($P6_3/mmc$, with lattice constants of a=4.57 Å, b=4.57 Å, c=2.83 Å), while the pre-alloyed Ti-54Al powder presented a combination of α-Ti phase, α_2-Ti_3Al ($P6_3/mmc$, with lattice constants of a=5.75 Å, b=5.75 Å, c=4.63 Å), and γ-TiAl (P4/mmm, with lattice constants of a=2.81 Å, b=2.81 Å, c=4.07 Å) phases, attributable to the Al concentration exceeding 50 at. % in pre-alloyed powders (Fig. 4.1a).

Figure 4.1b presents the phase constituents of the as-built homogeneous Ti, homogeneous TiAl, and heterogeneous TiAl samples, observed in the cross-sectional surface parallel to the build direction. The homogeneous Ti sample disclosed only the α-Ti phase, whereas the homogeneous TiAl displayed additional peaks associated with α_2-Ti_3Al. The γ-TiAl peak identified in the pre-alloyed TiAl powder was absent, indicating complete melting and mixing of CP-Ti and pre-alloyed TiAl powders during the fabrication process. Notably, despite employing identical fabrication parameters, such as laser power and powder feed rate, for both the homogeneous TiAl and heterogeneous TiAl samples, the presence of peaks in the heterogeneous TiAl sample (only α-Ti phase was found) resembled those in the homogeneous Ti samples rather than those observed in the homogeneous TiAl sample. This discrepancy will be further discussed in the following sections.

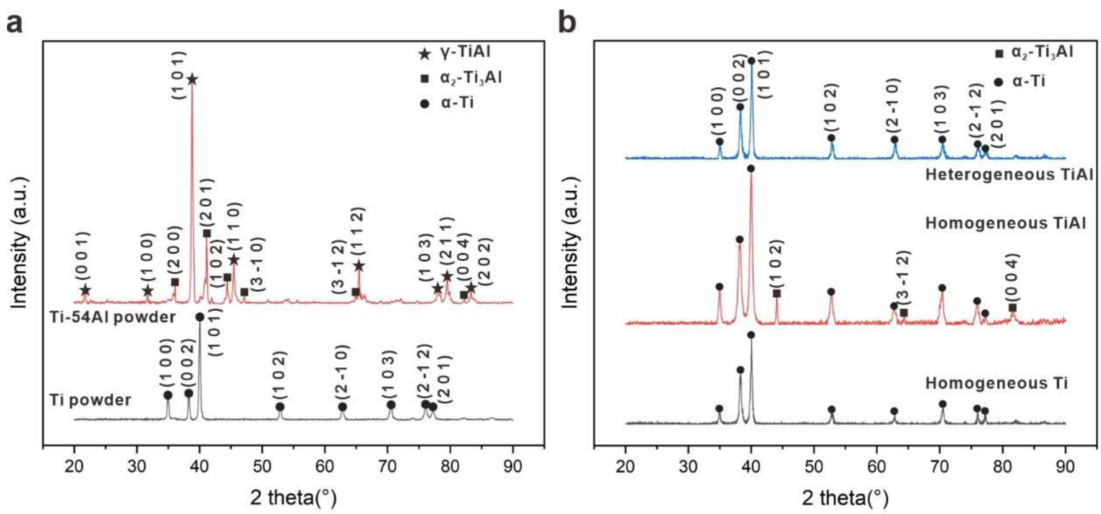

Fig. 4.1 Phase constituents of the powders and the as-built specimens. (a) XRD spectra of as-received CP-Ti and pre-alloyed Ti-54Al powders. (b) XRD patterns of the as-built homogeneous Ti, homogeneous TiAl, and the heterogeneous TiAl samples, observed in the cross-sectional surface parallel to the build direction.

4.2.2 Mechanical performance

4.2.2.1 Tensile properties

Figure 4.2a illustrates the tensile engineering stress-strain curves for the as-built homogeneous Ti, homogeneous TiAl, and heterogeneous TiAl samples. The homogeneous Ti sample, as anticipated, exhibited superior ductility and moderate strength, initiating to yield at a stress of ~440 MPa (σ_y) and reaching an ultimate tensile strength (σ_{UTS}) of ~560 MPa, accompanied by a large ductility (ε_f) of 37.6%. In stark contrast, the homogeneous TiAl sample displayed a substantial increase in strength, with σ_y and σ_{UTS} approximating 910 MPa and 1000 MPa, respectively, but a substantial decrease in ductility to only 6.1%. This phenomenon is likely attributed to the formation of secondary, hard but brittle α_2-Ti_3Al phases, as corroborated by prior XRD analysis [218]. Remarkably, the heterogeneous TiAl alloy manifests a pronounced enhancement in strength, with σ_y and σ_{UTS} at ~760 MPa and ~890 MPa, respectively, while concurrently sustaining a commendable ductility of ε_f~33.4%. In comparison with the homogeneous Ti alloy, this heterogeneous TiAl alloy signifies an enhancement in yield strength by nearly 70% with only a minor compromise in ductility. Moreover, compared to the homogeneous TiAl, the heterogeneous TiAl sample exhibits an almost six-fold enhancement in ductility and only a slight reduction in strength. It is well known that the improvement of strength always comes at the significant expense of ductility [219], a trade-off observed extensively in various α-Ti alloys, including SLM CP-Ti [220, 221], SLM hydride-dihydride (HDH) Ti [222, 223], SLM TiN_x [224] and powder metallurgical (PM) $TiAl_x$ alloys [225]. Remarkably, our heterogeneous TiAl alloy outperformed the strength and ductility combinations reported for other α-Ti alloys to date, demonstrating a considerably improved balance between the yield strength and ductility, as shown in Fig. 4.2b.

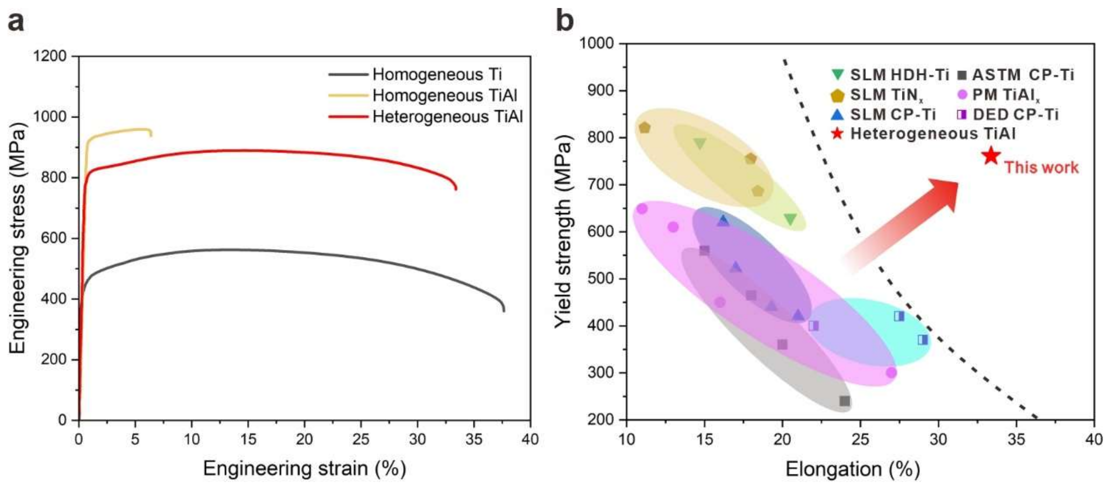

Fig. 4.2 Mechanical properties of the as-built homogeneous Ti, homogeneous TiAl, and heterogeneous TiAl at room temperature. (a) The engineering stress-strain curves. (b) Comparison of the yield strength and total elongation of the present work to other reported high strength α-Ti alloys to date, including SLM CP-Ti [220, 221], SLM HDH-Ti [222, 223], SLM TiNX [224], DED CP-Ti [226, 227] and PM TiAlx [225].

To ensure reproducibility, a minimum of three tensile samples were tested, with the average values (yield strength, ultimate tensile strength and elongation) reported and presented in Fig. 4.3. The yield strength was determined using the 0.2 % offset method for plastic strain.

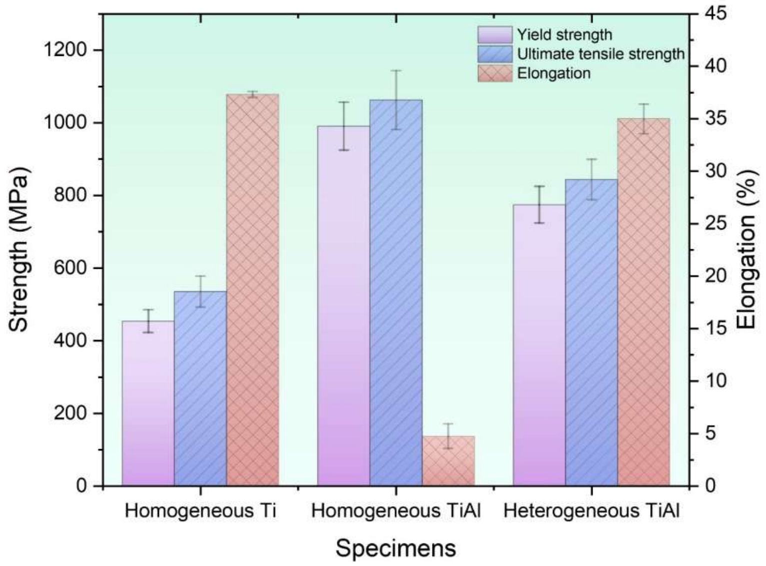

Fig. 4.3 The yield strength, ultimate tensile strength and elongation of the different specimens.

4.2.2.2 Microhardness distributions

Following the evaluation of overall mechanical performance, we extended our investigation to conduct a microhardness experiment, intending to analyse the hardness distribution relative to the build distance, as depicted in Fig. 4.4. The homogeneous Ti and homogeneous TiAl samples demonstrated a uniform distribution of microhardness along the build direction, with average microhardness values of 212 HV and 367 HV, respectively. Conversely, for the heterogeneous TiAl sample, the microhardness values exhibited periodic variations as the build distance increased. The microhardness value was higher near the TiAl layers, while a reduced value was observed in proximity to the Ti layers, validating the successful design of the heterogeneous TiAl alloy. Notably, the hardness values exhibited gradual changes in line with the increasing build distance. Additionally, the maximum hardness value (334 HV) for the heterogeneous TiAl sample was lower compared to that of the homogeneous TiAl sample, while the minimum hardness value (253 HV) was higher compared to the homogeneous Ti sample. This observation potentially implied an interaction between Ti and TiAl layers during the fabrication process. Furthermore, this could provide further insights into the absence of the α_2-Ti_3Al phase in the heterogeneous TiAl sample, corroborating our earlier XRD experimental findings.

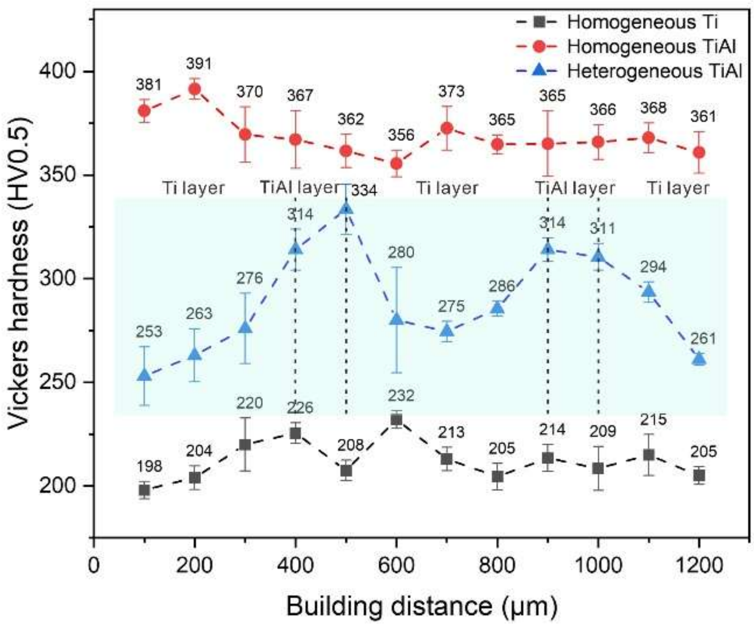

Fig. 4.4 Microhardness distribution over the building distance.

4.2.2.3 Local strain evolution process

Tensile test and microhardness results substantiate the successful conceptualization of a heterogeneous TiAl alloy, showcasing a remarkable interplay of strength and ductility. To unravel the mechanisms underlying this simultaneous enhancement, in-situ DIC experiments were conducted. This analysis elucidates strain profiles across discrete macro strain increments, visualized in Fig. 4.5. It was paramount to emphasize that the loading direction was aligned perpendicular to the build direction to evaluate the mechanical contributions of the Ti and TiAl layers during deformation.

In Fig. 4.5a, a tensile curve for the heterogeneous TiAl alloy is presented. Correspondingly, the progression of local strains at varying strain levels has been outlined to elucidate the details of the deformation mechanism. This strain evolution can be systematically categorized into five discernible stages, as evidenced by the DIC images in Figs. 4.5b to 4.5i:

(1) Stage I (0-4.0% macro strain): The preliminary deformation stage registered homogeneous strain distribution across both the Ti and TiAl layers. At this stage, the material seemed to accommodate the external stress with minimal evidence of strain localization (Figs. 4.5b and 4.5c). Dash horizontal lines highlighted the TiAl layers in the DIC images.

(2) Stage II (4.0-18.4% macro strain): As the macro strain continued to increase, there was a gradual emergence of heterogeneity in strain distribution. Notably, the onset of strain localization is perceptible at the TiAl layer (Figs. 4.5d and 4.5e).

(3) Stage III (18.4%-21.1% macro strain): At this stage, the strain localization in the TiAl layer region intensified as the macro strain continued to increase. Moreover, the strain localization began to spread from the TiAl layer to the adjacent regions, indicating that the deformation is becoming less uniform and more concentrated in specific areas (Fig. 4.5f).

(4) Stage IV (21.1-27.9% macro strain): Further diffusion of strain localization was observed, spreading from the initial TiAl layer region to the Ti layer region. Additionally, strain localizations that initially manifested in separate TiAl layer regions begin to merge under the increasing strain (Figs. 4.5g and 4.5h).

(5) Stage V (27.9% and onwards): At this stage, strain localization permeated the entirety of the specimen, growing in intensity. Eventually, this culminated in the fracture of the specimen, which occurred along the area where the strain localization is most pronounced (Fig. 4.5i).

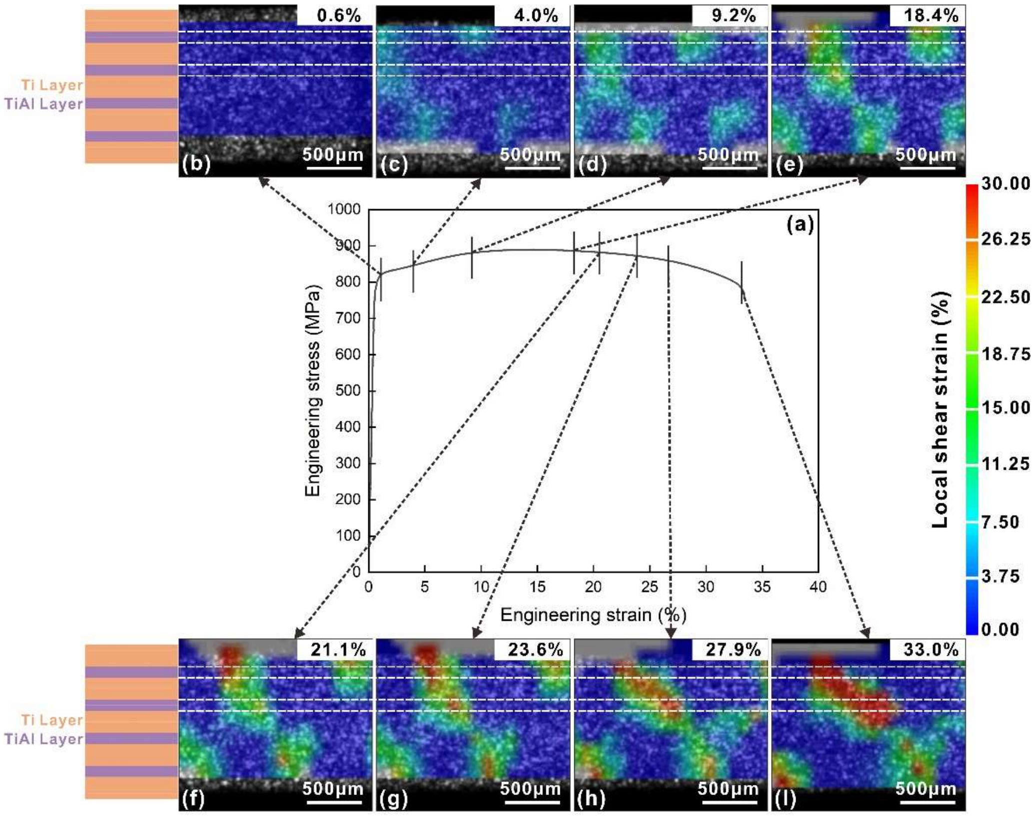

Fig. 4.5 In-situ DIC visualizations depict strain distributions along the loading direction at distinct macro strain levels. (a) Stress-strain curves corresponding to the heterogeneous TiAl alloy. (b and c) Initial phase (Stage I) with scant indications of strain localization. (d and e) Intermediate phase (Stage II) marking the onset of heterogeneous strain distribution. (f) Subsequent development (Stage III) characterized by expanded strain localization. (g and h) Advanced phase (Stage IV) illustrating extensive strain localization, transitioning from the TiAl layer to the adjacent Ti regions. (i) Terminal phase (Stage V) capturing the comprehensive spread of strain localization culminating in sample rupture.

This progression underscored the importance of understanding how different layers, i.e. the Ti and TiAl layers, influence the mechanical response under loading. Comparative in-situ DIC experiments were conducted on homogeneous Ti and TiAl, as illustrated in Fig. 4.6. The homogeneous Ti demonstrated excellent plasticity during tensile testing. During plastic deformation, strain localization occurred predominantly at the mid-section, leading to necking and subsequent fracture at higher strain levels. In contrast, the homogeneous TiAl sample exhibited markedly lower plasticity, fracturing readily upon the onset of strain localization.

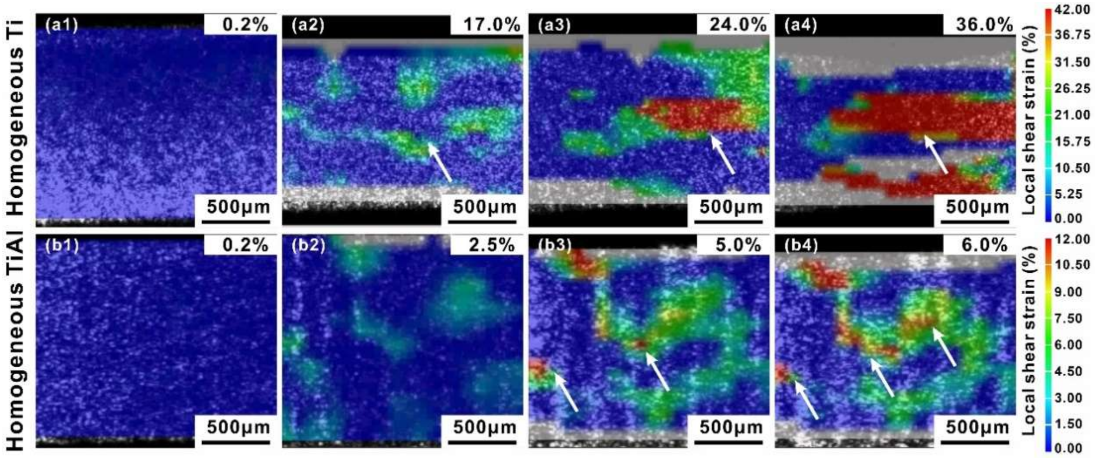

Fig. 4.6 The in-situ DIC visualizations of the homogeneous Ti and TiAl specimens. (a1-a4) Homogeneous Ti sample. (b1-b4) Homogeneous TiAl sample.

The results of this in-situ DIC experiment, which will be further elaborated upon in the subsequent sections combined with our in-situ EBSD findings, offer valuable insights into how microstructural heterogeneity can influence deformation behaviour and eventual failure mechanism of the material.

4.2.3 Compositional and microstructural analysis

4.2.3.1 Cross-sectional features of as-built parts

To establish a correlation between mechanical properties and microstructural characteristics, SEM observations were conducted on the cross-sectional surface parallel to the build direction. Fig 4.7 exhibited the cross-sectional microstructures of the as-built homogeneous Ti, homogeneous TiAl, and heterogeneous TiAl samples. As depicted in Figs. 4.7a1 and 4.7a2, the inherent high cooling rate differentiated the microstructure of LENS fabricated Ti from cast Ti alloy, leading to the dominance of lamellae-like and plate-like α grain morphologies. This observation is consistent with prior studies [198]. The incorporation of pre-alloyed TiAl powders during the fabrication process prompts morphological shifts toward primarily short rod-like morphologies, conventionally referred to as basketweave morphologies [207], as portrayed in Figs. 4.7b1 and 4.7b2. Furthermore, it was significant to highlight that in the as-fabricated homogeneous Ti or homogeneous TiAl samples, no conspicuous changes in grain morphologies are discernible within the matrix along the build direction.

In contrast, the heterogeneous TiAl sample manifested pronounced microstructural changes along the build direction, as depicted in Fig. 4.7c1. It presented a mix of plate-like (Fig. 4.7c1), lamella-like (Fig. 4.7c2), and basketweave morphologies (Fig. 4.7c3), all of which were previously identified in the homogeneous Ti and TiAl samples. Combining this with EDS results, it can be concluded that the plate-like and lamellae-like grains predominantly populated the Al-deficient region. In comparison, the basketweave morphologies were predominantly situated in the Al-rich region. Further quantitative EDS analysis conducted in the Al-rich regions indicates that the Al concentration was marginally lower than that found in the homogeneous TiAl, falling below 8 at% as opposed to the designed value of approximately 10 at%. This discrepancy elucidates the disappearance of the α_2-Ti_3Al phases. Furthermore, the subsequent EDS line scan highlights the gradual decrease in Al content transitioning from Al-rich to Al-deficient areas. This transition is mirrored by a shift in grain morphology from primarily basketweave structures to predominantly lamellae-like and plate-like grains. Such observations suggest that these morphological changes in grains are not abrupt but rather transition incrementally along the build direction from the TiAl to subsequent Ti layers.

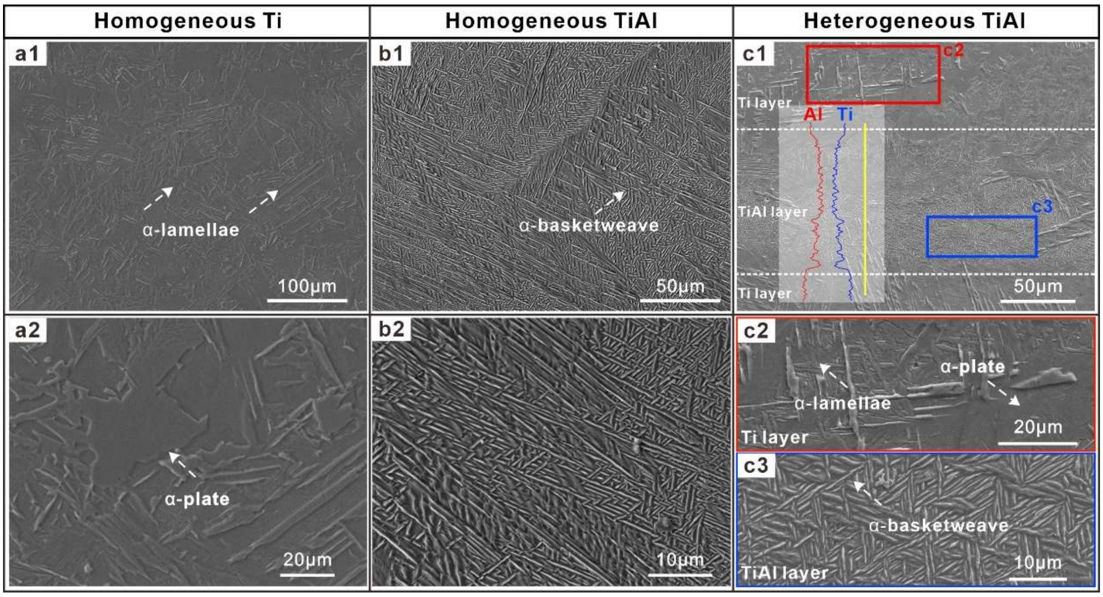

Fig. 4.7 SEM-based microstructural examination of the as-built homogeneous Ti, homogeneous TiAl, and heterogeneous TiAl samples. (a1 and a2) Homogeneous Ti, presented at low and high magnifications, respectively. (b1 and b2) Detailed microstructure of the homogeneous TiAl at the low and high magnifications. (c1) An overview image underscoring both microstructural and elemental discrepancies within the specimen. The accompanying EDS line scan illustrates the gradational variation in Al and Ti concentrations, transitioning from the TiAl layer to the adjacent Ti regions. (c2) A closer magnified inspection of the Ti layer reveals predominantly plate-like and lamella grain morphologies. (c3) Microstructural examination of the TiAl layer at a higher magnification reveals predominantly basketweave grain morphologies.

4.2.3.2 Elemental distribution of as-built heterogeneous TiAl

To further understand the gradual morphological changes at the Ti/TiAl interface of the heterogeneous TiAl sample, EPMA was employed to ascertain the elemental distribution, as displayed in Fig. 4.8, which indicates that heterogenous TiAl alloy with alternating Ti and TiAl layers was successfully fabricated along the build direction (Figs. 4.8a to 4.8c). Concurrently, the boundaries of the molten pool were demarcated by high concentrations of Al. Interestingly, originating from each TiAl layer, the Al concentration displayed a gradual decrement, transitioning from approximately 8 at% at the TiAl layer to ultimately reaching pure Ti within the Ti layer, in accordance with the build direction. This strongly indicates that compositional heterogeneity was formed with a gradual change in compositional gradience.

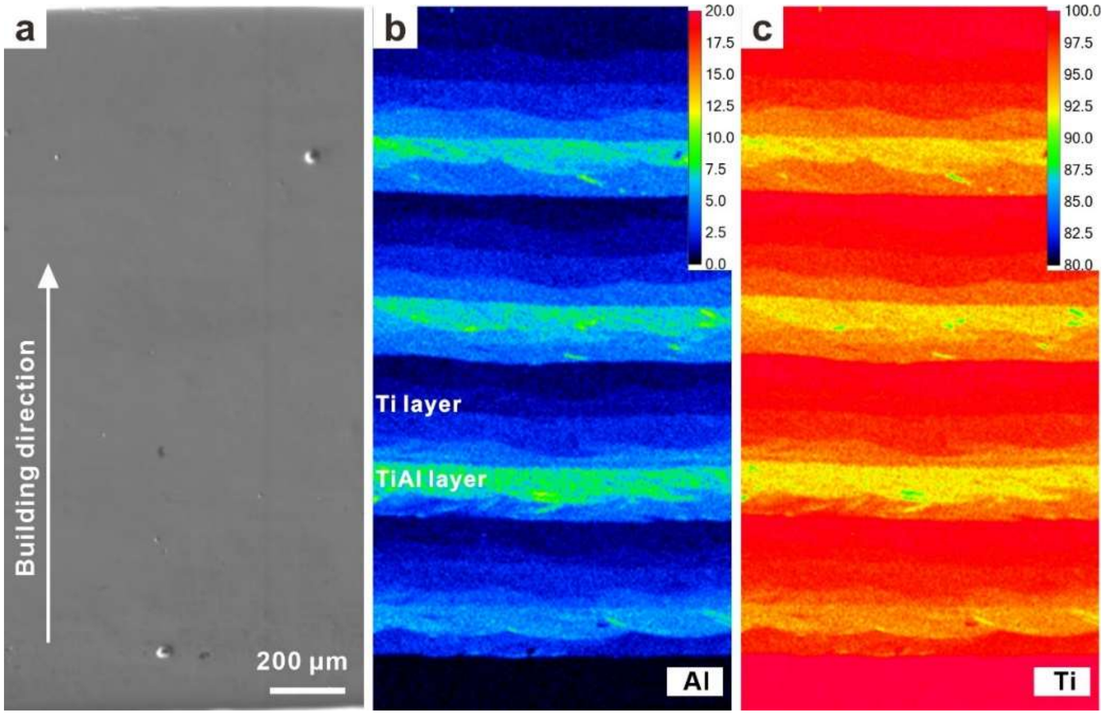

Fig. 4.8 EPMA visualization of the cross-sectional area of the heterogeneous TiAl specimen. (a) Image captured in secondary electron mode, showcasing the intricate structural details at the examined cross-section. (b and c) Elemental distribution maps derived from the same area, highlighting the spatial distribution and localization of Al and Ti, respectively.

4.2.3.3 Microstructural evolution of the heterogeneous TiAl alloy during the deformation process

To further elucidate the impact of gradient Al additions on Ti during deformation, a thorough crystallographic and microstructural examination was conducted on a heterogeneous TiAl sample through in-situ EBSD analysis.

The inverse pole figure (IPF) colour maps (Fig. 4.9a1) illustrate the distinct microstructures of the Ti and TiAl layers in the as-built sample, characterized by smoothly curved and continuous interfaces. Notably, the transition between these layers is gradual, featuring a change from finer basketweave grains in the TiAl layer to lamellar-like and plate-like grains in the adjacent Ti layer. Simultaneously, the geometrically necessary dislocation (GND) map (Fig. 4.9a2) reveals a uniform dislocation distribution across both layers, with no significant variance in dislocation density, corroborating the microstructural continuity across the heterogeneous interface. Statistical analyses confirm this observation, with Ti layers exhibiting coarser grains (average size ~ 39.29 μm), compared to the finer grains in TiAl layers (average size ~ 11.13 μm) as shown in Fig. 4.9a3. The GND densities, illustrated in Fig. 4.9a4, are closely matched between the layers, supporting the uniformity observed in the dislocation distribution.

Upon applying an 8% strain (Fig. 4.9b1), both the Ti and TiAl layers underwent notable grain rotation and refinement during deformation, evidenced by the reduced grain sizes to 37.29 μm in the Ti layer and 9.87 μm in the TiAl layer (Fig. 4.9b3). The accompanying GND map (Fig. 4.9b2) indicates a significant increase in dislocation densities, particularly in the TiAl layer, which exhibited greater contrast relative to the Ti layer, corroborating our in-situ DIC findings (Fig. 4.5) that indicated initial strain localization within the TiAl layer. The increasing GND densities is statistically substantiated in Fig. 4.9b4, where the value in the TiAl layer is notably higher than in the Ti layer.

Further increasing the macro strain until fracture allowed for an extended analysis of the same area (Fig. 4.9c1), where continued grain rotation and refinement was observed (further reduced to 33.58 μm for Ti and 7.42 μm for TiAl as shown in Fig. 4.9c3). The GND maps (Fig. 4.9c2) documented a subsequent rise in dislocation densities, achieving values of 4.44×10^{14} /m^2 for the TiAl layer and 3.48×10^{14} /m^2 for the Ti layer, as detailed in Fig. 4.9c4. Notably, high-density GND traces connecting two separate TiAl layers are evident within the Ti layer, as highlighted by red dash lines and indicated by white arrows in Fig. 4.9c2.

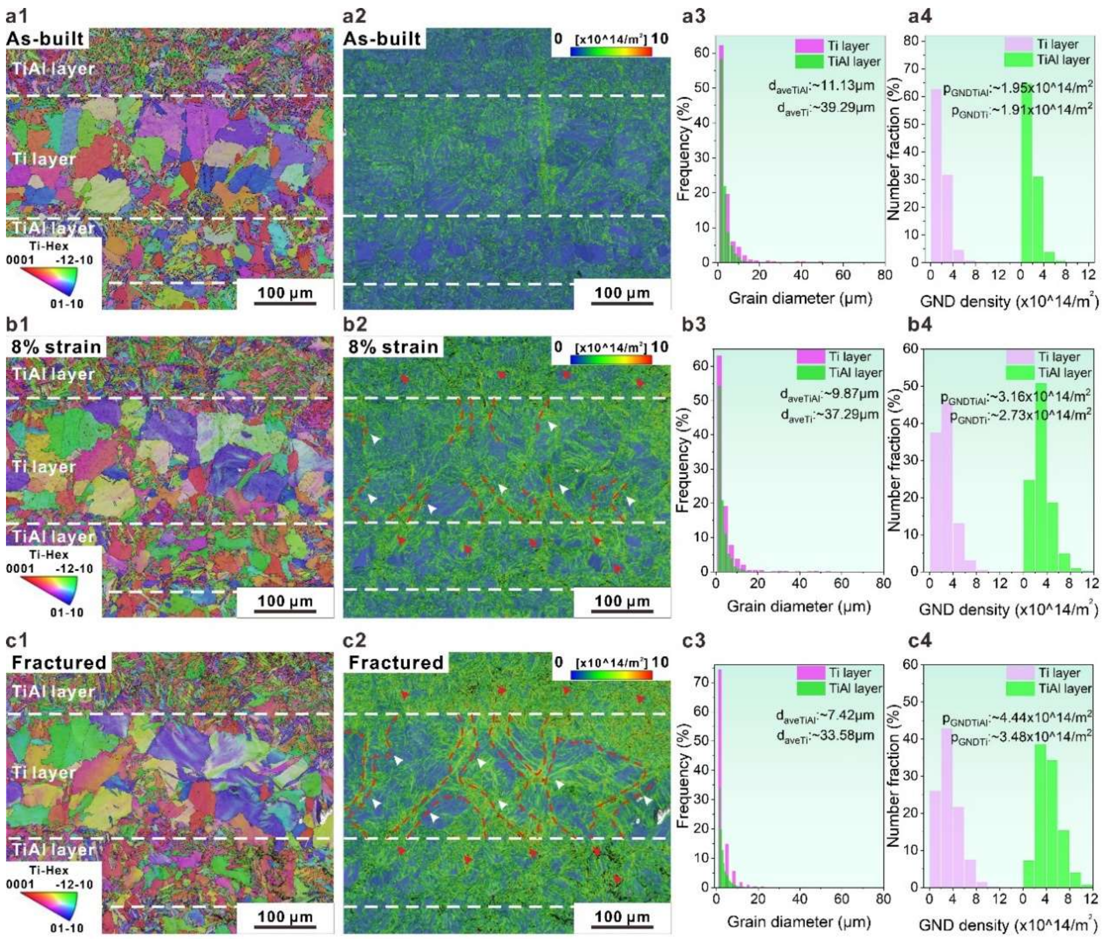

Fig. 4.9 In-situ EBSD results of the LENS^{TM} fabricated heterogeneous TiAl sample. (a1) Overview of the cross-section aligned with the build direction, showcasing the general structural layout of the Ti and TiAl layers. (a2) A GND map displaying a uniform distribution of dislocation densities across both the Ti and TiAl layers. (a3) Statistical analysis of the grain size distribution within the Ti and TiAl layers. (a4) Histograms that detail the distribution of GND densities with the Ti and TiAl layers. (b1 and c1) Crystallographic analysis demonstrating microstructural evolution after applying 8% strain and upon reaching fracture, respectively. (b2 and c2) Corresponding GND maps that trace the progression of GND densities at the different strain levels, 8%

and at fracture, while the red dash lines delineated the high-density GND traces. (b3 and c3) Statistical analysis of grain size distribution subsequent to 8% strain and at fracture. (b4 and c4) Histograms delineating GND densities at two different strain levels, 8% and at fracture.

A sequence of in-situ EBSD images at higher magnification was captured from another region to illustrate the detailed microstructural evolution within the Ti layer (Figs. 4.10a1 to 4.10c1). Initially, the Ti layers are characterized by large plate-like and lamellar grains, displaying a uniform distribution of GND across the layers. Upon application of an 8% strain, the grains began to rotate, and large plate-like grains started to fragment into smaller grains, leading to a heterogeneity in GND distribution. This increased GND density was particularly marked around the newly formed smaller grains, as indicated by white arrows in Figs. 4.10a2 and b2.

As the strain further increased to the point of fracture, these large plate-like grains underwent further deformation, accompanied by an escalation in dislocation densities. The dislocations become entangled, evolving into high-angle/low-angle grain boundaries, which result in much finer grain size, as highlighted by white arrows in Fig. 4.10c2. These newly formed grain boundaries exhibited high GND densities, suggesting that strain and cracks were more likely to propagate along these paths, culminating in material failure once defect channels formed between two distinct TiAl layers.

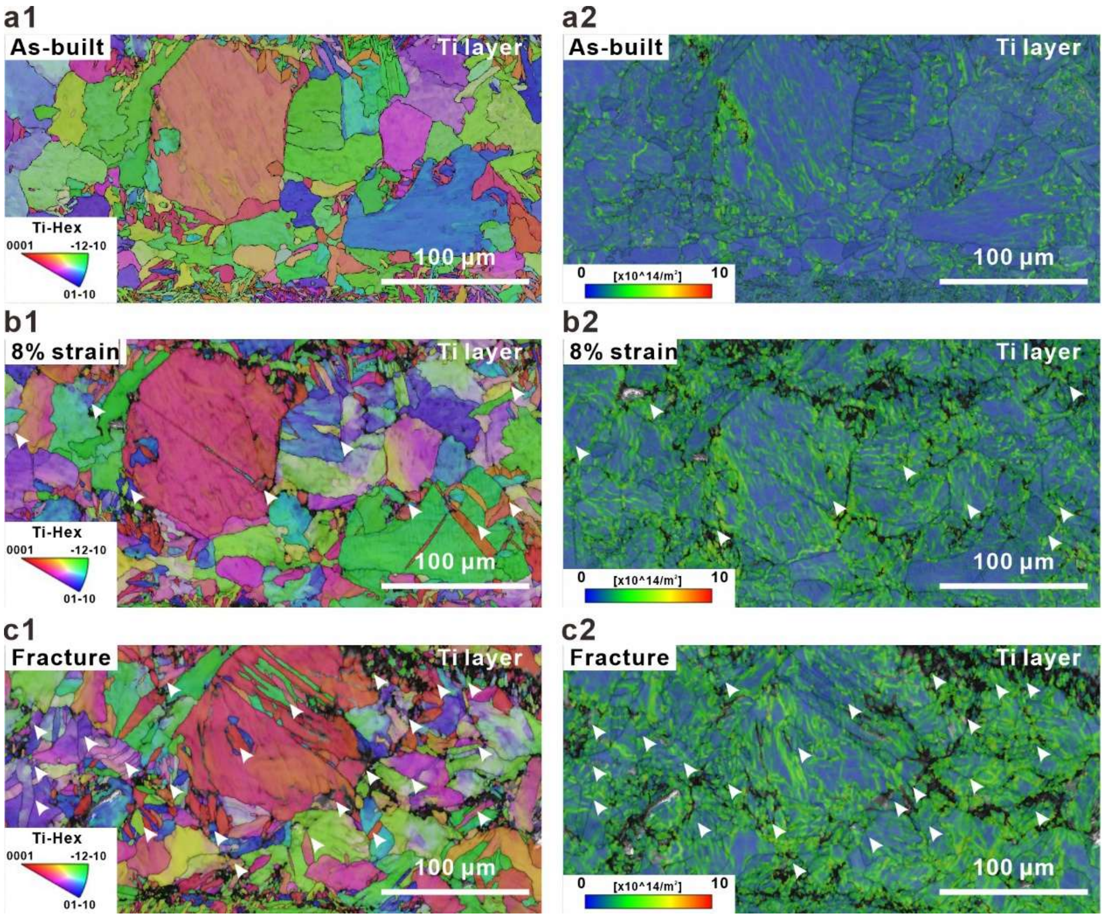

Fig. 4.10 In-situ EBSD results of the Ti layer in the heterogeneous TiAl sample. (a1-a3) Crystallographic analysis revealing the microstructural evolution within the Ti layer at various strain levels, with notable grain refinement observed as strain increases: initial as-built state (a1), at 8% strain (b1), and upon reaching fracture (c1). (b1-b3) GND maps for each strain state, highlighting the progressive increase in dislocation densities and their propagation through the increasingly finer grains: as-built sample (a2), at 8% strain (b2), and at fracture (c2).

This progression from Figs. 4.9 and 4.10 illustrates that as strain increases, there is an emergence of heterogeneity in GND densities across the Ti and TiAl layers. The finer basketweave grains in the hard TiAl layers act as barriers, accumulating GNDs and localizing strain. Conversely, the softer Ti layers with larger grains facilitate dislocation slip, indicating an absence of significant GND accumulation and strain localization. However, the mechanical incompatibility between the hard TiAl and softer Ti layers induces extra work hardening [228], enhancing dislocation densities in both layers. For the soft Ti layer with large grains, the increasing number of dislocations entangle with each other, and eventually transform into high-angle/low-angle grain boundaries, leading to noticeable grain refinement [229, 230], which facilitates the transfer of initially localized strain in the TiAl layers to these refined regions. This is corroborated by in-situ DIC results (Fig. 4.5) that observed strain localization progressively transferring to the nearby Ti regions under elevated strain. When large plate-like grains in the Ti layer evolve into smaller high-angle/low-angle grain boundaries and connect two separate TiAl layers, strain and defects propagate along this newly formed "defect channel" throughout the specimen, culminating in material failure. Additionally, significant dislocation entanglement within the large grains of the Ti layer was observed, indicating that both intergranular and intragranular fractures occur concurrently [231].

4.2.3.4 Microstructure characteristics of the heterogeneous TiAl alloy

Given the substantial impact of Al addition on grain size and morphologies, as previously discussed, in-depth TEM analysis was carried out on the different layers found within both Al-deficient and Al-rich regions, as depicted in Fig. 4.11. Predominantly lamellae and plate-like grains were revealed in the Al-deficient regions, consistent with our earlier findings, shown in Figs. 4.11a and 4.11b. The high-resolution TEM (HRTEM) image in Fig. 4.11c exhibited a d-spacing of 0.224 nm for the $(10\overline{1}\overline{1})$ plane, aligning well with the one in pure Ti ($P6_3/mmc$) and further affirming the negligible effects of Al within these regions. Fig. 4.11d presented a STEM image, showcasing the interface between the Al-deficient and Al-rich regions. The boundary separating the two regions was a prior β boundary, defined by white dotted lines, which distinguished two different α colonies that had transformed from two different β grains during cooling [232]. It can be inferred from the image that the microstructure within the upper prior β grain was primarily characterized by lamellae (exhibiting a larger aspect ratio and grain size) and a small quantity of basketweave grains. Comparatively, the lower β grain was primarily populated by basketweave grains with finer grain size, as more clearly observed in the bright-field TEM (BF-TEM) image (Fig. 4.11e). This evidence further indicates that the concentration of Al significantly impacted the morphology of the child α grains post-solidification. Detailed analysis conducted using HRTEM imaging (Fig. 4.11f) revealed that the d-spacing of all crystalline planes in the Al-rich regions is slightly smaller than the corresponding planes in pure Ti. This attests to the effect of Al solid solution within the region, which distorted the Ti lattice, resulting in lattice shrinkage.

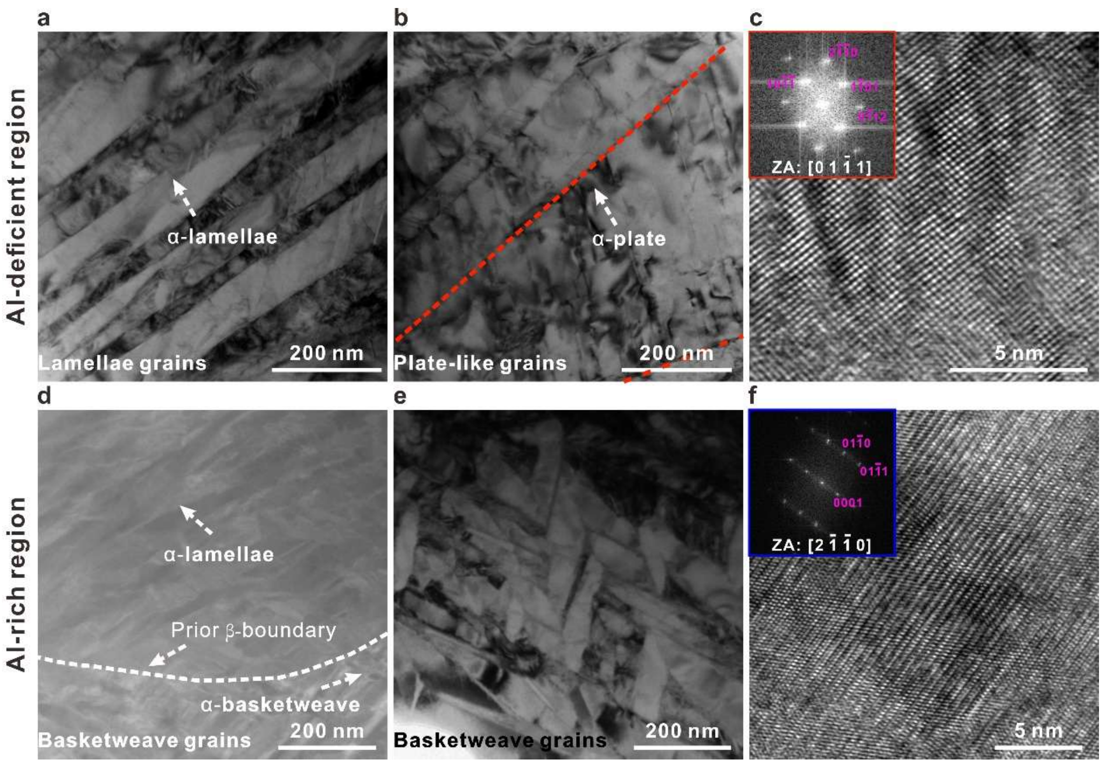

Fig. 4.11 TEM characterizations of Al-deficient and Al-rich regions in the LENS fabricated heterogeneous TiAl alloy. (a) and (b) TEM micrographs delineate the lamellae and plate-like grain structures within Al-deficient regions. The red dashed lines mark the grain boundaries associated with plate-like grains. (c) HRTEM image of

the Al-deficient region, with the Fast-Fourier Transformation (FFT) image inset. (d) A representative STEM micrograph showing the interface between Al-rich and Al-deficient regions. The white dashed line highlights the prior β-boundary, which distinguishes lamellae and basketweave grain structures. (e) TEM image reveals characteristic basketweave grains predominant in Al-rich areas. (f) HRTEM depiction of the Al-rich domain, complemented with the FFT inset.

The microstructural evolution of different layers after fracture was further characterized by TEM, as shown in Fig. 4.12. After fracture, high densities of dislocations were observed decorating the interior of the plate-like grains (indicated by yellow arrows), which were initially identified in the Al-deficient regions (Fig. 4.12a). Accompanied by this, numerous nanoscale dislocation cells were evident within the grain interiors (encircled by purple dash lines and indicated by purple arrows in Fig. 4.12a). These cellular structures emerged as a result of intricate entanglement within a complex network of high-density dislocations, serving to facilitate unrestricted movement of dislocations within the extensive domain of the plate-like grains during deformation [233, 234]. The HRTEM image presented in Fig. 4.12b provides further evidence of extensive deformation occurring in the Al-deficient region during the deformation process, which is supported by the insert IFFT image revealing a significant presence of dislocations.

The microstructural evolution in the Al-rich region is depicted in Figs. 4.12c and 4.12d. Here, basketweave grains (indicated by blue arrows in Fig. 4.12c) are characterized by their finer grain size and high dislocation density, consistent with our observations in the Al-deficient regions. However, a notable difference was that in the Al-rich region, the majority of the dislocations were found to be segregated at the grain boundaries of the basketweave grains rather than forming dislocation cells as seen in the Al-deficient regions (presented by green arrows in Fig. 4.12c). This segregation is likely attributable to the finer grain sizes in the Al-rich region. Comparatively, the Al-deficient region with larger grain sizes could offer more plasticity due to the freedom for dislocation slip. Conversely, the Al-rich regions, with finer grain size and potential solid solution effects, were likely to contribute more towards strength. The grain boundaries act as barriers to dislocation movement, hence enhancing the strength of the heterogeneous TiAl alloy. Furthermore, the HRTEM image presented in Fig. 4.12d provides additional evidence of high densities of dislocations present within the Al-rich regions. Echoing our in-situ EBSD observations, the finer grains observed in these images result from grain refinement and rotation driven by dislocation interplay during the deformation process.

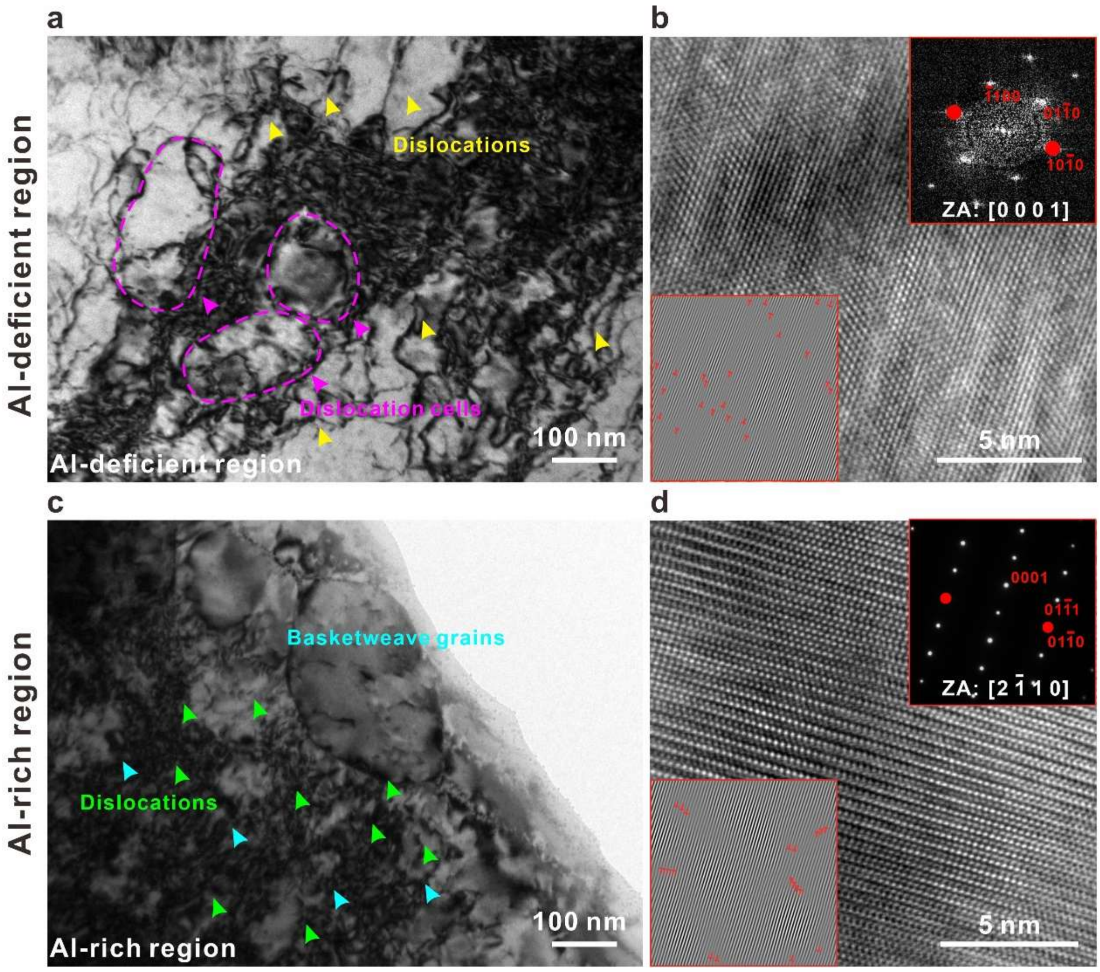

Fig. 4.12 TEM characterization of the fractured heterogeneous TiAl sample at Al-deficient and Al-rich regions. (a) Bright-field TEM (BF-TEM) image showing the

microstructural evolution within the plate-like grains at the Al-deficient region after fracture. Features of high dislocation densities are highlighted by yellow arrows, and dislocation cells are delineated with purple dashed circles. (b) HRTEM image from the fractured Al-deficient region. The inset shows an IFFT image processed to mask $(10\bar{1}0)$ and $(\bar{1}010)$ reflections, which illuminates the presence of dislocations. (c) BF-TEM image displaying the post-fracture microstructure at the Al-rich region. Fine basketweave grains are indicated by blue arrows, and areas of high dislocation densities are marked by green arrows. (d) HRTEM image of the fractured area at the Al-rich region. The inset presents an IFFT image processed to mask $(01\bar{1}0)$ and $(0\bar{1}10)$ reflections, revealing dislocations.

4.3 Discussion

4.3.1 Formation of heterogeneous multi-gradient structure

It is widely acknowledged that in AM, both the internal and external regions of a molten pool experience distinct thermal conditions, leading to a significant thermal gradient [235, 236]. This observation is affirmed by our in-situ molten pool temperature measurements, as shown in Fig. 4.13a. The temperature at the centre of the melt pool can reach as high as 1900 °C. As it radiates outward from the centre, the temperature at the melt pool boundary drops to a minimum of approximately 1400 °C. Given this substantial thermal gradient, a noticeable differential in the Al diffusion distance in Ti appears, contributing to the formation of a distinctive heterogeneous multi-gradient structure. It has been documented that the diffusion distance (L) of alloying elements is determined by the diffusion time period (t) and the diffusion coefficient (D), which can be simply calculated through the equation 4.1:

$$L = \sqrt{Dt} \quad [217, 237] \tag{4.1}$$

Considering that the Al in both the interior and exterior of the molten pool experiences the same diffusion time period, the diffusion distance largely should depend on the diffusion coefficient (D), which can be determined using the Arrhenius law, given by the equation 4.2:

$$D = D_0 \exp(-Q / k_B T) \tag{4.2}$$

where k_B is the Boltzmann's constant, D_0 and Q represents the pre-exponential factor and the activation energy, respectively, both regarded as constants [238]. Obviously, the diffusion coefficient is fundamentally influenced by the temperature, leading to a reduction in the distance of Al diffusion as the temperature decreases. As a result, owing to the higher temperature at the centre of the molten pool, Al elements initially positioned in this region will exhibit enhanced diffusion distance towards the periphery of the molten pool and subsequently migrate alongside other Al elements within the adjacent zone characterized by a deficiency of Al.

Moreover, the pronounced thermal gradient ushered in during the AM creates a potent surface tension that draws the liquid metal from its centre towards its periphery [239], which will generate a Marangoni force, and the magnitude of which is proportional to both the surface tension and the temperature gradient, as schematically shown in Fig. 4.13b [240, 241].

This Marangoni effect engenders a dynamic fluid motion, inciting circular flows in the melt pools and thus affecting the elemental redistribution within the molten pool, impacting both melting dynamics and mass transfer [242-244]. A visualization of this process, as depicted in Fig. 4.13c, reveals the intricate interplay between Al diffusion and its interactions with Marangoni-induced flows. During the deposition of TiAl layer, Al diffused from the molten pool boundary into the previously deposited Ti layer.

However, the Marangoni-induced convection retained a significant portion of Al within the Ti-Al layer. Subsequent deposition of a Ti layer reactivates the diffusion of residual Al through circular flows, thereby diluting Al concentration as additional Ti layers are consecutively added. Eventually, the combined effects of the Marangoni force and Al diffusion explain the phenomenon: Along the build direction, the Al concentration decreases gradually. Instead of an abrupt change from pure TiAl to pure Ti at the interface, the transition is smooth. This gradual change leads to the formation of a novel heterogeneous multi-gradient structure.

Additionally, the microstructure of different layers is also significantly influenced by the diffusion of Al, especially for the layers with the highest and lowest Al concentrations. Previous studies have reported analogous observations, where an increase in added Al element concentration markedly alters the microstructure of Ti alloys [245].

It is generally understood that during the solidification process, α-phase titanium transforms from β-phase Ti following the Burgers orientation relationship (BOR) [205, 232]. This mechanism fosters the creation of a semi-coherent interface with low energy, though it necessitates the co-existence of incoherent interfaces with higher energy [246]. A vital factor influencing this process is the morphology of α-precipitates, which tend to adopt a plate-like shape, resembling oblate spheroids to minimize both incoherent interfacial energy and strain energy, facilitated through reduced strain energy. This preference emerges from an intrinsic drive to decrease both forms of energy mentioned above.

In scenarios where the content of alloying elements introduced is low, the lattice distortion within the α- and parent β-phase remains limited, promoting low interfacial energy for α/β interface guided by the BOR, which is consequent to the marginal misfit existing between the two phases [247]. Such a microstructural ambience is favourable for the formation of thick colonies of α-laths, which in turn contributes to a decreased strain energy, as illustrated in Figs. 4.7a1, 4.7a2 and 4.13d.

The introduction of alloying elements, such as Al, which serves to stabilize the α-phase, results in a reduction in the lattice constant of the α-phase, as illustrated in Fig. 4.11f. This reduction leads to an escalation in the semicoherency strain energy at the α/β interfaces, consequently impeding the growth of α-laths [245, 248]. To mitigate the anisotropy of strain and interfacial energy, α-laths embrace a basketweave microstructure characterized by random orientations, diverging from the typical Widmanstätten colonies, as seen in Figs. 4.7b1, 4.7b2, and 4.13d. This morphological transition exemplifies a strategy to reduce both strain and interfacial energy, resulting in microstructural changes at the different Al composition levels.

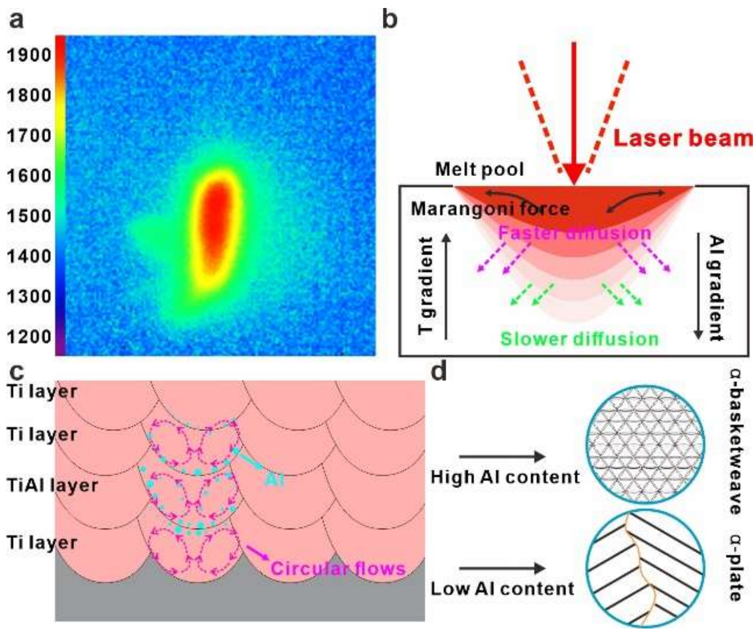

Fig. 4.13 Schematic illustration elucidating the evolution of the heterogeneous multi-gradient structure. (a) Temperature profile of the molten pool obtained from the LENS^{TM} software during the AM process. (b) The established Al gradient and Marangoni force, triggered by the temperature differential within the molten pool during AM. (c) Schematic detailing the diffusion of Al from the TiAl layer to the adjacent Ti layers throughout the AM. (d) Microstructural transformations corresponding to varied Al concentrations.

4.3.2 Gradient strain partitioning during hetero deformation

In the multi-gradient heterogeneous TiAl alloys, chemical homogeneity with an Al gradient is introduced. This is coupled with a structural gradient that involves a fine-grained microstructure in Al-rich regions and a coarse-grained microstructure in Al-deficient regions.

The influence of Al content on the grain size of Ti alloys is well-established, as an increased Al content consistently results in grain refinement [248]. According to the Hall-Petch equation (Equation 4.3), finer grains in Al-rich regions contribute to improved yield strength (σ_S) compared to the coarser-grained Al-deficient counterparts [249].

$$\sigma_S = \sigma_0 + kd^{-1/2} \tag{4.3}$$

where k is a constant, σ_0 represents the initial yield stress, and d denotes the average grain size.

Furthermore, the incorporation of Al not only reduces grain size, but also strengthens the material via solid solution strengthening. The presence of Al atoms induces lattice distortions, which consequently impedes dislocation movement. It's worth noting that this lattice distortion is accentuated with an increased concentration of Al atoms [224, 250]. Therefore, the migration of Al from regions abundant in Al to those deficient in it results in a distinct multi-gradient microstructure, which is characterized by successive variances in grain size and solute-induced strengthening, both of which considerably engender substantial implications on the mechanical properties of the alloys [250, 251].

During tensile testing, non-uniform deformation behaviour is discernible at the microscopic scale across the heterogeneous alloy layers, as evidenced earlier in Figs. 4.5, 4.9, and 4.10. This, in turn, affects mechanical properties.

Figure 4.14 provides a schematic illustration delineating the deformation behaviour within the heterogeneous multi-gradient TiAl alloy. It is evident that the combined effects of Al diffusion and Marangoni force lead to a gradient decrease in Al content from TiAl layers to the adjacent Ti layers, as supported by previous EPMA results in Fig. 4.8. In the initial stage of deformation (Stage I in Fig. 4.5, depicted in Fig. 4.14a1), both the Al-rich and Al-deficient regions, despite their gradient microstructural variations in grain size and Al concentrations (as emphasized in Fig. 4.14a2), concurrently display compatible deformation, reciprocating similar strain levels. At this stage, the heterogeneous multi-gradient TiAl alloy undergoes uniform deformation.

With increasing applied strain (Stage II in Fig. 4.5, depicted in Fig. 4.14b1), the microstructural and mechanical discrepancies between the Al-rich and Al-deficient regions result in deformation disparities, leading to strain partitioning during deformation. Recent studies have demonstrated that the incorporation of hard and soft zones induces strain partitioning, contributing to enhanced mechanical properties [252-255]. In this scenario, the softer Al-deficient regions sustain higher elastic strain, while the hard Al-rich regions initiate plastic deformation [256, 257]. The consequent result is a faster lateral contraction of the Al-rich regions relative to the Al-deficient regions, inducing tensile stresses in the former and compressive stresses in the latter [255], as schematically represented in Fig. 4.14b2. Consequently, the mechanical incompatibility present in the multi-gradient structure transforms uniaxial tensile stresses into complex bidirectional stresses along the Al-decreasing gradient, inducing both gradient strain partitioning and stress partitioning. From the perspective of the microstructural realm, the Al-rich regions are observed to be rich in fine basketweave structures and larger lattice distortions (Figs. 4.11d to 4.11f). These characteristics make them potent barriers to dislocation slip, causing accumulation of dislocations and strains in these regions. Conversely, the Al-deficient regions are characterized by larger grains, which allows dislocations to move with relative freedom, promoting uniform deformation and strain dispersion. Therefore, strain localization (indicated by red circles in Fig. 4.14b1) is observed to be present in the Al-rich regions.

As the applied strain continued to increase (Stage III and IV in Fig. 4.5, depicted in Fig. 4.14c1), the hetero-deformation that happened between soft Al-deficient and hard Al-rich regions, inducing back and forward stresses in soft and hard zones, respectively [228]. This interaction between the hard Al-rich and the softer Al-deficient regions creates long-range internal stresses in the soft regions, which oppose the direction of the resolved shear stress. Overcoming these back stresses in the soft regions requires additional yielding, which inherently strengthens these areas. This is further evidenced by the formation of an increased number of dislocation cells within the Al-deficient regions, as shown in Fig. 4.14c1 [258]. Furthermore, as the number of dislocations in the Al-deficient regions increases with the escalating strain, these dislocations evolve into high-angle/low-angle grain boundaries, promoting significant grain refinement, especially in the vicinity of the Al-rich regions (as evident by Figs. 4.10a2 to c2). These newly refined grains in the Al-deficient regions act as ideal places for strain that previously concentrated in the Al-rich regions to spread. This redistribution of strain alleviates the localization of strain and enhances the overall ductility of the alloy. This shift in strain concentration from the Al-rich to the adjacent lower Al-content regions is well supported by the in-situ EBSD KAM results shown in Figs. 4.9a2 to c2, confirming a dynamic transition in microstructural behaviour under stress.

Additionally, it is widely acknowledged that the hard Al-rich regions possess an intrinsically low strain hardening rate, leading to magnified localized deformation, with necking imminent post-yielding [259, 260]. However, the Al-deficient regions, owing to their heightened strain hardening capabilities, support the inherently fragile Al-rich regions. Even though the brittle Al-rich regions may manifest necking and incipient internal fractures along grain boundaries upon continuously increasing strain, the propagation of these defects is impeded by neighbouring Al-deficient regions, endowing the material with commendable ductility (as depicted in Fig. 4.14c2).

Upon reaching critical stress thresholds (Stage V in Fig. 4.5, depicted in Fig. 4.14d1), terminal sample rupture occurs when the softer Al-deficient regions also undergo necking. This initiation of cracks merges with existing cracks in the Al-rich regions, ultimately forming a fracture path [215, 261]. Microstructural analysis reveals significant and continuous grain refinement within the Al-deficient regions, as shown in Figs. 4.10a1 to c1, accompanied by high GND densities. These factors facilitate the transfer of strain and the propagation of cracks. Here, a critical stage is reached as the defect channel between two distinct TiAl layers is established, leading to subsequent catastrophic failure.

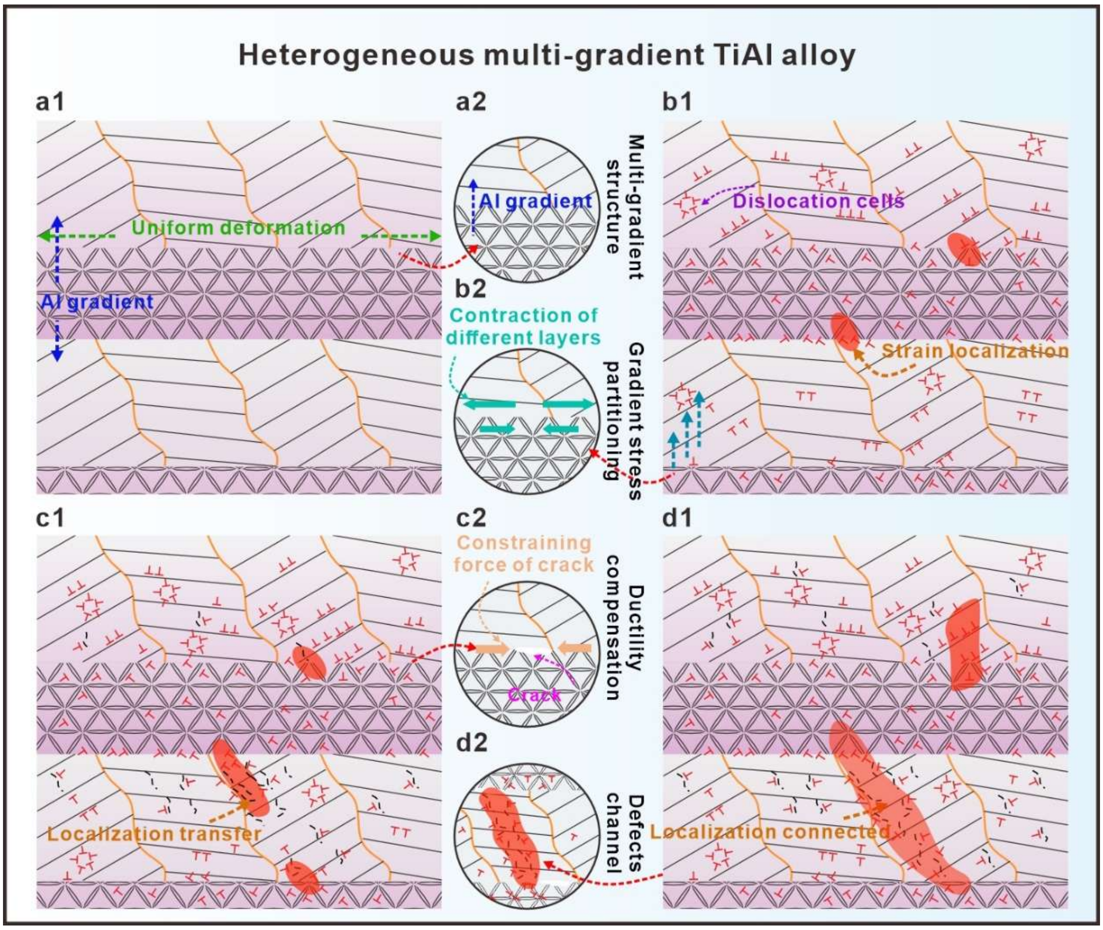

Fig. 4.14 Schematic representations illustrating the progressive deformation stages of the heterogeneous multi-gradient TiAl alloy. (a1) The initial stage of deformation, showcasing the emerging form of the alloy as it undergoes the earliest strain. Green vectors represent the deformation direction, and the vertical blue vectors represent the Al gradience. (a2) Illustration highlighting the multi-gradient structure induced by the gradational variation in Al concentration. The blue arrow underscores the transition in microstructure, evolving from finer basketweave grains towards coarser plate-like grains corresponding with diminishing Al concentrations. (b1) A depiction of the alloy during a heightened phase of increasing strain at stage II. Dislocations and dislocation cells are marked by red "T" symbols. The blue vectors denote the transformation direction of the gradient stress partitioning effect. (b2) A schematic that visually reveals the gradient stress partitioning, which arises from the interaction between tensile stresses generated in Al-deficient regions and compressive stresses in Al-rich regions

during deformation. (c1) A schematic of microstructures at stages III and IV during deformation, where an increase in dislocation cells can be observed in the Al-deficient regions at elevated strain, evolved into high-angle/low-angle grain boundaries (represented by dark dot lines), exhibiting significant grain refinement in Al-deficient regions, decorated by high GND densities. (c2) A schematic portraying the mechanism of ductility compensation at this stage. The crack, which was marked by white colour, was constrained by neighbouring layers. (d1) The pre-fracture stage, presenting the alloy just before the onset of fracturing. Stress-concentrated areas between two Ti-Al layers were connected. The red patterns represent strain localization connections across the whole Al-deficient regions. (d2) Schematic illustration of the defects channel formations at this advanced stage, elucidating the pathways and structures established through grain refinements and GND accumulation just prior to fracture.

The additional work hardening derived from the interaction between Al-rich and Al-deficient regions in heterogeneous multi-gradient TiAl samples is also substantiated by the corresponding strain hardening rate curve depicted in Fig. 4.15. For homogeneous Ti and TiAl samples, the strain hardening rate monotonically decreases with the increase of strain, indicating uniform deformation upon tensile loading [262].

However, the deformation behaviour of the heterogeneous multi-gradient TiAl sample is notably different. The heterogeneous multi-gradient TiAl alloy manifests a reduced strain hardening rate at the initial deformation stage, indicating a prevailing free deformation mechanism. Such a behaviour can be attributed to the unrestrained dislocation movement within both Al-rich and Al-deficient regions during the early stages. As deformation proceeds, a noticeable increase in strain hardening is evident. This phenomenon, rooted in the hetero-deformation process elaborated previously, arises from the chemical and microstructural differences in the Al-rich and Al-deficient regions. The chemical and structural heterogeneity lead to different deformation behaviours, as described earlier, the more robust Al-rich regions exhibit pronounced contraction but are constrained by adjacent Al-deficient regions. This interplay induces forces perpendicular to the direction of contraction, thereby enhancing the rate of strain hardening. Furthermore, Al diffusion in the build direction induces progressive alterations in microstructure and mechanical properties. Consequently, each Al-rich zone experiences restraint from its subsequent Al-deficient neighbours, resulting in the generation of multiple interaction stresses along the build direction, referred to as gradient stress partitioning. The presence of such partitioning not only enhances the strength of the samples, but also mitigates premature fractures resulting from significant disparities in mechanical properties and microstructure [263, 264]. As strain continues to intensify, a reappearance in the diminishing trend of strain hardening is observed. This aligns with the hypothesis that once the peak of persistent Al-rich and Al-deficient region interactions is attained, the strain previously confined to the most formidable Al-rich regions begins diffusing to adjacent Al-deficient regions, leading to the modest attenuation in strain hardening rate. Concurrently, the heterogeneous TiAl preserves a uniform elongation that is commensurate with that of homogeneous Ti, affirming the good ductility of the heterogeneous multi-gradient TiAl alloy. This combination of comparable elongation and enhanced strain hardening leads to an enhanced synergy between strength and plasticity.

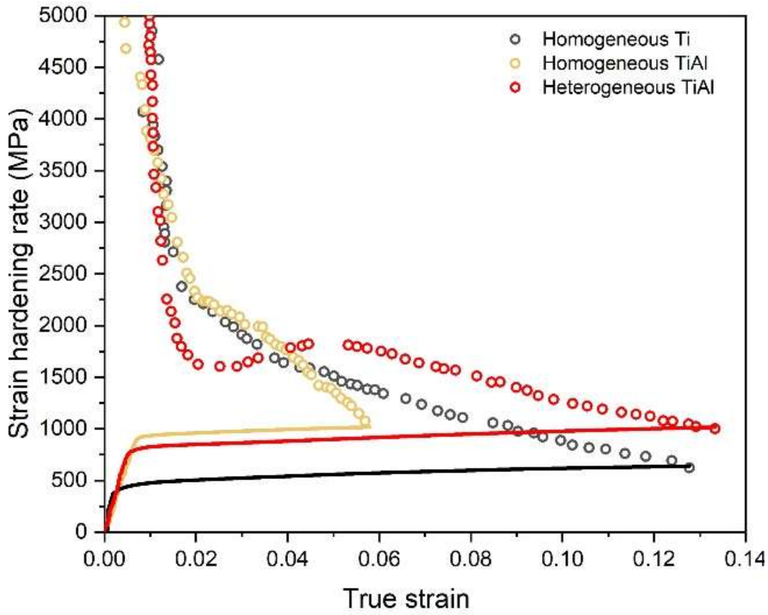

Fig. 4.15 Corresponding true stress-strain curves and the strain-hardening rate curves of homogeneous Ti and homogeneous TiAl and heterogeneous TiAl alloys.

In addition to the strain hardening rate curve, the outstanding ductility of the heterogeneous TiAl sample is further validated by the fracture morphologies depicted in Fig. 4.16. The fracture surface of the homogeneous Ti sample exhibited predominantly microscopic ductile dimples (Figs. 4.16a1 and 4.16a2), signifying commendable ductility [264, 265]. In contrast, the homogeneous TiAl sample presents staircase-like features with a flat fracture surface (marked by yellow dotted lines in Fig. 4.16b1). Upon closer inspection (Fig. 4.16b2), large cleavage facets with a width of 30-40 μm are noticeable. This implies that the addition of Al significantly deteriorates the ductility of Ti, and cracks have a heightened tendency to propagate along these cleavage facets [219, 266].

Interestingly, the heterogeneous TiAl sample exhibits typical ductile dimples and cleavage facets, which are distinctly separated by a white dotted line that delineates the interface (Figs. 4.16c1 and 4.16c2) [267]. Importantly, both the cleavage facets and dimples in the heterogeneous TiAl sample are noticeably smaller compared to their homogeneous Ti and TiAl counterparts. Combining this observation with EDS analysis, it is noteworthy that the colonies of cleavage facets are predominantly located on the Al-rich side, whereas the Al-deficient side is predominantly adorned with smaller shallow dimples (supported by the EDS line scan in Fig. 4.16c2). This observation in the heterogeneous TiAl sample supports the hypothesis that, during deformation, the softer Al-deficient regions serve as barriers, effectively obstructing the propagation of cracks along the cleavage facets. This impediment prevents premature failure of the entire specimen, resulting in commendable overall ductility.

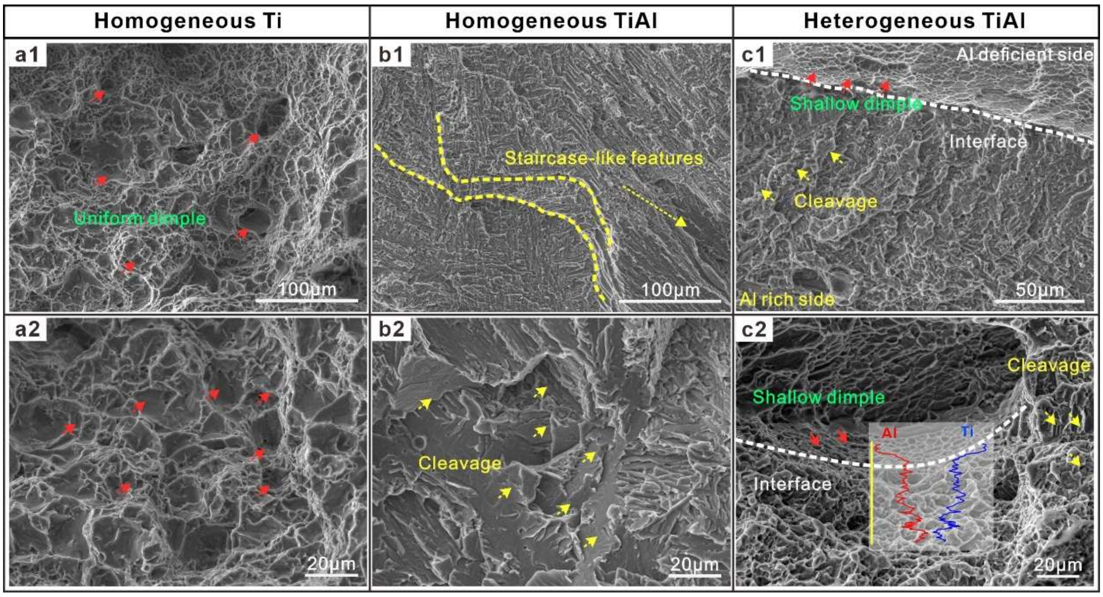

Fig. 4.16 Fractographic examination of the homogeneous Ti, homogeneous TiAl and heterogeneous TiAl specimens. (a1 and a2) Fractured surface of the homogeneous Ti, with red arrows highlighting uniform dimple features. (b1 and b2) Fractographic features of the homogeneous TiAl, where yellow dashed lines delineate the characteristic stair-like features, and yellow arrows highlight prominent cleavage facets. (c1 and c2) Fractured morphology of the heterogeneous TiAl sample. Red arrows denote shallow dimples found in the Al-deficient regions, while yellow arrows emphasize cleavage facets in Al-rich regions. An EDS line scan elucidates the Al gradient, spanning from the shallow dimple regions to the cleavage-dominated regions.

4.4 Conclusions

Alloy optimization through elemental integration frequently enhances the material's strength, albeit often at the expense of reduced ductility, thereby restricting its broader applicability. Heterostructured materials offer a potential solution, as they often exhibit commendable mechanical properties. Such properties are typically achieved through microstructural alternation by mechanical post-processing or through compositional modifications. Building on this concept, we synthesized a novel heterogeneous multi-gradient TiAl alloy. The alloy was produced by applying in-situ chemical composition modulations during the additive manufacturing process. The principal conclusions drawn from this study are as follows:

(1) The as-fabricated heterogeneous multi-gradient Ti/Ti-10Al alloy unveils a remarkable combination of strength and ductility, characterized by a yield strength of approximately 760 MPa and a fracture strain of around 33.4%. When compared to the homogeneous Ti alloy, which exhibits the yield strength and fracture strain of approximately 440 MPa and 37.6%, respectively, the heterogeneous TiAl alloy demonstrates an increase in yield strength of nearly 70%, while maintaining a negligible compromise in ductility. Moreover, in contrast to the homogeneous TiAl alloy (with the yield strength and fracture strain measuring 910 MPa and 6.1%, respectively), there is an almost six-fold enhancement in ductility with minor loss in strength.

(2) The well-organized heterogeneous multi-gradient configuration is facilitated by the Marangoni effect invoked during additive manufacturing, coupled with the diffusion of Al into Ti. This results in a controlled variation in Al concentration, subsequently inducing grain morphologies gradient and solid solution gradient that traverse from TiAl layers to adjacent Ti layers along the building direction.

(3) The inherent microstructural and mechanical properties divergences between Ti/Ti-Al layers in the heterogeneous multi-gradient TiAl alloy facilitate gradient

stress partitioning during the deformation process, which has enhanced strain hardening. Concurrently, the presence of softer Ti layers serves to compensate for ductility, thereby effectively mitigating crack initiation and progression within the Ti-Al layers. The synergistic collaboration of gradient stress partitioning and ductility compensation engenders substantial enhancements in both strength and ductility.

(4) The adoption of this novel strengthening strategy not only expands the potential applications of economically viable α-Ti alloys in a more achievable way but also visualizes promising prospects for an array of alloy systems. This approach is particularly beneficial in scenarios where the strengthening element exhibits pronounced solubility in the matrix, and its incorporation can significantly compromise the inherent ductility of the alloy.

Chapter 5 Transcending the Rule-of-Mixtures via Coefficient of Thermal Expansion Mismatch-Driven Interfacial Strengthening in Additively Manufactured Ti Alloy Heterostructures

5.1 Introduction

In Chapter 4, it was demonstrated that strategically designed heterogeneous multi-gradient TiAl alloys fabricated by AM can effectively overcome the conventional strength-ductility trade-off by utilizing compositional gradients. Despite these significant advancements, further opportunities remain to fully exploit and understand the role of interfacial phenomena, particularly those driven by thermomechanical mismatches and localized deformation mechanisms, within additive-manufactured layered structures. Building on these findings, this chapter aims to deepen our fundamental understanding of how interfacial strain localization and dislocation-mediated strengthening mechanisms contribute to the exceptional mechanical performance observed in AM heterostructures.

The strength-ductility trade-off remains a persistent challenge in structural metallic materials [268, 269]. Conventional strengthening methods, such as grain refinement and solid-solution alloying, typically enhance strength at the expense of ductility, primarily due to a limited strain-hardening capacity and reduced dislocation storage capability [134, 177, 270]. This fundamental compromise has constrained the application of high-strength alloys in demanding structural components. Heterostructured (HS) materials have recently emerged as a promising strategy to overcome this limitation [92]. By integrating domains with contrasting mechanical properties, HS materials promote strain partitioning and hetero-deformation-induced (HDI) hardening, enabling concurrent improvements in strength and ductility [228].

Among various HS designs—including bimodal [99, 271], gradient [272, 273], harmonic [274, 275], and layered structures [98, 102, 103]— the layered configuration is particularly advantageous due to its straightforward fabrication, tunable interfacial spacing, controllable strength contrast, and well-defined load transfer pathways [98, 276-278]. Despite these advantages, many layered HS systems exhibit mechanical properties that only approximate the rule-of-mixtures (ROM), failing to substantially exceed the performance of their individual constituents [102, 103]. Moreover, conventional processing routes like cold rolling and annealing often induce severe plastic deformation, resulting in sharp interfaces that can act as preferential sites for damage initiation and crack propagation. These methods are also frequently limited by poor interfacial bonding and flexibility in chemical or architectural design [279].

Additive manufacturing (AM), particularly laser directed energy deposition (L-DED), offers a transformative approach to overcoming these limitations by enabling the design of sophisticated layered heterostructures [97, 280]. Multi-powder feeder systems permit controlled compositional transitions during fabrication, facilitating spatially programmed heterogeneity that is difficult to achieve through conventional means [97, 215]. The fusion-based nature of AM also ensures strong metallurgical bonding between layers, in contrast to the mechanical interlocking typical of traditional joining methods, thereby enhancing interfacial integrity and load transfer efficiency while reducing the risk of debonding or premature failure [281]. Moreover, the inherent characteristics of AM—including rapid melting, solidification, and steep thermal gradients—produce high cooling rates and recurrent thermal cycling, which are known to generate elevated dislocation densities and residual stresses [124, 132, 282, 283]. In homogeneous alloys, where thermal properties are uniform, these process-induced features typically yield only marginal improvements in mechanical strength [284]. In contrast, studies on composite systems have demonstrated that mismatches in coefficients of thermal expansion (CTE) between constituent phases can generate significant internal stresses and interface-localized dislocation structures during thermal cycling [285-287]. For instance, Taya and Lulay [288] quantitatively attributed yield strength enhancement in metal-matrix composites (MMCs) to punched-out dislocations and long-range back stresses resulting from CTE mismatch during cooling. Similarly, Ho and Saigal [289] reported that increased cooling rates in cast Al-SiC MMCs led to higher yield strength, which they ascribed to thermally induced plastic incompatibility and dislocation accumulation at phase boundaries. These findings underscore thermal expansion mismatch as an effective mechanism for promoting residual stress development and dislocation generation at interfaces, raising the critical question of whether such AM process-induced effects can be amplified in layered heterostructures. Specifically, by deliberately introducing a contrast in thermophysical properties across the interface, it may be possible to enhance mechanical performance beyond the predictions of the ROM.

Building on this foundation, the present study employs an interface-engineering strategy based on thermal expansion mismatch to enhance the mechanical properties of Ti-6Al-4V fabricated via L-DED. This alloy was selected due to its exceptional specific strength, widespread industrial adoption, and increasing performance requirements under severe service conditions [290]. Soft Ti-3.5Al layers were incorporated into the layered structure owing to their well-documented combination of moderate strength and high ductility [9]. This design offers several inherent advantages. First, within the selected compositional range, no brittle intermetallic phases are expected to form between the two alloys, thereby minimizing the risk of interfacial decohesion during fabrication. Second, the two constituents exhibit markedly different thermophysical properties—a disparity that is amplified by the rapid thermal cycles inherent to AM. Specifically, Ti-6Al-4V has a thermal conductivity of approximately 7.06 $W \cdot m^{-1} \cdot K^{-1}$, compared to approximately 10.05 $W \cdot m^{-1} \cdot K^{-1}$ for Ti-3.5Al, with thermal diffusivities of approximately 3.26 $mm^2 \cdot s^{-1}$ and 4.26 $mm^2 \cdot s^{-1}$, respectively. Literature values also indicate a noticeable difference in CTE between Ti-6Al-4V and low-Al α-Ti alloys [14]. This thermomechanical disparity induces localized expansion and contraction during the AM process, establishing residual stress and strain gradients across the Ti-3.5Al/Ti-6Al-4V layers and preconditioning the interfaces for the storage of geometrically necessary dislocations (GNDs) and HDI strengthening upon mechanical loading. Furthermore, the diffusion of vanadium (V) from Ti-6Al-4V into the Al-rich α-Ti phase is both thermodynamically suppressed—due to the reduced solubility of V at higher Al content—and kinetically limited under rapid solidification conditions [291]. As a result, interlayer interdiffusion is minimized, which (i) reduces undesired compositional gradients in thermomechanical properties, (ii) preserves sharp yet well-bonded interfaces without forming brittle intermetallic, and (iii) maintains the designed mechanical and thermophysical contrast necessary for effective interface-mediated strengthening. Together, these conditions achieve an optimal balance between interfacial integrity and functional contrast, both of which are essential for realizing robust HDI hardening and crack-arrest capability in the layered Ti-3.5Al/Ti-6Al-4V architecture.

Through this design, the as-built Ti-3.5Al/Ti-6Al-4V heterostructure demonstrates a superior strength-ductility synergy, exhibiting higher strength than either of its homogeneous counterparts while retaining sufficient tensile ductility. Both strength and ductility exceed those of the Ti-6Al-4V matrix, representing a clear deviation from the ROM that ranks among the most pronounced reported for HS materials. These findings establish a thermomechanically driven interface-engineering paradigm for additively manufactured Ti alloys, providing a versatile pathway to surpass the ROM and informing scalable design strategies for high-performance, lightweight structural components.

5.2 Results

5.2.1 Layer structures

Figure 5.1a presents the XRD patterns of the homogeneous Ti-3.5Al, Ti-6Al-4V, and hetero-sample, obtained from cross-sectional surfaces parallel to the build direction. All samples exhibit diffraction peaks corresponding exclusively to the α-Ti phase ($P6_3/mmc$), indicating the formation of a single-phase microstructure across all compositions. Notably, although Ti-6Al-4V is conventionally classified as an α+β alloy, only α-phase peaks were detected, which is consistent with previous observations in AM-fabricated Ti-6Al-4V where rapid solidification suppresses β phase retention [292, 293]. This uniformity suggests effective mixing and melting during the AM process, despite the compositional differences among the feedstock powders.

SEM analysis, as shown in Figs. 5.1b to d, revealed distinct microstructural features for each sample. The homogeneous Ti-3.5Al specimen exhibits a microstructure comprising lamellar and relatively coarse plate-like α grains, indicative of low alloying element contents and limited β-stabilizer addition [9]. In contrast, the homogeneous Ti-6Al-4V sample exhibits a fine acicular α′ martensitic structure with needle-like morphology, resulting from the rapid solidification rate inherent to the AM process. Columnar prior-β grains aligned along the build direction are also observed, reflecting directional solidification during layer-by-layer deposition.

As a comparison, the hetero-sample presents a well-defined layered architecture, with clear interfaces delineating the alternating Ti-3.5Al and Ti-6Al-4V layers. Within the Ti-3.5Al layers, the microstructure mirrors that of the homogeneous Ti-3.5Al sample, characterized by lamellar and plate-like α grains. Similarly, the Ti-6Al-4V layers retain the acicular α′ martensitic morphology observed in the corresponding homogeneous specimen. EPMA analysis (Fig. 5.1e) confirms the distinct elemental partitioning across the heterostructure, with abrupt changes in Al and V content across the Ti-6Al-4V/Ti-3.5Al interfaces. These compositional profiles validate the successful realization of the intended layered configuration. According to the printing parameters described in Section 2.2.2.3, the as-built Ti-3.5Al and Ti-6Al-4V layers exhibit thicknesses of approximately 200 μm and 300 μm, respectively. Notably, the interfaces remain sharp and well preserved, indicating limited elemental interdiffusion and effective retention of the designed chemical and structural contrast.

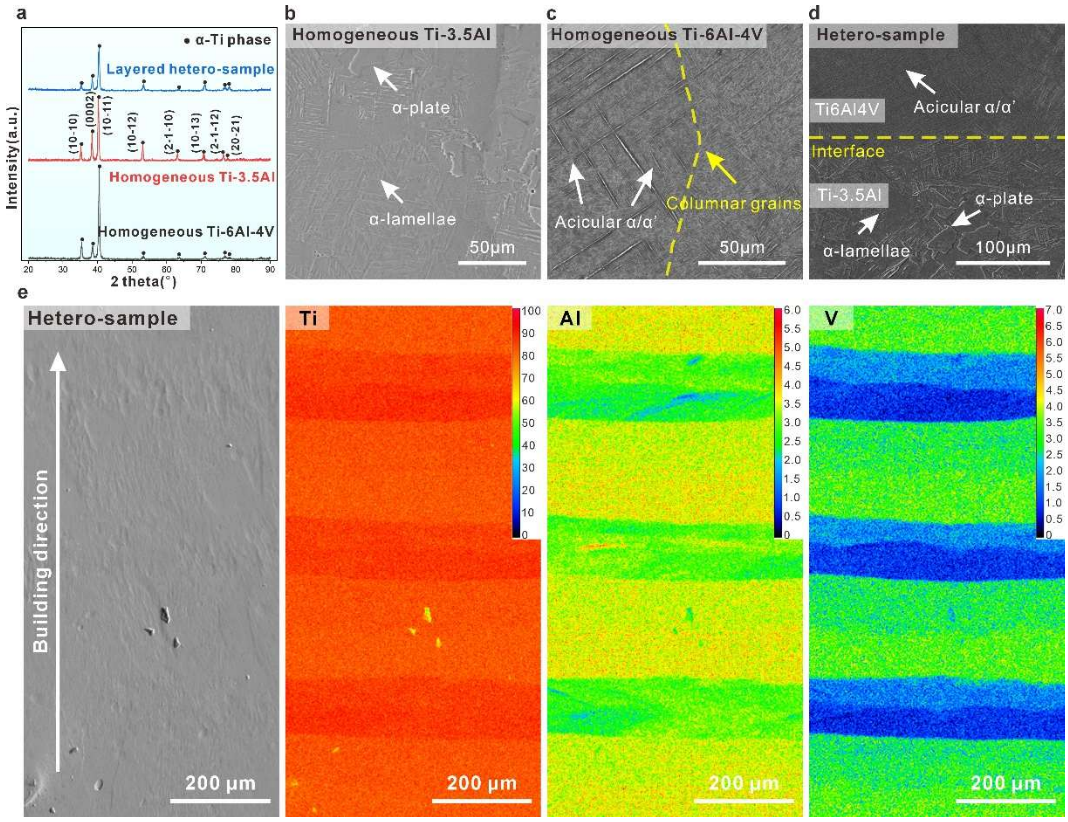

Fig. 5.1 Microstructural characterization of the as-built homogeneous Ti-3.5Al, Ti-6Al-4V, and hetero-sample specimens. (a) XRD patterns of the specimens, identifying the phase constituents. (b-d) SEM images showing the microstructural features of the three samples. (e) EPMA mapping of the hetero-sample, illustrating the spatial distribution of Ti, Al, and V across the sample matrix.

5.2.2 Mechanical performances

Figure 5.2a presents the representative engineering tensile stress-strain curve obtained from tensile tests of the as-built Ti-3.5Al, Ti-6Al-4V, and hetero-sample specimens. Among these, the as-built Ti-3.5 Al alloy exhibited the lowest strength, with a yield strength (σ_y) of approximately 740 MPa and an ultimate tensile strength (σ_{UTS}) of around 830 MPa, coupled with an elongation to failure (ε_f) of ~ 18.0%. Although its substantial elongation indicates considerable ductility, the relatively low strength restricts its suitability for demanding structural applications. In contrast, the as-built Ti-6Al-4V alloy demonstrates significantly enhanced tensile strength, with σ_y and σ_{UTS} values of approximately 1037 MPa and 1058 MPa, respectively. However, this substantial strength gain is accompanied by a notable reduction in ductility, with an elongation to failure of only ~7.2%. This behavior aligns with the widely reported strength–ductility trade-off typical in titanium alloys, wherein improvements in strength usually occur at the expense of ductility.

Notably, the hetero-sample demonstrated superior mechanical performance, achieving a desirable combination of higher strength and improved ductility relative to both constituent alloys. This hetero-sample yielded at σ_y ~ 1090 MPa and attained an σ_{UTS} ~ 1150 MPa, exceeding the strength of as-built Ti-6Al-4V by ~10%. Concurrently, the elongation to failure (with the value of ~10%) indicates a notable improvement in ductility compared to Ti-6Al-4V alone. Thus, it is obvious that the hetero-sample architecture effectively leverages the high strength of Ti-6Al-4V alloys while retaining a substantial portion of the ductility inherent in the softer Ti-3.5Al alloys. Although previous studies on “soft-hard” layered structures have often reported mechanical properties intermediate to their individual constituents, our hetero-sample distinctly achieves enhanced strength and ductility simultaneously, a significant and uncommon outcome in titanium alloys. This remarkable combination of properties will be further examined in subsequent sections. To verify reproducibility, three tensile specimens from each category were evaluated under identical conditions, yielding consistent and repeatable results.

Figure 5.2b shows the true stress–strain responses and corresponding strain hardening rates of all three samples. The Ti-3.5Al alloy exhibits the lowest strain hardening rate, consistent with its comparatively limited strength. In contrast, both the Ti-6Al-4V and hetero-sample show noticeably higher strain hardening capabilities. Notably, the hetero-sample exhibits a slightly elevated strain hardening rate compared to the Ti-6Al-4V sample, reflecting its enhanced capacity for dislocation accumulation and strain accommodation. Such improved strain-hardening behavior underlies the heterostructure's ability to sustain plastic deformation, contributing substantially to its superior mechanical performance.

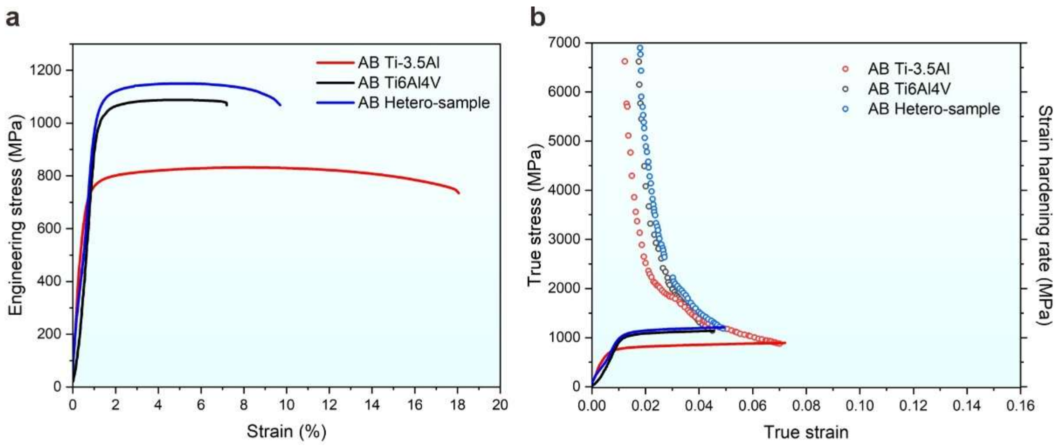

Fig. 5.2 Mechanical performance of the as-built Ti-3.5Al, Ti-6Al-4V, and hetero-sample specimens. (a) Engineering stress-strain curves comparing the mechanical response of the three specimens. (b) Corresponding work-hardening curves, illustrating the strain-hardening behavior during deformation.

Fracture morphology analysis is essential for understanding deformation behavior and provides direct insight into the mechanical properties of alloys. Figure 5.3 compares representative fracture surfaces of the as-built Ti-3.5Al, Ti-6Al-4V, and hetero-sample, revealing distinct deformation characteristics associated with each specimen's mechanical performance.

The fracture surface of the homogeneous Ti-3.5Al specimen exhibits a classical ductile fracture morphology, characterized by a cup-and-cone profile and pronounced macroscopic necking (marked by dashed line in Fig. 5.3a1) [294]. Higher-magnification observations (Fig. 5.3a2) reveal a uniform distribution of deep dimples (highlighted in red dashed line), indicative of micro-void nucleation, growth and coalescence during significant plastic deformation [160, 295]. In contrast, the homogeneous Ti-6Al-4V specimen presents a markedly different fracture response. As shown in Fig. 5.3b1, the macroscopic fracture surface features a staircase-like morphology devoid of necking, coupled with numerous flat cleavage facets (marked by blue dashed lines and arrows), suggesting brittle fracture behavior [296, 297]. Higher-magnification imaging (Fig. 5.3b2) further reveals small, smooth, brittle fracture facets (marked by yellow circles) and elongated, needle-like features (delineated by white dashed lines) characteristic of cleavage fracture along the acicular α′-martensite structure. These observations indicate that crack propagation in the Ti-6Al-4V sample is dominated by trans-granular cleavage through brittle martensitic grains, with minimal plastic deformation prior to failure.

Remarkably, the hetero-sample exhibits a hybrid fracture morphology that combines features of both ductile and brittle failure, reflecting the layered architecture of the material. As illustrated in Fig. 5.3c1, the overall fracture surface resembles that of the ductile Ti-3.5Al specimen, featuring a cup-and-cone profile and visible necking. However, higher-magnification examination (Fig. 5.3c2) reveals the coexistence of ductile regions with evident dimples (red circles) and brittle regions with smooth cleavage facets (yellow circles). These regions are spatially separated by sharp interfacial boundaries (white dashed lines in Fig. 5.3c2), indicating that each layer retains its intrinsic deformation and fractured behavior. This localized partitioning of fracture modes underscores the effectiveness of the layered design in integrating the favorable attributes of both constituent alloys—namely, the high ductility of Ti-3.5Al and the high strength of Ti-6Al-4V.

The fracture surface features of the hetero-sample thus provide compelling microstructural evidence of its superior mechanical performance. The ability of the soft Ti-3.5Al layer to accommodate strain and arrest crack propagation contributes to enhanced ductility, while the hard Ti-6Al-4V layer provides strength. The sharp delineation of fracture modes at the interface further reflects the absence of interfacial degradation during deformation, highlighting the structural integrity and mechanical synergy of the as-built heterostructure.

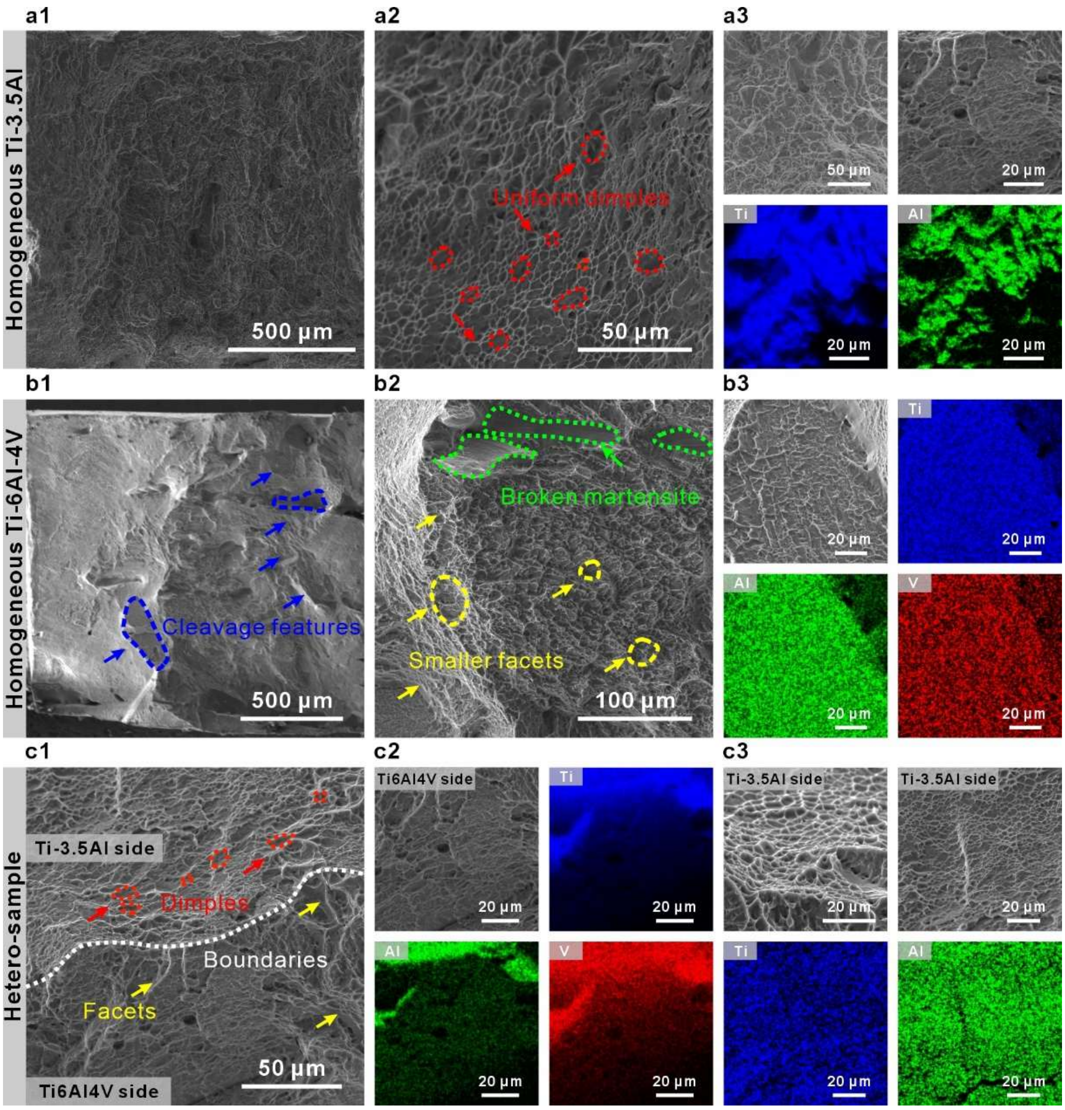

Fig. 5.3 Fractographic analysis of the as-built Ti-3.5Al, Ti-6Al-4V, and hetero-sample specimens. (a1-a2) SEM images of the homogeneous Ti-3.5Al fracture surface, exhibiting a classic ductile fracture morphology, characterized by pronounced cup-and cone profiles and uniformly distributed deep dimples, indicative of extensive plastic deformation via micro-void coalescence. (b1-b2) The homogeneous Ti-6Al-4V sample reveals a stepped fracture surface decorated with cleavage facets and limited necking, reflecting brittle fracture behavior associated with the acicular α′ martensitic structure. (c1-c2) The hetero-sample displays a mixed fracture mode, with both ductile dimples and brittle facets confined to distinct regions corresponding to the Ti-3.5Al and Ti-6Al-4V layers, respectively. The spatially localized fracture features highlight the preserved

mechanical contrast between constituent layers and the interface-mediated deformation compatibility enabled by the layered architecture.

5.2.3 Initial microstructures before deformation

To establish a correlation between mechanical performance and microstructural characteristics, detailed crystallographic analyses were performed on cross-sectional surfaces parallel to the build direction. Figures 5.4a1 and b1 present IPF maps of the as-built Ti-3.5Al and Ti-6Al-4V sample, respectively. The Ti-3.5Al sample (Fig. 5.4a1) reveals a microstructure composed of large, randomly oriented plate-like α-grains, with an average grain size of approximately 15.5 μm (as shown in the inset), along with a small fraction of lamellar grains, indicating minimally preferred crystallographic texture. In contrast, the Ti-6Al-4V specimen (Fig. 5.4b1) predominantly exhibit fine, acicular α′ martensite grains with needle-like morphologies and a significantly smaller average grain size of ~4.3 μm (inset of Fig. 5.4b1), consistent with previous studies on laser-deposited Ti-6Al-4V alloys [298]. The corresponding GND density maps are shown in Figs. 5.4a2 and 5.4b2, which provide insight into the local dislocation distributions within the samples. For the as-built Ti-3.5Al alloy, a relatively uniform and comparatively low GND density is observed throughout the matrix, indicative of its softer, more ductile microstructure (Fig. 5.4a2). Conversely, the Ti-6Al-4V specimen exhibits higher overall GND densities, which are also uniformly distributed within the matrix (Fig. 5.4b2). This elevated dislocation density likely arise from rapid cooling-induced martensitic transformations, producing a harder and more dislocation-rich microstructure.

The differences in the grain boundaries and spatial variation in GND density reflect the internal residual strains imposed during the AM process. As shown in Figs. 5.4a3 and 5.4b3, EBSD-derived strain contour maps were employed to qualitatively assess residual strain distribution within the as-built microstructures [299, 300]. These strain maps, which capture orientation gradients associated with lattice curvature, reveal that the Ti-3.5Al exhibits a relatively uniform and low-magnitude strain distribution across the matrix. This is consistent with its coarse-grained structure, which facilitates more homogeneous strain accommodation and minimizes intragranular distortion. In contrast, the Ti-6Al-4V specimen displays slightly higher overall strain levels and localized strain concentrations, likely attributed to the presence of fine martensitic α′ grains, which hinder homogeneous deformation and promote localized strain buildup.

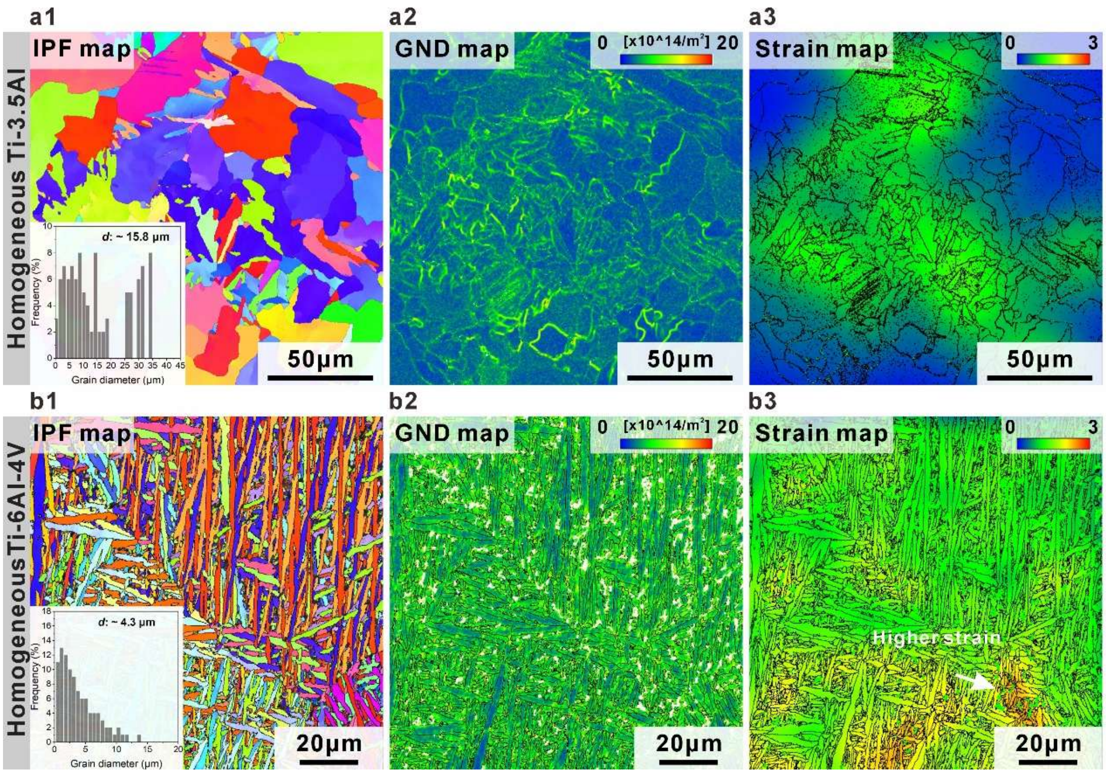

Fig. 5.4 EBSD characterization of the as-built homogeneous samples. (a1-b1) IPF maps showing dominant large plate-like grains in the Ti-3.5Al sample, and fine, needle-like α′ martensitic grains in Ti-6Al-4V, reflecting distinct microstructural evolution due to differences in alloy composition. (a2-b2) Corresponding GND density maps illustrating a low and uniform dislocation density in Ti-3.5Al, and higher GND density in Ti-6Al-4V due to brittle martensitic microstructure. (a3–b3) Strain contour maps

showing low strain levels in Ti-3.5Al and moderately elevated, localized strain in Ti-6Al-4V, associated with its finer grain structure.

Crystallographic analysis of the hetero-sample is presented in Fig. 5.5. The IPF map (Fig. 5.5a) clearly delineates alternating Ti-3.5Al and Ti-6Al-4V layers, each preserving their respective microstructural characteristics. The Ti-3.5Al layers display coarse, plate-like α grains, while the Ti-6Al-4V layers retain a fine, needle-like α′ martensitic structure. The average grain size measured across the entire heterostructure is approximately 11.8 μm (inset of Fig. 5.5a), falling between the values observed for the two homogeneous samples. These observations are consistent with the phase analysis results from XRD and SEM (Fig. 5.1), confirming that the rapid thermal cycles of AM preserved the distinct microstructural features of each alloy without forming secondary phases. The corresponding GND density map of the heterostructure (Fig. 5.5b) reveals a pronounced contrast in dislocation density between the two layers. The Ti-6Al-4V regions exhibit significantly higher GND densities owing to their fine martensitic microstructure, whereas the Ti-3.5Al layers maintain lower GND levels consistent with their coarser grains. Importantly, enhanced GND accumulation is observed near the layer interfaces, suggesting localized strain concentration and dislocation storage at the interface during the cyclic thermal loading of the AM process. These interface regions likely serve as barriers to dislocation motion and promote back-stress development.

Strain contour mapping derived from EBSD data (Fig. 5.5c) further elucidates the unique strengthening behavior of the hetero-sample. Unlike the relatively uniform strain distributions seen in the homogeneous Ti-3.5Al and Ti-6Al-4V samples, the layered heterostructure exhibits pronounced localized strain at the interfaces between dissimilar layers. Notably, such localized strain is consistently observed in regions where the deposition sequence transitions from Ti-3.5Al to Ti-6Al-4V or vice versa, as highlighted by the white arrows in Fig. 5.5c. These interface-adjacent zones show significant strain contrast, reflecting the build-up of thermal mismatch-induced residual stresses during AM processing. In contrast, for the regions far from any compositionally graded boundaries display minimal strain localization, indicating that the abrupt change in alloy chemistry and thermophysical properties across the interface is the dominant contributor to the observed residual strain gradients. These findings provide direct microstructural evidence that CTE-mismatch interfaces are the primary positions of strain partitioning, fostering the formation of GND-rich interfacial architectures that underpin the interface-mediated strengthening mechanisms discussed in subsequent sections.

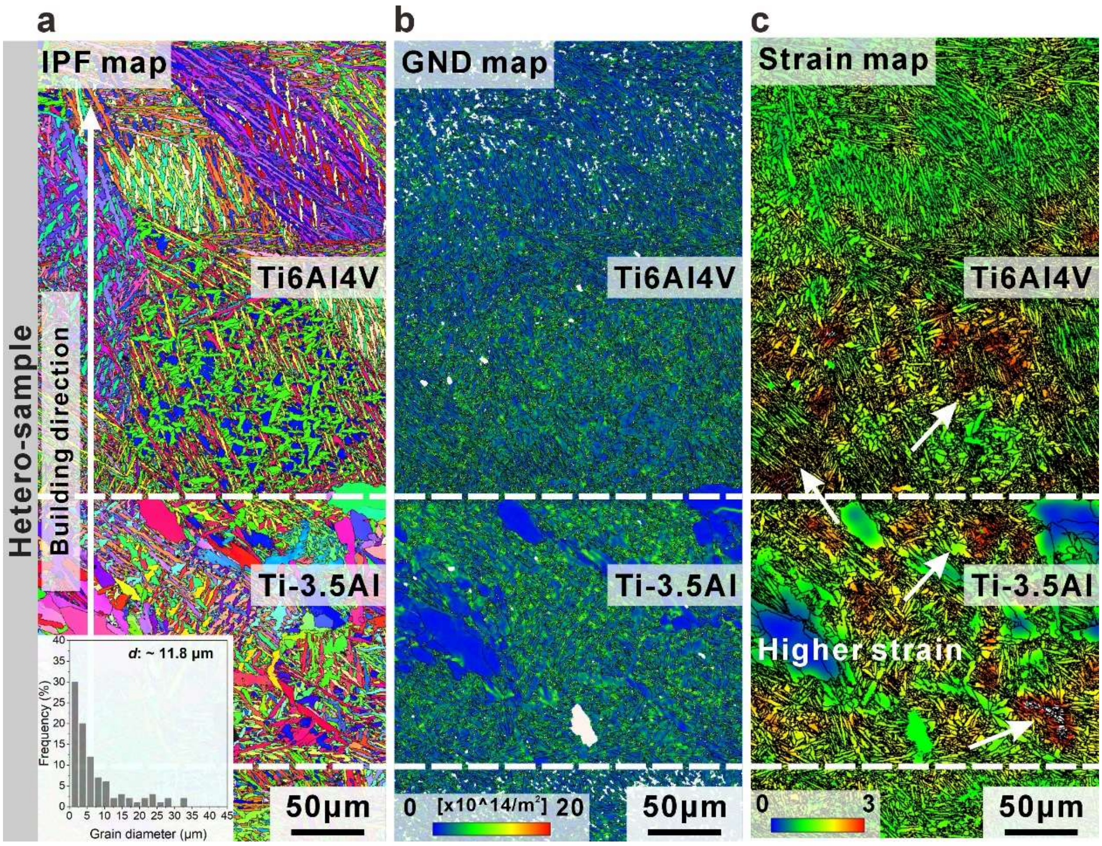

Fig. 5.5 EBSD characterization of the as-built Ti-3.5Al/Ti-6Al-4V hetero-sample. (a) IPF maps showing alternating layers of Ti-3.5Al and Ti-6Al-4V, with coarse, plate-like α grains in the Ti-3.5Al regions and fine, acicular α′ martensitic grains in the Ti-

6Al-4V regions. (b) GND density map revealing higher dislocation densities in the Ti-6Al-4V layers and lower densities in the Ti-3.5Al layers, with enhanced GND accumulation near the layer interfaces. (c) Strain contour map showing localized strain concentrations at the Ti-3.5Al/Ti-6Al-4V interfaces, indicative of interfacial plastic incompatibility and strain partitioning during the AM process.

5.2.4 Microstructural evolutions during deformation

To further elucidate the origin of the enhanced mechanical performance observed in the layered heterostructure, in-situ EBSD analyses were conducted to characterize the microstructural evolution and strain localization during deformation, with a particular focus on the interfacial regions between the Ti-3.5Al and Ti-6Al-4V layers.

At the as-built state (Fig. 5.6a1), the Ti-3.5Al and Ti-6Al-4V regions exhibit distinct grain morphologies, consistent with earlier EBSD results (Fig. 5.5). The Ti-3.5Al region is composed of coarse, plate-like α grains, while the Ti-6Al-4V region presents a fine, acicular grain structure, with a sharp and well-defined interface separating the two layers (highlighted by white dashed lines). The corresponding strain contour map (Fig. 5.6a2) reveals localized strain concentration at or near the interface (white arrows), particularly at positions where the deposition sequence transitions between the two alloys. This interfacial strain localization diminishes with increasing distance from the interface, indicating a strong gradient effect imposed by the thermophysical mismatch.

Upon deformation to a global strain of ~4% (Fig. 5.6b1), the IPF maps reveal no significant changes in grain morphology in either region. However, the corresponding strain contour map (Fig. 5.6b2) indicates that the initial strain localization at the Ti-3.5Al/Ti-6Al-4V interface becomes more pronounced and begins to propagate into the adjacent regions (highlighted by purple dashed lines). This intensification is primarily attributed to the deformation incompatibility between the soft Ti-3.5Al and hard Ti-6Al-4V layers, which amplifies the pre-existing interfacial strain gradients. Additionally, new zones of strain localization emerge within the Ti-6Al-4V regions that were initially distant from the interface. This behavior is likely a consequence of the inherently brittle nature of the fine α′ martensitic microstructure in Ti-6Al-4V, which severely limits its capacity for accommodating localized plastic deformation.

As the applied strain increases to ~8% (Fig. 5.6c1), microcrack initiation is observed within the Ti-6Al-4V regions, particularly in areas farther from the interface. In contrast, the Ti-3.5Al layers mainly exhibit grain rotation without evidence of microcracking. The associated strain contour map (Fig. 5.6c2) further supports these findings. First, severe strain concentration develops within the Ti-6Al-4V regions remote from the interface, where the martensitic structure lacks the capacity for plastic accommodation. Conversely, strain localization within Ti-6Al-4V layers adjacent to the Ti-3.5Al layer is notably less intense, suggesting that the soft Ti-3.5Al layers play a crucial role in accommodating strain and mitigating stress concentration in the hard domains. Simultaneously, the Ti-3.5Al layers themselves exhibit increasing strain accumulation, with localization shifting toward the center of the soft region. This redistribution of strain toward the more ductile Ti-3.5Al layer likely helps delay damage accumulation in the hard Ti-6Al-4V layers, reflecting active strain partitioning between the two constituents.

At the fracture stage (Fig. 5.6d1), the Ti-6Al-4V regions display severe cracking, while the Ti-3.5Al layers undergo pronounced grain reorientation, indicative of intense plastic activity. This grain reorientation indicates strong plastic activity, likely driven by interfacial strain transfer and continued strain accommodation [229]. The final strain contour map (Fig. 5.6d2) shows a continuous high-strain path bridging adjacent Ti-6Al-4V layers through the intervening Ti-3.5Al layer. This observation underscores the critical role of interfacial interaction in directing strain redistribution and highlights the function of soft Ti-3.5Al layers as plastic agents under high constraint. In general, the ability of the layered architecture to sustain localized deformation through interface-mediated strain partitioning and sequential load redistribution contributes directly to its superior strength and delayed failure behavior.

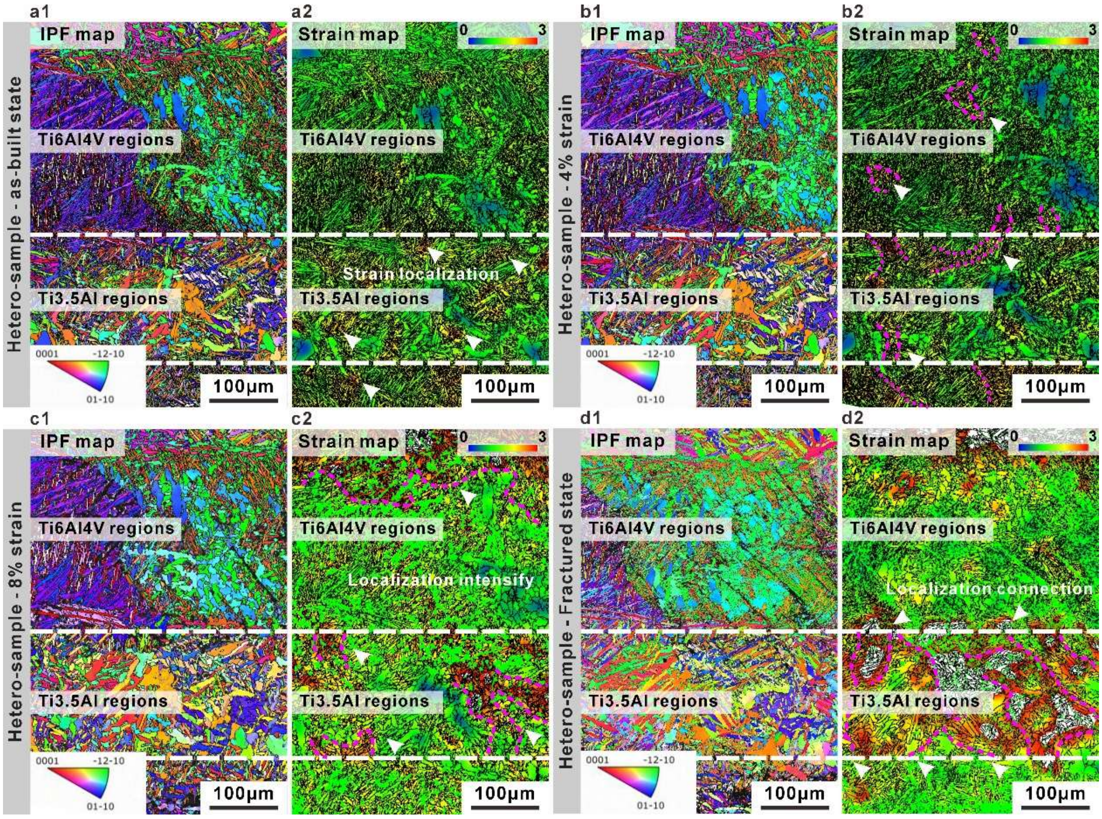

Fig. 5.6 In-situ EBSD analysis showing the microstructural evolution of the hetero-sample at the different deformation stages (as-built, ~4% strain, ~8% strain, and fractured). (a1-d1) IPF maps illustrate grain structure evolution. (a2-d2) Strain contour maps depicting strain distribution throughout the deformation process.

In addition, the dynamic evolution of dislocation behavior across the interface and within the soft and hard regions was quantitatively assessed to elucidate the underlaying strengthening mechanism. As shown in Fig. 5.7, the progression of dislocation networks was evaluated at various strain levels using average GND density profiles. In the as-built state (Figs. 5.7a1-a2), the average GND density along the build direction—

from the Ti-6Al-4V region into the adjacent Ti-3.5Al layer—exhibits a distinct gradient. Although local fluctuations exist within each domain, the overall tendency reveals a monotonic increase in GND density as it approaches the interface from the Ti-6Al-4V side. This increase reaches a peak near the interface and then decreases as it extends deeper into the soft Ti-3.5Al layer. This distribution supports earlier observations of strain localization near interfaces and reflects dislocation pile-up at the mechanically dissimilar boundary during the AM fabrication. Upon deformation to ~4% global strain (Figs. 5.7b1-b2), GND densities increase across both layers. Notably, the Ti-3.5Al region near the interface generates additional dislocations, resulting in dislocation densities comparable to those in the Ti-6Al-4V region. This behavior is consistent with previous observations in the strain localization propagation into the soft Ti-3.5Al sides seen in Fig. 5.6b2, and likely arises from early-stage plastic incompatibility between the hard and soft layers. This behavior aligns well with the HDI hardening mechanism [228], wherein interfacial stress gradients generate long-range back stresses that resist applied shear and enhance the effective strength of the soft phase. As a result, the dislocation densities in the interfacial Ti-3.5Al region becomes comparable to that of the adjacent Ti-6Al-4V, while regions farther from the interface retain lower GND levels.

At higher strain levels (~8%), the average GND density further increases (Figs. 5.7c1-c2). In the Ti-3.5Al region, the strain localization zone extends deeper into the soft domain (as also observed in Fig. 5.6c2), indicating that the ductile Ti-3.5Al region accommodates increasing dislocation activity, even in areas farther from the interface. In contrast, the brittle Ti-6Al-4V layers exhibit dislocation clustering and more localized strain accumulation due to their limited plastic deformability, resulting in pronounced GND fluctuations in the Ti-6Al-4V domains.

At the onset of fracture (Figs. 5.7d1-d2), the GND densities further boosted, and its distribution becomes more spatially uniform across the heterostructure, suggesting improved deformation compatibility between the layers. However, once the Ti-3.5Al region reaches its capacity to accommodate additional dislocations—as evidenced by the merging of strain localization zones in the previous strain contour maps—further dislocation storage becomes restricted. This limitation ultimately leads to the initiation of failure [103].

T

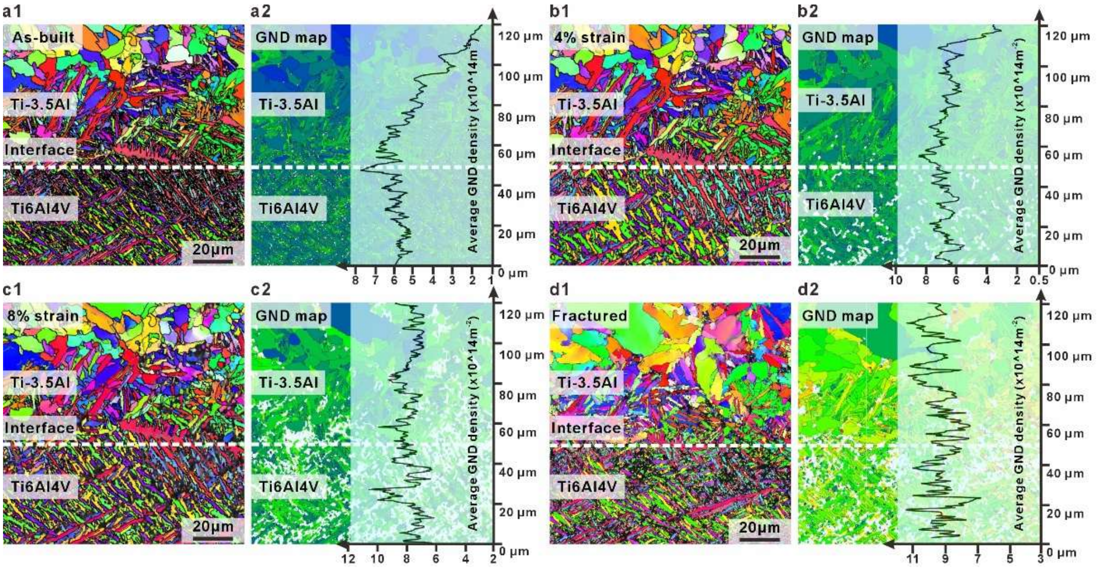

Fig. 5.7 Evolution of average GND distributions in the hetero-sample during tensile deformation at different strain levels. (a1-d1) IPF maps revealing the interface region between Ti-3.5Al and Ti-6Al-4V layers at different deformation stages: (a) as-built, (b) ~4% strain, (c) ~8% strain, and (d) fracture. (a2-d2) Corresponding average GND density maps showing the progression of dislocation accumulation across the layered architecture throughout the deformation process.

5.3 Discussion

A remarkable combination of high yield strength and ductility is achieved in the layered Ti-3.5Al/Ti-6Al-4V hetero-sample, surpassing the mechanical performance typically observed in homogeneous alloys of similar composition. As previously discussed, this enhanced mechanical behavior is attributed to strain localization at internal interfaces and the resultant deformation incompatibility between the soft and hard layers. Unlike homogeneous Ti-3.5Al and Ti-6Al-4V samples, the yield strength of the hetero-sample deviates significantly from predictions based on the Hall-Petch relationship and the ROM [97, 301], suggesting the activation of strengthening mechanisms beyond those related solely to grain size or composition. Subsequent sections analyze the distinct role of AM in tailoring the mechanical response of layered heterostructures composed of materials with divergent thermal and physical properties. Specifically, the analysis considers how rapid melting and solidification, combined with thermal mismatch during AM, generates interfacial stress fields and dislocation structures that enhance strength. Furthermore, the layered architecture is shown to promote strain partitioning and plastic compatibility during deformation, thereby contributing to the concurrent improvement in both strength and ductility.

5.3.1 The effect of layer structure on strength improvement

5.3.1.1 AM-boosted interfacial dislocation preconditioning

This section first establishes how thermal cycling during additive manufacturing pre-conditions the layered structure with interfacial dislocations by generating steep, cyclic residual stress and strain gradients. In laser-based AM processes, such as powder bed fusion or DED, each pass of the moving heat source induces rapid melting followed by high-rate solidification, resulting in significant spatial and temporal temperature gradients [124, 302]. During irradiation, the newly deposited and underlying layers undergo swift thermal expansion, developing transient tensile fields; subsequent to the laser's departure, accelerated cooling induces contraction and the accumulation of compressive fields, particularly within constrained subsurface regions [303, 304]. Even in homogeneous alloys, such non-uniform thermal histories produce substantial residual stresses and distortions; however, the resulting stress and strain fields remain relatively smooth spatially due to the absence of sharp material property discontinuities [305-307].

In contrast, within layered heterostructures, the identical cyclic thermal loading is applied across Ti-3.5Al and Ti-6Al-4V layers, which possess contrasting thermophysical properties, including thermal conductivity, thermal diffusivity, and temperature-dependent coefficients of thermal expansion. These differences amplify the local incompatibility between adjacent layers during expansion and contraction, generating pronounced interfacial tensile and compressive stresses. Consequently, steep residual strain gradients become concentrated at the interfaces, promoting the storage of GNDs in the as-built state, as schematically illustrated in Fig. 5.9. This AM-induced interfacial dislocation preconditioning elevates the initial flow resistance, thereby increasing the yield strength of the layered heterostructure compared to the as-built homogeneous Ti-6Al-4V processed under identical conditions [65].

To assess the magnitude of this effect, the effective thermal mismatch strain can be estimated using the following relation:

$$\sigma_{interface} = \alpha_T \cdot E \cdot \left(T - T_{ref}\right) \tag{5.1}$$

where α_T is the temperature-dependent CTE, E is the elastic modulus, and T_{ref} represents the reference temperature [308]. The transient temperature field $T(x,y)$ during AM is influenced by laser power P, scan speed v, thermal conductivity k, and thermal diffusivity D, and can be approximated using Rosenthal's moving heat source model [284, 309, 310]:

$$T_{(x,y)} = T_0 + \frac{P}{2\pi kR} \exp\left(-\frac{v(x-x_0)}{2D}\right) \tag{5.2}$$

where T_0 is the ambient temperature, and $R = \sqrt{x^2 + y^2}$ is the radial distance from the moving heat source. Integrating these expressions yields the following scaling relation for interfacial thermal stress:

$$\sigma_{interface} \propto \Delta a(T) \cdot E(T) \cdot \frac{P}{2\pi Rk} \cdot \exp\left(-\frac{v(x-x_0)}{2D}\right) \tag{5.3}$$

From this analysis, it is evident that the interfacial thermal stress scales with the thermal expansion mismatch ($\Delta\alpha$), the temperature-dependent elastic modulus $E(T)$, and the local transient thermal field governed by processing and material parameters such as laser power P, thermal conductivity k, scan speed v, and thermal diffusivity D.

Among these factors, the coefficient of thermal expansion mismatch ($\Delta\alpha(T)$) plays a primary role in generating incompatible contraction and expansion across the dissimilar layers. As shown in Fig. 5.8, Ti-6Al-4V exhibits a steeper temperature-dependent increase in CTE than Ti-3.5Al, particularly within the elevated temperature regime characteristic of AM thermal cycles. This mismatch persists across a wide high-temperature range and can approach ~10% at peak processing temperatures, leading to significant residual strain accumulation at the interface. During rapid thermal cycling, this disparity in thermal expansion drives localized contraction mismatches between the layers, promoting interfacial strain gradients that become preserved upon solidification. The elastic moduli of the two alloys are relatively similar at ambient conditions (Ti-3.5Al: ~100–110 GPa; Ti-6Al-4V: ~110–120 GPa) and both decrease moderately with increasing temperature. Given this similarity, $E(T)$ contributes less to the thermal stress disparity, and the thermal expansion mismatch $\Delta\alpha(T)$ remains the dominant driver.

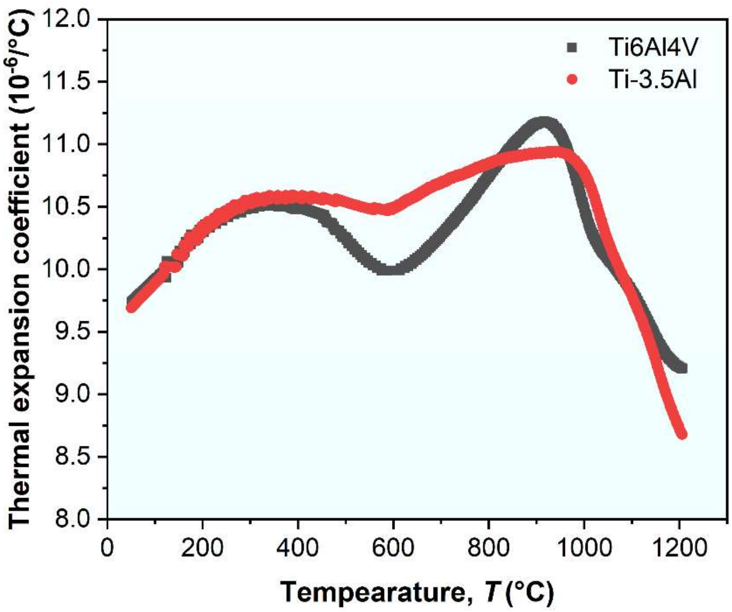

Fig. 5.8 Thermal expansion coefficient of the Ti-6Al-4V and Ti-3.5Al samples.

The asymmetry in thermal transport properties further exacerbates interfacial stress. Ti-3.5Al possesses higher thermal conductivity (~10.05 $W \cdot m^{-1} \cdot K^{-1}$) and thermal diffusivity (~4.26 mm^2/s) compared to Ti-6Al-4V (k ≈ 7.06 $W \cdot m^{-1} \cdot K^{-1}$; D ≈ 3.26 mm^2/s) [311, 312]. According to Eq. (5.3), although process parameters such as P and v are held constant during AM, their effects are modulated by the layer-specific thermal properties. The lower conductivity in Ti-6Al-4V results in a steeper local temperature rise under constant laser power (via $P/2\pi Rk$), while its lower diffusivity shortens the thermal diffusion length (via $\exp(-v(x-x_0)/2D$). These effects compound to generate steeper thermal gradients and larger residual thermal strains in the Ti-6Al-4V region, particularly near the interface.

Altogether, the interfacial thermal stress is amplified by: (i) substantial thermal expansion mismatch ($\Delta\alpha(T)$ over the relevant temperature range), (ii) asymmetric heat conduction ($k_{Ti6Al4V}/k_{Ti\ .5Al} \approx 0.7$), and (iii) differences in heat diffusion behavior

($D_{Ti6Al4V}/D_{Ti\ .5Al} \approx 0.77$). These thermophysical mismatches promote the development of steep residual strain gradients that oriented perpendicular to the build direction, driving the preferential accumulation of GNDs at the interfaces even in the as-built state. These GND-rich interfacial zones serve as preconditioned microstructural features that underpin the CTE mismatch–driven, interface-mediated strengthening mechanism, ultimately contributing to the enhanced yield strength and mechanical performance of the hetero-sample.

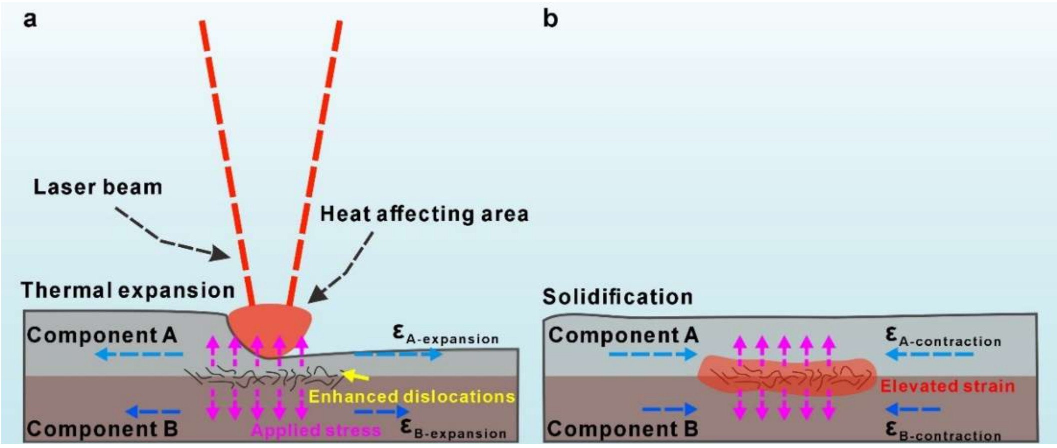

Fig. 5.9 Schematic illustration of stress evolution during the AM process. (a) Thermal expansion and melting of the material, leading to volumetric changes and stress accumulation. (b) Rapid solidification causing material contraction, contributing to the development of residual stress.

The hypothesis of interfacial dislocation preconditioning induced by thermophysical mismatch is directly substantiated by the correlated strain localization and GND density distributions revealed through EBSD analysis (Figs. 5.6 and 5.7). Local strain maps indicate pronounced plastic localization concentrated near the Ti-3.5Al/Ti-6Al-4V interfaces, which is consistent with incompatibility-driven deformation. Concurrently, quantitative GND density maps exhibit sharp peaks in dislocation density at the interfaces, with the density gradually decaying with increasing distance into each constituent layer. This gradient directly reflects the accumulation of residual strain and GNDs resulting from differential thermal contraction between the layers during rapid AM thermal cycling. The physical origin of this GND localization resides in the mismatch of temperature-dependent thermophysical properties—specifically thermal expansion, conductivity, and diffusivity—which cause adjacent layers to undergo dissimilar volumetric changes during heating and cooling [215]. These incompatibilities impose mechanical constraints at the interfaces, generating residual strain gradients and necessitating dislocation generation to accommodate the resulting plastic mismatch. Once formed, these interfacial GNDs act as long-range obstacles to subsequent dislocation motion during external loading, thereby elevating the initial flow stress and contributing to the higher yield strength observed in the layered heterostructure [92, 228].

Further microstructural evidence is provided by TEM observations of the as-built structure (Fig. 5.10). Within the Ti-6Al-4V region, the martensitic α′ phase contains straight, parallel dislocations aligned along the grain interiors, suggesting limited dislocation mobility due to the phase's high intrinsic strength. In contrast, the Ti-3.5Al region exhibits coarser grains and a more randomized dislocation population, consistent with its superior capacity for plastic accommodation. Most notably, dense networks of tangled and intersecting dislocations are observed at the interfaces, confirming severe local strain accumulation. These entangled dislocation structures affirm the role of the interfaces as strain-accommodation zones and substantiate the formation of GNDs driven by thermal and mechanical incompatibilities during solidification. Collectively, these findings demonstrate that AM-induced thermomechanical mismatch not only dictates the interfacial microstructure but also preconditions the material for enhanced mechanical performance through an interface-mediated strengthening mechanism.

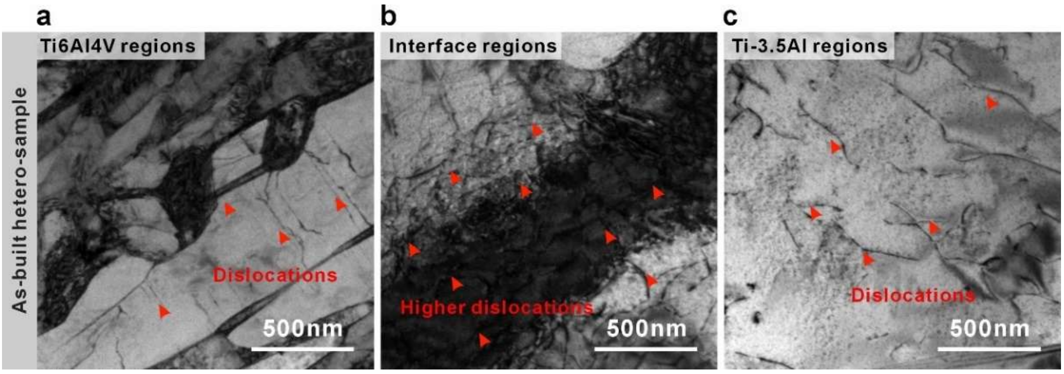

Fig. 5.10 Representative TEM images illustrating characteristic dislocation structures in different regions of the as-built hetero-sample. (a) Ti-6Al-4V region, showing fine, acicular α′ martensitic grains with uniformly distributed linear dislocations. (b) Interfacial region, exhibiting markedly elevated dislocation densities characterized by dense entanglements and intersecting networks. (c) Ti-3.5Al region, featuring larger grains with comparatively limited and randomly distributed dislocations.

To further probe the role of AM-induced interfacial dislocation structures in enhancing strength, a stress-relief heat treatment was performed on the as-built heterostructure to eliminate dislocation networks accumulated near the interfaces. The heat treatment was conducted at 600°C for 4 hours [313]. As shown in Fig. 5.11a, the yield strength of the hetero-sample decreased significantly after annealing treatment, indicating that internal stress fields and dislocation structures play a critical role in the enhanced strength of the as-built condition. EBSD analysis conducted on the stress-relief sample (Fig. 5.11b) shows that both the Ti-3.5Al and Ti-6Al-4V regions retain their grain morphologies and sizes. The negligible difference in grain size distribution (inset of Fig. 5.11b) indicates that Hall-Petch relationship is not the source of strength loss [314]. Importantly, the strain localization map (Fig. 5.11c) and GND density map (Fig. 5.11d) confirm that the pronounced interfacial dislocation pile-up and strain gradients observed in the as-built sample are eliminated after annealing. These findings reinforce the conclusion that the as-built sample strengthening arises from AM-induced dislocation preconditioning at the layer interfaces.

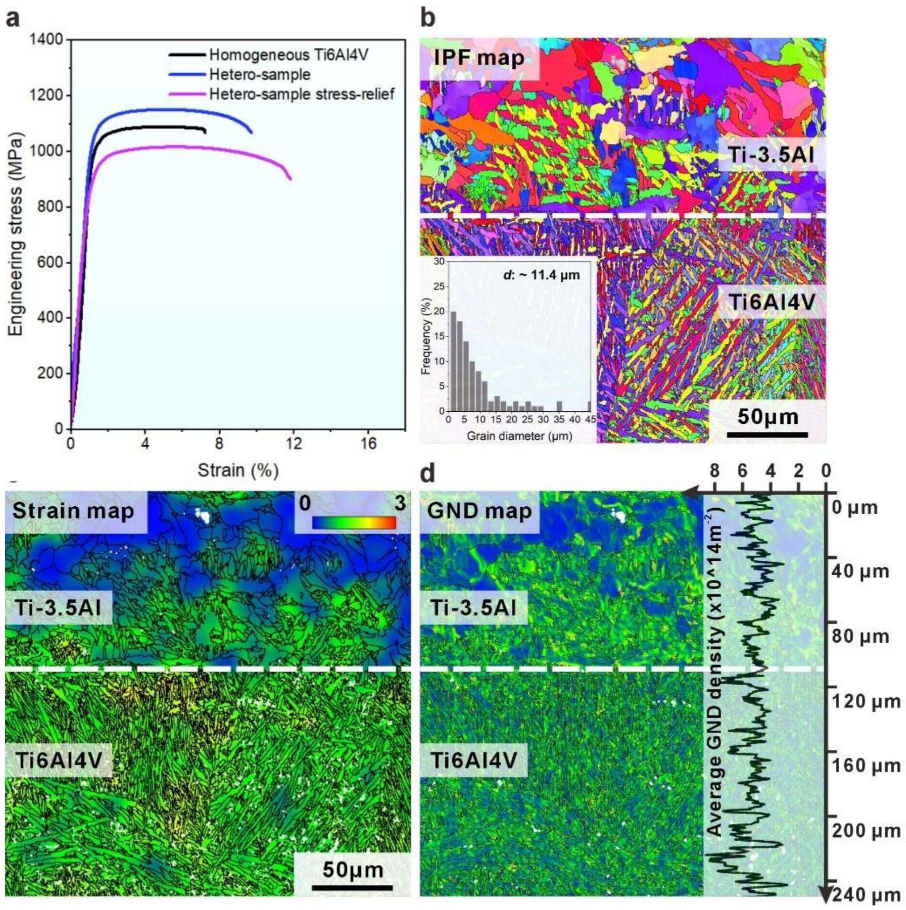

Fig. 5.11 Mechanical and microstructural characterization of the stress-relieved hetero-sample. (a) Tensile properties of the stress-relief sample compared to the as-built samples. (b) IPF maps show that the layered structure is retained with no significant changes in grain morphology. (c) Strain map revealing a more uniform strain distribution across matrix, with a significant reduction in the strain concentration previously observed at the interface. (d) Corresponding GND maps indicating a generally uniform distribution of GND density, with slightly higher dislocation density in the Ti-6Al-4V region.

5.3.1.2 Interfacial strengthening during deformation in layered heterostructures

The preceding section established that the as-built Ti-3.5Al/Ti-6Al-4V heterostructure exhibits enhanced strength relative to its constituent materials, an effect attributed to strain localization and interface-driven dislocation accumulation during the additive manufacturing process. To further elucidate the microstructural evolution governing these mechanical responses, ex-situ TEM observations were conducted on the hetero-sample at different deformation stages (4%, 8%, and fracture strains), as illustrated in Fig. 5.12.

At a low global strain of ~4% (Fig. 5.12a), the Ti-6Al-4V region displays a high density of linear dislocations confined within fine acicular α′ martensitic laths (Fig. 5.12a1, marked by purple arrows). This dislocation configuration is characteristic of the high intrinsic strength and limited slip capacity of α′ martensite, where dislocation motion is constrained by both fine lath boundaries and a high lattice friction stress [315]. The absence of widespread dislocation multiplication or tangling suggests the Ti-6Al-4V layer remains predominantly elastic at this early stage. In contrast, the softer Ti-3.5Al domain initiates plastic deformation, evidenced by the activation of sparse <c+a> dislocations (Fig. 5.12a3, indicated by yellow arrows) [102, 316]. The coarse grain structure in this region facilitates dislocation nucleation and motion, allowing it to accommodate the majority of the initial plastic strain. This mechanical asymmetry between the hard and soft layers leads to incompatible strain partitioning across the interface. To maintain strain continuity under this elastic-plastic mismatch, GNDs nucleate and accumulate at the Ti-3.5Al/Ti-6Al-4V interface, forming dense dislocation tangles (Fig. 5.12a2, delineated by white dashed lines). These interfacial structures amplify the pre-existing dislocation network from AM-induced thermal mismatch and mark the onset of local strain accommodation. The accumulated GNDs establish long-range internal back stresses that activate HDI hardening, serving as effective barriers to subsequent dislocation motion and reinforcing the layered structure from the earliest stages of plastic deformation [103, 317].

With further loading to ~8% global strain (Fig. 5.12b), the deformation response evolves from initial elastic-plastic incompatibility toward a more coordinated, interface-mediated plasticity [92, 318]. In the Ti-6Al-4V region, intra-lath shear bands become apparent within the acicular α′ martensitic matrix (Fig. 5.12b1, delineated by blue lines), indicating localized deformation instability. This reflects the limited strain-hardening capability of the α′ phase, where dislocation mobility is increasingly restricted by lath-boundary confinement and high lattice friction stress [319, 320]. Consequently, the hard layer progressively saturates its capacity to store additional dislocations, intensifying the mechanical constraint on the adjacent soft layer. At the interface, the initial dislocation tangles observed at ~4% strain undergo a morphological transition into more extended, semi-aligned configurations at ~8% strain (Fig. 5.12b2, delineated by green lines). This reorganization likely results from increased local stress concentration, compelling the tangled network to reconfigure under sustained shear [233]. The partial alignment suggests the activation of dynamic recovery mechanisms such as cross-slip or climb, which reduce local entanglement while maintaining high dislocation density. These extended interfacial dislocations may facilitate partial slip transfer or dislocation absorption/re-emission across the interface, enabling more uniform plastic strain redistribution between the mechanically distinct layers [321]. Critically, these intermediate configurations remain effective in bridging the elastic-plastic mismatch. Their alignment parallel to the interface accommodates interfacial shear while sustaining localized GND accumulation, contributing to long-range back stress development—a characteristic feature of the HDI strengthening mechanism, where interfacial structures mediate strain compatibility and act as barriers to dislocation motion [92, 228].

Meanwhile, the Ti-3.5Al regions exhibit pronounced activation of non-basal <c+a> dislocation activity (Fig. 5.12b3). This can be attributed to two concurrent factors. First, the increasing back stress from the hard layer raises the resolved shear stress on pyramidal systems in the α-phase, exceeding the activation threshold for <c+a> slip [102, 322]. Second, the triaxial mechanical constraint imposed by the adjacent hard Ti-6Al-4V layer and interfacial dislocation structures necessitates out-of-basal slip to maintain strain compatibility [103, 279]. As deformation progresses, the soft domain assumes a greater share of plastic strain, facilitated by its coarser grain size and greater slip system availability, while the interface acts as a site for dislocation storage and shear pathway regulation. This tripartite cooperation—where the hard layer provides strength, the interface mediates strain transfer and storage, and the soft layer offers accommodation—characterizes the HDI hardening at intermediate strains and underpins the sustained work hardening observed in the laminate.

At the fracture stage (Fig. 5.12c), the microstructural evolution reaches its terminal state. In the Ti-6Al-4V region, a high density of intra-lath shear bands is observed within the acicular α′ martensitic matrix (Fig. 5.12c1), alongside pronounced dislocation accumulation at lath boundaries and indications of lath fragmentation. This signifies that the hard α′ phase has largely exhausted its capacity for uniform plastic deformation. As dislocation motion becomes severely constrained, plastic instability occurs and deformation localizes along shear bands, limiting further strain transfer to the soft layer [323]. At the interface (Fig. 5.12c2), the semi-aligned dislocation arrays observed at ~8% strain evolve into more continuous, wall-like configurations. These high-density structures resemble dense low-energy dislocation walls, which form under sustained interfacial shear via progressive dislocation rearrangement mechanisms such as cross-slip, climb, and annihilation of like-signed segments [324-326]. Functionally, these walls act as both long-range back-stress sources and interfacial shear conduits, helping to accommodate persistent strain gradients and maintain mechanical compatibility. Their capacity to sustain high GND densities under large global strains ensures the continued activation of HDI hardening and delays strain localization [327, 328]. However, as deformation approaches fracture, the further accumulation and alignment of these low-energy dislocation walls render them densely packed and immobile, diminishing their ability to mediate plastic strain and relax interfacial stress gradients. This saturation of interfacial dislocation storage transforms the boundary from a compliant shear-transfer zone into a potential site for micro-void or microcrack nucleation, initiating the terminal stage of deformation [97, 278]. In the Ti-3.5Al region, continued strain transfer and rising triaxial constraints activate extensive non-basal <c+a> slip, leading to the formation of dense, entangled dislocation networks within coarse grains (Fig. 5.12c3). These structures provide substantial storage capacity for strain accommodation via out-of-basal shear, a mechanism well-established in HCP α-Ti under constraint-dominated conditions [102]. However, the extensive and uniform distribution of high dislocation densities indicates that the soft domain's accommodation capacity is nearing exhaustion. As both soft and hard layers approach their limits of plastic strain storage, further deformation becomes unsustainable. In the hard Ti-6Al-4V regions, severe strain localization and lath fragmentation lead to dislocation saturation and likely initiate micro-voids. These micro-voids may then propagate toward the interface, where the saturated low-energy dislocation wall structures can no longer mediate interlayer strain mismatch effectively. Once the interfacial accommodation capacity is exceeded, strain localizes across the boundary and transfers into the Ti-3.5Al layer, ultimately culminating in fracture.

Collectively, the TEM observations reveal a hierarchical deformation mechanism: the hard Ti-6Al-4V layer provides strength, the soft Ti-3.5Al layer supplies ductility via <c+a> slip and dislocation networks, and the interface stores GNDs and enables strain transfer. This architecture—integrating strength, accommodation, and interfacial coordination—underpins the strength-ductility synergy of the designed Ti-3.5Al/Ti-6Al-4V layered heterostructure.

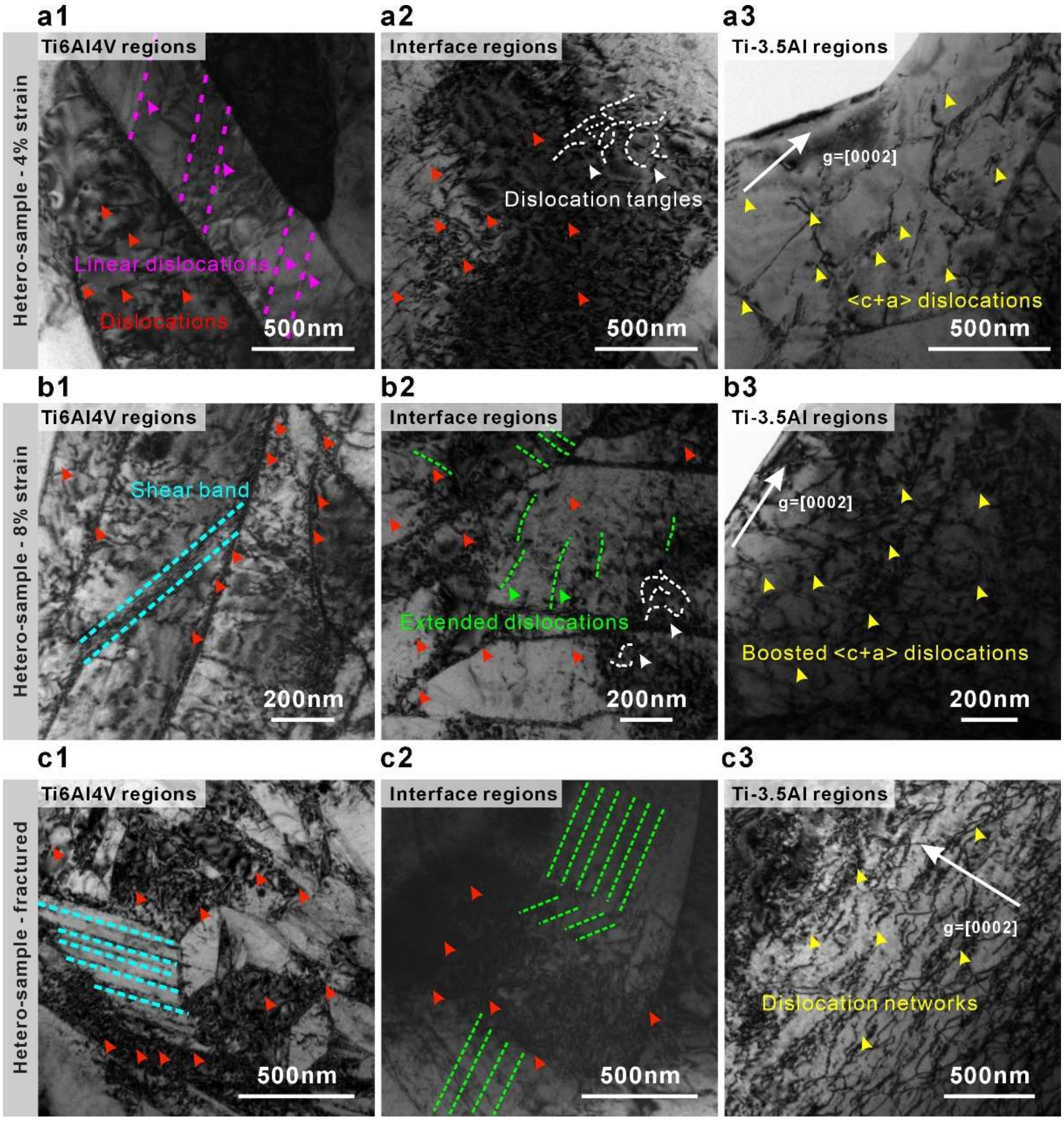

Fig. 5.12 Progressive microstructural evolution of the Ti-3.5Al/Ti-6Al-4V hetero-sample under increasing tensile strain (4%, 8%, and fracture). (a1) At 4% strain, dense linear dislocations initiate within fine acicular α′ grains in the Ti-6Al-4V region. (a2) Dislocation tangles emerge at the interface, reflecting early-stage strain incompatibility. (a3) Sparse <c+a> dislocations appear in the Ti-3.5Al region under g = [0002] two-beam imaging. (b1) At 8% strain, intra-lath shear bands form in the Ti-6Al-4V region, indicating localized plastic instability. (b2) Interfacial dislocations evolve into extended arrays, suggesting enhanced shear transfer and redistribution. (b3) The Ti-3.5Al region shows increased activation of <c+a> dislocations. (c1) At fracture, severe grain distortion and coalesced shear bands in Ti-6Al-4V denote saturated

plasticity. (c2) Interface regions exhibit dense, wall-like dislocation structures, marking sustained interfacial hardening. (c3) The Ti-3.5Al region shows dense, entangled dislocation networks, underscoring its critical role in absorbing and accommodating severe deformation.

5.3.1.3 Elevated interface-mediated HDI strengthening revealed by back stress evolution

To further substantiate the role of interface-mediated strengthening in the Ti-3.5Al/Ti-6Al-4V hetero-sample, loading-unloading-reloading tests were conducted on both the as-built and stress-relieved specimens to probe the evolution of internal back stresses. As shown in Fig. 5.13a, the as-built sample exhibits pronounced hysteresis loops in its stress-strain curves, indicating a Bauschinger effect that is a signature of kinematic hardening associated with long-range internal back stresses [329, 330]. In contrast, the stress-relieved sample displays narrower hysteresis loops under identical loading conditions, signifying the mitigation of interface-induced strain gradients and their associated dislocation structures following heat treatment.

Quantitative analysis of the loading-unloading-reloading curves allows for decomposition of the flow stress (σ) into back stress (σ_b) and effective stress (σ_f), using the standard relationships [90]:

$$\sigma_b = \frac{\sigma_r + \sigma_u}{2}, \text{ and } \sigma_f = \frac{\sigma_r - \sigma_u}{2} \tag{5.4}$$

where σ_u and σ_r denote the unloading and reloading yield stresses, respectively. As shown in Fig. 5.13b, both the back stress and effective stress increase with applied strain; however, the back stress is dominant in the early stages. This suggests that strain incompatibility at the layer interfaces contributes more significantly to work hardening than dislocation friction alone [92, 331]. Notably, the as-built hetero-sample exhibits simultaneously high σ_b and σ_f, reflecting not only substantial GND accumulation at the interface but also an increased resistance to dislocation motion within the individual layers. The enhanced back stress confirms the activation of HDI strengthening, while the elevated effective stress indicates additional contributions from short-range barriers such as dislocation interactions and microstructural constraints. Together, these dual contributions explain the high strength and robust strain hardening behavior observed in the AM-fabricated heterostructure.

These findings support the conclusion that the hierarchical mechanical response of the hetero-sample arises from the synergistic action of long-range interfacial back stresses and localized hardening mechanisms, with the AM-induced strain architecture serving as a fundamental enabler. In contrast, the elimination of strain localization and dislocation pile-ups through heat treatment results in a substantial reduction of both σ_b and σ_f, leading to pronounced softening. This comparison affirms the central role of the as-built interface in enabling the material's superior mechanical performance.

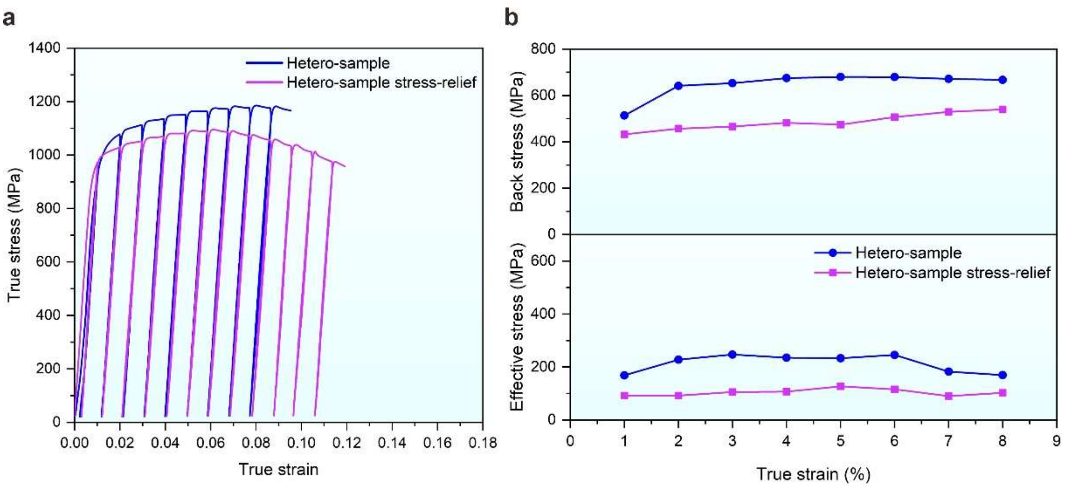

Fig. 5.13 HDI stress analysis of the Ti-3.5Al/Ti-6Al-4V heterostructure in the as-built and stress-relieved conditions. (a) LUR hysteresis loops showing pronounced Bauschinger effect in the as-built sample, indicative of strong internal back stress. (b)

Evolution of back stress and effective stress as a function of true strain, illustrating enhanced hardening in the as-built sample compared to the heat-treated counterpart.

5.3.2 The effect of layer structure on ductility improvement

In addition to the significant strengthening imparted by the heterogeneous structure, the incorporation of soft Ti-3.5Al layers substantially enhances the overall ductility of the hetero-sample by effectively suppressing strain localization and impeding crack propagation during deformation. Figure 5.14 presents representative SEM images of the fracture surfaces from homogeneous Ti-3.5Al, Ti-6Al-4V, and the layered hetero-sample, revealing distinct differences in their crack initiation and propagation behaviors.

In the homogeneous Ti-3.5Al alloy (Figs. 5.14a1-a3), microcracks are uniformly distributed within the coarse, plate-like α grains and are segregated along grain boundaries. This cracking pattern reflects the intrinsic ability of the alloy to accommodate deformation through plastic strain before failure, thereby contributing to its relatively high ductility. In contrast, the homogeneous Ti-6Al-4V alloy (Figs. 5.14b1-b3) displays dense microcrack networks aligned with the acicular α′ martensitic structure. Such cracking indicates severe strain localization within the hard, brittle α′ martensite phase, which allows cracks to nucleate and propagate rapidly without significant resistance. The extensive shear localization and facile propagation of microcracks observed here significantly limit overall ductility, a finding consistent with prior reports on martensitic alloys [332, 333].

Remarkably, the hetero-sample exhibits a fundamentally different cracking behavior attributable to its layered architecture. As shown in Fig. 5.14c1, crack initiation predominantly occurs within the brittle Ti-6Al-4V regions, where cracks propagate along the martensitic laths. However, these cracks are effectively arrested upon reaching the interfaces with the adjacent Ti-3.5Al layers, as illustrated in Fig. 5.14c2. Elemental mapping (Fig. 5.14c3) confirms the compositional transition at the interface, further supporting the microstructural origin of this crack-arrest behavior. The soft Ti-3.5Al layer plays a critical role in impeding crack propagation from the hard Ti-6Al-4V side by redistributing localized stress and accommodating plastic strain through enhanced deformation mechanisms. When a crack encounters the more ductile Ti-3.5Al layer, the crack tip experiences a significant reduction in local stress intensity, leading to blunting and the suppression of further advancement [301, 328].

This crack-arrest phenomenon is analogous to behaviors observed in other multiphase or layered alloys, where ductile constituents act as sinks for strain energy and barriers to crack propagation, thereby enhancing fracture toughness and delaying catastrophic failure [103, 327]. Beyond the role of the soft layer, the interface itself functions as a mechanical discontinuity that resists direct crack transmission. The mismatch in plasticity, toughness, and interfacial cohesion between the hard and soft domains compels cracks to deflect, branch, or terminate at the boundary, significantly increasing the energy required for continued crack growth [97, 334].

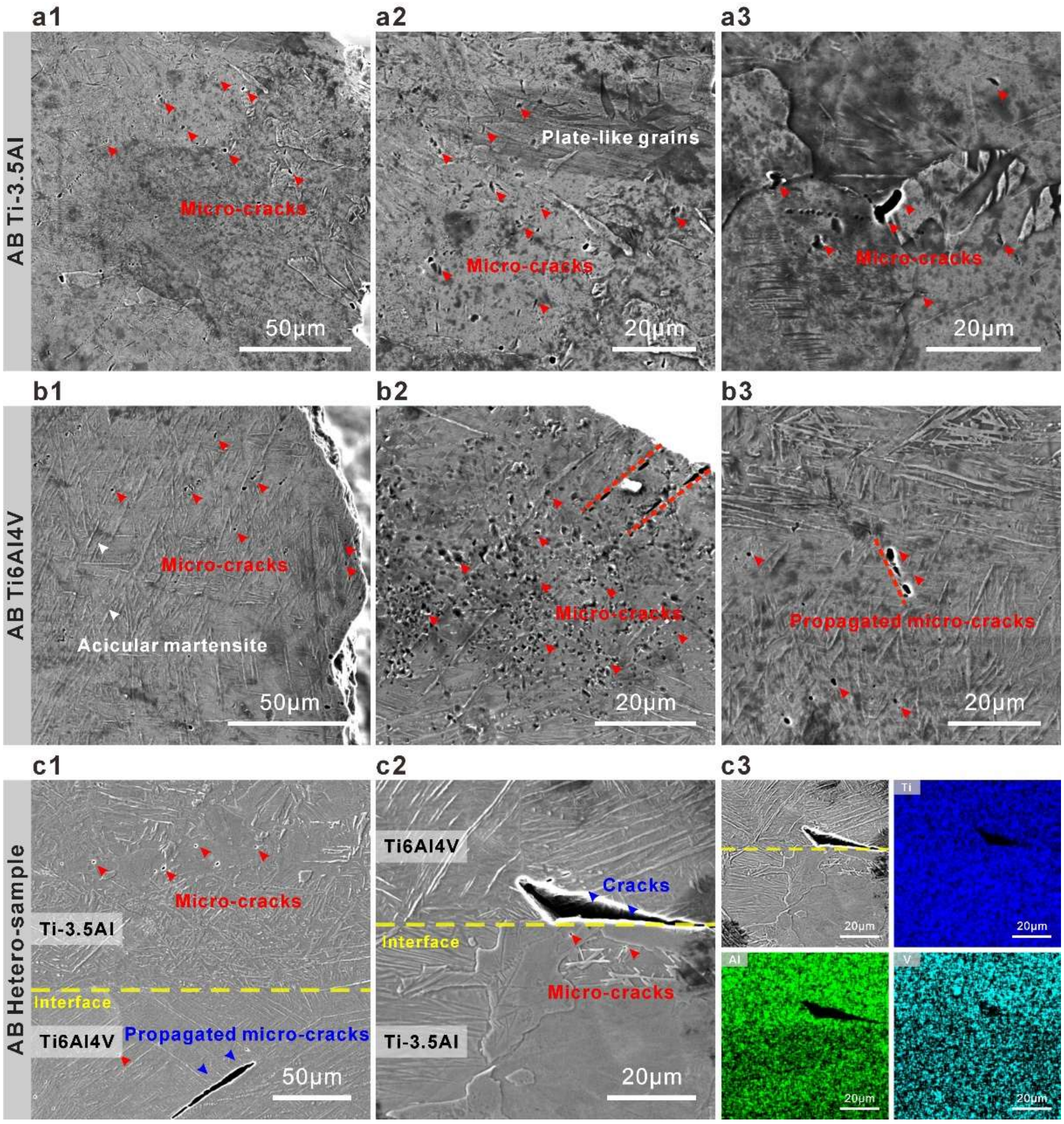

Fig. 5.14 SEM images of cross-sectional necking regions illustrating distinct micro-cracking behaviors across different samples. (a1-a3) The homogeneous Ti-3.5Al sample reveals uniformly distributed microcracks, segregated within the grains and along the grain boundaries. (b1-b3) The homogeneous Ti-6Al-4V sample displays extensive microcracking localized along acicular α′ martensitic laths, reflecting severe strain localization and brittle fracture behavior. (c1-c3) The hetero-sample shows crack initiation within the brittle Ti-6Al-4V region, but cracks are effectively arrested upon reaching the soft Ti-3.5Al layer, as further confirmed by EDS composition mapping.

5.4 Conclusions

By leveraging the inherent rapid thermal cycling of the L-DED process, this study exploits thermomechanical effects induced by the CTE mismatch to engineer interfaces with pre-stored dislocation structures and residual stress gradients. The resulting architecture achieves strong metallurgical bonding, sharp yet mechanically compatible interfaces, and synergistic mechanical responses that surpass the predictions of the ROM. The principal findings of this work are summarized as follows:

(1) The as-fabricated Ti-3.5Al/Ti-6Al-4V heterostructure exhibited a remarkable synergy of high strength and enhanced ductility, exceeding the performance of its homogeneous counterparts. Specifically, the heterostructure achieved a yield strength of approximately 1090 MPa and an ultimate tensile strength of approximately 1150 MPa, representing an improvement of roughly 10% over the homogeneous Ti-6Al-4V alloy (σ_y ~ 1037 MPa, σ_{UTS} ~ 1058 MPa), while also increasing the elongation to failure to ~10% compared to ~7.2%. In contrast to traditional "soft-hard" layered materials, which typically exhibit intermediate properties, this layered structure uniquely demonstrated concurrent improvements in both strength and ductility.

(2) The significant enhancement in yield strength originated from the deliberate exploitation of the CTE mismatch between Ti-3.5Al and Ti-6Al-4V under the rapid melting and solidification conditions inherent to additive manufacturing. This engineered thermomechanical mismatch induced pronounced interfacial residual stress fields, which generated localized strain gradients and drove the formation of dense, pre-existing GNDs concentrated at the interfaces. These interfacial GNDs serve as preconditioned barriers to dislocation motion, substantially elevating the initial flow resistance and yield strength of the as-built structure.

(3) Detailed microstructural and mechanical analyses established HDI hardening as

the dominant strengthening mechanism in the layered heterostructure. The elastic-plastic incompatibility across the soft/hard interfaces promotes substantial GND accumulation, generating long-range internal back stresses. Quantitative data from loading-unloading-reloading tests confirm that these interface-mediated back stresses contribute significantly to the elevated ultimate tensile strength and sustained strain-hardening capacity of the as-built sample. These findings identify HDI strengthening as a central factor in the superior mechanical performance of the as-built layered heterostructure.

(4) The soft Ti-3.5Al layers play a crucial role in enhancing ductility by effectively mitigating strain localization and arresting microcrack propagation initiated within the brittle Ti-6Al-4V regions. Fractographic analyses reveal that microcracks formed in the hard domain are blunted or deflected upon reaching the soft/hard interface. This demonstrates the dual role of the interface as both a barrier for stress redistribution and a zone for enhanced strain accommodation. The localized strain gradients across the interface, combined with its capacity to dissipate mechanical energy, contribute to a more tortuous and delayed crack propagation path. Consequently, this interface-mediated toughening mechanism significantly improves the overall fracture resistance of the layered heterostructure.

(5) The developed thermomechanically-driven interface engineering concept represents a substantial advancement beyond traditional compositional or microstructural optimization, demonstrating a new pathway for achieving superior combinations of strength and ductility. These insights hold promising implications not only for the development of high-performance, lightweight titanium components in aerospace and biomedical applications but also present a versatile and scalable strategy applicable to various alloy systems, where precise interfacial thermomechanical control can substantially enhance structural material performance.

In conclusion, this study provides a clear experimental validation of utilizing AM-induced thermomechanical mismatch as a strategic design approach to engineer tailored residual stress fields and strain gradients in titanium alloys. The developed thermomechanically-driven interface engineering concept offers substantial advancements beyond traditional compositional or microstructural optimization, demonstrating a new pathway for achieving superior combinations of strength and ductility. These insights hold promising implications not only for the development of high-performance, lightweight titanium components in aerospace and biomedical applications but also present a versatile and scalable strategy applicable to various alloy systems, where precise interfacial thermomechanical control can substantially enhance structural material performance.

Chapter 6 Overall Conclusions

In this thesis, a series of advanced titanium-based materials were designed and fabricated via AM, with the aim of achieving a superior combination of strength and ductility through elemental alloying and structural heterogeneity. Three core research objectives were pursued: (1) exploring the effect of aluminum addition on the microstructure and properties of α-Ti alloys fabricated via AM; (2) leveraging AM-induced composition modulation to create heterogeneous multi-gradient Ti/Ti-Al structures; and (3) engineering thermomechanical mismatches to induce interface-driven strengthening in layered heterostructures. The key conclusions drawn from each phase of the work are summarized below:

(1) AM of low-alloy α-Ti alloys enables simultaneous enhancement of strength and ductility: The comparative analysis between as-cast and AM-fabricated Ti-6Al alloys clearly demonstrates that the AM process significantly improves both strength and ductility. Specifically, AM Ti-6Al achieved nearly double the yield strength and elongation compared to its as-cast counterpart. This enhancement is attributed to the formation of fine basketweave microstructures during rapid solidification in AM, leading to higher dislocation density and stronger resistance to deformation. Moreover, the dislocation mechanisms in AM Ti-6Al transition from planar to wavy slip due to suppressed short-range order (SRO), promoting strain hardening and delaying failure. These findings underscore the capacity of AM to produce high-strength, high-ductility low-alloy α-Ti, expanding its potential for aerospace and biomedical applications.

(2) In-situ AM of heterogeneous multi-gradient Ti/Ti-10Al alloys achieves strength-ductility synergy: A novel strategy was developed to fabricate heterogeneous Ti/Ti-10Al alloys using dual powder hoppers in a LENS system, enabling layer-by-layer compositional modulation. The resulting multi-gradient architecture featured alternating soft and hard regions with graded Al concentrations and microstructures. This structure achieved a yield strength of ~760 MPa and elongation of ~33.4%,

significantly outperforming both homogeneous Ti and Ti-10Al alloys. These enhancements resulted from the solid solution gradient formation, which in turn resulted in a continuous gradient in grain morphology and local strength. This work demonstrates that AM can be utilized not only for geometric freedom but also for real-time chemical engineering of materials.

(3) Gradient stress partitioning and ductility compensation underpin the mechanical performance of multi-gradient heterostructures: Detailed deformation analysis of the Ti/Ti-10Al multi-gradient alloy revealed that its mechanical performance improvement originates from the interplay between gradient stress partitioning and ductility compensation. The inherent contrast in mechanical response between adjacent layers induces heterogeneous train distribution, facilitating enhanced strain hardening and delaying necking. The softer Al-deficient regions accommodate plastic deformation and prevent microcrack propagation within the harder Al-rich regions. This synergistic mechanism allows for simultaneous improvement in both strength and ductility, overcoming the classical trade-off. These findings provide a mechanistic basis for designing functionally graded materials via AM for damage-tolerant structural applications.

(4) Interface engineering via thermomechanical mismatch in layered Ti-3.5Al/Ti-6Al-4V heterostructures enables HDI strengthening: By exploiting the thermal expansion mismatch between Ti-3.5Al and Ti-6Al-4V under rapid thermal cycles in AM, a layered heterostructure was fabricated that achieved superior tensile strength (~1090 MPa) and ductility (~10%) compared to homogeneous counterparts. This performance enhancement I attributed to interface-driven hardening, whereby plastic incompatibility across the layers generates back-stress via pile-up of geometrically necessary dislocations (GNDs). Quantitative validation through load-unload-reload (LUR) testing confirmed substantial back-stress hardening contributions. Meanwhile, the softer Ti-3.5Al layers served as crack arresters, mitigating strain localization and enhancing fracture resistance. This study introduces a scalable AM-based strategy for

thermomechanical interface engineering, which may be generalized to other alloy systems seeking property synergies.

Chapter 7 Future Work

This thesis has explored a range of compelling topics and demonstrated the feasibility and effectiveness of AM in designing high-performance titanium alloys with heterogeneous microstructures. However, many intriguing scientific and engineering questions remain to be addressed. Building on the current findings, several promising directions for future research are outlined below:

7.1 Post-treatment effects on AM-fabricated heterostructures

Post-processing techniques such as cold rolling, annealing, or tailored heat treatments have long been used in conventional metallurgy to tailor microstructure and improve mechanical properties. These treatments can refine grains, redistribute solute elements, and relieve residual stress. However, how such treatments interact with AM-induced heterostructures, which often consist of layered chemical and microstructural gradients, is still poorly understood.

In future studies, systematic post-treatment techniques should be applied to AM-fabricated heterogeneous titanium alloys to investigate:

(1) Whether the heterogeneity can be retained or becomes homogenized;

(2) How residual stress profiles evolve post-treatment;

(3) Whether post-processing enhances or deteriorates the mechanical synergy improvement;

(4) Whether unique deformation mechanisms emerge under combined AM + post-treatment processing routes.

7.2 Real-time monitoring for microstructural control

AM offers a unique opportunity to control material structure in real-time by tuning processing parameters such as laser power, scan speed, and powder feed rate. However, the lack of real-time feedback and robust process simulations currently limits the ability to precisely predict or control heterostructure formations. Future research can be conducted on:

(1) Integrating real-time thermal monitoring tools (e.g., pyrometry, IR imaging) with closed-loop control systems;

(2) Developing multiphysics models to simulate thermal fields, solidification front evolution, and solute diffusion;

(3) Establishing predictive modes for grain orientation, residual stress, and phase transformation under realistic AM conditions;

(4) Using these insights to guide structure-by-design manufacturing with locally tunable properties.

7.3 Comparison between AM and conventional heterostructures

Heterostructured materials have traditionally been produced via post-deformation methods, such as accumulative roll bonding, gradient rolling, or friction stir processing. These processes introduce grain size gradients, strain gradients, or compositional interfaces, yet they differ significantly from the AM-induced heterostructures, which often include thermal gradients, compositional layering, and melt-solidification interfaces. Future studies can be conducted on the comparison between the AM-induced and conventional fabricated heterostructures:

(1) The types of interfaces formed via AM and conventional methods;

(2) The evolution of dislocation structures, GNDs and back stress generation mechanisms;

(3) The effectiveness of each method in promoting strain hardening, damage tolerance, and interface strengthening;

(4) The scalability and geometry limitations of each manufacturing method.

Reference

[1] C. Leyens, M. Peters, Titanium and titanium alloys: fundamentals and applications, Wiley Online Library2006.

[2] C. Veiga, J.P. Davim, A. Loureiro, Properties and applications of titanium alloys: a brief review, Rev. Adv. Mater. Sci 32(2) (2012) 133-148.

[3] L. Thomas, M. Ramachandra, Advanced materials for wind turbine blade-A Review, Materials Today: Proceedings 5(1) (2018) 2635-2640.

[4] D. Gospodinov, N. Ferdinandov, S. Dimitrov, Classification, properties and application of titanium and its alloys, Proceedings of university of ruse 55(2) (2016) 27-32.

[5] P. Yadav, K.K. Saxena, Effect of heat-treatment on microstructure and mechanical properties of Ti alloys: An overview, Materials Today: Proceedings 26 (2020) 2546-2557.

[6] L. Yang-huan-zi, G. Ji, S. Min, Phase transformation in titanium alloys: A review, Transactions of Nonferrous Metals Society of China 34(10) (2024) 3093-3117.

[7] S. Semiatin, An overview of the thermomechanical processing of α/β titanium alloys: current status and future research opportunities, Metallurgical and Materials Transactions A 51(6) (2020) 2593-2625.

[8] D.M. Stefanescu, R. Ruxanda, Solidification structures of titanium alloys, Metallography and Microstructures, ASM International2004, pp. 116-126.

[9] X. Dan, C. Ren, D. Zhang, X. Chen, Q. Liu, H. Shi, K. Chan, N. Song, D. Xiang, H. Sun, Enhanced Strength and Ductility in α-Titanium Alloys through in-situ Alloying via Additive Manufacturing, J. Alloys Compd. (2025) 180598.

[10] S. Huang, J. Zhang, Y. Ma, S. Zhang, S.S. Youssef, M. Qi, H. Wang, J. Qiu, D. Xu, J. Lei, Influence of thermal treatment on element partitioning in α+ β titanium alloy, J. Alloys Compd. 791 (2019) 575-585.

[11] Y. Liu, H. Wang, S. Li, S. Wang, W. Wang, W. Hou, Y. Hao, R. Yang, L. Zhang, Compressive and fatigue behavior of beta-type titanium porous structures fabricated by electron beam melting, Acta Materialia 126 (2017) 58-66.

[12] J. Peters, G. Lütjering, Comparison of the fatigue and fracture of α+ β and β titanium alloys, Metallurgical and materials transactions A 32 (2001) 2805-2818.

[13] P. Pushp, S. Dasharath, C. Arati, Classification and applications of titanium and its alloys, Materials Today: Proceedings 54 (2022) 537-542.

[14] G. Welsch, R. Boyer, E. Collings, Materials properties handbook: titanium alloys, ASM international1993.

[15] D. Banerjee, J. Williams, Perspectives on titanium science and technology, Acta

Mater. 61(3) (2013) 844-879.

[16] J.W. Foltz, B. Welk, P.C. Collins, H.L. Fraser, J.C. Williams, Formation of grain boundary α in β Ti alloys: its role in deformation and fracture behavior of these alloys, Metallurgical and Materials Transactions A 42(3) (2011) 645-650.

[17] H. Li, Z. Zhao, Y. Ning, H. Guo, Z. Yao, Characterization of microstructural evolution for a near-α titanium alloy with different initial lamellar microstructures, Metals 8(12) (2018) 1045.

[18] K. Chan, C. Wojcik, D. Koss, Deformation of an alloy with a lamellar microstructure: experimental behavior of individual widmanstatten colonies of an α-β titanium alloy, Metallurgical Transactions A 12(11) (1981) 1899-1907.

[19] K. Maruyama, N. Yamada, H. Sato, Effects of lamellar spacing on mechanical properties of fully lamellar Ti–39.4 mol% Al alloy, Mater. Sci. Eng. A. 319 (2001) 360-363.

[20] Y. Chong, T. Bhattacharjee, N. Tsuji, Bi-lamellar microstructure in Ti–6Al–4V: Microstructure evolution and mechanical properties, Mater. Sci. Eng. A. 762 (2019) 138077.

[21] J. Bai, H. Zhang, Z. Zhao, R. Yang, S. Zhang, T. Chen, X. Zhang, S. Liang, R. Liu, Strong and plastic near-α titanium alloy by Widmanstätten structure spheroidization, Journal of Materials Science & Technology 225 (2025) 95-110.

[22] T. Parthasarathy, M. Keller, M. Mendiratta, The effect of lamellar lath spacing on the creep behavior of Ti-47at% Al, Scripta Materialia 38(7) (1998) 1025-1031.

[23] K. Maruyama, R. Yamamoto, H. Nakakuki, N. Fujitsuna, Effects of lamellar spacing, volume fraction and grain size on creep strength of fully lamellar TiAl alloys, Mater. Sci. Eng. A. 239 (1997) 419-428.

[24] X. Gao, W. Zeng, Y. Wang, Y. Long, S. Zhang, Q. Wang, Evolution of equiaxed alpha phase during heat treatment in a near alpha titanium alloy, Journal of Alloys and Compounds 725 (2017) 536-543.

[25] C. Yang, L. Liu, Q. Cheng, D. You, Y. Li, Equiaxed grained structure: A structure in titanium alloys with higher compressive mechanical properties, Mater. Sci. Eng. A. 580 (2013) 397-405.

[26] M. Zang, H. Niu, J. Yu, H. Zhang, T. Zhang, D. Zhang, Cryogenic tensile properties and deformation behavior of a fine-grained near alpha titanium alloy with an equiaxed microstructure, Mater. Sci. Eng. A. 840 (2022) 142952.

[27] J.H. Kim, S. Semiatin, C.S. Lee, High-temperature deformation and grain-boundary characteristics of titanium alloys with an equiaxed microstructure, Mater. Sci. Eng. A. 485(1-2) (2008) 601-612.

[28] S. Semiatin, F. Montheillet, G. Shen, J. Jonas, Self-consistent modeling of the flow behavior of wrought alpha/beta titanium alloys under isothermal and nonisothermal

hot-working conditions, Metallurgical and Materials Transactions A 33(8) (2002) 2719-2727.

[29] X. Gao, W. Zeng, S. Zhang, Q. Wang, A study of epitaxial growth behaviors of equiaxed alpha phase at different cooling rates in near alpha titanium alloy, Acta Mater. 122 (2017) 298-309.

[30] S.K. Vajpai, M. Ota, T. Watanabe, R. Maeda, T. Sekiguchi, T. Kusaka, K. Ameyama, The development of high performance Ti-6Al-4V alloy via a unique microstructural design with bimodal grain size distribution, Metallurgical and Materials Transactions A 46(2) (2015) 903-914.

[31] V. Moiseev, E. Polyak, A.Y. Sokolova, Martensite strengthening of titanium alloys, Metal Science and Heat Treatment 17(8) (1975) 687-691.

[32] T. Inamura, J. Kim, H. Kim, H. Hosoda, K. Wakashima, S. Miyazaki, Composition dependent crystallography of α ″-martensite in Ti–Nb-based β-titanium alloy, Philosophical Magazine 87(23) (2007) 3325-3350.

[33] J. Yang, H. Yu, J. Yin, M. Gao, Z. Wang, X. Zeng, Formation and control of martensite in Ti-6Al-4V alloy produced by selective laser melting, Materials & Design 108 (2016) 308-318.

[34] Y.L. Zhou, M. Niinomi, T. Akahori, Decomposition of martensite α ″during aging treatments and resulting mechanical properties of Ti− Ta alloys, Mater. Sci. Eng. A. 384(1-2) (2004) 92-101.

[35] F. Bridier, P. Villechaise, J. Mendez, Slip and fatigue crack formation processes in an α/β titanium alloy in relation to crystallographic texture on different scales, Acta Mater. 56(15) (2008) 3951-3962.

[36] A. Ismaeel, D. Xu, X. Li, J. Zhang, R. Yang, Effect of texture on the mechanical and micromechanical properties of a dual-phase titanium alloy, Journal of Materials Research and Technology 27 (2023) 6833-6846.

[37] W.E. Frazier, Metal additive manufacturing: a review, Journal of Materials Engineering and performance 23 (2014) 1917-1928.

[38] T. DebRoy, H.L. Wei, J.S. Zuback, T. Mukherjee, J.W. Elmer, J.O. Milewski, A.M. Beese, A.d. Wilson-Heid, A. De, W. Zhang, Additive manufacturing of metallic components–process, structure and properties, Progress in materials science 92 (2018) 112-224.

[39] F. Froes, B. Dutta, The additive manufacturing (AM) of titanium alloys, Advanced Materials Research 1019 (2014) 19-25.

[40] D. Herzog, V. Seyda, E. Wycisk, C. Emmelmann, Additive manufacturing of metals, Acta Materialia 117 (2016) 371-392.

[41] D. Gu, Q. Shi, K. Lin, L. Xi, Microstructure and performance evolution and underlying thermal mechanisms of Ni-based parts fabricated by selective laser melting,

Additive Manufacturing 22 (2018) 265-278.

[42] J.C. Najmon, S. Raeisi, A. Tovar, Review of additive manufacturing technologies and applications in the aerospace industry, Additive manufacturing for the aerospace industry (2019) 7-31.

[43] M. Javaid, A. Haleem, Additive manufacturing applications in medical cases: A literature based review, Alexandria Journal of Medicine 54(4) (2018) 411-422.

[44] M. Gill, E. Terry, Y. Abdi, S. Hawkes, J. Rindler, D. Schick, A. Ramirez, E.D. Herderick, Joining technologies for metal additive manufacturing in the energy industry, Jom 72 (2020) 4214-4220.

[45] K. Ukoba, K.O. Yoro, A.E. Adeoye, J.D. Ampah, A.A. Yusuf, F.O. Samuel, O. Eterigho-Ikelegbe, T.-C. Jen, Additive manufacturing in the energy sector and the fourth industrial revolution, Progress in Additive Manufacturing (2025) 1-21.

[46] X. Li, X. Wang, M. Saunders, A. Suvorova, L. Zhang, Y. Liu, M. Fang, Z. Huang, T.B. Sercombe, A selective laser melting and solution heat treatment refined Al–12Si alloy with a controllable ultrafine eutectic microstructure and 25% tensile ductility, Acta Materialia 95 (2015) 74-82.

[47] L.E. Murr, S.M. Gaytan, D.A. Ramirez, E. Martinez, J. Hernandez, K.N. Amato, P.W. Shindo, F.R. Medina, R.B. Wicker, Metal fabrication by additive manufacturing using laser and electron beam melting technologies, Journal of Materials Science & Technology 28(1) (2012) 1-14.

[48] M. Galati, L. Iuliano, A literature review of powder-based electron beam melting focusing on numerical simulations, Additive Manufacturing 19 (2018) 1-20.

[49] S.M. Thompson, L. Bian, N. Shamsaei, A. Yadollahi, An overview of Direct Laser Deposition for additive manufacturing; Part I: Transport phenomena, modeling and diagnostics, Additive Manufacturing 8 (2015) 36-62.

[50] C. Qiu, G. Ravi, C. Dance, A. Ranson, S. Dilworth, M.M. Attallah, Fabrication of large Ti–6Al–4V structures by direct laser deposition, Journal of Alloys and Compounds 629 (2015) 351-361.

[51] A. Davis, C.I. Breheny, J. Fellowes, U. Nwankpa, F. Martina, J. Ding, T. Machry, P. Prangnell, Mechanical performance and microstructural characterisation of titanium alloy-alloy composites built by wire-arc additive manufacture, Materials Science and Engineering: A 765 (2019) 138289.

[52] H. Liu, H. Yu, C. Guo, X. Chen, S. Zhong, L. Zhou, A. Osman, J. Lu, Review on fatigue of additive manufactured metallic alloys: microstructure, performance, enhancement, and assessment methods, Advanced Materials 36(17) (2024) 2306570.

[53] K. Yamanaka, W. Saito, M. Mori, H. Matsumoto, A. Chiba, Preparation of weak-textured commercially pure titanium by electron beam melting, Additive Manufacturing 8 (2015) 105-109.

[54] S. Lu, M. Qian, H. Tang, M. Yan, J. Wang, D. StJohn, Massive transformation in Ti–6Al–4V additively manufactured by selective electron beam melting, Acta Materialia 104 (2016) 303-311.

[55] Q. Guo, C. Zhao, M. Qu, L. Xiong, L.I. Escano, S.M.H. Hojjatzadeh, N.D. Parab, K. Fezzaa, W. Everhart, T. Sun, In-situ characterization and quantification of melt pool variation under constant input energy density in laser powder bed fusion additive manufacturing process, Additive Manufacturing 28 (2019) 600-609.

[56] P.A. Hooper, Melt pool temperature and cooling rates in laser powder bed fusion, Additive Manufacturing 22 (2018) 548-559.

[57] W. Xu, M. Brandt, S. Sun, J. Elambasseril, Q. Liu, K. Latham, K. Xia, M. Qian, Additive manufacturing of strong and ductile Ti–6Al–4V by selective laser melting via in situ martensite decomposition, Acta Materialia 85 (2015) 74-84.

[58] M.L. Griffith, M.T. Ensz, J.D. Puskar, C.V. Robino, J.A. Brooks, J.A. Philliber, J.E. Smugeresky, W. Hofmeister, Understanding the microstructure and properties of components fabricated by laser engineered net shaping (LENS), MRS Online Proceedings Library (OPL) 625 (2000) 9.

[59] N. Shamsaei, A. Yadollahi, L. Bian, S.M. Thompson, An overview of Direct Laser Deposition for additive manufacturing; Part II: Mechanical behavior, process parameter optimization and control, Additive manufacturing 8 (2015) 12-35.

[60] Z. Liu, D. Zhao, P. Wang, M. Yan, C. Yang, Z. Chen, J. Lu, Z. Lu, Additive manufacturing of metals: Microstructure evolution and multistage control, Journal of Materials Science & Technology 100 (2022) 224-236.

[61] L. Emanuelli, A. Molinari, L. Facchini, E. Sbettega, S. Carmignato, M. Bandini, M. Benedetti, Effect of heat treatment temperature and turning residual stresses on the plain and notch fatigue strength of Ti-6Al-4V additively manufactured via laser powder bed fusion, International Journal of Fatigue 162 (2022) 107009.

[62] H. Wang, Q. Chao, H. Chen, Z. Chen, S. Primig, W. Xu, S. Ringer, X. Liao, Formation of a transition V-rich structure during the α'to α+ β phase transformation process in additively manufactured Ti-6Al-4 V, Acta Materialia 235 (2022) 118104.

[63] J. Damon, R. Koch, D. Kaiser, G. Graf, S. Dietrich, V. Schulze, Process development and impact of intrinsic heat treatment on the mechanical performance of selective laser melted AISI 4140, Additive Manufacturing 28 (2019) 275-284.

[64] M. Tang, P.C. Pistorius, J.L. Beuth, Prediction of lack-of-fusion porosity for powder bed fusion, Additive Manufacturing 14 (2017) 39-48.

[65] W. Chen, T. Voisin, Y. Zhang, J.-B. Forien, C.M. Spadaccini, D.L. McDowell, T. Zhu, Y.M. Wang, Microscale residual stresses in additively manufactured stainless steel, Nature communications 10(1) (2019) 4338.

[66] P. Ferro, R. Meneghello, G. Savio, F. Berto, A modified volumetric energy density–

based approach for porosity assessment in additive manufacturing process design, The International Journal of Advanced Manufacturing Technology 110 (2020) 1911-1921.

[67] C.-L. Li, J.W. Won, S.-W. Choi, J.-H. Choe, S. Lee, C.H. Park, J.-T. Yeom, J.K. Hong, Simultaneous achievement of equiaxed grain structure and weak texture in pure titanium via selective laser melting and subsequent heat treatment, Journal of Alloys and Compounds 803 (2019) 407-412.

[68] Y.M. Wang, T. Voisin, J.T. McKeown, J. Ye, N.P. Calta, Z. Li, Z. Zeng, Y. Zhang, W. Chen, T.T. Roehling, Additively manufactured hierarchical stainless steels with high strength and ductility, Nature materials 17(1) (2018) 63-71.

[69] M.J. Bermingham, S.D. McDonald, D.H. StJohn, M.S. Dargusch, Beryllium as a grain refiner in titanium alloys, Journal of Alloys and Compounds 481(1-2) (2009) L20-L23.

[70] H. Okamoto, Desk handbook: phase diagrams for binary alloys, ASM international2000.

[71] H. Okamoto, Al-Ti (aluminum-titanium), Journal of Phase Equilibria and Diffusion 21(3) (2000) 311.

[72] A. Roy, A.K. Singh, A. Arora, B. McWilliams, C. Mock, K. Cho, R.S. Mishra, Columnar-to-equiaxed transition in laser fusion additive manufacturing, Scripta Mater. 259 (2025) 116565.

[73] M. Yan, W. Xu, M. Dargusch, H. Tang, M. Brandt, M. Qian, Review of effect of oxygen on room temperature ductility of titanium and titanium alloys, Powder metallurgy 57(4) (2014) 251-257.

[74] J. Su, F. Jiang, J. Teng, L. Chen, M. Yan, G. Requena, L.-C. Zhang, Y.M. Wang, I.V. Okulov, H. Zhu, Recent innovations in laser additive manufacturing of titanium alloys, International Journal of Extreme Manufacturing 6(3) (2024) 032001.

[75] Y. Dong, J. Tang, D. Wang, N. Wang, Z. He, J. Li, D. Zhao, M. Yan, Additive manufacturing of pure Ti with superior mechanical performance, low cost, and biocompatibility for potential replacement of Ti-6Al-4V, Materials & Design 196 (2020) 109142.

[76] D. Wang, Y. Zhou, J. Shen, Y. Liu, D. Li, Q. Zhou, G. Sha, P. Xu, T. Ebel, M. Yan, Selective laser melting under the reactive atmosphere: a convenient and efficient approach to fabricate ultrahigh strength commercially pure titanium without sacrificing ductility, Materials Science and Engineering: A 762 (2019) 138078.

[77] H. Attar, M. Calin, L. Zhang, S. Scudino, J. Eckert, Manufacture by selective laser melting and mechanical behavior of commercially pure titanium, Materials Science and Engineering: A 593 (2014) 170-177.

[78] M. Seifi, A. Salem, D. Satko, J. Shaffer, J.J. Lewandowski, Defect distribution and microstructure heterogeneity effects on fracture resistance and fatigue behavior of EBM

Ti–6Al–4V, International Journal of Fatigue 94 (2017) 263-287.

[79] A. Khorasani, I. Gibson, U.S. Awan, A. Ghaderi, The effect of SLM process parameters on density, hardness, tensile strength and surface quality of Ti-6Al-4V, Additive manufacturing 25 (2019) 176-186.

[80] P. Kumar, O. Prakash, U. Ramamurty, Micro-and meso-structures and their influence on mechanical properties of selectively laser melted Ti-6Al-4V, Acta Materialia 154 (2018) 246-260.

[81] T.S. Tshephe, S.O. Akinwamide, E. Olevsky, P.A. Olubambi, Additive manufacturing of titanium-based alloys-A review of methods, properties, challenges, and prospects, Heliyon 8(3) (2022).

[82] W. Xu, S. Xiao, X. Lu, G. Chen, C. Liu, X. Qu, Fabrication of commercial pure Ti by selective laser melting using hydride-dehydride titanium powders treated by ball milling, Journal of Materials Science & Technology 35(2) (2019) 322-327.

[83] L.-C. Zhang, Y. Liu, Additive manufacturing of titanium alloys for biomedical applications, Additive Manufacturing of Emerging Materials, Springer2018, pp. 179-196.

[84] Y. Ma, D. Cuiuri, C. Shen, H. Li, Z. Pan, Effect of interpass temperature on in-situ alloying and additive manufacturing of titanium aluminides using gas tungsten arc welding, Additive Manufacturing 8 (2015) 71-77.

[85] D. Huang, Q. Tan, Y. Zhou, Y. Yin, F. Wang, T. Wu, X. Yang, Z. Fan, Y. Liu, J. Zhang, The significant impact of grain refiner on γ-TiAl intermetallic fabricated by laser-based additive manufacturing, Additive Manufacturing 46 (2021) 102172.

[86] Y. Zhu, X. Wu, Heterostructured materials, Progress in materials science 131 (2023) 101019.

[87] X. Dong, B. Gao, L. Xiao, J. Hu, M. Xu, Z. Li, J. Meng, X. Han, H. Zhou, Y. Zhu, Heterostructured metallic structural materials: research methods, properties, and future perspectives, Advanced Functional Materials 34(51) (2024) 2410521.

[88] L. Zhao, W. Zheng, Y. Hu, Q. Guo, D. Zhang, Heterostructured metal matrix composites for structural applications: a review, Journal of Materials Science 59(22) (2024) 9768-9801.

[89] Y. Zhu, X. Wu, Perspective on hetero-deformation induced (HDI) hardening and back stress, Materials Research Letters 7(10) (2019) 393-398.

[90] M. Yang, Y. Pan, F. Yuan, Y. Zhu, X. Wu, Back stress strengthening and strain hardening in gradient structure, Mater. Res. Lett. 4(3) (2016) 145-151.

[91] X. Wu, P. Jiang, L. Chen, F. Yuan, Y. Zhu, Extraordinary strain hardening by gradient structure, Heterostructured Materials, Jenny Stanford Publishing2021, pp. 53-71.

[92] Y. Zhu, K. Ameyama, P.M. Anderson, I.J. Beyerlein, H. Gao, H.S. Kim, E. Lavernia, S. Mathaudhu, H. Mughrabi, R.O. Ritchie, Heterostructured materials: superior properties from hetero-zone interaction, Mater. Res. Lett. 9(1) (2021) 1-31.

[93] L. Yan, Y. Chen, F. Liou, Additive manufacturing of functionally graded metallic materials using laser metal deposition, Additive Manufacturing 31 (2020) 100901.

[94] H. Chen, Y. He, S.S. Dash, Y. Zou, Additive manufacturing of metals and alloys to achieve heterogeneous microstructures for exceptional mechanical properties, Materials Research Letters 12(3) (2024) 149-171.

[95] L. Lu, X. Chen, X. Huang, K. Lu, Revealing the maximum strength in nanotwinned copper, Science 323(5914) (2009) 607-610.

[96] Z. Cheng, H. Zhou, Q. Lu, H. Gao, L. Lu, Extra strengthening and work hardening in gradient nanotwinned metals, Science 362(6414) (2018) eaau1925.

[97] S. Guan, D. Wan, K. Solberg, F. Berto, T. Welo, T. Yue, K. Chan, Additively manufactured CrMnFeCoNi/AlCoCrFeNiTi0. 5 laminated high-entropy alloy with enhanced strength-plasticity synergy, Scr. Mater. 183 (2020) 133-138.

[98] X. Wu, M. Yang, F. Yuan, G. Wu, Y. Wei, X. Huang, Y. Zhu, Heterogeneous lamella structure unites ultrafine-grain strength with coarse-grain ductility, Proceedings of the National Academy of Sciences 112(47) (2015) 14501-14505.

[99] C.-S. Wang, C.-L. Li, Y.-T. Zuo, J.-K. Hong, S.-W. Choi, G.-D. Zhang, Q. Mei, C.H. Park, J.-T. Yeom, Tailoring bimodal structure for high strength and ductility in pure titanium manufactured via laser powder bed fusion, J. Alloys Compd. 901 (2022) 163590.

[100] L. Liu, S. Li, D. Pan, D. Hui, X. Zhang, B. Li, T. Liang, P. Shi, A. Bahador, J. Umeda, Loss-free tensile ductility of dual-structure titanium composites via an interdiffusion and self-organization strategy, Proc. Natl. Acad. Sci. 120(28) (2023) e2302234120.

[101] J. Bach, M. Stoiber, L. Schindler, H. Höppel, M. Göken, Deformation mechanisms and strain rate sensitivity of bimodal and ultrafine-grained copper, Acta Mater. 186 (2020) 363-373.

[102] D. Li, G. Fan, X. Huang, D.J. Jensen, K. Miao, C. Xu, L. Geng, Y. Zhang, T. Yu, Enhanced strength in pure Ti via design of alternating coarse-and fine-grain layers, Acta Mater. 206 (2021) 116627.

[103] M. Huang, C. Xu, G. Fan, E. Maawad, W. Gan, L. Geng, F. Lin, G. Tang, H. Wu, Y. Du, Role of layered structure in ductility improvement of layered Ti-Al metal composite, Acta Mater. 153 (2018) 235-249.

[104] Z. Wang, X. Cui, L. Chen, Y. Zhang, H. Ding, Y. Zhang, N. Gao, G. Cong, Q. An, S. Wang, Achieving superior strength-ductility synergy in a unique multi-scale heterostructured titanium laminate fabricated by temperature-controlled rolling and

subsequent annealing, Mater. Sci. Eng. A. 891 (2024) 145926.

[105] Z. Chen, L. Yang, X. Ma, Q. Sun, F. Li, X. Fang, Tensile deformation behavior of a heterogeneous structural dual-phase metastable β titanium alloy, Metallurgical and Materials Transactions A 53(7) (2022) 2754-2767.

[106] B. Sharma, G. Dirras, K. Ameyama, Harmonic structure design: a strategy for outstanding mechanical properties in structural materials, Metals 10(12) (2020) 1615.

[107] W. Ji, R. Zhou, P. Vivegananthan, M.S. Wu, H. Gao, K. Zhou, Recent progress in gradient-structured metals and alloys, Progress in Materials Science 140 (2023) 101194.

[108] T. Fang, W. Li, N. Tao, K. Lu, Revealing extraordinary intrinsic tensile plasticity in gradient nano-grained copper, science 331(6024) (2011) 1587-1590.

[109] G. Li, J. Jiang, H. Ma, R. Zheng, S. Gao, S. Zhao, C. Ma, K. Ameyama, B. Ding, X. Li, Superior strength–ductility synergy in three-dimensional heterogeneous-nanostructured metals, Acta Mater. 256 (2023) 119143.

[110] X. Fang, G. He, C. Zheng, X. Ma, D. Kaoumi, Y. Li, Y. Zhu, Effect of heterostructure and hetero-deformation induced hardening on the strength and ductility of brass, Acta Mater. 186 (2020) 644-655.

[111] H. Xiao, S. Li, J. Li, Z. Xie, M. Peng, M. Li, Y. Zhao, L. Zhou, X. Du, A novel method for the preparation of heterostructures 5083 aluminum alloys to enhancing comprehensive mechanical properties, Materials Today Communications 41 (2024) 110926.

[112] J. Huang, Y.-n. Liu, T. Xu, X. Chen, Q. Lai, L. Xiao, Z. Pan, B. Gao, H. Zhou, Y. Zhu, Dual-phase hetero-structured strategy to improve ductility of a low carbon martensitic steel, Mater. Sci. Eng. A. 834 (2022) 142584.

[113] X. Zhang, R. Teng, T. Liu, Y. Shi, Z. Lv, Q. Zhou, X. Wang, Y. Wang, H. Liu, Z. Xing, Improving strength–ductility synergy in medium Mn steel by combining heterogeneous structure and TRIP effect, Mater. Charact. 184 (2022) 111661.

[114] A. Skowronek, E. Cordova-Tapia, P. Tobajas-Balsera, C. Garcia-Mateo, J.A. Jiménez, R. Petrov, A. Grajcar, Bainite plate thickness reduction and microstructure tailoring by double austempering of Al-rich 3Mn steel, Mater. Sci. Eng. A. 853 (2022) 143743.

[115] T. Wang, M. Zha, Y. Gao, S.-Q. Wang, H.-L. Jia, C. Wang, H.-Y. Wang, Deformation mechanisms in a novel multiscale hetero-structured Mg alloy with high strength-ductility synergy, Int. J. Plast. 170 (2023) 103766.

[116] P. Sharma, V. Dwivedi, S.P. Dwivedi, Development of high entropy alloys: A review, Materials Today: Proceedings 43 (2021) 502-509.

[117] M. Yang, D. Yan, F. Yuan, P. Jiang, E. Ma, X. Wu, Dynamically reinforced heterogeneous grain structure prolongs ductility in a medium-entropy alloy with gigapascal yield strength, Proc. Natl. Acad. Sci. 115(28) (2018) 7224-7229.

[118] D. Li, G. Fan, X. Huang, D.J. Jensen, K. Miao, C. Xu, L. Geng, Y. Zhang, T. Yu, Enhanced strength in pure Ti via design of alternating coarse-and fine-grain layers, Acta Materialia 206 (2021) 116627.

[119] Y. Zhao, M. Wang, Y. Lei, Y. Fan, A. Xue, X. Lin, Fabrication of heterostructured Ti alloys with exceptional strength and ductility by direct laser deposition, J. Mater. Res. Technol. 28 (2024) 1597-1610.

[120] S. Sunny, R. Mathews, G. Gleason, A. Malik, J. Halley, Effect of metal additive manufacturing residual stress on post-process machining-induced stress and distortion, Int. J. Mech. Sci. 202 (2021) 106534.

[121] S. Wang, J. Ning, L. Zhu, Z. Yang, W. Yan, Y. Dun, P. Xue, P. Xu, S. Bose, A. Bandyopadhyay, Role of porosity defects in metal 3D printing: Formation mechanisms, impacts on properties and mitigation strategies, Mater. Today 59 (2022) 133-160.

[122] Y. Zhang, X. Liu, Q. Zhu, Y. Zuo, C. Chen, H. Jiang, Improved Uniformity of As-Cast Structure, Composition, and Mechanical Properties of 2524 Aluminum Alloy by Intensive Melt Shearing, Journal of Materials Engineering and Performance (2024) 1-11.

[123] Q. Chen, B. Yuan, J. Lin, X. Xia, Z. Zhao, D. Shu, Comparisons of microstructure, thixoformability and mechanical properties of high performance wrought magnesium alloys reheated from the as-cast and extruded states, J. Alloys Compd. 584 (2014) 63-75.

[124] T. Song, Z. Chen, X. Cui, S. Lu, H. Chen, H. Wang, T. Dong, B. Qin, K.C. Chan, M. Brandt, Strong and ductile titanium–oxygen–iron alloys by additive manufacturing, Nature 618(7963) (2023) 63-68.

[125] P.-J. Arrazola, A. Garay, L.-M. Iriarte, M. Armendia, S. Marya, F. Le Maître, Machinability of titanium alloys (Ti6Al4V and Ti555. 3), Journal of materials processing technology 209(5) (2009) 2223-2230.

[126] Y. Chong, M. Poschmann, R. Zhang, S. Zhao, M.S. Hooshmand, E. Rothchild, D.L. Olmsted, J. Morris Jr, D.C. Chrzan, M. Asta, Mechanistic basis of oxygen sensitivity in titanium, Science advances 6(43) (2020) eabc4060.

[127] C. Han, Q. Fang, Y. Shi, S.B. Tor, C.K. Chua, K. Zhou, Recent advances on high-entropy alloys for 3D printing, Adv. Mater. 32(26) (2020) 1903855.

[128] K. Ma, H. Wen, T. Hu, T.D. Topping, D. Isheim, D.N. Seidman, E.J. Lavernia, J.M. Schoenung, Mechanical behavior and strengthening mechanisms in ultrafine grain precipitation-strengthened aluminum alloy, Acta Materialia 62 (2014) 141-155.

[129] C. Choi, H.J. Kim, Y.-T. Lee, Y.-W. Kim, C.S. Lee, Effects of microstructural parameters on the fatigue crack growth of fully lamellar γ-TiAl alloys, Materials Science and Engineering: A 329 (2002) 545-556.

[130] R. Imayev, V. Imayev, M. Oehring, F. Appel, Microstructural evolution during

hot working of Ti aluminide alloys: Influence of phase constitution and initial casting texture, Metallurgical and Materials Transactions A 36(3) (2005) 859-867.

[131] Y.-W. Kim, D.M. Dimiduk, Progress in the understanding of gamma titanium aluminides, Jom 43(8) (1991) 40-47.

[132] X. Dan, C. Ren, Z. Song, S. Waqar, D. Zhang, M. Wang, Q. Liu, Y. Sun, X. Chen, W. Jiang, Exceptional strength and ductility in heterogeneous multi-gradient TiAl alloys through additive manufacturing, Acta Mater. 281 (2024) 120395.

[133] S.S. Youssef, X. Zheng, M. Qi, Y. Ma, S. Huang, J. Qiu, S. Zheng, J. Lei, R. Yang, Effects of Al content and α2 precipitation on the fatigue crack growth behaviors of binary Ti–Al alloys, Mater. Sci. Eng. A. 819 (2021) 141513.

[134] Y. Chong, R. Zhang, M.S. Hooshmand, S. Zhao, D.C. Chrzan, M. Asta, J. Morris Jr, A.M. Minor, Elimination of oxygen sensitivity in α-titanium by substitutional alloying with Al, Nat. Commun. 12(1) (2021) 6158.

[135] W. Jiang, R. Li, J. He, S. Ni, L. Wang, Z. Chen, Y. Huang, C. Li, J. Yi, M. Song, Nitrogen-doping assisted local chemical heterogeneity and mechanical properties in CoCrMoW alloys manufactured via laser powder bed fusion, Adv. Powder Mater. 3(5) (2024) 100217.

[136] M. Molitch-Hou, Overview of additive manufacturing process, Additive manufacturing, Elsevier2018, pp. 1-38.

[137] Q. Liu, C. Ren, Z. Song, X. Dan, J. Ju, T. Yang, S. Ni, J. Lu, L. Liu, J. Pan, High-strength and high-conductivity additively manufactured Cu-O alloy enabled by cellular microstructure, Addit. Manuf. (2024) 104244.

[138] B. Dong, Z. Wang, H. Zhu, O. Muránsky, Z. Qiu, C. Shen, Z. Pan, H. Li, Low neutron cross-section FeCrVTiNi based high-entropy alloys: Design, additive manufacturing and characterization, (2022).

[139] Z. Liu, D. Zhao, P. Wang, M. Yan, C. Yang, Z. Chen, J. Lu, Z. Lu, Additive manufacturing of metals: Microstructure evolution and multistage control, J. Mater. Res. Technol. 100 (2022) 224-236.

[140] N.A. Zumdick, L. Jauer, L.C. Kersting, T.N. Kutz, J.H. Schleifenbaum, D. Zander, Additive manufactured WE43 magnesium: A comparative study of the microstructure and mechanical properties with those of powder extruded and as-cast WE43, Mater. Charact. 147 (2019) 384-397.

[141] M. Cabibbo, R. Montanari, A. Pola, M. Tocci, A. Varone, Mechanical spectroscopy study of as-cast and additive manufactured AlSi10Mg, J. Alloys Compd. 914 (2022) 165361.

[142] J.C. Pereira, E. Gil, L. Solaberrieta, M. San Sebastián, Y. Bilbao, P.P. Rodríguez, Comparison of AlSi7Mg0. 6 alloy obtained by selective laser melting and investment casting processes: Microstructure and mechanical properties in as-built/as-cast and

heat-treated conditions, Mater. Sci. Eng. A. 778 (2020) 139124.

[143] J. Zeng, Y. Yang, H. Peng, P. Wang, C. Liu, Z. Chen, W. Chen, X. Liu, Y. Wu, Z. Liu, Additive manufacturing of high entropy shape memory alloy with outstanding properties through multi-remelting in-situ alloying, Addit. Manuf. (2024) 104253.

[144] W. Zhang, X. Shang, S. Chen, L. Zhang, Comparison of microstructural characteristics and mechanical properties of the high-strength low-alloy steels fabricated by wire arc additive manufacturing versus conventional casting, Mater. Sci. Eng. A. 885 (2023) 145593.

[145] M. Avateffazeli, P. Carrion, B. Shachi-Amirkhiz, H. Pirgazi, M. Mohammadi, N. Shamsaei, M. Haghshenas, Correlation between tensile properties, microstructure, and processing routes of an Al–Cu–Mg–Ag–TiB2 (A205) alloy: Additive manufacturing and casting, Mater. Sci. Eng. A. 841 (2022) 142989.

[146] J. Kang, R. Li, M. Wang, D. Zheng, P. Niu, T. Yuan, Comparative analysis of microstructure and mechanical properties in FeMnAlNi alloys fabricated via casting and additive manufacturing, Mater. Sci. Eng. A. 915 (2024) 147216.

[147] A. Mitchell, A. Kawakami, S. Cockcroft, Segregation in titanium alloy ingots, High Temp. Mater. Process. 26(1) (2007) 59-78.

[148] A. Mitchell, Melting, casting and forging problems in titanium alloys, Mater. Sci. Eng. A. 243(1-2) (1998) 257-262.

[149] M.H. Mosallanejad, B. Niroumand, A. Aversa, A. Saboori, In-situ alloying in laser-based additive manufacturing processes: A critical review, J. Alloys Compd. 872 (2021) 159567.

[150] W. Zhai, W. Zhou, S.M.L. Nai, Grain refinement of 316L stainless steel through in-situ alloying with Ti in additive manufacturing, Mater. Sci. Eng. A. 840 (2022) 142912.

[151] R. Xi, H. Jiang, G. Li, S. Kustov, Z. Zhang, H. Wei, Z. Liu, G. Zhao, J. Van Humbeeck, X. Wang, In-situ alloying of NiTiNb ternary shape memory alloys via laser powder bed fusion using pre-alloyed NiTi and elemental Nb powders: microstructure, phase transformation behavior and functional properties, Addit. Manuf. 79 (2024) 103933.

[152] A. Fitzner, D.L. Prakash, J.Q. Da Fonseca, M. Thomas, S.-Y. Zhang, J. Kelleher, P. Manuel, M. Preuss, The effect of aluminium on twinning in binary alpha-titanium, Acta Mater. 103 (2016) 341-351.

[153] H. Yu, S. Cao, S.S. Youssef, Y.-J. Ma, J.-F. Lei, Y. Qi, Q.-M. Hu, R. Yang, Generalized stacking fault energies and critical resolved shear stresses of random α-Ti-Al alloys from first-principles calculations, J. Alloys Compd. 850 (2021) 156314.

[154] L. Bolzoni, S. Raynova, F. Yang, Strengthening mechanisms of Ti via Al addition, J. Alloys Compd. 820 (2020) 153447.

[155] I. Ohnuma, Y. Fujita, H. Mitsui, K. Ishikawa, R. Kainuma, K. Ishida, Phase equilibria in the Ti–Al binary system, Acta Mater. 48(12) (2000) 3113-3123.

[156] B. Rajesh Kumar, B. Hymavathi, X-ray peak profile analysis of solid-state sintered alumina doped zinc oxide ceramics by Williamson–Hall and size-strain plot methods, J ASIAN CERAM SOC. 5(2) (2017) 94-103.

[157] T. Ahmed, H. Rack, Phase transformations during cooling in α+ β titanium alloys, Mater. Sci. Eng. A. 243(1-2) (1998) 206-211.

[158] C. Ng, M. Bermingham, M. Dargusch, Controlling grain size, morphology and texture in additively manufactured β-titanium alloy with super transus hot isostatic pressing, Addit. Manuf. 59 (2022) 103176.

[159] S. Tedman-Jones, S. McDonald, M. Bermingham, D. StJohn, M. Dargusch, Investigating the morphological effects of solute on the β-phase in as-cast titanium alloys, J. Alloys Compd. 778 (2019) 204-214.

[160] J. Zhang, Y. Liu, M. Bayat, Q. Tan, Y. Yin, Z. Fan, S. Liu, J.H. Hattel, M. Dargusch, M.-X. Zhang, Achieving high ductility in a selectively laser melted commercial pure-titanium via in-situ grain refinement, Scr. Mater. 191 (2021) 155-160.

[161] G.-H. Zhao, X. Liang, B. Kim, P. Rivera-Díaz-del-Castillo, Modelling strengthening mechanisms in beta-type Ti alloys, Materials Science and Engineering: A 756 (2019) 156-160.

[162] C. Zhang, X. Bao, D. Zhang, W. Chen, J. Zhang, J. Kuang, G. Liu, J. Sun, Achieving superior strength-ductility balance in a novel heterostructured strong metastable β-Ti alloy, International Journal of Plasticity 147 (2021) 103126.

[163] K. Lu, J. Li, Y. Wang, X. Ma, Excellent strength-ductility synergy and corrosion resistance in a metastable high entropy alloy via heterogeneous structure design, Journal of Alloys and Compounds 941 (2023) 168979.

[164] D. Lesuer, C. Syn, O. Sherby, J. Wadsworth, J. Lewandowski, W. Hunt, Mechanical behaviour of laminated metal composites, Int. Mater. Rev. 41(5) (1996) 169-197.

[165] G.-H. Zhao, X. Xu, D. Dye, P.E. Rivera-Díaz-del-Castillo, Microstructural evolution and strain-hardening in TWIP Ti alloys, Acta Mater. 183 (2020) 155-164.

[166] A. Bahador, J. Umeda, R. Yamanoglu, A. Amrin, A. Alhazaa, K. Kondoh, Ultrafine-grain formation and improved mechanical properties of novel extruded Ti-Fe-W alloys with complete solid solution of tungsten, J. Alloys Compd. 875 (2021) 160031.

[167] Y. Lu, R. Kotoka, J. Ligda, B. Cao, S. Yarmolenko, B. Schuster, Q. Wei, The microstructure and mechanical behavior of Mg/Ti multilayers as a function of individual layer thickness, Acta Mater. 63 (2014) 216-231.

[168] P. Kwasniak, H. Garbacz, Screw dislocation mediated solution strengthening of

substitutional α-Ti alloys-First principles investigation, Acta Mater. 141 (2017) 405-418.

[169] S.S. Kumar, B. Pavithra, V. Singh, P. Ghosal, T. Raghu, Tensile anisotropy associated microstructural and microtextural evolution in a metastable beta titanium alloy, Mater. Sci. Eng. A. 747 (2019) 1-16.

[170] M. Calcagnotto, D. Ponge, E. Demir, D. Raabe, Orientation gradients and geometrically necessary dislocations in ultrafine grained dual-phase steels studied by 2D and 3D EBSD, Mater. Sci. Eng. A. 527(10-11) (2010) 2738-2746.

[171] Z. Yan, D. Wang, X. He, W. Wang, H. Zhang, P. Dong, C. Li, Y. Li, J. Zhou, Z. Liu, Deformation behaviors and cyclic strength assessment of AZ31B magnesium alloy based on steady ratcheting effect, Mater. Sci. Eng. A. 723 (2018) 212-220.

[172] C. Pande, K. Cooper, Nanomechanics of Hall–Petch relationship in nanocrystalline materials, Prog. Mater. Sci. 54(6) (2009) 689-706.

[173] T. Zhang, J. Zhu, T. Yang, J. Luan, H. Kong, W. Liu, B. Cao, S. Wu, D. Wang, Y. Wang, A new α+ β Ti-alloy with refined microstructures and enhanced mechanical properties in the as-cast state, Scr. Mater. 207 (2022) 114260.

[174] Y. Dong, Y. Li, S. Zhou, Y. Zhou, M. Dargusch, H. Peng, M. Yan, Cost-affordable Ti-6Al-4V for additive manufacturing: Powder modification, compositional modulation and laser in-situ alloying, Addit. Manuf. 37 (2021) 101699.

[175] F. Zhang, M. Yang, A.T. Clare, X. Lin, H. Tan, Y. Chen, Microstructure and mechanical properties of Ti-2Al alloyed with Mo formed in laser additive manufacture, J. Alloys Compd. 727 (2017) 821-831.

[176] Y. Liu, J. Ren, S. Guan, C. Li, Y. Zhang, S. Muskeri, Z. Liu, D. Yu, Y. Chen, K. An, Microstructure and mechanical behavior of additively manufactured CoCrFeMnNi high-entropy alloys: Laser directed energy deposition versus powder bed fusion, Acta Materialia 250 (2023) 118884.

[177] R. Zhang, S. Zhao, C. Ophus, Y. Deng, S.J. Vachhani, B. Ozdol, R. Traylor, K. Bustillo, J. Morris Jr, D.C. Chrzan, Direct imaging of short-range order and its relationship to deformation in Ti-6Al, Sci. Adv 5.

[178] D.C. Pagan, P.A. Shade, N.R. Barton, J.-S. Park, P. Kenesei, D.B. Menasche, J.V. Bernier, Modeling slip system strength evolution in Ti-7Al informed by in-situ grain stress measurements, Acta Mater. 128 (2017) 406-417.

[179] P. Kwasniak, S. Delannoy, F. Prima, E. Clouet, Competition between prismatic and basal slip in hexagonal titanium–aluminum alloys with short-range order, Materials Research Letters 11(6) (2023) 407-413.

[180] T. Neeraj, M. Mills, Short-range order (SRO) and its effect on the primary creep behavior of a Ti–6wt.% Al alloy, Mater. Sci. Eng. A. 319 (2001) 415-419.

[181] H. Weng, Q. Wang, Y. Ma, D. Xu, S. Huang, M. Qi, J. Qiu, J. Lei, R. Yang, Effect

of Al content on the fracture toughness and deformation behavior of Ti-Al binary alloys, Mater. Sci. Eng. A. 911 (2024) 146914.

[182] D. Truax, C. McMahon Jr, Plastic behavior of titanium-aluminum alloys, Materials Science and Engineering 13(2) (1974) 125-139.

[183] N. Takata, M. Liu, H. Kodaira, A. Suzuki, M. Kobashi, Anomalous strengthening by supersaturated solid solutions of selectively laser melted Al–Si-based alloys, Addit. Manuf. 33 (2020) 101152.

[184] J. Yaokawa, K. Oh-ishi, S. Dong, M. Hara, T. Masutani, H. Sato, Dimensional changes induced by precipitation of supersaturated solid solution Si in selectively laser-melted AlSi10Mg alloy during heat treatment, Mater. Charact. 182 (2021) 111533.

[185] J. Williams, A. Sommer, P. Tung, The influence of oxygen concentration on the internal stress and dislocation arrangements in α titanium, Metall. Mater. Trans. B 3 (1972) 2979-2984.

[186] X.-Q. Wang, W.-Z. Han, Oxygen-gradient titanium with high strength, strain hardening and toughness, Acta Materialia 246 (2023) 118674.

[187] J. Chen, Y. Han, Z. Wei, S. Li, Z. Sun, L. Zhang, G. Huang, J. Le, D. Zhang, W. Lu, Heterostructured titanium composites with superior strength-ductility synergy via controllable bimodal grains and< c+ a> dislocation activity, Materials Research Letters 11(10) (2023) 863-871.

[188] Y. Dong, D. Wang, Q. Li, X. Luo, J. Zhang, K.G. Prashanth, P. Wang, J. Eckert, L. Mädler, I.V. Okulov, Strong and ductile titanium via additive manufacturing under a reactive atmosphere, Mater Today Adv. 17 (2023) 100347.

[189] H. Wang, Q. Zhao, S. Xin, Y. Zhao, W. Zhou, W. Zeng, Microstructural morphology effects on fracture toughness and crack growth behaviors in a high strength titanium alloy, Mater. Sci. Eng. A. 821 (2021) 141626.

[190] J. Wang, Y. Zhao, W. Zhou, Q. Zhao, S. Huang, W. Zeng, In-situ investigation on tensile deformation and fracture behaviors of a new metastable β titanium alloy, Materials Science and Engineering: A 799 (2021) 140187.

[191] Q. Song, C. Sun, Mechanism of crack initiation and early growth of high strength steels in very high cycle fatigue regime, Mater. Sci. Eng. A. 771 (2020) 138648.

[192] D. Zhang, J. Zhang, J. Kuang, G. Liu, J. Sun, The B2 phase-driven microstructural heterogeneities and twinning enable ultrahigh cryogenic strength and large ductility in NiCoCr-based medium-entropy alloy, Acta Mater. 233 (2022) 117981.

[193] H. Yang, H. Li, H. Sun, Y. Zhang, X. Liu, M. Zhan, Y. Liu, M. Fu, Anisotropic plasticity and fracture of alpha titanium sheets from cryogenic to warm temperatures, Int. J. Plast. 156 (2022) 103348.

[194] Y. Wu, X. Zhao, Q. Chen, C. Yang, M. Jiang, C. Liu, Z. Jia, Z. Chen, T. Yang, Z. Liu, Strengthening and fracture mechanisms of a precipitation hardening high-entropy

alloy fabricated by selective laser melting, Virtual Phys. Prototyp. 17(3) (2022) 451-467.

[195] Z. Li, K.G. Pradeep, Y. Deng, D. Raabe, C.C. Tasan, Metastable high-entropy dual-phase alloys overcome the strength-ductility trade-off, Nature 534 (7606) (2016) 227-230.

[196] R.O. Ritchie, The conflicts between strength and toughness, Nat. Mater. 10 (11) (2011) 817-822.

[197] T. Song, Z. Chen, X. Cui, S. Lu, H. Chen, H. Wang, T. Dong, B. Qin, K.C. Chan, M. Brandt, Strong and ductile titanium-oxygen-iron alloys by additive manufacturing, Nature 618 (7963) (2023) 63-68.

[198] H. Attar, M. Calin, L. Zhang, S. Scudino, J. Eckert, Manufacture by selective laser melting and mechanical behavior of commercially pure titanium, Mater. Sci. Eng. A 593 (2014) 170-177.

[199] G. Zhang, X. Chen, Y. Cai, L. Lu, Y. Xin, D. Jia, Y. Tian, J. Han, Microstructure and mechanical properties of Ti-3Al-2V alloy by dual wire + arc additive manufacturing, Mater. Lett. 299 (2021) 130109.

[200] Y. Wang, C. Huang, Q. He, F. Guo, M. Wang, L. Song, Y. Zhu, Heterostructure induced dispersive shear bands in heterostructured Cu, Scr. Mater. 170 (2019) 76-80.

[201] L. Lu, X. Chen, X. Huang, K. Lu, Revealing the maximum strength in nanotwinned copper, Science 323 (5914) (2009) 607-610.

[202] X. Wu, M. Yang, F. Yuan, G. Wu, Y. Wei, X. Huang, Y. Zhu, Heterogeneous lamella structure unites ultrafine-grain strength with coarse-grain ductility, Proc. Natl. Acad. Sci. U. S. A. 112 (47) (2015) 14501-14505.

[203] H. Wang, Q. Chao, X. Cui, Z. Chen, A. Breen, M. Cabral, N. Haghdadi, Q. Huang, R. Niu, H. Chen, Introducing C phase in additively manufactured Ti-6Al-4V: A new oxygen-stabilized face-centred cubic solid solution with improved mechanical properties, Mater. Today 61 (2022) 11-21.

[204] B. Lim, H. Chen, Z. Chen, N. Haghdadi, X. Liao, S. Primig, S.S. Babu, A.J. Breen, S.P. Ringer, Microstructure-property gradients in Ni-based superalloy (Inconel 738) additively manufactured via electron beam powder bed fusion, Addit. Manuf. 46 (2021) 102121.

[205] H. Wang, Q. Chao, H. Chen, Z. Chen, S. Primig, W. Xu, S. Ringer, X. Liao, Formation of a transition V-rich structure during the α' to α+β phase transformation process in additively manufactured Ti-6Al-4V, Acta Mater. 235 (2022) 118104.

[206] Y. Zhang, A. Bandyopadhyay, Direct fabrication of bimetallic Ti6Al4V+Al12Si structures via additive manufacturing, Addit. Manuf. 29 (2019) 100783.

[207] J. Kennedy, A. Davis, A. Caballero, M. White, J. Fellowes, E. Pickering, P. Prangnell, Microstructure transition gradients in titanium dissimilar alloy (Ti-5Al-5V-

5Mo-3Cr/Ti-6Al-4V) tailored wire-arc additively manufactured components, Mater. Charact. 182 (2021) 111577.

[208] Y.-J. Liang, D. Liu, H.-M. Wang, Microstructure and mechanical behavior of commercial purity Ti/Ti-6Al-2Zr-1Mo-1V structurally graded material fabricated by laser additive manufacturing, Scr. Mater. 74 (2014) 80-83.

[209] S. Zhao, S. Li, S. Wang, W. Hou, Y. Li, L. Zhang, Y. Hao, R. Yang, R. Misra, L. Murr, Compressive and fatigue behavior of functionally graded Ti-6Al-4V meshes fabricated by electron beam melting, Acta Mater. 150 (2018) 1-15.

[210] R.W. Messler Jr, Principles of welding: processes, physics, chemistry, and metallurgy, John Wiley & Sons, 2008.

[211] D.C. Hofmann, S. Roberts, R. Otis, J. Kolodziejska, R.P. Dillon, J.-o. Suh, A.A. Shapiro, Z.-K. Liu, J.-P. Borgonia, Developing gradient metal alloys through radial deposition additive manufacturing, Sci. Rep. 4 (1) (2014) 5357.

[212] L.D. Bobbio, R.A. Otis, J.P. Borgonia, R.P. Dillon, A.A. Shapiro, Z.-K. Liu, A.M. Beese, Additive manufacturing of a functionally graded material from Ti-6Al-4V to Invar: Experimental characterization and thermodynamic calculations, Acta Mater. 127 (2017) 133-142.

[213] D. Huang, Y. Dong, H. Chen, Y. Zhou, M.-X. Zhang, M. Yan, Effects of processing parameters on a β-solidifying TiAl alloy fabricated by laser-based additive manufacturing, Microstructures 2 (4) (2022) 2022019.

[214] Y. Liu, Y. Zhang, Microstructure and mechanical properties of TA15-Ti2AlNb bimetallic structures by laser additive manufacturing, Mater. Sci. Eng. A 795 (2020) 140019.

[215] W. Meng, Y. Xiaohui, W. Zhang, F. Junfei, G. Lijie, M. Qunshuang, C. Bing, Additive manufacturing of a functionally graded material from Inconel625 to Ti6Al4V by laser synchronous preheating, J. Mater. Process. Technol. 275 (2020) 116368.

[216] S. Guan, D. Wan, K. Solberg, F. Berto, T. Welo, T. Yue, K. Chan, Additively manufactured CrMnFeCoNi/AlCoCrFeNiTi0.5 laminated high-entropy alloy with enhanced strength-plasticity synergy, Scr. Mater. 183 (2020) 133-138.

[217] C. Zhang, X. Bao, M. Hao, W. Chen, D. Zhang, D. Wang, J. Zhang, G. Liu, J. Sun, Hierarchical nano-martensite-engineered a low-cost ultra-strong and ductile titanium alloy, Nat. Commun. 13 (1) (2022) 5966.

[218] W. Jia, W. Zeng, H. Yu, Effect of aging on the tensile properties and microstructures of a near-alpha titanium alloy, Mater. Des. 58 (2014) 108-115.

[219] D. Zhang, D. Qiu, M.A. Gibson, Y. Zheng, H.L. Fraser, D.H. StJohn, M.A. Easton, Additive manufacturing of ultrafine-grained high-strength titanium alloys, Nature 576 (7785) (2019) 91-95.

[220] A. Barbas, A.S. Bonnet, P. Lipinski, R. Pesci, G. Dubois, Development and

mechanical characterization of porous titanium bone substitutes, J. Mech. Behav. Biomed. Mater. 9 (2012) 34-44.

[221] Y. Hou, B. Liu, Y. Liu, Y. Zhou, T. Song, Q. Zhou, G. Sha, M. Yan, Ultra-low cost Ti powder for selective laser melting additive manufacturing and superior mechanical properties associated, Opto-Electron. Adv. 2 (5) (2019) 180028.

[222] Q. Tao, Z. Wang, G. Chen, W. Cai, P. Cao, C. Zhang, W. Ding, X. Lu, T. Luo, X. Qu, Selective laser melting of CP-Ti to overcome the low cost and high performance trade-off, Addit. Manuf. 34 (2020) 101198.

[223] W. Xu, S. Xiao, X. Lu, G. Chen, C. Liu, X. Qu, Fabrication of commercial pure Ti by selective laser melting using hydride-dehydride titanium powders treated by ball milling, J. Mater. Sci. Technol. 35 (2) (2019) 322-327.

[224] D. Wang, Y. Zhou, J. Shen, Y. Liu, D. Li, Q. Zhou, G. Sha, P. Xu, T. Ebel, M. Yan, Selective laser melting under the reactive atmosphere: a convenient and efficient approach to fabricate ultrahigh strength commercially pure titanium without sacrificing ductility, Mater. Sci. Eng. A 762 (2019) 138078.

[225] S.S. Youssef, X. Zheng, M. Qi, Y. Ma, S. Huang, J. Qiu, S. Zheng, J. Lei, R. Yang, Effects of Al content and α2 precipitation on the fatigue crack growth behaviors of binary Ti-Al alloys, Mater. Sci. Eng. A 819 (2021) 141513.

[226] H. Attar, M. Bermingham, S. Ehtemam-Haghighi, A. Dehghan-Manshadi, D. Kent, M. Dargusch, Evaluation of the mechanical and wear properties of titanium produced by three different additive manufacturing methods for biomedical application, Mater. Sci. Eng. A 760 (2019) 339-345.

[227] K. Yamanaka, W. Saito, M. Mori, H. Matsumoto, A. Chiba, Preparation of weak-textured commercially pure titanium by electron beam melting, Addit. Manuf. 8 (2015) 105-109.

[228] Y. Zhu, X. Wu, Perspective on hetero-deformation induced (HDI) hardening and back stress, Mater. Res. Lett. 7(10) (2019) 393-398.

[229] A. Zafari, K. Xia, Grain refinement in a metastable beta Ti alloy deformed to large strains at high strain rates, Acta Mater. 157 (2018) 174-185.

[230] S. Wu, K. Fan, P. Jiang, S. Chen, Grain refinement of pure Ti during plastic deformation, Mater. Sci. Eng. A 527(26) (2010) 6917-6921.

[231] X. Zhang, S. Zhang, Q. Zhao, Y. Zhao, R. Li, W. Zeng, In-situ observations of the tensile deformation and fracture behavior of a fine-grained titanium alloy sheet, J. Alloys Compd. 740 (2018) 660-668.

[232] H. Wang, Q. Chao, L. Yang, M. Cabral, Z. Song, B. Wang, S. Primig, W. Xu, Z. Chen, S. Ringer, Introducing transformation twins in titanium alloys: an evolution of α-variants during additive manufacturing, Mater. Res. Lett. 9 (3) (2021) 119-126.

[233] Y. Dong, D. Wang, Q. Li, X. Luo, J. Zhang, K.G. Prashanth, P. Wang, J. Eckert,

L. Mädler, I.V. Okulov, Strong and ductile titanium via additive manufacturing under a reactive atmosphere, Mater. Today Adv. 17 (2023) 100347.

[234] Z. Zhao, J. Chen, H. Tan, G. Zhang, X. Lin, W. Huang, Achieving superior ductility for laser solid formed extra low interstitial Ti-6Al-4V titanium alloy through equiaxial alpha microstructure, Scr. Mater. 146 (2018) 187-191.

[235] Y. Liu, J. Ren, S. Guan, C. Li, Y. Zhang, S. Muskeri, Z. Liu, D. Yu, Y. Chen, K. An, Microstructure and mechanical behavior of additively manufactured CoCrFeMnNi high-entropy alloys: Laser directed energy deposition versus powder bed fusion, Acta Mater. 250 (2023) 118884.

[236] Y. Liu, J. Zhang, Q. Tan, Y. Yin, S. Liu, M. Li, M. Li, Q. Liu, Y. Zhou, T. Wu, Additive manufacturing of high strength copper alloy with heterogeneous grain structure through laser powder bed fusion, Acta Mater 220 (2021) 117311.

[237] G. Gibbs, D. Graham, D. Tomlin, Diffusion in titanium and titanium-niobium alloys, Phil. Mag. 8 (92) (1963) 1269-1282.

[238] Y. Mishin, C. Herzig, Diffusion in the Ti-Al system, Acta Mater 48 (3) (2000) 589-623.

[239] J. Song, Y. Chew, G. Bi, X. Yao, B. Zhang, J. Bai, S.K. Moon, Numerical and experimental study of laser aided additive manufacturing for melt-pool profile and grain orientation analysis, Mater. Des 137 (2018) 286-297.

[240] P. Manneville, Dissipative structures and weak turbulence, Chaos-The Interplay Between Stochastic and Deterministic Behaviour: Proceedings of the XXXIst Winter School of Theoretical Physics Held in Karpacz, Poland 13-24 February 1995, Springer 2005, pp. 257-272.

[241] C. Wei, H. Gu, Q. Li, Z. Sun, Y.-h. Chueh, Z. Liu, L. Li, Understanding of process and material behaviours in additive manufacturing of Invar36/Cu10Sn multiple material components via laser-based powder bed fusion, Addit. Manuf. 37 (2021) 101683.

[242] S. Shakerin, A. Hadadzadeh, B.S. Amirkhiz, S. Shamsdini, J. Li, M. Mohammadi, Additive manufacturing of maraging steel-H13 bimetals using laser powder bed fusion technique, Addit. Manuf. 29 (2019) 100797.

[243] T.-N. Le, Y.-L. Lo, Effects of sulfur concentration and Marangoni convection on melt-pool formation in transition mode of selective laser melting process, Mater. Des. 179 (2019) 107866.

[244] Y. Bai, J. Zhang, C. Zhao, C. Li, H. Wang, Dual interfacial characterization and property in multi-material selective laser melting of 316L stainless steel and C52400 copper alloy, Mater. Charact. 167 (2020) 110489.

[245] Y.-J. Liang, X.-J. Tian, Y.-Y. Zhu, J. Li, H.-M. Wang, Compositional variation and microstructural evolution in laser additive manufactured Ti/Ti–6Al–2Zr–1Mo–1V

graded structural material, Mater. Sci. Eng. A 599 (2014) 242-246.

[246] D. Bhattacharyya, G. Viswanathan, H.L. Fraser, Crystallographic and morphological relationships between β phase and the Widmanstätten and allotriomorphic α phase at special β grain boundaries in an α/β titanium alloy, Acta Mater. 55(20) (2007) 6765-6778.

[247] D.A. Porter, K.E. Easterling, Phase transformations in metals and alloys, Van Nostrand Reinhold Co Ltd., Wokingham, Berkshire, England, 1984.

[248] M. Bermingham, S. McDonald, M. Dargusch, D. StJohn, Grain-refinement mechanisms in titanium alloys, J. Mater. Res. 23 (1) (2008) 97-104.

[249] H. Yu, C. Li, Y. Xin, A. Chapuis, X. Huang, Q. Liu, The mechanism for the high dependence of the Hall-Petch slope for twinning/slip on texture in Mg alloys, Acta Mater. 128 (2017) 313-326.

[250] H. Conrad, Effect of interstitial solutes on the strength and ductility of titanium, Prog. Mater. Sci. 26 (2-4) (1981) 123-403.

[251] D.G. McCartney, Grain refining of aluminium and its alloys using inoculants, Int. Mater. Rev. 34 (1) (1989) 247-260.

[252] X. Wu, P. Jiang, L. Chen, J. Zhang, F. Yuan, Y. Zhu, Synergetic strengthening by gradient structure, Mater. Res. Lett. 2(4) (2014) 185-191.

[253] W. Su, M. Wang, F. Guo, H. Ran, Q. Cheng, Q. Wang, Y. Zhu, X. Ma, C. Huang, Heterostructure enables anomalous improvement of cryogenic mechanical properties in titanium, Acta Mater. 273 (2024) 119982.

[254] J. Fan, T. Fu, S. Ma, L. Fu, M. Wen, A. Shan, Study on the strain partitioning behavior in heterostructured complex-concentrated alloy via high-resolution digital image correlation, Mater. Sci. Eng. A. 908 (2024) 146809.

[255] Q. Han, A. Asgari, P.D. Hodgson, N. Stanford, Strain partitioning in dual-phase steels containing tempered martensite, Mater. Sci. Eng. A 611 (2014) 90-99.

[256] X. Wu, Y. Zhu, Heterogeneous materials: a new class of materials with unprecedented mechanical properties, Mater. Res. Lett. 5(8) (2017) 527-532.

[257] H.K. Park, K. Ameyama, J. Yoo, H. Hwang, H.S. Kim, Additional hardening in harmonic structured materials by strain partitioning and back stress, Mater. Res. Lett. 6(5) (2018) 261-267.

[258] Y.T. Zhu, X. Liao, Retaining ductility, Nat. Mater. 3(6) (2004) 351-352.

[259] F. Yuan, D. Yan, J. Sun, L. Zhou, Y. Zhu, X. Wu, Ductility by shear band delocalization in the nano-layer of gradient structure, Mater. Res. Lett. 7(1) (2019) 12-17.

[260] I. Ovid'Ko, R. Valiev, Y. Zhu, Review on superior strength and enhanced ductility of metallic nanomaterials, Prog. Mater. Sci. 94 (2018) 462-540.

[261] C. Shang, C. Wang, C. Li, G. Yang, G. Xu, J. You, Eliminating the crack of laser 3D printed functionally graded material from TA15 to Inconel718 by base preheating, Opt. Laser Technol. 126 (2020) 106100.

[262] X. Ji, S. Emura, X. Min, K. Tsuchiya, Strain-rate effect on work-hardening behavior in β-type Ti-10Mo-1Fe alloy with TWIP effect, Mater. Sci. Eng. A 707 (2017) 701-707.

[263] P. Shi, Y. Zhong, Y. Li, W. Ren, T. Zheng, Z. Shen, B. Yang, J. Peng, P. Hu, Y. Zhang, Multistage work hardening assisted by multi-type twinning in ultrafine-grained heterostructural eutectic high-entropy alloys, Mater. Today 41 (2020) 62-71.

[264] W. Xu, M. Brandt, S. Sun, J. Elambasseril, Q. Liu, K. Latham, K. Xia, M. Qian, Additive manufacturing of strong and ductile Ti-6Al-4V by selective laser melting via in situ martensite decomposition, Acta Mater. 85 (2015) 74-84.

[265] J.-X. Chen, T. Li, Y. Chen, F.-H. Cao, H.-Y. Wang, L.-H. Dai, Ultra-strong heavy-drawn eutectic high entropy alloy wire, Acta Mater. 243 (2023) 118515.

[266] K. Majchrowicz, Z. Pakieła, T. Brynk, B. Romelczyk-Baishya, M. Płocińska, T. Kurzynowski, E. Chlebus, Microstructure and mechanical properties of Ti-Re alloys manufactured by selective laser melting, Mater. Sci. Eng. A 765 (2019) 138290.

[267] Y. Wei, Y. Li, L. Zhu, Y. Liu, X. Lei, G. Wang, Y. Wu, Z. Mi, J. Liu, H. Wang, H. Gao, Evading the strength-ductility trade-off dilemma in steel through gradient hierarchical nanotwins, Nat. Commun. 5 (2014) 3580.

[268] L. Thomas, M. Ramachandra, Advanced materials for wind turbine blade-A Review, Mater. Today: Proc. 5(1) (2018) 2635-2640.

[269] D. Zhang, D. Qiu, M.A. Gibson, Y. Zheng, H.L. Fraser, D.H. StJohn, M.A. Easton, Additive manufacturing of ultrafine-grained high-strength titanium alloys, Nature 576(7785) (2019) 91-95.

[270] C. Zhang, X. Bao, M. Hao, W. Chen, D. Zhang, D. Wang, J. Zhang, G. Liu, J. Sun, Hierarchical nano-martensite-engineered a low-cost ultra-strong and ductile titanium alloy, Nat. Commun. 13(1) (2022) 5966.

[271] F. Hao, X. Liu, Y. Du, Y. Mao, H. Chen, S. Li, K. Wang, L. Lei, Excellent dynamic mechanical properties of a newly developed titanium alloy with bimodal structure, J. Alloys Compd. 961 (2023) 170980.

[272] H. Qu, P. Li, S. Zhang, A. Li, H. Wang, Microstructure and mechanical property of laser melting deposition (LMD) Ti/TiAl structural gradient material, Materials & Design 31(1) (2010) 574-582.

[273] X. Li, B.-H. Sun, B. Guan, Y.-F. Jia, C.-Y. Gong, X.-C. Zhang, S.-T. Tu, Elucidating the effect of gradient structure on strengthening mechanisms and fatigue behavior of pure titanium, Int. J. Fatigue 146 (2021) 106142.

[274] G. Dirras, D. Ueda, A. Hocini, D. Tingaud, K. Ameyama, Cyclic shear behavior

of conventional and harmonic structure-designed Ti-25Nb-25Zr β-titanium alloy: Back-stress hardening and twinning inhibition, Scr. Mater. 138 (2017) 44-47.

[275] X. Wang, J. Li, F. Cazes, A. Hocini, G. Dirras, Numerical modeling on strengthening mechanisms of the harmonic structured design on CP-Ti and Ti–6Al–4V, Int. J. Plast. 133 (2020) 102793.

[276] F. Liang, Z.-X. Wang, M.-Y. Li, B. Zhang, X.-M. Luo, X.-F. Zhu, G.-P. Zhang, Exceptional ductility through interface-constrained grain growth for the ultrafine-scale Ni/Ni-W layered composites, Int. J. Plast. 176 (2024) 103959.

[277] X. Lu, Y. Xu, H. Ran, G. Fan, S. Gao, N. Tsuji, C. Huang, H. Gao, Y.-W. Zhang, The role of layer strength ratio in enhancing strain hardening and achieving strength-ductility synergy in heterostructured materials, Acta Mater. 289 (2025) 120928.

[278] C. Huang, Y. Wang, X. Ma, S. Yin, H. Höppel, M. Göken, X. Wu, H. Gao, Y. Zhu, Interface affected zone for optimal strength and ductility in heterogeneous laminate, Mater. Today 21(7) (2018) 713-719.

[279] M. Huang, G. Fan, L. Geng, G. Cao, Y. Du, H. Wu, T. Zhang, H. Kang, T. Wang, G. Du, Revealing extraordinary tensile plasticity in layered Ti-Al metal composite, Sci. Rep. 6(1) (2016) 38461.

[280] Y. Zhang, A. Bandyopadhyay, Direct fabrication of bimetallic Ti6Al4V+ Al12Si structures via additive manufacturing, Addit. Manuf. 29 (2019) 100783.

[281] A. Chen, D. Li, J. Zhang, F. Liu, X. Liu, J. Lu, Study of toughening mechanisms through the observations of crack propagation in nanostructured and layered metallic sheet, Mater. Sci. Eng. A. 528(29-30) (2011) 8389-8395.

[282] X. Zhao, Y. Lv, S. Dong, S. Yan, P. He, X. Liu, Y. Liu, T. Lin, B. Xu, The effect of thermal cycling on direct laser-deposited gradient H13 tool steel: Microstructure evolution, nanoprecipitation behaviour, and mechanical properties, Mater. Today Commun. 25 (2020) 101390.

[283] B. Guo, D. Cui, Q. Wu, Y. Ma, D. Wei, K. LS R, Y. Zhang, C. Xu, Z. Wang, J. Li, Segregation-dislocation self-organized structures ductilize a work-hardened medium entropy alloy, Nat. Commun. 16(1) (2025) 1475.

[284] E. Mirkoohi, J.R. Dobbs, S.Y. Liang, Analytical mechanics modeling of in-process thermal stress distribution in metal additive manufacturing, J. Manuf. Process. 58 (2020) 41-54.

[285] W. Miller, F. Humphreys, Strengthening mechanisms in particulate metal matrix composites, Scripta metallurgica et materialia 25(1) (1991) 33-38.

[286] N. Fleck, M. Ashby, J. Hutchinson, The role of geometrically necessary dislocations in giving material strengthening, Scr. Mater. 48(2) (2003) 179-183.

[287] F. Bonollo, R. Guerriero, E. Sentimenti, I. Tangerini, W. Yang, The effect of quenching on the mechanical properties of powder metallurgically produced Al SiC

(particles) metal matrix composites, Mater. Sci. Eng. A. 144(1-2) (1991) 303-309.

[288] M. Taya, K. Lulay, D. Lloyd, Strengthening of a particulate metal matrix composite by quenching, Acta Metallurgica et Materialia 39(1) (1991) 73-87.

[289] S. Ho, A. Saigal, Three-dimensional modelling of thermal residual stresses and mechanical behavior of cast SiC/A1 particulate composites, Acta metallurgica et materialia 42(10) (1994) 3253-3262.

[290] H. Rafi, N. Karthik, H. Gong, T.L. Starr, B.E. Stucker, Microstructures and mechanical properties of Ti6Al4V parts fabricated by selective laser melting and electron beam melting, Journal of materials engineering and performance 22 (2013) 3872-3883.

[291] G. Lindwall, K.-W. Moon, Z. Chen, M. Mengason, M.E. Williams, J.M. Gorham, J.-C. Zhao, C.E. Campbell, Diffusion in the Ti-Al-V system, Journal of Phase Equilibria and Diffusion 39(5) (2018) 731-746.

[292] P.A. Kobryn, S. Semiatin, Microstructure and texture evolution during solidification processing of Ti–6Al–4V, J. Mater. Process. Technol. 135(2-3) (2003) 330-339.

[293] C. Cao, P. Liu, Y. Zou, F. Liao, H. Luo, J. Zhang, Z. Zhao, W. Xiang, W. Yin, Y. Xiao, Microstructure and mechanical properties of additively manufactured Ti–6Al–4V alloy based on large area, high-resolution EBSD mapping, J. Mater. Process. Technol. 33 (2024) 2812-2830.

[294] Y. Xu, E. Liu, S. Wei, Investigation on tensile fracture properties of TA15 specimen formed by selective electron beam melting, Mater. Sci. Eng. A. 773 (2020) 138826.

[295] P.J. Noell, R.B. Sills, A.A. Benzerga, B.L. Boyce, Void nucleation during ductile rupture of metals: A review, Prog. Mater. Sci. 135 (2023) 101085.

[296] K. Majchrowicz, Z. Pakieła, T. Brynk, B. Romelczyk-Baishya, M. Płocińska, T. Kurzynowski, E. Chlebus, Microstructure and mechanical properties of Ti–Re alloys manufactured by selective laser melting, Mater. Sci. Eng. A. 765 (2019) 138290.

[297] B. He, J. Li, X. Cheng, H.-M. Wang, Brittle fracture behavior of a laser additive manufactured near-β titanium alloy after low temperature aging, Mater. Sci. Eng. A. 699 (2017) 229-238.

[298] C. Qiu, G. Ravi, C. Dance, A. Ranson, S. Dilworth, M.M. Attallah, Fabrication of large Ti–6Al–4V structures by direct laser deposition, J. Alloys Compd. 629 (2015) 351-361.

[299] X. Liang, Z. Liu, Q. Wang, B. Wang, X. Ren, Tool wear-induced microstructure evolution in localized deformation layer of machined Ti–6Al–4V, J. Mater. Sci. 55(8) (2020) 3636-3651.

[300] S.J. Lainé, K.M. Knowles, P.J. Doorbar, R.D. Cutts, D. Rugg, Microstructural

characterisation of metallic shot peened and laser shock peened Ti–6Al–4V, Acta Mater. 123 (2017) 350-361.

[301] X. Ma, C. Huang, J. Moering, M. Ruppert, H.W. Höppel, M. Göken, J. Narayan, Y. Zhu, Mechanical properties of copper/bronze laminates: Role of interfaces, Acta Mater. 116 (2016) 43-52.

[302] S. Gudur, V. Nagallapati, S. Pawar, G. Muvvala, S. Simhambhatla, A study on the effect of substrate heating and cooling on bead geometry in wire arc additive manufacturing and its correlation with cooling rate, Mater. Today Proc. 41 (2021) 431-436.

[303] J.L. Bartlett, X. Li, An overview of residual stresses in metal powder bed fusion, Addit. Manuf. 27 (2019) 131-149.

[304] K. Bertsch, G.M. De Bellefon, B. Kuehl, D. Thoma, Origin of dislocation structures in an additively manufactured austenitic stainless steel 316L, Acta Mater. 199 (2020) 19-33.

[305] E.R. Denlinger, J.C. Heigel, P. Michaleris, Residual stress and distortion modeling of electron beam direct manufacturing Ti-6Al-4V, Proc. Inst. Mech. Eng. B: J. Eng. Manuf. 229(10) (2015) 1803-1813.

[306] P. Mercelis, J.P. Kruth, Residual stresses in selective laser sintering and selective laser melting, Rapid Prototyp. J. 12(5) (2006) 254-265.

[307] K. Dai, L. Shaw, Distortion minimization of laser-processed components through control of laser scanning patterns, Rapid Prototyp. J. 8(5) (2002) 270-276.

[308] M. Yakout, M. Elbestawi, S.C. Veldhuis, A study of the relationship between thermal expansion and residual stresses in selective laser melting of Ti-6Al-4V, J. Manuf. Process. 52 (2020) 181-192.

[309] O. Fergani, F. Berto, T. Welo, S. Liang, Analytical modelling of residual stress in additive manufacturing, Fatigue & Fracture of Engineering Materials & Structures 40(6) (2017) 971-978.

[310] W. Keeley, R. Turner, B. Mitchell, N. Warnken, A Development of the Rosenthal Equation for Predicting Thermal Profiles During Additive Manufacturing, Thermo 5(2) (2025) 16.

[311] E. Strumza, P. Landau, G. Kimmel, Y.I. Ganor, O. Yeheskel, S. Hayun, Thermophysical properties of Ti-6Al-4V fabricated by powder bed fusion methods, Addit. Manuf. 58 (2022) 103045.

[312] G. Mi, Y. Wei, X. Zhan, C. Gu, F. Yu, A coupled thermal and metallurgical model for welding simulation of Ti–6Al–4V alloy, Journal of Materials Processing Technology 214(11) (2014) 2434-2443.

[313] D. Kouprianoff, W. du Preez, Reducing time and cost of the heat treatment post-processing of additively manufactured Ti6Al4V, Mater. Today Commun. 35 (2023)

106186.

[314] N. Hansen, Hall–Petch relation and boundary strengthening, Scr. Mater. 51(8) (2004) 801-806.

[315] T. Ahmed, H. Rack, Phase transformations during cooling in α+ β titanium alloys, Materials Science and Engineering: A 243(1-2) (1998) 206-211.

[316] Y. Chong, T. Tsuru, B. Guo, R. Gholizadeh, K. Inoue, N. Tsuji, Ultrahigh yield strength and large uniform elongation achieved in ultrafine-grained titanium containing nitrogen, Acta Mater. 240 (2022) 118356.

[317] P. Shi, Y. Li, Z. Li, X. Jiang, J. Yan, R. Zhou, Y. Qin, Y. Lin, J. Huang, B. Tan, Strong, ductile, and hierarchical hetero-lamellar-structured alloys through microstructural inheritance and refinement, Proceedings of the National Academy of Sciences 122(2) (2025) e2409317121.

[318] G. Liu, S. Wang, A. Misra, J. Wang, Interface-mediated plasticity of nanoscale Al–Al2Cu eutectics, Acta Mater. 186 (2020) 443-453.

[319] Q. Xue, M. Meyers, V. Nesterenko, Self-organization of shear bands in titanium and Ti–6Al–4V alloy, Acta Mater. 50(3) (2002) 575-596.

[320] J. Peirs, W. Tirry, B. Amin-Ahmadi, F. Coghe, P. Verleysen, L. Rabet, D. Schryvers, J. Degrieck, Microstructure of adiabatic shear bands in Ti6Al4V, Mater. Charact. 75 (2013) 79-92.

[321] J. Wang, A. Misra, An overview of interface-dominated deformation mechanisms in metallic multilayers, Current Opinion in Solid State and Materials Science 15(1) (2011) 20-28.

[322] L. Gu, A. Meng, X. Chen, Y. Zhao, Simultaneously enhancing strength and ductility of HCP titanium via multi-modal grain induced extra< c+ a> dislocation hardening, Acta Mater. 252 (2023) 118949.

[323] X. Wu, Y. Zhu, Gradient and lamellar heterostructures for superior mechanical properties, MRS Bulletin 46(3) (2021) 244-249.

[324] P. Cizek, S.R. Kada, N. Armstrong, R.A. Antoniou, S. Slater, P.A. Lynch, Dislocation structures in a Ti–6Al–4V alloy subjected to cyclic tensile deformation, Mater. Sci. Eng. A. 836 (2022) 142700.

[325] X. Li, B. Guan, Y.-L. Wang, Y.-L. Wei, B. Li, Ascertaining the microstructural evolution and strengthening mechanisms of the gradient nanostructured pure titanium fabricated by ultrasonic surface rolling process, Surf Coat Tech. 473 (2023) 130047.

[326] J.-K. Kim, J.H. Kim, H. Park, J.-S. Kim, G. Yang, R. Kim, T. Song, D.-W. Suh, J. Kim, Temperature-dependent universal dislocation structures and transition of plasticity enhancing mechanisms of the Fe40Mn40Co10Cr10 high entropy alloy, Int. J. Plast. 148 (2022) 103148.

[327] P. Liu, B. Hou, A. Wang, J. Xie, Z. Wang, F. Ye, Superior strength-plasticity synergy in a heterogeneous lamellar Ti2AlC/TiAl composite with unique interfacial microstructure, J. Mater. Sci. Technol. 159 (2023) 21-32.

[328] E. Ma, T. Zhu, Towards strength–ductility synergy through the design of heterogeneous nanostructures in metals, Mater. Today 20(6) (2017) 323-331.

[329] S. Qin, Z. Zhang, Z. Yu, L. Zhang, F. Yuan, X. Yao, Tailoring multi-type nanoprecipitates in high-entropy alloys towards superior tensile properties at cryogenic temperatures, Int. J. Plast. 182 (2024) 104132.

[330] B. Fournier, M. Sauzay, C. Caës, M. Mottot, M. Noblecourt, A. Pineau, Analysis of the hysteresis loops of a martensitic steel: Part II: study of the influence of creep and stress relaxation holding times on cyclic behaviour, Mater. Sci. Eng. A. 437(2) (2006) 197-211.

[331] Y. Sun, C. Wang, C. Ren, D. Zhang, K. Li, C.F. Cheung, Z. Chen, Multiscale chemical ordering heterogeneity facilitates exceptional strength and ductility in additively manufactured Ti-added AlCoCrFeNi2. 1 high-entropy alloys at intermediate temperatures, Int. J. Plast. (2025) 104373.

[332] S. Sun, D. Zhang, S. Palanisamy, Q. Liu, M.S. Dargusch, Mechanical properties and deformation mechanisms of martensitic Ti6Al4V alloy processed by laser powder bed fusion and water quenching, Mater. Sci. Eng. A. 839 (2022) 142817.

[333] A. Zafari, M. Barati, K. Xia, Controlling martensitic decomposition during selective laser melting to achieve best ductility in high strength Ti-6Al-4V, Mater. Sci. Eng. A. 744 (2019) 445-455.

[334] M. Tilbrook, K. Rozenburg, E. Steffler, L. Rutgers, M. Hoffman, Crack propagation paths in layered, graded composites, Compos. B: Eng. 37(6) (2006) 490-498.